The University of Sheffield

Investigation of Novel Axial Flux Magnetically Geared Machine

Mohammed F. Hamad Khatab

A thesis submitted for the degree of Doctor of Philosophy (PhD)

Department of Electronic and Electrical Engineering

The University of Sheffield, UK

March 2019

ABSTRACT

As axial flux permanent magnet (AFPM) machines are currently the most appropriate topologies for limited axial space applications, a novel axial flux magnetically geared permanent magnet (AFMGPM) machine is investigated in this thesis. Based on a yokeless and segmented YASA machine, a new AFMGPM topology was designed and studied. The proposed AFMGPM machine consists of stator segments equipped with concentrated windings and two PM rotors with different pole-pair numbers: a high speed rotor (HSR) and low speed rotor (LSR). The proposed AFMGPM offers the merit of simple mechanical structure and is suitable for applications with limited axial space.

Two possible rotor pole combinations were selected and designed with the same stator segments: MG12/5-7 with HSR pole pairs of 5 and LSR pole pairs of 7, and MG12/4-8 with HSR pole pairs of 4 and LSR pole pairs of 8. These were optimised for maximum torque capability. Performance comparisons at no-load and on-load conditions using 3D-finite element analysis (FEM) reveal that the machine torque performance is sensitive to the PM dimensions and better performance can be obtained with the MG12/5-7 topology.

It is demonstrated that the MG machines are a valid alternative to the conventional planetary gear function in HEVs. Combining the conventional PM machine with the MG machine has made it possible to replace the power split components using only one electrical device. Additionally, the proposed machine can work as a conventional magnetic gear (MG) and a generator. It is shown that the new AFMGPM machine can realise the function of power split devices in conventional HEVs, as a mechanical planetary gear, motor and generator. It is further shown that the rotor manufacturing tolerance has a significant effect in terms of stator/LSR misalignment on the no-load and on-load performances of the machine.

Finally, a performance comparison between the novel machine and the conventional axial flux YASA machine is performed. To validate the predicted results of finite element analysis, a prototype of the new topology and a conventional YASA machine are manufactured and tested. It has, showing that with the benefit of two rotors with different torques and speeds, the new AFMGPM machine has a superior performance at all load conditions.

ACKNOWLEDGEMENTS

I would like to express my gratitude to my supervisor, **Prof. Z.Q. Zhu**, for his encouragement, technical discussions and securing the finances to conduct this research. As I am a strong believer that opportunities separate high achievers from their peers, most importantly, I would like to thank him for giving me the opportunity to study for a PhD under his supervision.

I would also like to thank the students and staff of the Electrical Machines and Drives (EMD) Research Group in the Department of Electronics and Electrical Engineering, University of Sheffield, U.K., for their kind unlimited support and assistance with my administrative tasks.

I would like to thank the Libyan Ministry of Higher Education and Scientific Research, for financial support for my PhD study.

Finally, I thank my wife ASMA AIAD for her patience. I dedicate this thesis to my parents (Faraj Khatab & Salema Dayhom), whose are the most important people in my life.

NOMENCLATURE

A_a	Coil area	mm^2
k_{pf}	Packing factor	
$\emptyset_g$	Air-gap flux	Wb
h_m	Magnet thickness	mm
h_s	Stator slot width	mm
B_g	Air-gap flux density	T
B_m	PM maximum flux density	T
C_T	Cogging torque factor	
D_{av}	Average diameter	mm
D_i	Inner diameter	mm
D_o	Outer diameter	mm
E_{Hm}	High speed rotor EMF amplitude	V
E_{Lm}	Low speed rotor EMF amplitude	V
E_{tm}	Total EMF amplitude	V
F_{axial}	Axial pull force	N
G_0	Air-gap axial length	mm
G_{max}	Maximum air-gap axial length	mm
G_{min}	Minimum air-gap axial length	mm
G_r	Gear ratio	
$I_{a\ RMS}$	RMS phase current	A
K_d	Distribution factor	
K_p	Pitch factor	
K_w	Winding factor	
K_T	Torque constant	Nm/Amp.
L_M	Total axial length	mm
L_a	Coil active length	mm
L_r	Rotor axial thickness	mm
L_s	Stator axial length	mm

N_a	Number of turns per phase	
N_c	Least (smallest) common multiple	
P_h	Hysteresis loss	W
P_{cu}	Copper loss	W
P_e	Eddy current loss	W
R_a	Phase resistance	Ω
R_o	Outer radius	mm
S_g	Magnet surface area	mm^2
S_{pp}	Number of slots per pole per phase	
T_{ripple}	Torque ripple	%
T_C	Cogging torque	Nm
T_{avg}	Average torque	Nm
T_{max}	Maximum torque	Nm
T_{min}	Minimum torque	Nm
T_o	Output torque	Nm
V_e	Element volume	m^3
Wh_e	Hysteresis loss for each element	W
W_e	Element Joule loss	W
n_c	Number of coils per phase	
n_s	Number of stator poles	
ne	Number of elements	
p_h	Number of high speed rotor pole pairs	
p_l	Number of low speed rotor pole pairs	
w_c	Stator slot depth	mm
α_p	Magnet surface area to air-gap area ratio	
θ_H	Angular position of high speed rotor	mech. deg.
θ_L	Angular position of low speed rotor	mech. deg.
θ_m	Magnet arc angle	mech. deg.
θ	Rotor angular position	elec. deg.
θ_o	Rotor initial position	elec. deg.

μ_r	Relative permeability	$H.m^{-1}$
τ_m	Rotor pole pitch	mech. deg.
τ_s	Stator pole pitch	mech. deg.
ω_h	High speed rotor rotation speed	rad/sec
ω_l	Low speed rotor rotation speed	rad/sec
ω_m	Rotor speed	rad/sec
ω_s	Modulator speed	rad/sec
ω	Angular frequency	rad/sec
R	Air-gap reluctance	AT/Ω
e	Phase back EMF	V
f	Frequency	Hz
m	Number of phases	
p	Rotor pole pairs	
t	Greatest common divisor	
α	Phase shift of total EMF waveform	elec. deg.
β	Current angle	elec. deg.
δ	Load angle (relative angle)	elec. deg.
δ_F	Maxwell stress tensor	N/mm^2
ρ	Copper resistivity at room temperature	Ω.m
σ	Skin depth	m

ABBREVIATIONS

2D-FEA	Two dimensional finite element analysis
3D-FEA	Three dimensional finite element analysis
AC	Alternating current
AF	Axial flux
AFHE	Axial Flux machine with hybrid excitation
AFMG	Axial flux magnetically geared
AFMGPM	Axial flux magnetically geared permanent magnet
AFPM	Axial flux permanent magnet
AFPS-SFPM	Axial flux partitioned stator switching flux PM
AFSFPM	Axial flux switching flux PM
DC	Direct current
DRAF-FSPM	Dual rotor axial flux - flux switching PM
FFT	Fast Fourier Transformation
GCD	Greatest common divisor
HEV	Hybrid electric vehicle
HSR	High speed rotor
ICE	Internal composite engine
LCM	Smallest common multiple
LSR	Low speed rotor
MFM-BDRM	Magnetic field modulated brushless double rotor motor
MG	Magnetic gear
MMF	Magneto-motive force
PM	Permanent magnet
RFPM	Radial flux permanent magnet
SMC	Soft magnetic composite
SPM	Surface mounted permanent magnet
UMF	Unbalanced magnetic force

CONTENTS

ABSTRACT I

ACKNOWLEDGEMENTS II

NOMENCLATURE III

ABBREVIATIONS VI

CONTENTS VII

CHAPTER 1

GENERAL INTRODUCTION

1.1 Introduction 1

1.2 Power split application in HEVs 2

1.3 Axial flux PM machine configurations 5

1.3.1 Single-sided AFPM machine topology 5

1.3.2 Double stator- single rotor AFPM machine topologies 6

1.3.3 Single stator-double rotor AFPM machine topologies. 8

1.3.4 Multi rotor- multi stator AFPM machine 13

1.4 Axial flux magnetic gear and magnetically geared machine topologies 14

1.4.1 Axial flux magnetic gear topologies 15

1.4.2 Axial flux magnetically geared machine topologies 18

1.5 Research scope, objectives and contributions 23

1.5.1 Research scope and objectives 23

1.5.2 Research contributions 27

PUBLICATIONS 28

CHAPTER 2

YOKELESS AND SEGMENTED ARMATURE (YASA) AXIAL FIELD PM MACHINE

2.1 Introduction 29

2.2 YASA machine configuration and principle of operation 30

2.3 Optimisation of YASA machine. 34

2.4 Influence of critical parameters on machine performance 36

2.4.1 Influence of PM dimensions 36

2.4.2 Influence of slot depth and slot width 38
2.5 Comparison of machine performance for different rotor pole combinations 40
2.5.1 Cogging torque 41
2.5.2 No-load flux density 41
2.5.3 No-load flux linkage and back EMF 45
2.5.4 Electromagnetic torque 46
2.5.5 Losses and efficiency 50
2.6 Summary 53

CHAPTER 3

NOVEL AXIAL FLUX MAGNETICALLY GEARED MACHINE DESIGN

3.1 Introduction 54
3.2 Proposed axial flux MG machine configuration 55
3.3 Principle of operation 56
3.3.1 Magnetic gear torque 57
3.3.2 PM flux density 58
3.3.3 Armature current flux density 61
3.4 Stator/rotor pole number combination of the proposed magnetically geared machine 62
3.5 Global optimisation of AFMGPM machine 63
3.6 Influence of critical parameters on machine performance 67
3.6.1 Influence of PM dimensions 67
3.6.2 Influence of slot depth 70
3.6.3 Influence of slot tips thickness 70
3.6.4 Influence of slot opening width 71
3.6.5 Influence of the ratio between outer and inner machine diameters 73
3.7 Performance analysis of proposed optimised AFMGPM machine 74
3.7.1 No-load flux density 75
3.7.2 No-load flux linkage and back EMF 79
3.7.3 Cogging torque 84
3.7.4 Torque 86
3.8 Performance comparison of axial flux magnetically geared machine and YASA machine 91

3.8.1 No-load flux linkage and back EMF 91
3.8.2 Torque 95
3.9 Summary 100

CHAPTER 4

AXIAL FLUX MAGNETICALLY GEARED MACHINE FOR POWER SPLIT APPLICATION IN HEVS

4.1 Introduction 101
4.2 Proposed system of axial flux magnetically geared machine. 102
4.2.1 Power split mode (Mode 1) 102
4.2.2 Magnetically geared motor mode (Mode 2) 102
4.2.3 Pure electric drive mode (Mode 3) 103
4.3 Performance analysis of the proposed magnetically geared machine at different operation modes. 103
4.3.1 Flux linkage and back EMF 104
4.3.2 Torque 109
4.3.3 Axial force 118
4.3.4 Losses and efficiency 120
4.3.5 Influence of machine size on power output 127
4.4 Proposed control method of AFMGPM machine 128
4.5 Summary 132

CHAPTER 5

INFLUENCE OF STATIC AND DYNAMIC ROTOR/STATOR MISALIGNMENTS IN AXIAL FLUX MAGNETICALLY GEARED MACHINES

5.1 Introduction 133
5.2 Static and dynamic LSR/stator misalignments 135
5.3 Influence of LSR/stator axis misalignment on machine performance 136
5.3.1 Cogging torque. 136
5.3.2 Air-gap flux density 140
5.3.3 Back EMF 143
5.3.4 Torque 145
5.3.5 Unbalanced force 147

5.4 Influence of LSR/stator angular misalignment on machine performance 155
5.4.1 Cogging torque 155
5.4.2 Air-gap flux density 157
5.4.3 Back EMF 159
5.4.4 Torque 163
5.4.5 Unbalanced force 165
5.5 Summary 173

CHAPTER 6

PROTOTYPE MACHINE DESIGN AND VALIDATION OF EXPERIMENTAL RESULTS

6.1 Introduction 175
6.2 Prototype dimensions and manufacturing process 176
6.2.1 YASA machine design and validation of test results 178
6.2.2 Magnetically geared machine prototype and validation of test results 184
6.3 Performance comparison of magnetically geared and YASA prototypes 196
6.3.1 Cogging torque 197
6.3.2 No load back –EMF 198
6.3.3 Static torque 199
6.4 Summary 202

CHAPTER 7

CONCLUSIONS AND FUTURE WORK

7.1 Conclusions 203
7.2 Future work 205
REFERENCES 208
APPENDIXES 219

APPENDIX A

THEORY OF ELECTROMAGNETIC AND DESIGN METHODOLOGY

A.1 Introduction 219
A.2 Basic magnetic principle of PM machines 219
A.2.1 PM magnetic flux density 219
A.2.2 Electromagnetic torque production 221

A.3 Design and analysis methodologies of axial flux machines 222
A.3.1 Design assumptions and constant parameters 222
A.3.2 Design and analysis methodology of 2-D models 223
A.3.3 Design and analysis methodology of 3-D model 225
APPENDIX B.
COMPARATIVE STUDY OF AXIAL FLUX MAGNETICALLY GEARED MACHINE AND YASA MACHINE.
B.1 Introduction 232
B.2 AFMGPM and YASA machine geometries 233
B.3 Comparison of MG12/5-7 with conventional YASA12/10 and YASA12/14 machines 234
B.3.1 Cogging torque 234
B.3.2 No-load air-gap flux density 235
B.3.3 Electromagnetic torque 236
B.4 Comparison of MG12/4-8 with conventional YASA12/8 and YASA12/16 machines 237
B.4.1 Cogging torque 237
B.4.2 No-load air-gap flux density 238
B.4.3 Electromagnetic torque 239
B.5 Losses and efficiency 246
B.6 Summary 248
APPENDIX C.
MATERIAL CHARACTERISTICS
C.1 Soft magnetic composite material characteristics 249
C.2 Mild steel lamination B-H curve 250
APPENDIX D.
PROTOTYPE DESIGN DRAWINGS 251

CHAPTER 1

GENERAL INTRODUCTION

1.1 Introduction

The current demand for high performance electrical machines for many applications has led to permanent magnet (PM) machines providing the best opportunity for meeting the necessary requirements. The progress in development of power electronics and PM materials has given a strong boost to PM machine innovations. PM machines have thus attracted considerable interest among researchers. Axial field permanent magnet (AFPM) machines have attracted significant research attention thanks to their unique advantages over radial flux PM (RFPM) machines, such as high torque density, low rotor losses, and high efficiency [AYD04]. The main difference between axial and radial machines is in the flux direction. In axial flux machines, the flux passes axially from the stator to the rotor, while in radial flux machines the flux flow passes radially from the stator towards the rotor. In fact, each kind of AFPM machine has its RFPM counterparts. Moreover, the disc type shape of the machine makes it suitable for limited axial space applications. The machine can also potentially be developed for many different topologies due to its axial air-gap.

In many industrial applications, mechanical gears are widely used for delivering torque and speed from the prime-mover to other rotating components [HES80]. However, due to the physical contact, frequent maintenance, high fraction losses and large vibration and noise are inevitable. Therefore, due to being contactless, magnetic gears (MGs) are currently being developed in an attempt to replace mechanical gears [ATA01]. The development of MG topologies in which modulation rings are located between the two rotors has encouraged researchers to create new types of cascaded electrical machines (i.e. magnetically geared machines) which are permanent magnet machines with MGs integrated into the same frame [TLA14].

Because of their high efficiency, fuel economy and low emission, hybrid electric vehicles (HEVs) have been regarded as the most realistic substitute for conventional fuel vehicles [MIL06]. In HEVs, a mechanical planetary gear is normally used to transmit and split the power produced by an internal combustion engine (ICE). However, planetary gears exhibit the same problems as conventional mechanical gears, namely, lubrication and mechanical loss [NIU13a]. To overcome these drawbacks, magnetically geared machines have been introduced to realise a power split function.

To study power split application to the HEV, this thesis develops a novel axial flux magnetically geared PM (AFMGPM) machine from the conventional yokeless and segmented armature YASA machine. The novel topology with different rotor pole combinations is comparatively studied with the conventional YASA machine. It is useful first to provide a definition of power split application and the configuration of AFPM machines as well as a review of the literature of the existing topologies of axial flux magnetic gear and magnetically geared machine topologies.

1.2 Power split application in HEVs

The requirements for environmental protection and energy saving have led to significant improvements in high performance electric machines and hence their Powertrain application. Among the motivation technologies, the HEV, a vehicle driven by a battery powered electric motor in addition to the conventional engine, has great potential in terms of energy saving and environmental protection since it has the merits of fuel economy, low carbon emission and energy efficiency. The HEV uses two power systems: a conventional internal combustion engine (ICE) and electric motor/generator set [EHS07]. In other words, additional power sources are added to the conventional power source of the vehicle, such as an electrical motor, a generator and a battery, and the vehicle is driven through linking these components [BOR09]. Different hybrid power configurations have been proposed according to the ways in which these components are combined, for example, series, parallel and series parallel (Power split). In series drive train applications, a motor is used to drive the wheels, fed by either a generator or a battery as depicted in Fig. 1.1(a). In this type of application, the generator is driven by the ICE and the electric motor can be either connected to a mechanical gear or be part of the vehicle wheel itself (in-wheel motor). Meanwhile, in a parallel configuration the drive wheels are driven by both the ICE and the motor individually and simultaneously, as shown in Fig. 1.1(b). Different configurations result in different drive train performance and operating characteristics. However, combining the series and parallel configurations results in a unique performance configuration known as power split whereby the ICE is decoupled from the drive wheels.

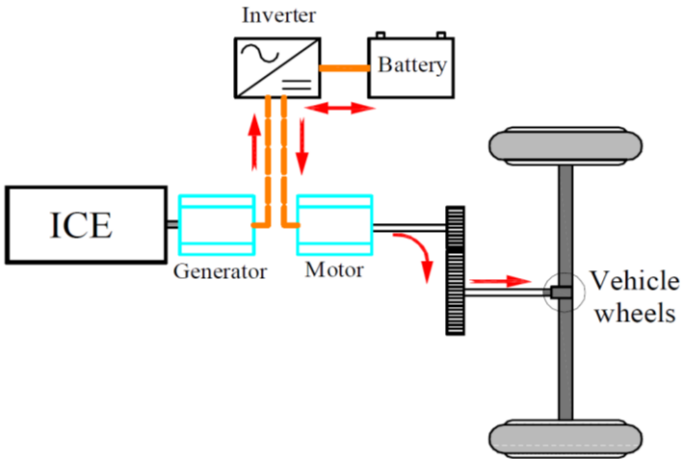

(a) Series hybrid configuration

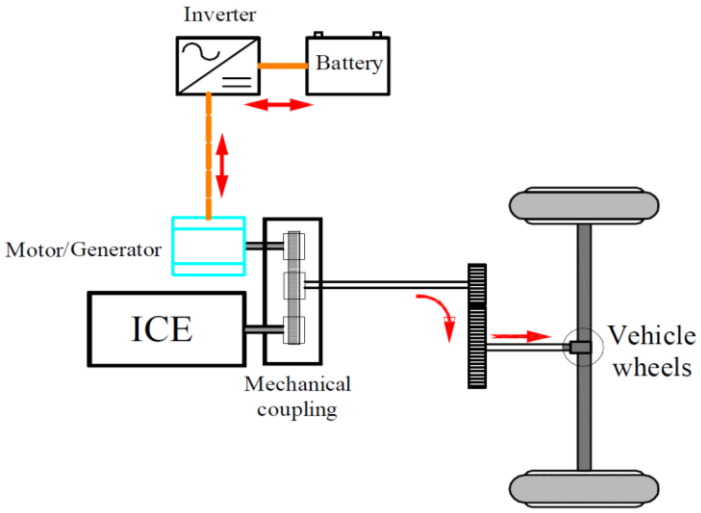

(b) Parallel hybrid configuration

Fig. 1.1. Drive train configurations in HEVs.

Significant improvements have been made to the series/parallel or power split drive train configuration. Recently a specific mechanical gear device known as planetary gear has been used in order to split the power obtained from the ICE between the generator and the wheels. This mechanical power splitting device was initially invented by Toyota and has recently been incorporated into commercial HEVs [SAS98]. Fig. 1.2 shows the planetary gear device construction, which consists of three components, the ring gear set, the carrier with planet gear set, and the sun gear set. The sun gear is located in the centre of the device and surrounded by a set of revolving planet gears which are linked together by a movable carrier. The ring gear is located in the outer side of the planet gears. The gear parts work at different speeds and the system has different operation modes depending on what component is connected to what part of the power split device [GOU11], [DU10].

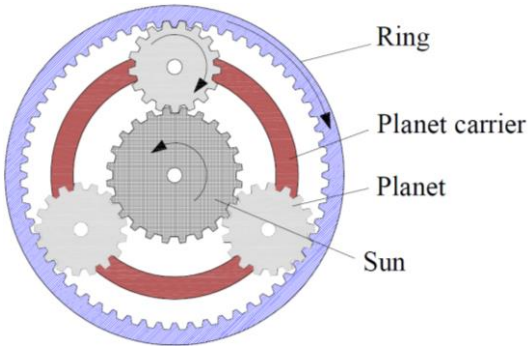

Fig. 1.2. Planetary gear configuration.

Fig. 1.3 depicts the power split scheme used in HEVs, in which the planetary gear unit functions to split the ICE input power into two output parts. When the carrier gear is connected to the ICE, the sun gear is used to drive the generator and the motor to the ring gear which is connected to the wheels. Alternatively, the generator can also work as a motor to deliver mechanical power to the conventional gear box and then to the wheels. Moreover, when the ICE is in high efficiency mode, the mechanical transmission drives the wheels directly, whereas in power split mode, a part of the ICE power must be delivered as electrical power by the generator which operates to charge the battery [YAN12].

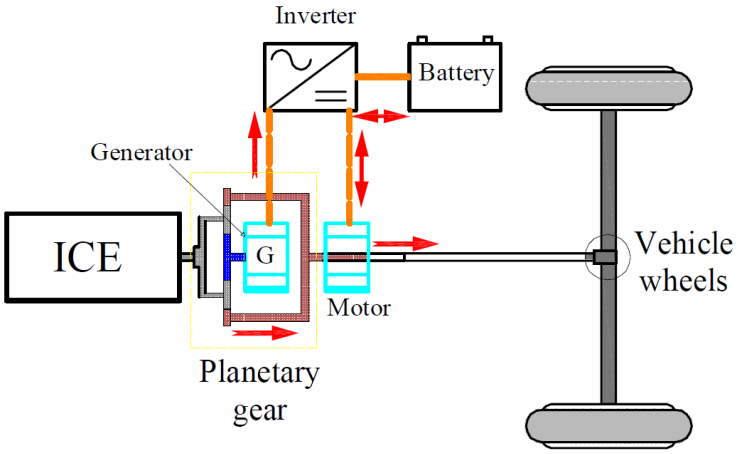

Fig. 1.3. Planetary gear function of power split in HEVs [YAN12].

Planetary gear can offer high power density, smooth torque transmission and the flexibility to drive the vehicle efficiently. In addition, the power split system minimises fuel consumption, while the incorporation of an electric traction system gives the vehicle high performance and quick acceleration [BOR09]. Furthermore, it can be independently operated at different speeds and torques regardless of the wheel speed. However, planetary gear has a large bearing load since it has several rotating gear sets [GOU11]. Moreover, due to the physical contact of the planetary components, lubrication and regular maintenance are required [HES80].

1.3 Axial flux PM machine configurations

Improvements to AFPM synchronous machines have led them to becoming an appropriate choice in the direct drive system for numerous applications. It has been confirmed that when the axial length is short, higher torque density can be produced by axial flux machines than by radial machines. These machines offer unique design features of short axial length, small magnet volume and easily adjustable air-gap, in addition to their merits of high torque density, smooth torque, and greater efficiency due to reduced rotor loss compared with the conventional RFPM machines [AYD02] [GIU12]. However, development of this machine has increased only gradually compared to that of RFPM machines because of fabrication difficulties with the stator lamination as well as the attraction force between stator and PM rotor [KAH14], [HUA14a]. The AFPM machine topologies can be classified with regard to their configuration as detailed in Fig. 1.4.

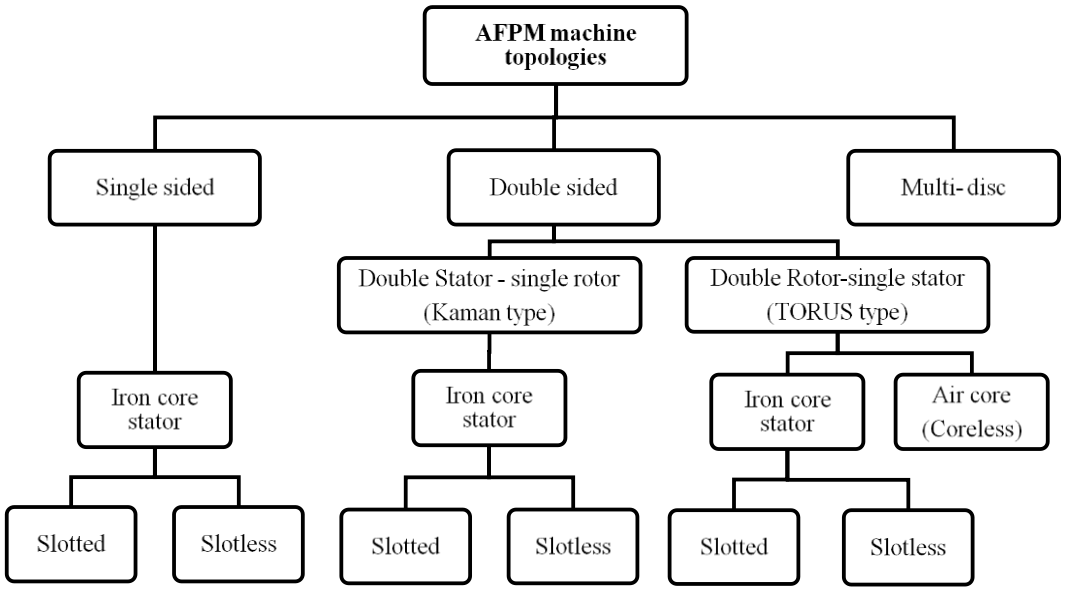

Fig. 1.4. AFPM machine topologies.

AFPM machines can in general be classified into four main types according to the machine stator and rotor numbers [AYD04]. Moreover, the different types can be with or without stator core, with or without stator slots, and can be classified with respect to the stator windings type, whereby the winding distribution is determined with regard to the flux direction through the stator core. The main types of AFPM machine topologies can be briefly described as follows.

1.3.1 Single-sided AFPM machine topology

This type, also known as the single stator – single rotor or disc type machine, has the simplest structure of all the AFPM machines. The topology, as seen in Fig.1.5, consists of a single iron

disc stator core with windings which are either wound axially around the stator core or fitted and embedded in slots. The rotor is formed from iron steel disc with PMs located in the rotor's inner surface, facing the stator windings [AYD04]. In other stator topologies the windings may be embedded in the stator slots, in what is called the slotted stator, Fig.1.5(a), or located on the surface of the stator, in what is known as the slotless stator single sided machine topology as illustrated in Fig.1.5(b). Further possible variations include concentrated or non-overlapping windings and distributed windings [KAH14].

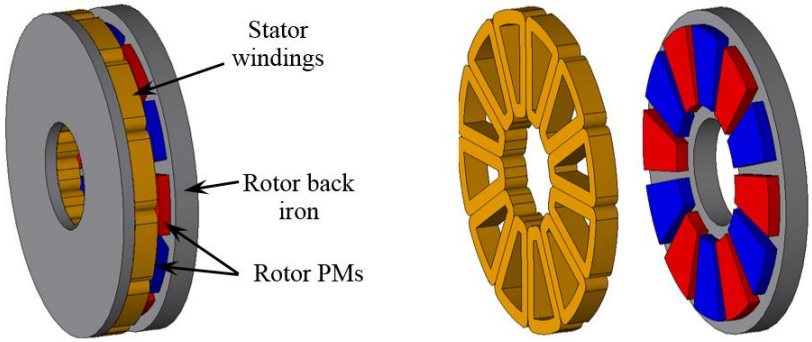

(a) Slotted stator with concentrated windings

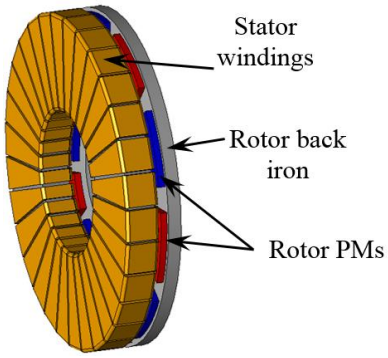

(b) Slotless stator with ring windings

Fig.1.5. Single sided AFPM machine structure [KAH14].

Nevertheless, despite the advantages of this topology and its applications in electromechanical drives and transportation, the machine has several drawbacks that include the large and unequal axial force exerted in the stator due to the rotor magnet, which may result in twisting of the machine structure. Moreover, although a complex bearing arrangement can be used to address this issue, this results in an increase in the machine manufacturing cost [CHE03][COL08].

1.3.2 Double stator- single rotor AFPM machine topologies

The double stator or interior rotor AFPM machine has one permanent magnet rotor disc, and two stators located on two sides of the rotor. The PMs can be located inside or on the surface of the rotor core, facing two stators. The machine stators can be slotted, in which case the windings are

embedded in the slots, (Fig. 1.6(a)), or slotless, where the windings are wound around the stator core as shown in Fig. 1.6(b). However, for slotless topologies, the torque is produced by the inner winding conductors facing the rotor PMs, while the conductors on the outer stator side will not contribute for torque production. On the other hand, in the slotless stator the end windings are fairly long, which leads to more copper loss, and consequently, lower efficiency compared to the slotted stator [KAH14].

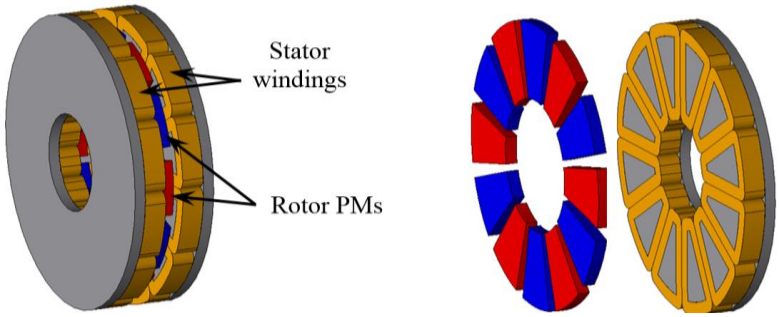

(a) Slotted interior PM motor configuration

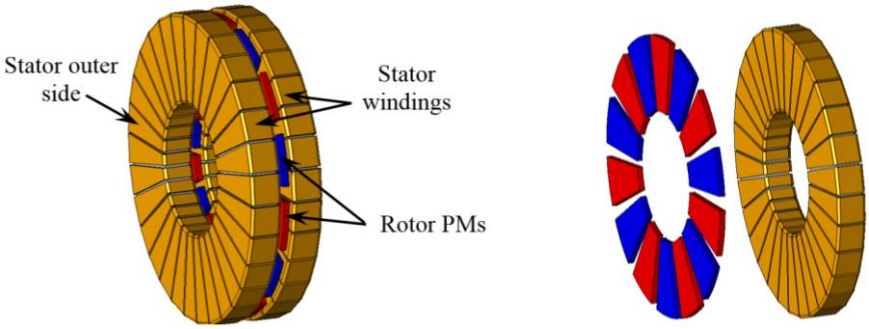

(b) Slotless interior PM motor configuration

Fig. 1.6. Interior rotor AFPM machine structure [HUA02].

The interior rotor axial flux topologies can also differ in terms of the PM location. The PMs can be fitted inside the rotor core where there is more space available in the air-gap for the stator winding. Moreover, since the main flux flows axially through the rotor, a non- ferromagnetic material is used for the rotor core, which provides rigidity of the rotor and significantly eliminates iron losses in the rotor. Nevertheless, despite the rotor being coreless, the stator iron loss and the copper loss are significantly high, since this topology utilises a double stator with armature windings [AYD06]. In fact, numerous topologies have been invented for interior rotor AFPM machine topology. In addition to the interior PM rotor, an axial flux switching flux PM (AFSFPM) topology has been presented in [MIN11]. The stator has armature windings and PMs, whereas the rotor is completely passive, which is preferable for high speed applications, as shown in Fig. 1.7. In addition, to achieve more winding space and thus more torque density, a modified topology known as axial flux partitioned stator switching flux PM (AFPS-SFPM) topology has been developed and analysed in

[ZHU15c] [KHA15]. The machine has two stators, each with different excitation, with one stator using armature winding and the other using magnets, as indicated in Fig. 1.8.

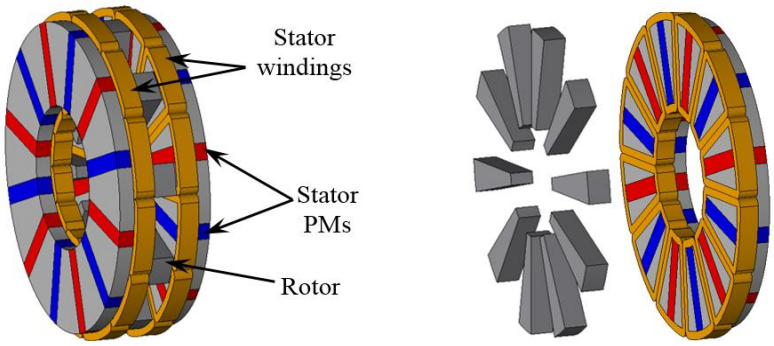

Fig. 1.7. AFSFPM machine topology [MIN11].

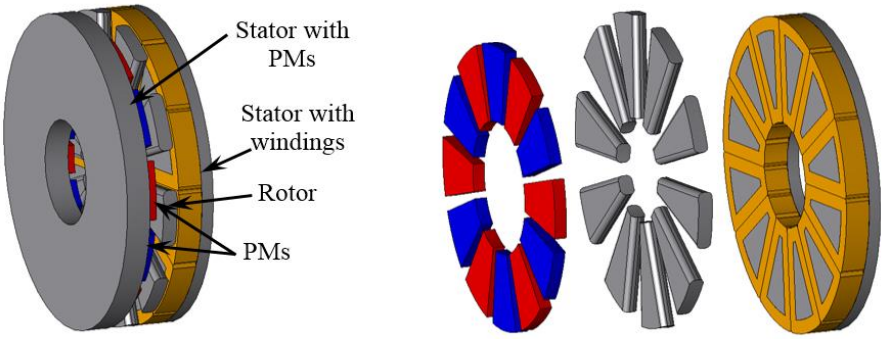

Fig. 1.8. AFPS-SFPM machine topology [ZHU15c].

1.3.3 Single stator-double rotor AFPM machine topologies.

This may be called the interior stator AFPM machine as it has a double sided stator sandwiched between two PM rotor discs. The stator may be either slotted with embedded winding or slotless with coils wound around the stator core. Identical disc shaped rotors face the two stator sides, each rotor having surface mounted PMs.

Several high performance interior stator AFPM machine topologies have been developed and analysed. Moreover, based on the presented topologies, these AFPM machines with internal stator configuration are inherently suited to drive train applications and have hence been widely developed and investigated. For example, a double-sided AFPM model with an internal ring shape stator core, known as the TORUS toroidal slotless stator machine, has been developed as a DC machine [SPO92]. Toroidal rectangular windings are wound on the surface of the core of the stator with air-gap portions between the windings filled with epoxy resin. However, a large PM volume is always required for this machine to produce a certain flux density in the air-gap. It has a relatively large air-gap since the windings are directly located on the stator sides (Fig. 1.9). Therefore, in the slotless TORUS topology, sectors or pie- shaped windings provide superior stator core utilisation

and less air-gap thickness, as can be seen in Fig. 1.9(b), [AYD06]. Moreover, because the machine has a slotless stator, there is practically no cogging torque. Following the concept of TORUS toroidal topology, a further slotted stator with windings sandwiched between surface mounted PM rotors has been presented in [HUA01]. The machine has two main topologies which depend on the arrangement of the PM polarity, and hence, the flux direction. The first type is TORUS NN, in which the arrangement of PMs allows the flux to pass axially from where the rotor enters the stator and pass circumferentially along the stator iron core. It then returns to the rotor core through the opposite polarity pole (Fig. 1.10). In this topology, large yoke thickness is employed to fit the flux entering from both rotors, which increases the iron losses and the end windings. However, in the phase winding layout, the same method of winding around the stator core can be used as in the toroidal rectangular stator winding topology. Therefore, due to the large windings fill factor, the copper loss is reduced, improving the efficiency of the machine.

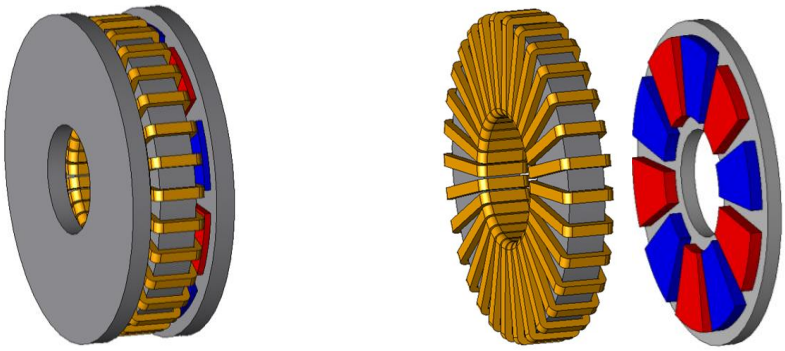

(a) Slotless rectangular stator windings TORUS topology

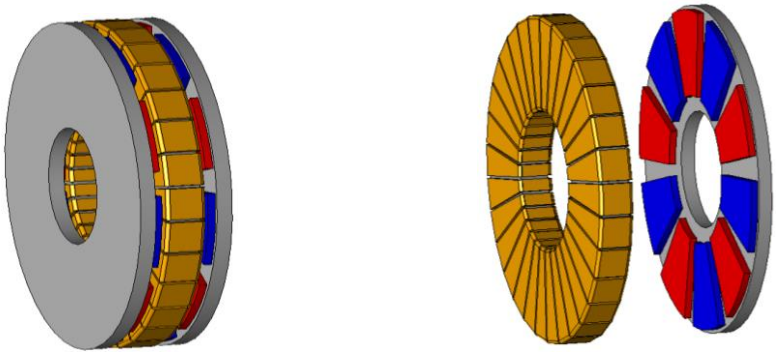

(b) Slotless pie-shaped stator windings TORUS topology

Fig. 1.9. TORUS toroidal slotless stator machine model [HUA02].

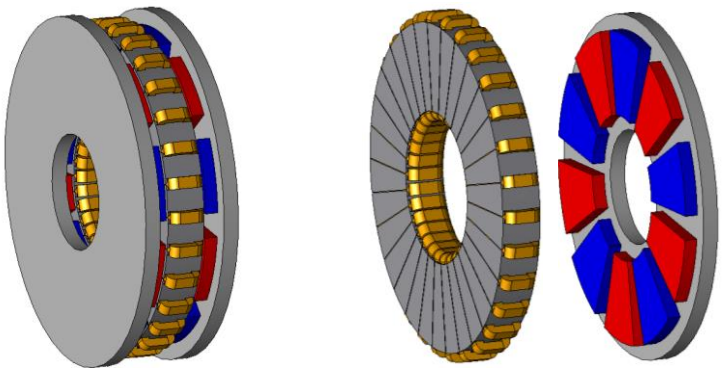

Fig. 1.10 TORUS NN topology [HUA01].

Fig. 1.11 shows the second topology of the TORUS-NS type machine. Either three phase distributed windings or concentrated windings can be employed for this topology. The magnets on the two rotors facing each other on either side of the stator are arranged to be N and S of PM poles. Therefore, the flux path passes axially through the stator and both air-gaps to the other rotor. Since the flux path passes axially instead of circumferentially through the stator core, the stator yoke is eliminated compared to the TORUS NN type. The design differences between TORUS NN and NS topologies are the thickness of the stator core and the arrangement of the PM polarity and windings. Moreover, TORUS NS topology has lower cogging torque and higher torque quality, whereas the torque ripple is low compared to TORUS NN topology [HUA01] [AYD06].

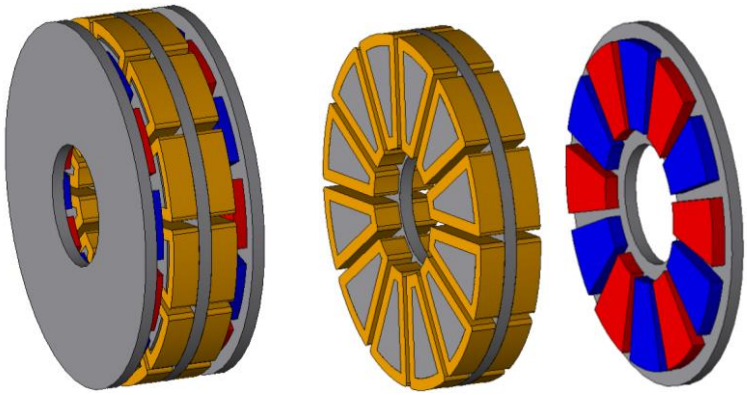

Fig. 1.11 NS machine structure [HUA01].

In addition, this topology has been designed having two PM rotors and proposed for HEVs application in [TUT12]. The topology has the same structure as the NS machine shown in Fig. 1.11. However, it consists of two surface mounted PM rotors with different numbers of poles, i.e. 10 and 14 poles. Both rotors are totally independent in which, one rotor is connected to the ICE and the other connected to the drive wheels. A stator with 12 slots is located between the two rotors. The windings of each stator side are used to control each rotor individually. Both rotors are

independently controlled by different frequency controllers. In other words, the machine is a combination of two single sided axial flux topologies sharing the same stator back iron, and hence different operations of the two electric machines could be achieved. One stator side can be used to drive the rotor which is connected to the load, while the winding on the other side is used as a generator. A method of coupling both rotors mechanically utilising magnetic clutch when the load is driven by the ICE is also presented.

Fig. 1.12 shows an additional topology which can be created from the TORUS-NS type, known as coreless or yokeless TORUS topology. The NS type has no stator core; instead, the stator structure contains windings wound around non-magnetic material sandwiched between two rotor discs with surface mounted PMs. Whilst either concentrated windings or distributed windings can be used for coreless TORUS topology, it has been verified that concentrated winding is the most beneficial in this application due to its shorter end windings [XIA15]. Furthermore, the absence of the stator core loss enhances the efficiency of yokeless topology. Moreover, the cogging torque as well as the torque ripple are negligible. However, since the windings are directly placed in the air-gap and exposed to the magnetic flux produced by the PMs on two rotors, significant eddy current loss in the stator windings may occur when operating at relatively high frequencies.

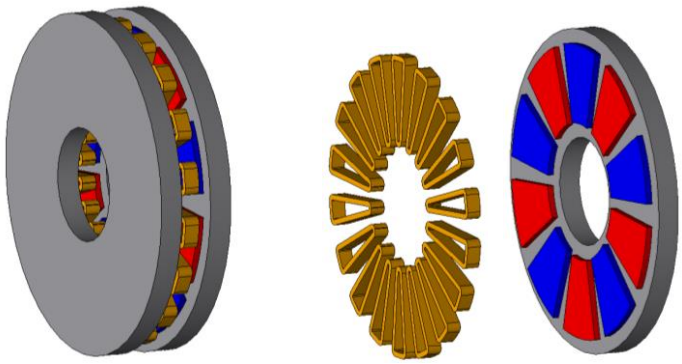

Fig. 1.12 Coreless NS machine structure [KAH14].

Additionally, an Axial Flux machine with Hybrid Excitation (AFHE) has been recently presented in [CAP14]. The machine has a single stator in which toroidal windings are placed around the stator core. With this machine two different rotor topologies are employed (Fig. 1.13). The first rotor is a disc core with surface mounted PMs. The second is a wound rotor with slip rings and brushes. The machine has three operation modes. In the first mode the rotor coil excitation current is zero in which the wound rotor is not contribute to the flux production and the PM flux linkage circulates between the PM rotor and the stator core. Meanwhile, in the second operation mode the positive excitation current is injected into the wound rotor coils and the PM and the rotor coil fluxes are

combined in the stator core. In this case, the no-load flux linkage of the stator winding increases to its maximum value since both the PM and the wound rotor are contributing to the stator flux linkage. This operation mode is magnetically equivalent to the TORUS machine shown in Fig. 1.10. The last operation mode involves the inversion of the excitation current. The rotor flux and the PM flux have the same direction and the stator flux linkage decreases to approximately zero value since the PM flux is totally short-circuited through the wound rotor. In terms of the performance, AFHE can be operated at speeds above the rated speed due to the possibility of wide stator flux linkage regulation capability. It can be obtained by controlling the excitation current and hence the back EMF produced by the wound rotor to compensate the rise of the PM EMF due to the increase of the speed. This strategy can achieve a constant power generation at different rotor speeds. However, this topology may suffer from copper loss since in addition to the armature reaction windings, more copper has to be used in the excitation rotor. Moreover, AFPM topologies with passive dual rotors have also been proposed; for example, a dual rotor axial flux - flux switching PM (DRAF-FSPM) that is presented in [HAO12] is illustrated in Fig. 1.14.

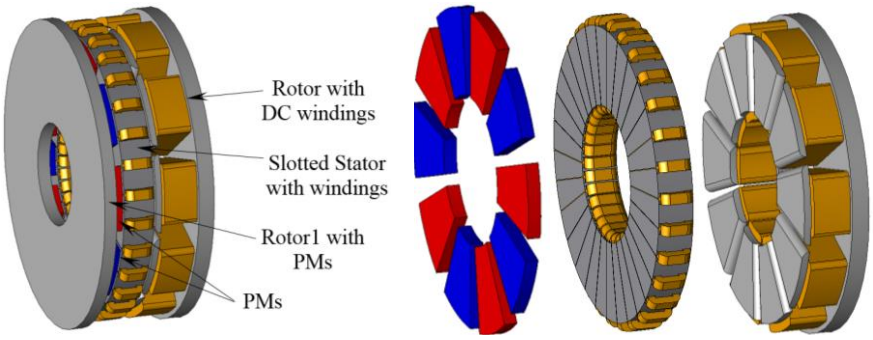

Fig. 1.13. Axial flux hybrid excitation synchronous machine [CAP14].

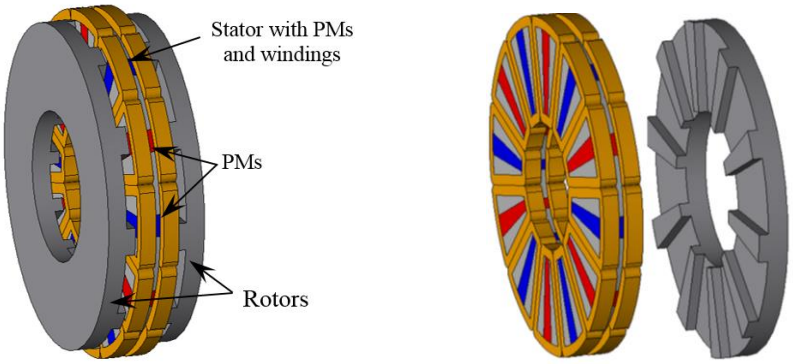

Fig. 1.14. DRAF-FSPM machine topology [HAO12].

It has been confirmed that dual PM rotor topologies have consistently high torque density and efficiency compared to the other AFPM topologies since they have low rotor loss and higher air-gap flux density. In addition, yokeless and segmented armature (YASA) topology, designed for

drive train applications, is an internal stator AFPM machine topology which has motivated the work of many researchers. This has been found to be the most suitable candidate yet for the application of soft magnetic composite (SMC) material. Description of the structure, optimisation and analysis of the YASA machine will be presented in Chapter 2.

1.3.4 Multi rotor- multi stator AFPM machine

A multistage axial field PM machine can be built using a combination of either interior rotor or interior stator topologies. The multistage structure of the machine has *n* stator and *n*+1 PM rotor where *n* is the number of machine stators, as shown in Fig. 1.15. The multi rotors are connected to the same shaft; additionally, the stator windings can be connected either in a series or parallel. In a coreless rotor structure, only the outer rotors are made from ferromagnetic material since they handle the machine main flux [AYD04].

Because torque production is a function of the outer diameter of the machine, this topology is used when more torque is needed with limitation of the outer diameter. When multi stators and multi rotors are employed, more power and torque can be achieved without increasing the diameter of the machine. Moreover, multistage AFPM machines may be built using slotted or slotless stators, iron or ironless rotors, and the arrangement of PMs is the same as for the single sided structure.

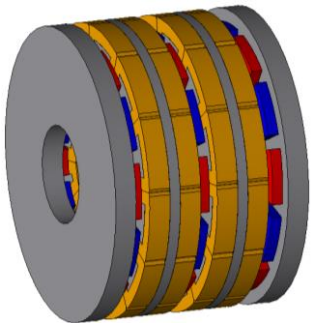

Fig. 1.15. Multi stage PM machine [KAH14].

In conclusion, numerous AFPM machine topologies have recently been employed for various applications, for example, in HEVs [MAL14]. In particular, aspects of HEVs such as torque, speed and electric machine space are currently being considered by many researchers in order to meet the requirements of this application. Hence, axial flux magnetic gear and magnetically geared machines have been proposed for electrical machine applications, due to the additional features they bring to such as the machine structure. These topologies are further discussed in the following section.

1.4 Axial flux magnetic gear and magnetically geared machine topologies

The idea of magnetic gears (MGs) has been discussed since the beginning of the 20th century. In fact, early magnetic gear topologies were designed according to their equivalent mechanical counterparts as indicated in Fig. 1.16. This can be achieved by replacing the slots and teeth of mechanical gears with N-poles and S-poles of PM arrangements. MGs can in general be classified into two configurations: converted topologies and field modulated topologies [NEV14], [TLA14]. A simple converted type was initially presented in [KIK93]. However, the torque densities of these MGs were poor compared to those of mechanical gears, a failing attributed to the poor performance of available PM materials as well as the utilisation of PMs [RAS03]. The second configuration, field modulated topology, has also been studied recently and design improvements have been made. Due to the advent of high energy density PMs, for example, neodymium iron boron (NdFeB), increasing attention has been paid to flux modulated MGs and these are currently being developed to replace conventional mechanical gears in various electromechanical systems [NEV14]. A significant improvement in this technology occurred with the development of a high performance radial field concentric MG topology presented in [ATA01]. In addition, rare- earth magnets have been employed for this topology. The set-up consists of two surface mounted PM rotors, which are rotated at different speeds according to their pole numbers, with ferromagnetic pole pieces interposed between the two rotors as can be seen in Fig. 1.17. This topology has a torque density of approximately 100 kNm/m^3. Following the same basic design for the radial MG, many other topologies have since proposed and developed.

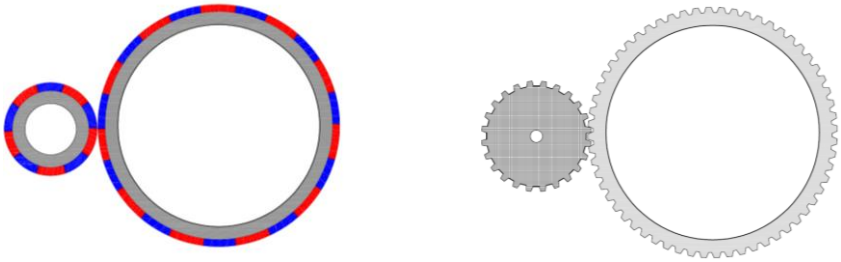

(a) External spur gear

(b) Internal spur gear

Fig. 1.16. Magnetic gears and corresponding mechanical topologies.

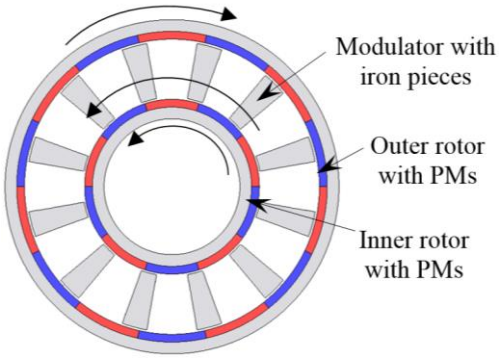

Fig. 1.17. Radial field concentric MG [ATA01].

1.4.1 Axial flux magnetic gear topologies

Since, as was stated earlier, axial flux topologies offer the advantage of high torque density compared to their radial counterparts, numerous axial flux MG topologies have been devised. An axial modulated flux magnetic gear was initially presented in [MEZ06]. The topology has the same structure as its radial counterpart shown in Fig. 1.17, consisting of two surface mounted PM rotors with different pole-pairs. A ferromagnetic modulator is arranged axially between the two rotors as can be seen in Fig. 1.18. The results show that a torque density of 70 kNm/m^3 can be gained by using this optimised topology. A flux focusing axial flux MG topology has been presented in [ACH13]. The machine has two spoke type parts comprising ferrite magnets separated by steel poles that are magnetised, which forces the flux to pass through the steel poles. A modulator with ferromagnetic material pieces is axially arranged between both spoke type parts as shown in Fig. 1.19. The simulation results state that at optimal dimensions of the topology, a torque density of 66 kNm/m^3 can be obtained. Moreover, the torque density of this topology is improved to 257 kNm/m^3 when using NdFeB magnets instead of ferrite magnets as presented in [ACH14]. Furthermore, with the same spoke type parts, an axial transverse flux MG topology with a modulator located on the outer diameter of the axial rotors is presented in [BOM14] as shown in Fig. 1.20. With the same machine volume, the topology was compared with a radial MG with different magnetisation directions of its PMs, and axial MG counterparts in [CHE14]. The comparison indicates that this topology suffers from a significantly low torque density and that radial flux MG has a higher torque density when the size limit is not considered, whereas axial flux MG topology has the highest torque density when the axial length limit is considered. Based on spoke arranged magnets topology, a hybrid flux axial MG is presented in [PEN14]. Fig. 1.21 shows the structure of this MG which comprises two high and low speed rotors with magnets that are axially arranged. The machine has a set of stationary radially magnetised magnets separated by iron segments. These are circumferentially arranged and located at the outer radius

of both rotors. The machine also has stationary iron segments with axially magnetised magnets located between the two rotors. Despite this topology having a complex structure as well as high PM volume usage, according to the obtained simulation results, a torque density of approximately 181 kNm/m^3 was obtained.

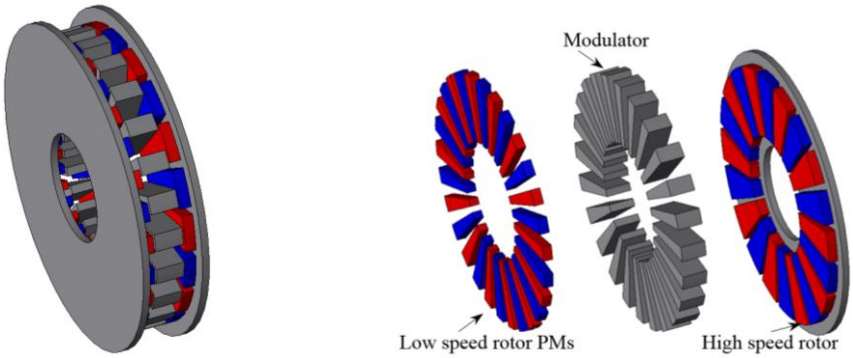

Fig. 1.18. MG machine topology presented in [MEZ06].

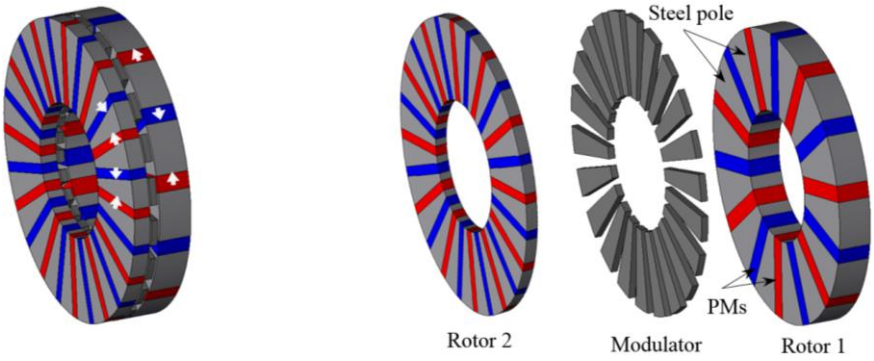

Fig. 1.19. MG machine topology presented in [ACH13].

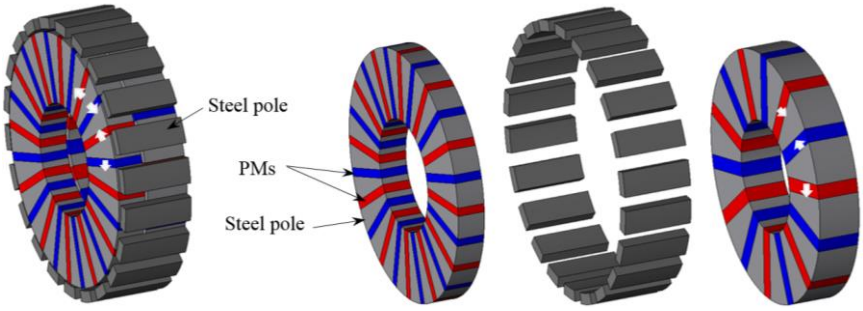

Fig. 1.20. MG machine topology presented in [BOM14].

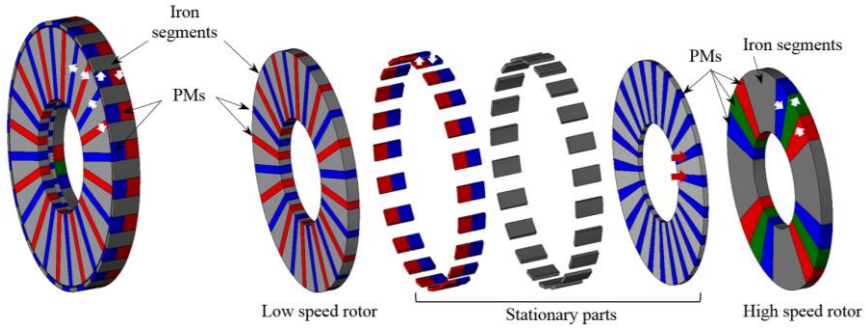

Fig. 1.21. MG machine topology presented in [PEN14].

In addition, with the aim of increasing the torque density of the spoke type axial flux MG topology, a topology with L – type modulator is proposed in [TSA15]. As can be seen in Fig. 1.22, the machine has two spoke type rotors separated by a moderator consisting of stationary ferromagnetic pieces. The pieces have a unique L- shape to increase the effective area of the modulator and to eliminate the leakage flux. The experimental results indicate that by utilising NdFeB magnets, a torque density of approximately 70 kNm/m^3 was achieved by the prototype of axial MG. Moreover, the flux density of the spoke type axial flux MG has been further increased by using the T- shape modulator made of soft magnetic material which is presented in [YAN15]. The machine, which is shown in Fig. 1.23, was analysed and the results indicated that it can obtain a significantly high torque density of 282.56 kNm/m^3.

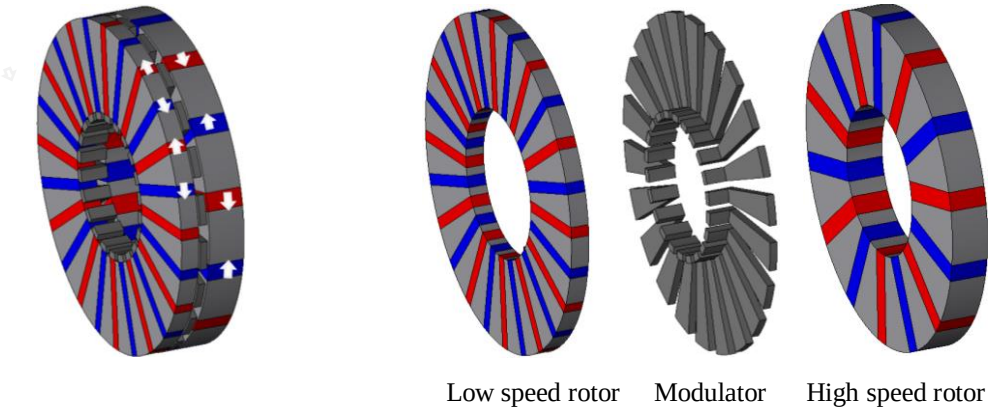

Fig. 1.22. MG machine topology presented in [TSA15].

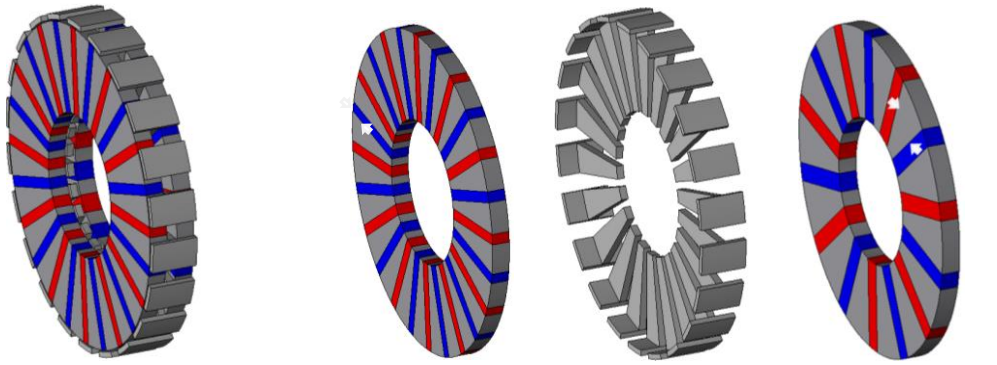

Fig. 1.23. MG machine topology presented in [YIN15].

1.4.2 Axial flux magnetically geared machine topologies

The integration of MGs into a conventional PM machine has resulted in development of a new machine category (i.e. magnetically geared machine) which has greatly broadened the scope of machine topologies. Numerous radial magnetically geared machines have been introduced for various applications such as HEVs [ATA04], [JIA10] and wind power generation [JIA09], [JIA11]. Fig. 1.24 and Fig. 1.25 show early examples of radial magnetically geared topologies.

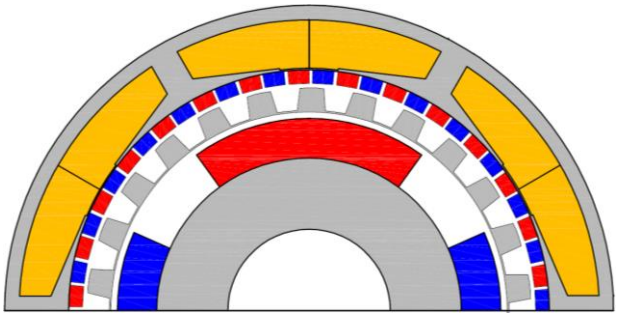

Fig. 1.24. Pseudo direct drive machine presented in [ATA04].

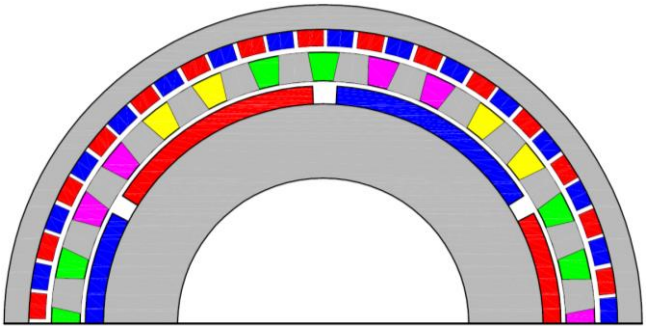

Fig. 1.25. Wound modulator magnetic geared machine presented in [JIA11].

However, axial flux magnetically geared machines have not attracted as much research attention as their radial counterparts [JOH17]. The axial flux magnetically geared machine was first

presented in [NIG12a]. The machine consists of a stator with embedded 3-phase windings, a high-speed rotor composed of a carbon steel yoke with 8 surface mounted PMs, and a low-speed rotor constructed of 20 iron pieces as shown in Fig. 1.26. Its operating principle can be analytically explained using the sub-domain method. The simulation results show that the machine suffers from a high cogging torque and inherently low torque density of approximately 15 kNm/m^3.

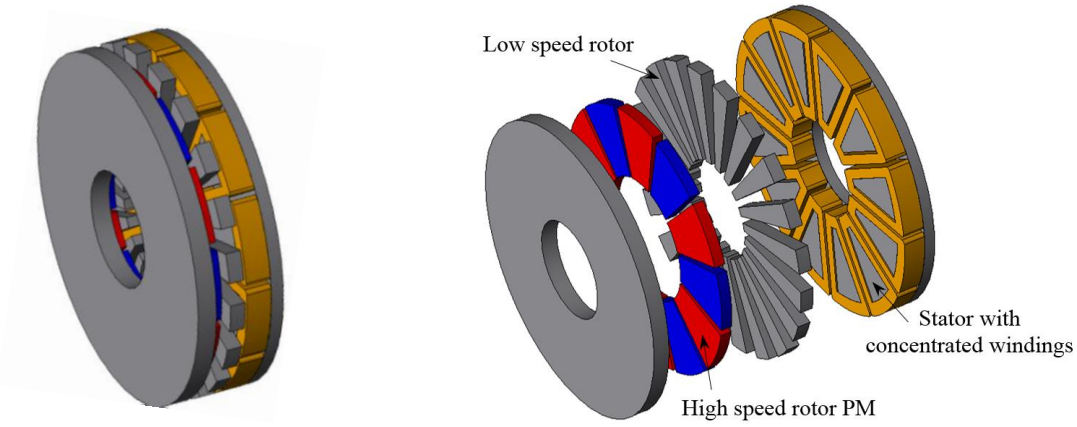

Fig. 1.26. Magnetic geared machine presented in [NIG12a].

In addition, several other AFMG topologies have been proposed and analysed. A disc type magnetically geared topology with 3 air-gaps for wind generation applications was presented and prototyped in [WAN13]. The machine has a stationary stator with windings and stationary modulator segments. The high-speed rotor is made of solid iron with PMs arranged on both rotor sides and is located between the modulator and the stator. The low–speed rotor is made of iron with surface mounted PMs as shown in Fig. 1.27. The machine has a relatively high torque density of 100 kNm/m^3. In addition to its complex structure, the prototype test results reveal that the machine has low efficiency due to high core loss in the low-speed rotor. In [ZAY14], an axial flux magnetic gear with electric power output is presented for wind power generation. As Fig. 1.28 illustrates, this machine has two axially arranged high- and low-speed PM rotors. A modulator of 9 pieces is located between the two rotors, with 9-phase coils embedded around each modulator piece. The simulation result shows that the machine can achieve the function of the MG concept and generate the output power through the electric power port. However, the machine has a non-sinusoidal back EMF and an axial force is exerted on the modulator as the electrical load increases.

It is worth mentioning that the topology presented in [ZAY14] has approximately the same structure to that to be presented in this thesis. However, for the machine in [ZAY14], a high axial force exerted on the modulator since a modulator with 9 pieces is employed and a high axial force

is applied to the stator as the winding current increases. Moreover, the windings used as electric power port are located without mechanical support, i.e. tooth tips. Furthermore, it can only work as MG and generator in which motoring mode was not presented. Therefore, as will be described later, in this thesis, a 3-phase concentrated winding employed for the new machine stator is based on the YASA machine design. Moreover, the new machine has stator tooth tips and different operating modes can be obtained by this new topology. Furthermore, in addition to the delivered MG torque, the output torque capability can be improved by the armature current torque with the aid of current angle control at motoring operating mode.

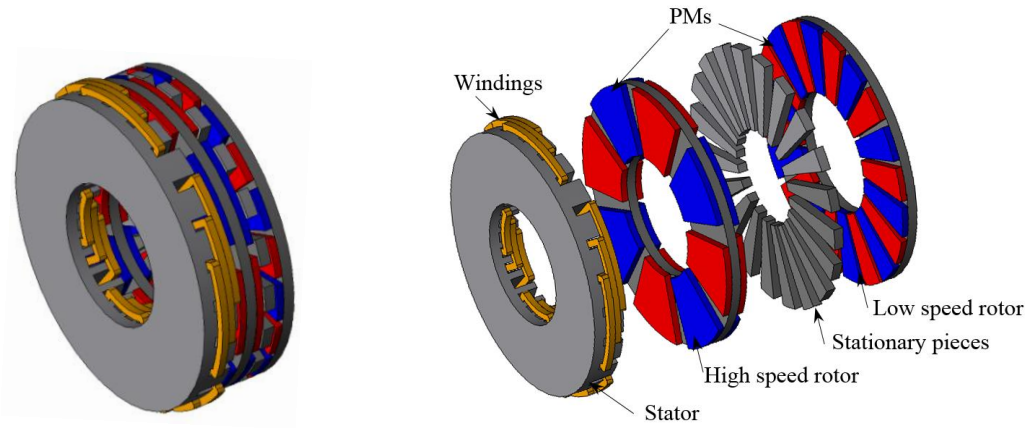

Fig. 1.27. Magnetic geared machine presented in [WAN13].

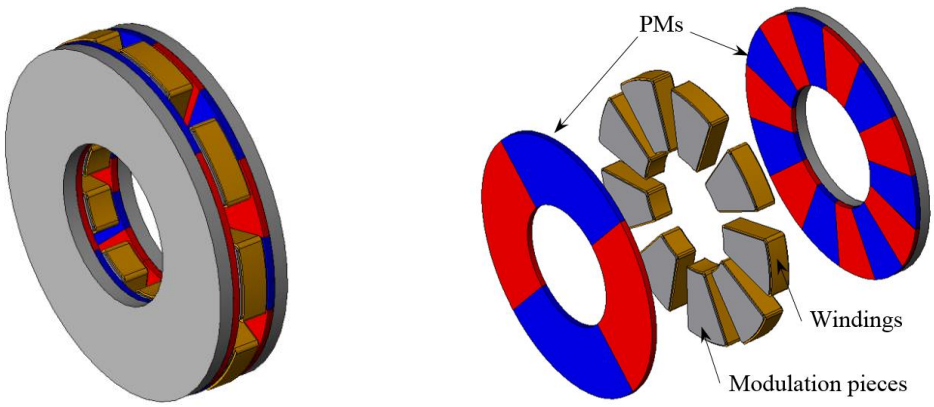

Fig. 1.28. Magnetic geared machine presented in [ZAY14].

For power split applications in wind power generation, an axial flux doubly fed stator and dual-rotor topology is presented in [NIU14]. The machine shown in Fig 1.29 contains primary and secondary PM rotors. The stator consists of two different windings; distributed windings (primary) and concentrated windings (secondary), with the primary winding controlling the secondary rotor to rotate at a constant speed to maintain a constant secondary winding frequency. The machine has superb performance in operations of variable speed and constant frequency wind

power application. However, it has a complex structure as well as flux distribution. In [JOH17], an axial flux PM machine is combined with an axial MG machine. The resulting machine consists of a single sided AFPM machine located in the radial bore of an axial MG. The rotor of the axial flux machine and the high-speed rotor of the MG are connected together by the same rotor core, while the modulation pieces are located between the high and low-speed rotors. The presented topology was designed and prototyped. The combined machine provides good space utilisation; however, the prototype has a low torque density of 7.8 kNm/m^3.

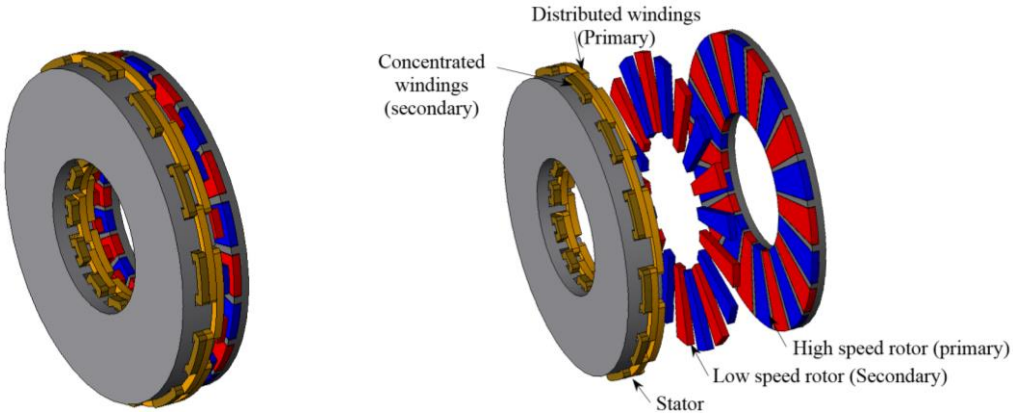

Fig. 1.29. Magnetic geared machine presented in [NIU14].

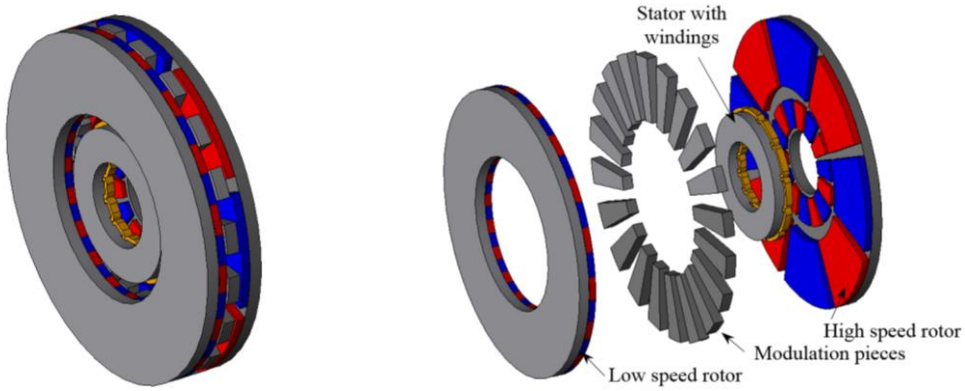

Fig. 1.30. Magnetic geared machine presented in [JOH17].

Several further topologies have also been introduced for HEV applications. An axial flux magnetically geared machine known as the magnetic field modulated brushless double rotor (MFM-BDRM) machine is presented in [TON14]. It utilises double stators with distributed windings. Additionally, a dual modulating ring rotor and one PM rotor are located between the two stators as indicated in Fig. 1.31. The simulation results confirm that the machine can realise the power split function in HEVs. However, the machine has complex structure and low power factor under the generating and motoring modes. In [LAI16], another axial flux magnetically

geared machine with dual stators and dual rotors has been presented for power split application in HEVs. The topology is a conventional AFPM machine axially arranged with a flux modulated machine as shown in Fig. 1.32. It consists of a modulating segment rotor and PM rotor located between two stator cores with different winding distribution. One stator has concentrated windings and the other has distributed windings. Investigation of the machine performance at different gear ratios indicated that its performance is sensitive to the gear ratio. Moreover, different operation modes can be obtained for such applications and it is capable of decoupling the input power obtained by the prime- mover and the output power connected to the load. However, despite of most axial flux MG topologies being based on flux focusing rotor structure, only one axial flux magnetically geared machine topology with flux focusing rotor has been proposed.

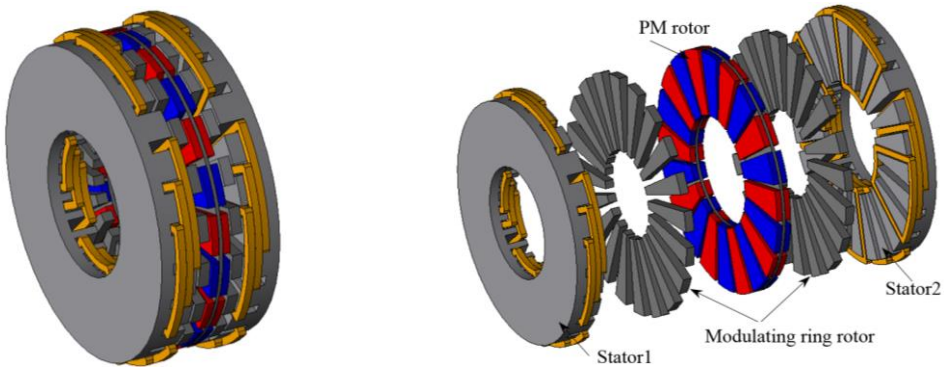

Fig. 1.31. Magnetic geared machine presented in [TON14].

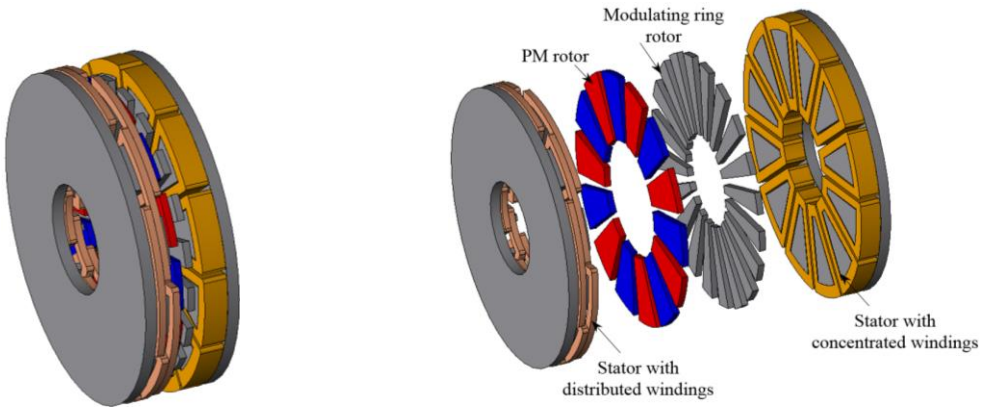

Fig. 1.32. Magnetic geared machine presented in [LAI16].

An axial flux MG machine with flux focusing magnets and integrated radial outer stator has been proposed in [KOU17]. The machine has approximately the same rotor structure as the MG obtained in Fig. 1.19. However, a radial stator with distributed windings is placed at the outer radius of the high speed rotor, as can be seen in Fig. 1.33. The machine was analysed utilising 3D-FEA and compared to the measured results obtained by the prototyped machine. According

to the obtained simulation results, a torque density of 127 kNm/m^3 is achieved by this machine when the low speed modulator is assumed as output torque.

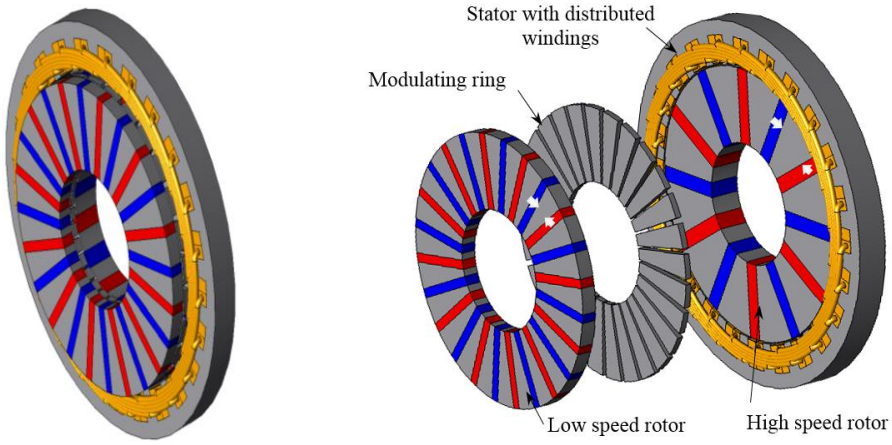

Fig. 1.33. Magnetic geared machine presented in [KOU17].

1.5 Research scope, objectives and contributions

1.5.1 Research scope and objectives

The research in this thesis focuses on a study of axial flux magnetically geared (AFMG) PM topologies. Based on the literature review of AFMG topologies, it reveals that the existing topologies have complex structures. The industry requirement for high performance machine with low manufacturing cost is critical for selecting the appropriate machine topology for the specific applications. The design of a magnetically geared topology involves the design of two different transferred torque components: magnetic gearing and conventional electrical machine torques. For interior stator magnetically geared topologies, a distributed winding is always utilised for the stator armature. The armature windings are directly inserted in the air gaps between the pieces as presented in [JIA11]. The pole pair number of the windings is designed to be the same as the pole pair number of the output rotor PMs since the fundamental harmonic is , working harmonic. Thus, the electromechanical energy conversion can be obtained by the flux interaction between the armature winding and the output rotor PMs only. When an external torque is applied to the input rotor and the machine operates in motoring mode, the output PM rotor is driven by both the armature field and the MG effect. Because of the different pole-pair numbers of the windings and the input rotor PMs, the input rotor will have slight impact on the generated electric power as well as armature winding torque. However, when a concentrated winding is utilised for interior stator magnetically geared machines, both rotors will be affected by the armature winding torque since the armature flux contains many harmonics. In general, the torque for concentrated winding always contributed by the armature flux density harmonic which has

the same order as the number of rotor pole-pairs (p^{th}). (i.e. the 5^{th} harmonic, when the rotor has 5 pole pairs). The proposed AFMGPM topology is based on the conventional YASA machine topology by employing different PM rotors. It has a simple structure since it is the same as YASA machine structure. However, the machine has a concentrated winding stator between the two rotors. Therefore, when the machine has two different rotor pole pairs, both input and output rotors will be affected by the armature flux.

The first objective of this work is to design the proposed AFMGPM machine with a concentrated winding stator and explore the possibility of using concentrated windings for this kind of machines. This study focuses on the electromagnetic performance of the proposed machine, and therefore, the mechanical and thermal aspects will not be considered. The electromagnetic performance with different rotor pole combinations are analysed. The project investigates the proposed machine design, optimisation and finite element simulation. The impact of design parameters on the machine torque is investigated. The machine performances at MG and generation modes are studied.

The second objective of the study is to investigate the machine performance under motoring mode. Since interior stator axial flux magnetically geared topology with concentrated windings has not be investigated under motoring mode, the methodology of matching the armature current torque with the output MG torque will be discussed. The third objective is the application of the proposed machine. It is proposed as a power split device for hybrid vehicle applications. Thus, the proposed machine is studied at different operating modes. Finally, the machine performance is compared with that of the conventional YASA machine and the principle of the axial flux magnetically geared machine is experimentally validated by constructing and testing the prototype machine. The study of the novel machine topology in this thesis is summarised in Fig. 1.34.

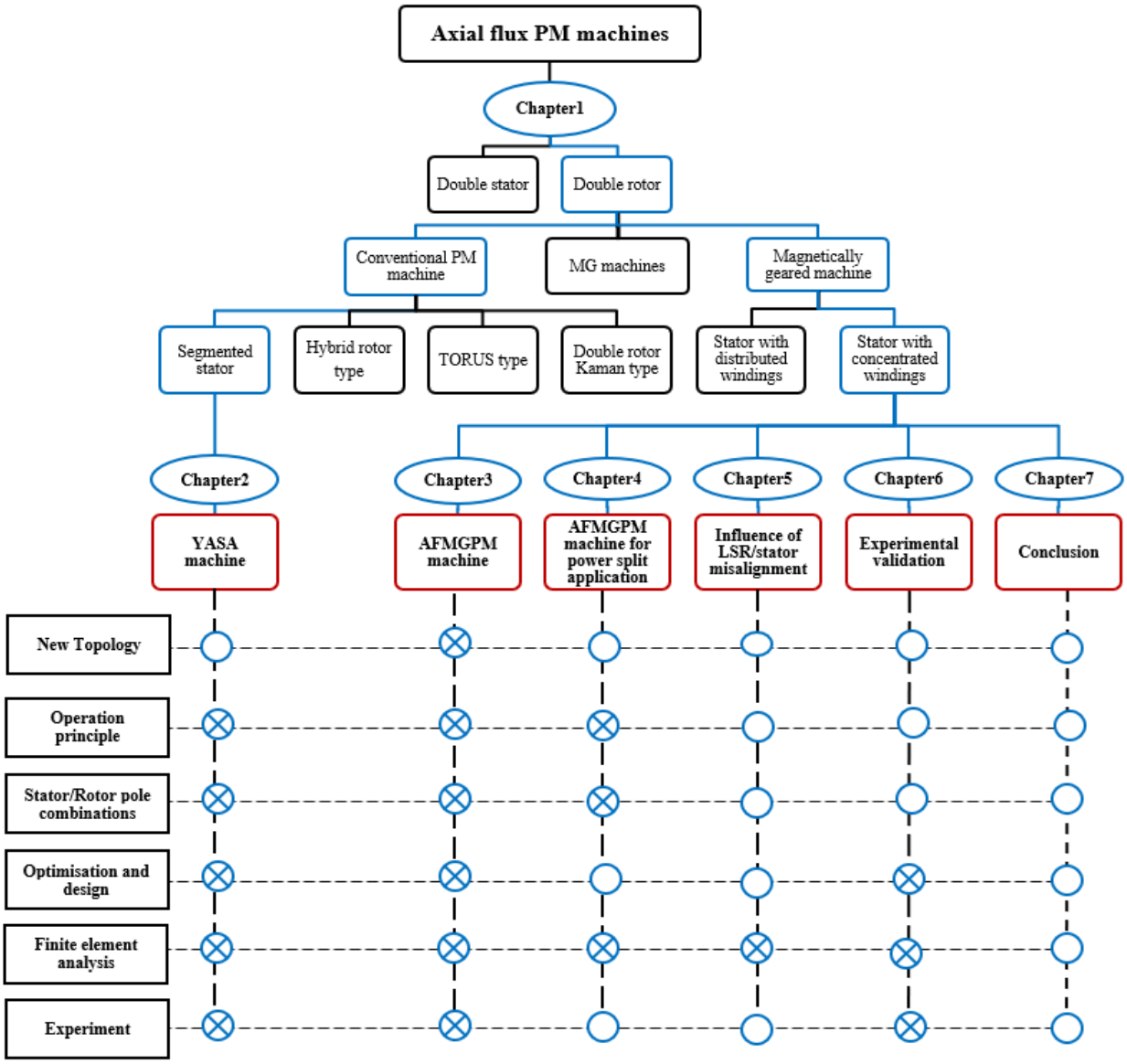

Fig. 1.34. Schematic diagram of research structure and research methods.

- **Chapter 1**

The thesis begins with a general review of the constructions and topologies of conventional AFPM machines. In addition, the chapter discusses the construction of the axial flux MG and magnetically geared topologies previously presented and developed.

- **Chapter 2**

In this chapter, a conventional YASA machine is designed and then constructed. To maximise the machine torque, the topology is optimised by means of three-dimensional finite element analysis (3D-FEA). The electromagnetic performance for different pole combinations is then analysed and compared.

- **Chapter 3**

The design for a novel topology of the proposed AFMGPM machine is described. The machine is optimised for optimal output torque. The principle of operation for MG and magnetically geared machine is explained. A comparative study of the possible rotor pole combinations is performed. Then, the electromagnetic performance is compared with the performance of YASA machine counterparts.

- **Chapter 4**

The proposed AFMGPM machine is analysed for power split application. The system is described, and the machine performance is analysed and investigated under different operation modes. The torques and axial forces obtained by both machine rotors are calculated at different load conditions. In addition, the loss and the efficiency of the proposed pole combinations are investigated and compared.

- **Chapter 5**

Since a prototype of the proposed machine will be built, this chapter investigates the manufacturing tolerance for such a machine. Rotor/stator axis and angular misalignments for the low speed rotor of the proposed machine are analysed. The performance of the machine at different load conditions under rotor/stator misalignments is analysed with reference to the normal condition.

- **Chapter 6**

The prototypes of the proposed AFMGPM machine and YASA machine are designed and built. Machine performance aspects such as cogging torque, no-load back EMF and static torque are measured and validated with 3D-FEA results. The measured performances of the two prototype machines are then compared.

- **Chapter 7**

In this chapter, the most important findings and the contributions of this thesis are summarised. The main outcomes of the research are highlighted, and some recommended future research work is also proposed. This includes considering design aspects such as the rotor geometry of the machine, in addition to performance aspects such as the machine performance for real drive cycle.

- **Appendix**

The appendix shows the principle of PM machines. Moreover, the research methodology such as 2D and 3D FEA models, software setting, and mesh generation are explained in details. A

complete comparative performance study between the proposed AFMGPM machine and the YASA machine is conducted. The proposed machine rotor pole combination performances at no-load and on-load are compared with their YASA machine counterparts. In addition, details of the machine iron material parameters such as magnetising curve and the loss characteristics at different frequencies are presented. Then, more details of the prototype machine dimensions and the fabrication processes are also described.

1.5.2 Research contributions

The contribution of this thesis is the development and analysis of a novel AFMGPM machine for power split application in HEVs. The stator consists of iron slotted segments with concentrated windings and is located between two rotors with different poles. The new topology has a simple structure and a superior performance compared to the topologies which have been presented so far. The machine is designed and optimised for different rotor pole combinations, and comparatively analysed utilising 3D-FEA. In addition, different operation modes of the machine are identified for HEV applications. The torque performance at no-load and on-load of the new machine is studied by considering both rotors as output torques. Finally, a comparative study is conducted of the performance of the new machine and YASA machine. The results show that the machine has a superior performance which make it convenient for HEV applications in which output torque can be increased with the aid of adjustment of the armature current angle.

PUBLICATIONS

Journal papers

[1] Z. Q. Zhu, M. F. H. Khatab, H. Y. Li, and Y. Liu, "A novel axial flux magnetically geared machine for power split application", *IEEE Trans. on Ind. Appl.,* vol. 54, no. 6, pp. 5954-5966, Nov./Dec. 2018.

[2] M. F. H. Khatab, Z. Q. Zhu, H. Y. Li and Y. Liu, "Comparative study of novel axial flux magnetically geared and conventional axial flux permanent magnet machines" *CES Trans. on Elec. Mach. and Sys.*, vol. 2, no. 4, pp. 392-398, Dec. 2018.

[3] M. F. H. Khatab, Z. Q. Zhu, H. Y. Li, and Y. Liu, "Influence of static and dynamic rotor/stator misalignments in axial flux magnetically geared machines", Journal of Engineering, IET, doi: 10.1049/joe.2018.8186, pp.1-6, 2019.

Conference papers

[1] M. F. Khatab, A. L. Shuraiji, and Z. Q. Zhu, "Parametric design optimisation of axial field partitioned stator switched flux PM machine," *Int. Conf. on Sustainable Mobility Appl., Renewables and Technology (SMART)*, 2015, pp. 1-6.

[2] M. F. H. Khatab, Z. Q. Zhu, H. Y. Li, and Y. Liu, "Optimal design of a novel axial flux magnetically geared PM machine", *Twelfth Int. Conf. on Ecological Vehicles and Renewable Energies* (EVER), 2017, pp. 1-8.

[3] Z. Q. Zhu, M. F. H. Khatab, H. Y. Li, and Y. Liu, "A novel axial flux magnetically geared machine for power split application", *Twelfth Int.Conf. Ecolo. Vehicles and Renewable Energies* (EVER), 2017, pp. 1-8.

[4] M. F. H. Khatab, Z. Q. Zhu, H. Y. Li, and Y. Liu, "Influence of static and dynamic rotor/stator misalignments in axial flux magnetically geared machines", *IET Conf. on Power Electronics, Machines and Drives* (PEMD), 2018, pp. 1-8.

[5] M. F. H. Khatab, Z. Q. Zhu, H. Y. Li, and Y. Liu, "Comparative study of axial flux magnetically geared machine with conventional axial flux YASA machine", *IEEE International Magnetic Conf.* (INTERMAG), 2018 April 23rd to 27th, Singapore.

CHAPTER 2

YOKELESS AND SEGMENTED ARMATURE (YASA) AXIAL FIELD PM MACHINE

2.1 Introduction

With the aim of improving the winding arrangements and eliminating the yoke iron so as to reduce the iron loss in the axial flux TORUS machine, a Yokeless and Segmented Armature (YASA) axial field permanent magnet machine was initially developed and prototyped for automotive applications in [WOO06]. The machine was formed by removing the stator yoke of the TORUS type since the flux of this topology passes axially through the stator poles. Compared to other axial flux machines, the YASA machine has the merits of short end windings, high efficiency, high torque density, high winding packing factor and easily fitted stator poles [WOO07] [VAN10]. However, since the stator is a combination of iron pieces, the mechanical design of the stator pole holder is still vitally important due to the axial force exerted between the stator and the rotors. This is the main drawback of double rotor axial flux machines [GIU12].

Numerous studies have been devoted to the YASA machine performance analysis and manufacturing fabrication for different applications, for example wind generation and electric vehicles. It was first presented and prototyped for a sports vehicle in [WOO06] and [WOO07]. With torque density of 17.6 Nm/Kg, a 10-pole 12-stator segment prototype was developed, and SMC material used for the machine stator segments. For in–wheel direct drive traction applications, 10 poles and 12 stator segments, a 6 kW YASA machine was investigated in [FEI08]. In order to increase the efficiency of YASA machine presented in [WOO07], a simple laminated steel for the stator segments was developed instead of SMC material. An approximate structural model of the prototype stator segments was utilised. The machine model was examined via 3D-FEA. The results were obtained and validated and an efficiency of approximately 90 % for the prototype was measured. In [VAN10], to minimise the machine's active mass and obtain maximum efficiency, a 16-pole and a 15-stator segment YASA generator was designed and prototyped. In order to simplify manufacturing, the stator poles were formed by overlapping two different lamination shapes made of grain-oriented material. The experimental results show that an efficiency of approximately 87% was obtained at rated speed. In other research, YASA machines were compared to the conventional RFPM and AFPM machines. In [VUN11], a 10-

pole, 12-stator segment YASA machine was presented and analysed for megawatt scale wind turbine generation. In terms of torque density and torque per magnet weight, it was also compared to a RFPM machine and double sided slotted AFPM machine at different power rating. The comparative investigation found that the YASA machine has a significantly higher torque density as well as low active material weight.

It can be concluded that internal stator AFPM machine topologies have been extensively developed and investigated for drive applications. Moreover, a YASA machine has superior performance amongst internal stator AFPM topologies. Furthermore, it has been found that based on a performance comparison of AFPM machine topologies, a YASA machine is inherently suited to direct drive application [WOO07], [STA15]. Therefore, in this chapter, since this machine has a unique topology, the machine performance will be investigated in order to provide a baseline of comparison for the subsequent proposed axial field machines. With 12 stator segments, the machine is designed and optimised with different rotor pole combinations. A performance comparison between YASA machine topologies at no-load and on-load conditions will be investigated. Moreover, the torque performance with respect to the current, current density and copper loss will be obtained and compared.

2.2 YASA machine configuration and principle of operation

A YASA machine, as illustrated in Fig. 2.1, has double rotors with PMs mounted on two opposing rotor discs, and a single stator between both PM rotors.

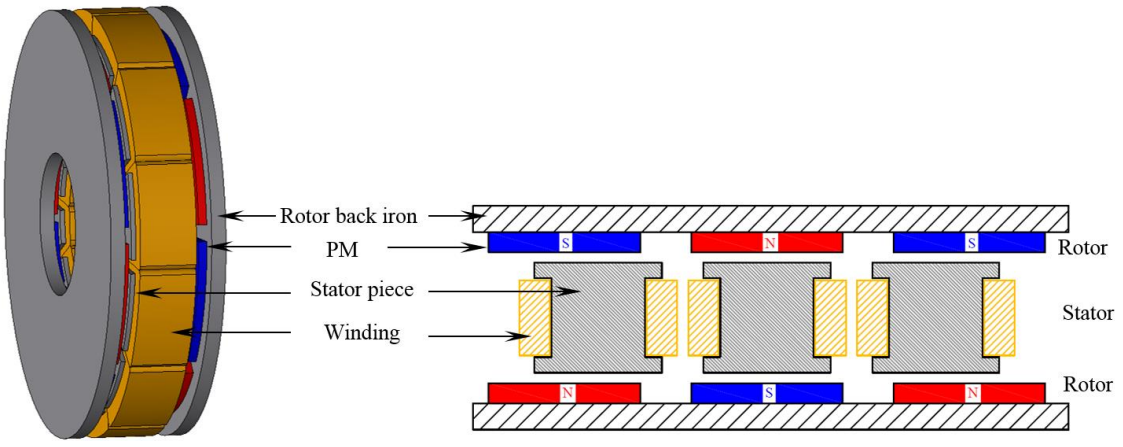

3-D view 2-D view

Fig. 2.1. YASA machine configuration.

The stator is individually segmented and stacked together with high strength material holder to form magnetically isolated stator poles. Moreover, fractional slot concentrated windings are wound around each of the individual stator poles and connected to form the stator phase windings. The magneto-motive force (MMF) produced by the currents applied to the windings contains a number of harmonics; however, the component that dominates the produced torque is the high harmonic component of the same order as the rotor pole pairs.

For a given volume of PM machines and for a specific of phase number, the design is essentially based on obtaining a combination of the stator and rotor pole pairs. The phase number is selected as three in this study, and therefore, for double layer 3-phase windings of YASA machine, the number of stator segments must be a multiple of 3 and the phases are shifted by 120 elec. deg. Moreover, the stator segment numbers n_s and the rotor pole-pair number p combinations are expressed by:

$$n_s = 2p \pm k, \qquad k = 1,2,3, \ldots \tag{2.1}$$

Furthermore, it has been verified by [ISH05] and [WAN08] that a high winding factor, and hence, high flux can be obtained when n_s and $2p$ are differ by the smallest possible integer (i.e. 1 and 2). However, when $k = 1$, this results in unbalanced magnetic pall exhibited in such machines. Therefore, for balanced magnetic pall as well as high winding factor, the PM machine stator and rotor pole numbers should be related by

$$n_s = 2p \pm 2 \tag{2.2}$$

A 12 pole with concentrated windings has been chosen for the YASA machine stator. The coils are connected in series to form the stator phase windings.

The selection of appropriate combination of slot and pole numbers should ensure the winding distribution balance in the machines. The number of slots per pole per phase (S_p) can be calculated by [CRO02]:

$$S_{pp} = \frac{n_s}{2pm} \tag{2.3}$$

where m is the number of phases.

Consequently, the most appropriate stator and rotor pole combination can be obtained by (2.1), when k is even. Table 2.1 lists the possible rotor pole combinations, their S_{pp} and the fundamental

winding factor k_{w1} for n_s of 12 poles. The fundamental winding factor for double – layer concentrated windings is calculated by:

$$K_{w1} = K_{d1}\, K_{p1} \tag{2.4}$$

where K_{d1} and K_{p1} are the main harmonic distribution and pitch factors, respectively. These can be obtained according to the number of stator poles n_s and the rotor pole pairs p by [BIA06]:

$$K_{d1} = \frac{\sin\left(\frac{\pi}{2m}\right)}{\frac{n_s}{2tm}\sin\left(\frac{\pi t}{n_s}\right)} \quad \ldots \text{if } \left(\frac{n_s}{tm}\right) is\ even.$$

$$K_{d1} = \frac{\sin\left(\frac{\pi}{2m}\right)}{\frac{n_s}{tm}\sin\left(\frac{\pi t}{2n_s}\right)} \quad \ldots \text{if } \left(\frac{n_s}{tm}\right) is\ odd. \tag{2.5}$$

$$K_{p1} = \sin\left(\frac{\pi p}{n_s}\right) \tag{2.6}$$

where t is the greatest common divisor (GCD) of the number of stator segments, n_s , and the number of pole pairs, p. It has been confirmed that high winding factor and balanced concentrated windings are normally adopted when $0.25 \leq S_{pp} \leq 0.5$, [CRO02]. The winding distribution whereby $S_{pp} < 0.25$ has a low fundamental winding factor causing a non-sinusoidal back EMF (i.e. 12/20, 12/22). Moreover, the pole combinations which have $S_{pp} > 0.5$, (i.e. 12/2, 12/4) and where S_{pp} is thus an integer must have distributed winding to obtain a high winding factor. In terms of the rotor pole combinations listed in Table 2.1, for YASA machine and due to the focus of this study, this chapter only explores YASA with $0.25 \leq S_{pp} \leq 0.5$ in which a high winding factor is gained.

Table 2.1 Rotor pole combinations for 12-slot, 3-phase concentrated windings

Name	$2p$	S_{pp}	K_{d1}	K_{p1}	$K_{w\,1}$
YASA12/22	22	0.18	0.966	0.25	0.25
YASA12/20	20	0.2	1	0.5	0.5
YASA12/16	**16**	**0.25**	**1**	**0.866**	**0.866**
YASA12/14	**14**	**0.28**	**0.966**	**0.966**	**0.933**
YASA12/10	**10**	**0.4**	**0.966**	**0.966**	**0.933**
YASA12/8	**8**	**0.5**	**1**	**0.866**	**0.866**
YASA12/4	4	1	1	0.5	0.5
YASA12/2	2	2	0.966	0.25	0.25

In fact, in AFPM machines, there are two types of stator slots and hence of the concentrated coil shape arrangements as indicated in Fig. 2.2. The first type employed when the stator slot is parallel, and therefore, the neighbouring coils at the same slot are parallel and are attached each other along the edge of the coils as indicated in Fig. 2.2(a). The second arrangement has unparalleled neighbouring coils since the slot sides is radially unparalleled, in which the coils in the same slot only touch each other at the stator inner radius as explained in Fig. 2.2(b). The first winding arrangement has the merit of a higher coil space and a higher teeth area compared to the second arrangement. It has been confirmed that since the coil band is wider, the first coil arrangement has a higher flux linkage than the second type at the same inner and outer diameters [AYD07], [XIA15]. Therefore, the coil distribution of concentrated winding indicated in Fig. 2.2(a) will be utilised for the design of all models.

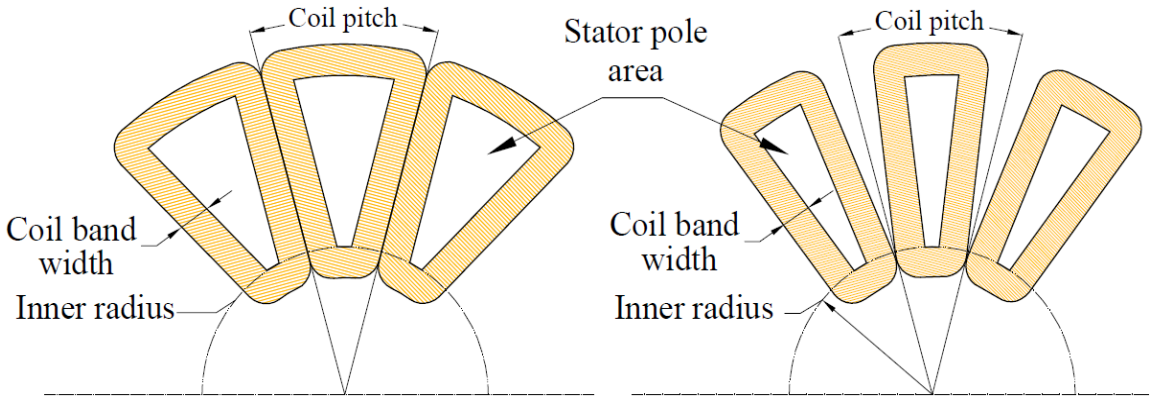

(a) Parallel slot (b) Radial slot

Fig. 2.2. Coil arrangements of concentrated windings.

For the selected rotor pole combinations, the distributions of the phase coils are determined by the induced back EMF phasor in each coil. The coils distributions for the proposed pole combination are illustrated in Fig. 2.3. Moreover, since the machine has 12 stator poles connected as a three-phase machine, each phase comprises four coils. Furthermore, for the topologies with 0.5> S_{pp} >0.25 (i.e. YASA12/10, YASA12/14), two successive stator segments are wound with coils of the same phase. In this case, a high fundamental winding factor can be obtained. However, the topologies with S_{pp}= 0.5 and 0.25, (i.e. YASA12/8, YASA12/16) have a relatively low fundamental winding factor of 0.866.

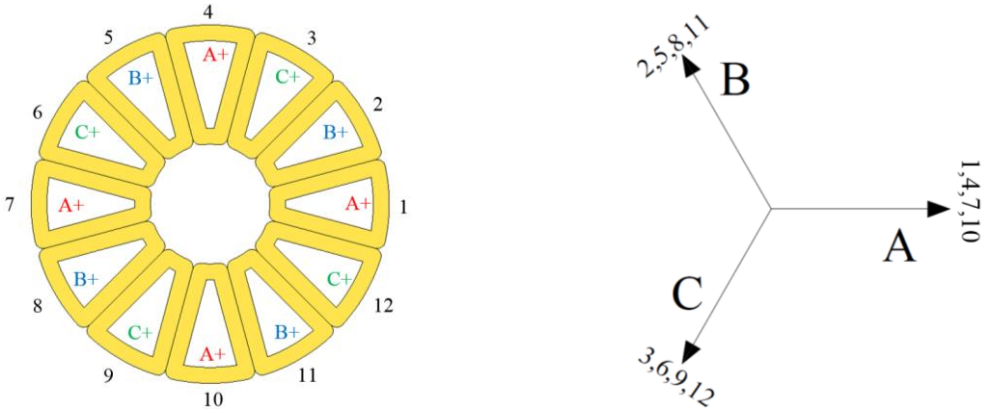

(a) YASA12/8 and YASA12/16

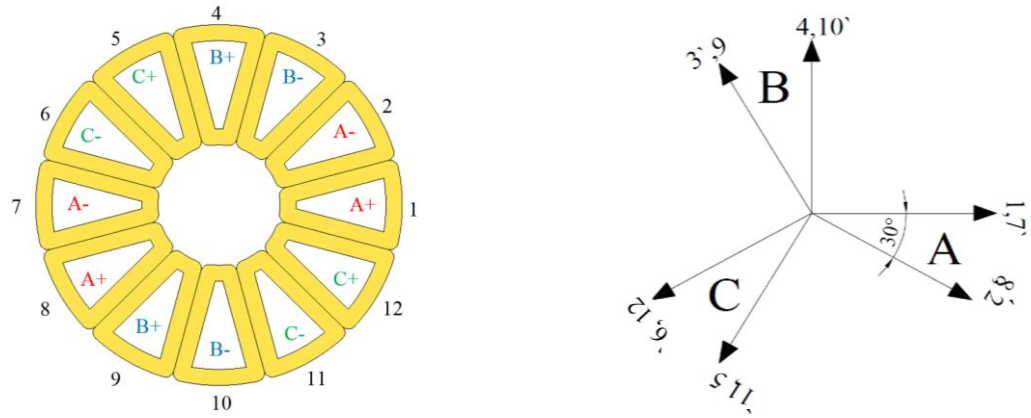

(b) YASA12/10 and YASA12/14

Fig. 2.3. Coils arrangments and the EMF phasor for YASA machines with different slot/pole number combinations.

2.3 Optimisation of YASA machine.

For axial flux machines, 3D-FEA is necessary for accurate modelling. Moreover, different analysis methods can be alternatively adopted to simplify the study. One of these methods is to conduct simulations utilising 2D-FEA [EGE12]. The method is based on taking a 2D plane of the geometry at a specific radius. The approximation of the 2D model used in this thesis is described in detail in Appendix A.

With the aim of maximising the average torque of the machine, 2D-FEM of YASA machine topologies listed in Table 2.1, which have high winding factors, are designed and analysed. Additionally, for different rotor pole combinations, the optimisations were carried out with the same constraints as listed in Table 2.2.The variable dimensions are shown in Fig. 2.4 and their

definitions listed in Table 2.3. Meanwhile, the characteristics of the SMC material are provided in Appendix C.

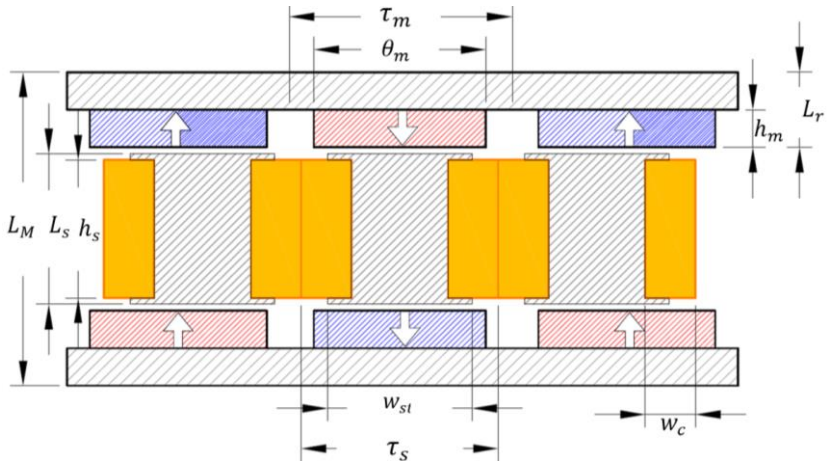

Fig. 2.4. Dimensional definitions of YASA topology.

Table 2.2 YASA machine constant dimensions and parameters.

Parameter	**Value**
Rated speed (rpm)	400
Stator pole number (n_s)	12
Machine inner diameter (mm)	30
Machine outer diameter (mm)	90
Axial length (mm)	25
Air-gap length (mm)	0.5
Number of turns /phase	80
Packing factor	0.5
Copper loss (W)	30
PM material	NdFeB
PM remanence B_r (T)	1.2
PM relative permeability (μ_r)	1.05
Iron material	GKN SMC 70H

Table 2.3 Variable Parameters of the YASA Machine.

Parameter	Symbol	Definition	Restrictions
Magnet angle ratio	r_{p_ratio}	$\frac{\theta_m}{\tau_m}$	[0.5-1]
Magnet thickness ratio	r_{ht_ratio}	$\frac{h_m}{L_r}$	[0.3-0.8]
Stator slot width ratio	s_{w_ratio}	$\frac{h_s}{L_s}$	[0.5-0.95]
Stator slot depth ratio	S_{d_ratio}	$\frac{w_c}{\tau_s}$	[0.1-0.35]
Rotor thickness ratio	$R_{\_ratio}$	$\frac{L_r}{L_M}$	[0.15-0.25]

2.4 Influence of critical parameters on machine performance

In order to achieve a suitable prediction accuracy of the axial flux machine's performance, a 3D FEA model is always superior than a 2D-FEA. The machine was thus designed using such a model and the influence of each parameter on the torque for different rotor pole combinations was studied. With the aim of examining the machine average torque, the thickness of the rotor for all topologies was obtained by 2D-FEA. Subsequently, the influence of each parameter (i.e. PM dimension, slot width and slot depth) on the torque was investigated.

2.4.1 Influence of PM dimensions

The machine torques for different magnet angles and thicknesses were investigated for YASA machine with different rotor pole combinations and are illustrated in Fig. 2.5. It was found that, the torque is sensitive to the PM volume. It is also evident from the figure that the optimal torque for YASA12/8 and YASA12/16 can be achieved at a PM angle ratio r_{p_ratio} of approximately 0.89 and 0.84 and at PM thickness ratios r_{ht_ratio} of 0.37 and 0.52, respectively. It is also apparent that the torque is maximised for YASA12/10 when the PM arc equals the rotor pole pitch with a magnet thickness ratio r_{ht_ratio} of approximately 0.4. In addition, the torque can reach its highest value for YASA12/14 when the magnet angle ratio r_{p_ratio} is approximately 0.9 and the magnet thickness ratio r_{ht_ratio} is slightly above 0.45. It can be shown that the optimal magnet thickness increases with the rotor pole number at the same stator pole number and optimisation conditions. Moreover, when the rotor pole number is less than the stator pole number (i.e. YASA12/8), the average torque increases with the increase of the PM pole arc to reach its optimal value. However,

after this value, the torque decreases with the increase of the rotor pole angle due to the leakage flux (Fig. 2.5(a)). The flux per pole passing through the rotor yoke is higher for lower rotor pole number. This results in saturation of the rotor back iron at a low PM thickness since the space of the rotor yoke is limited. Moreover, for YASA12/10, since the stator and rotor pole numbers are close, the leakage flux and the saturation are lower, resulting in the ability for an optimal torque to be obtained at larger PM thickness and angle ratios compared with YASA12/8. On the other hand, when the rotor pole number is larger with respect to the stator pole number (i.e. YASA12/14 and YASA12/16), the optimal magnet thickness is approximately half that of the rotor thickness. Meanwhile, the leakage flux is lower since the rotor pole arc is always less than the stator pole arc. Therefore, the optimal magnet thickness is larger compared to the other topologies: since the flux per pole is lower, more flux can be handled by the rotor yoke at larger thicknesses.

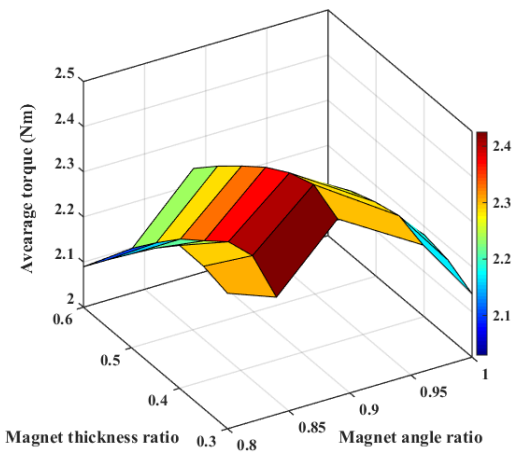

(a) YASA12/8

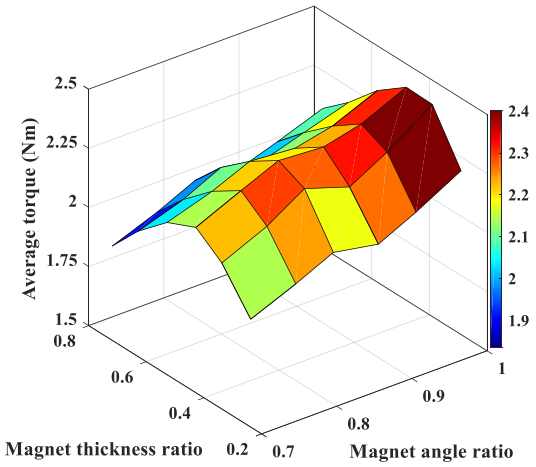

(b) YASA12/10

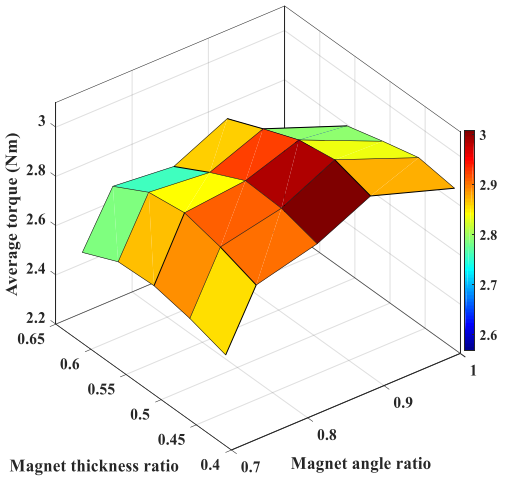

(c) YASA12/14

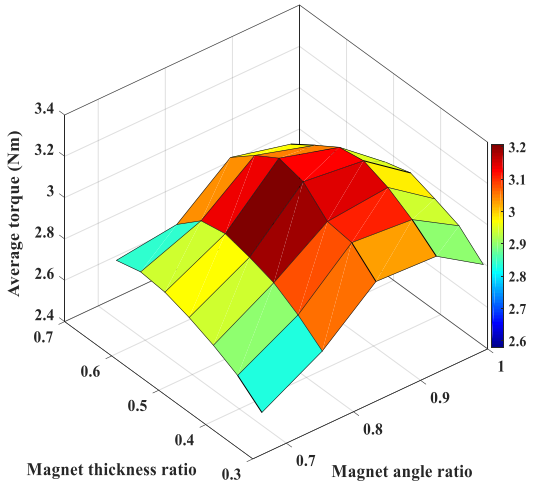

(d) YASA12/16

Fig. 2.5. Influence of the rotor PM dimensions of YASA topologies on the torque performance.

2.4.2 Influence of slot depth and slot width

At optimal PM dimensions, the influences of slot depth and width on the machine torque performance for the proposed stator/rotor pole combinations are studied. It should be mentioned that for simplicity in the 3D model, the machine slot is assumed to be rectangular, which results in rectangular tooth tips, as indicated in Fig. 2.6. The phase winding resistance and the copper loss when the end winding is neglected are given by:

$$R_a = \frac{n \times 2\rho\, L_a N_a^2}{A_a\, k_{pf}} \tag{2.7}$$

$$P_{cu} = {I_{a\,RMS}}^2 \times 3\, R_a \tag{2.8}$$

where ρ is the copper resistivity, L_a is the coil active length, N_a is the number of winding turns per phase, k_{pf} is the winding packing factor, A_a is the coil area, and *n* is the number of coils per phase. Therefore, the rated current at a fixed copper loss of 30 W, can be calculated by:

$$I_{a\,RMS} = \sqrt{\frac{P_{cu}}{3\, R_a}} = \sqrt{\frac{P_{cu}\ A_a\, k_{pf}}{3n\ 2\rho\, L_a N_a^2}} \tag{2.9}$$

where $I_{a\,RMS}$ is the RMS phase current and P_{cu} is the copper loss. Fig. 2.7 shows a comparison of the influence of the stator slot depth on the machine performance. It is obvious that the optimal average torque can be obtained when the slot depth ratio S_{d_ratio} is just below 0.26 (4mm) for all stator / rotor pole combinations. The current capability increases as the slot depth increases. However, when the slot depth increases further, the stator pole active area decreases which results in the stator pole being saturated. Additionally, at optimal slot depth, the influence of the slot width ratio s_{w_ratio} and the corresponding segment tip thickness for all topologies is obtained (see Fig. 2.8). The comparison shows that the average torque of YASA12/16 increases as the slot width ratio increases while YASA12/8 and YASA12/10 have optimal slot width before the torque tends to decrease with the rise of slot width. The average torques for YASA12/8, YASA12/10 and YASA12/14 reach their maximum values when the slot width ratios are approximately 0.86, 0.88 and 0.92, respectively. However, it can be clearly shown that the optimal average torque increases with the increase of rotor PM pole number. Even though YASA12/16 has lower winding factor compared with those in YASA12/10 and YASA12/14, the machine has higher torque at higher slot opening (without tips). This is clearly explained in detail in [LIU17], which states that, the torque of slotted PM machines has two components, the torque produced by the principle of conventional PM synchronous machines (the interaction between the fundamental harmonic component of the armature reaction flux and the PM flux fundamental harmonic), and

the torque produced by the magnetic gearing effect due to the slotting effect. The armature reaction torque decreases as the slot opening decreases due to the decrease of the air-gap permeance. This thus decreases the air-gap flux density. However, the gearing effect torque has a significant value since more harmonics are obtained and contribute to the torque production. Therefore, the reduction in the armature reaction torque is compensated by the gearing effect, because the gearing effect contributes more to the machine torque with a larger rotor pole number at the same number of stator poles. Consequently, as indicated in Fig. 2.8, the torque of YASA12/16 can be further increased when the stator pole tips are removed. However, since the tips are used for holding the stator winding, the maximum slot width ratio was identified as 0.93.

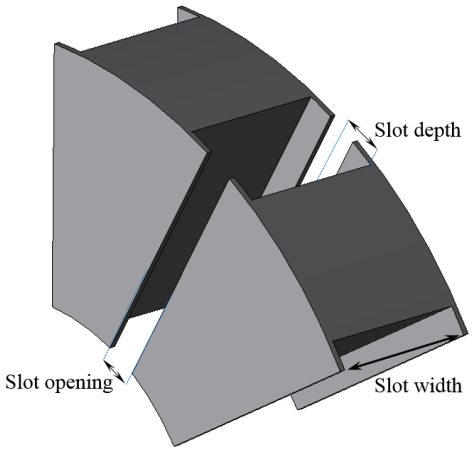

Fig. 2.6. Stator segment geometry and dimension definitions.

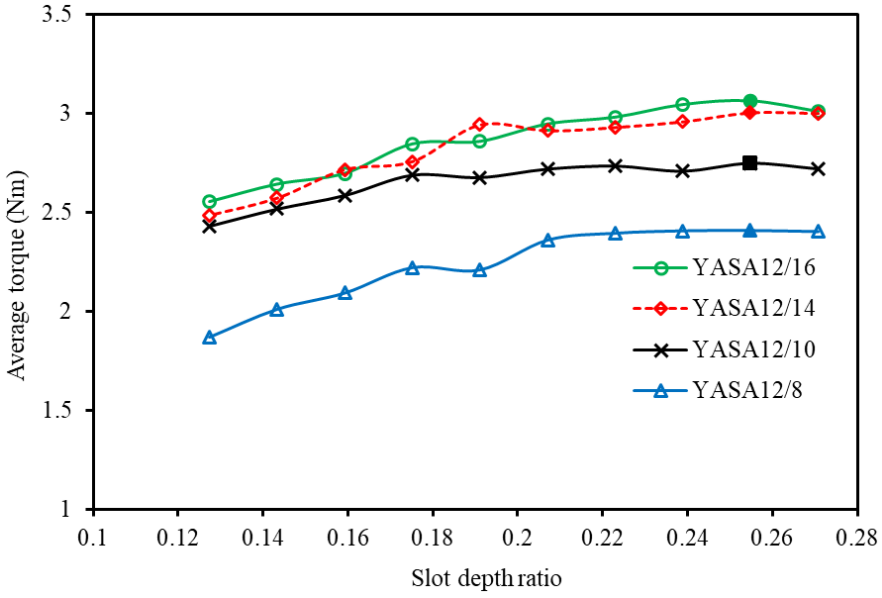

Fig. 2.7. Influence of slot depth on average torque of YASA topologies.

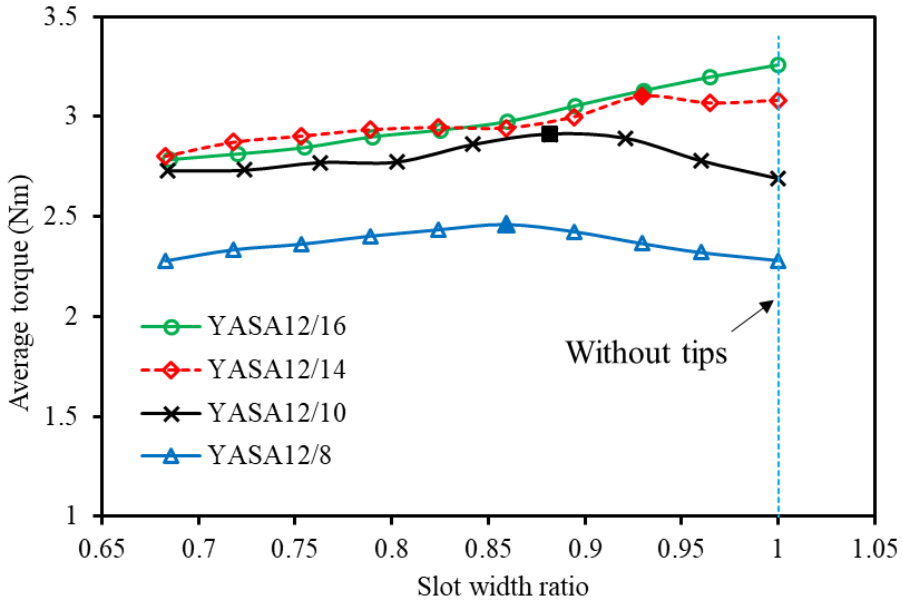

Fig. 2.8. Influence of slot width on average torque of YASA topologies.

2.5 Comparison of machine performance for different rotor pole combinations

With the aim of comparing rotor pole combinations of YASA machine, the optimised machines were designed and analysed with the aid of JMAG 3-D FEA software. The optimal dimensions and the machine parameters are compared and listed in Table 2.4. The machine topologies were studied at no-load and on-load conditions, details of which can be found in the following sections.

Table 2.4 YASA machine pole combination optimal dimensions and parameters

Parameter	YASA 12/8	YASA 12/10	YASA 12/14	YASA 12/16
Rated speed (RPM)	400	400	400	400
Rotor pole no. ($2p$)	8	10	14	16
Stator slot no. (n_s)	12	12	12	12
Machine inner diameter (mm)	30	30	30	30
Machine outer diameter (mm)	90	90	90	90
Axial length (mm)	25	25	25	25
Air gap length (mm)	0.5	0.5	0.5	0.5
Number of turns of armature coil/phase	80	80	80	80
Packing factor	0.5	0.5	0.5	0.5
Rotor pole pitch (degree)	45	36	25.7	22.5
PM angle (degree)	38.7	36	22.8	18.9
PM thickness (mm)	2.22	2.34	2.7	3
Slot area (mm^2)	48.8	48	52	52
Armature stator axial length (mm)	14.2	13.66	14	14.3
Tip thickness (mm)	1	0.75	0.5	0.5
Rotor axial length (mm)	4.9	5.17	5	4.85
I_{rms} (A)	14.4	14.3	14.8	15
PM volume (mm^3)	13270.0	16587.6	16691.20	17509.13

2.5.1 Cogging torque

Cogging torque exists in PM machines because of the variation of the permeance of air-gap due to stator slots. Therefore, the interaction of the permeance harmonics and the magnet MMF harmonics results in unwanted torque harmonics and thus torque pulsating.

The cogging torque was studied for the selected YASA machine topologies. Fig. 2.9 compares the cogging torques and the corresponding harmonics for YASA machine topologies. YASA12/8 has the highest peak-peak cogging torque while YASA12/10 has the lowest cogging torque. The cogging torque level can be estimated for the slot and pole number combinations of PM machines by the cogging torque factor C_T which can be expressed as indicated in [ZHU00] as:

$$C_T = \frac{2p\ n_s}{N_C} \tag{2.10}$$

where: N_C is the least common multiple between the number of stator poles and the number of rotor pole. Higher C_T value indicates higher cogging torque value. However, the minimum value for C_T is unity, which constitutes a proper selection for rotor pole pair combination. For YASA12/8 and YASA12/16, the cogging torque factor is 4. It equals 2 for YASA12/10 and YASA12/14.

2.5.2 No-load flux density

The no-load flux density produced by the PM is one of the most essential for analysing the PM machine performance. Fig. 2.10 shows the flux distribution of the stator and rotor of YASA topologies. Moreover, the axial component of the air-gap flux density waveform of YASA machine topologies was calculated and is indicated in Fig. 2.11. The flux density was calculated in the middle of the air-gap along the mean radius in mechanical degree. It can be seen that the topologies in which the rotor pole-arc is bigger than the stator pole-arc have a significant leakage flux since the effective magnet area is smaller than the full rotor pole-arc (i.e. YASA12/8), as indicated in Fig. 2.10(a). Moreover, the saturation in the back iron is higher in YASA12/8 compared to the other topologies since the flux per pole is higher. The fundamental harmonic amplitudes of YASA12/8 and YASA12/10 are approximately 0.93 T and 0.94 T, respectively. Moreover, the fundamental harmonic order of the air-gap flux density for each model represents the number of rotor pole pairs. Furthermore, YASA12/14 has the highest fundamental harmonic amplitude of approximately 1.0 T. In this case, the rotor pole-arc is approximately the same as the stator pole-arc without tips. Thus, the leakage flux is minimised, and the flux passed through

the stator pole reaches its maximum value, as indicated in Fig. 2.10(c). YASA12/16 has a fundamental harmonic amplitude of approximately 0.97 as shown in Fig. 2.11(c).

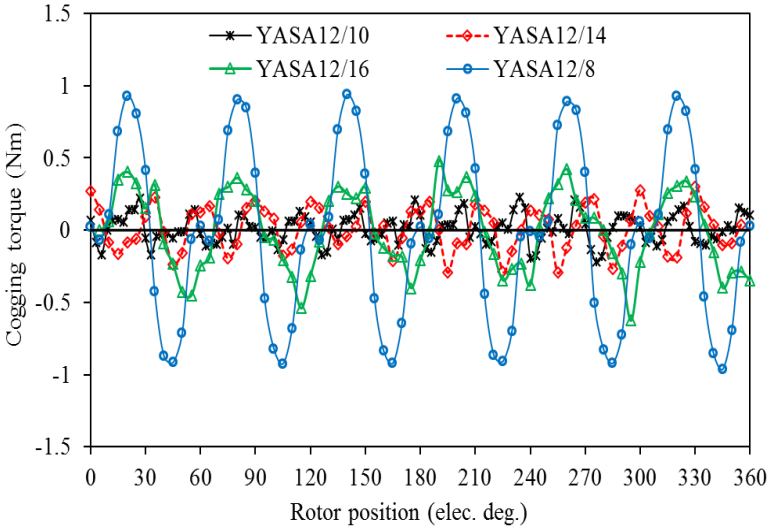

(a) Waveforms

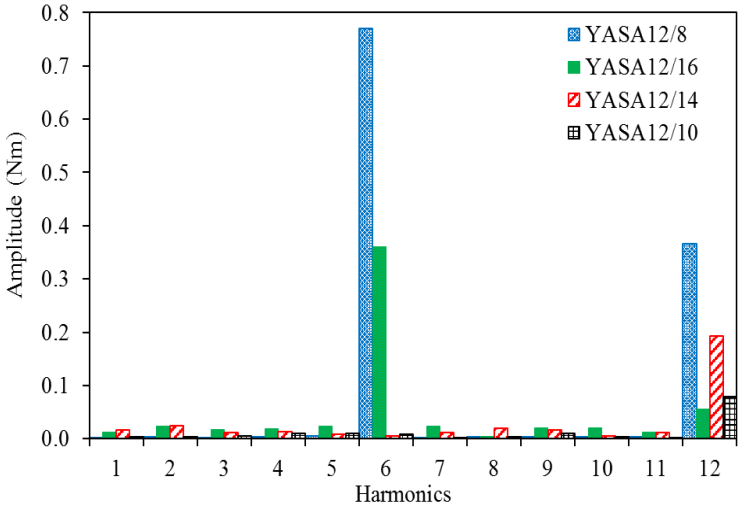

(b) Harmonic spectra

Fig. 2.9. Comparison of cogging torques of YASA machine topologies.

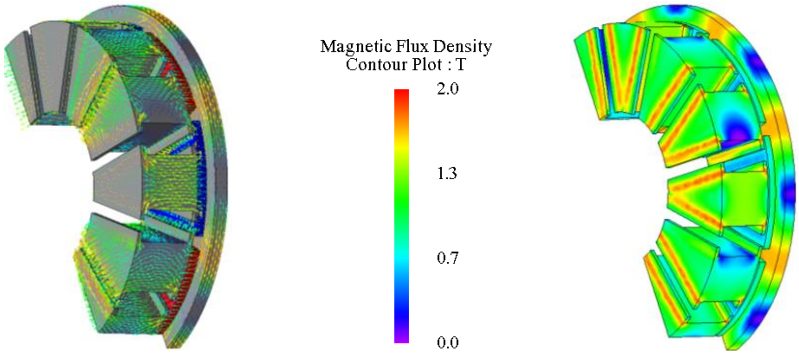

(a) YASA12/8

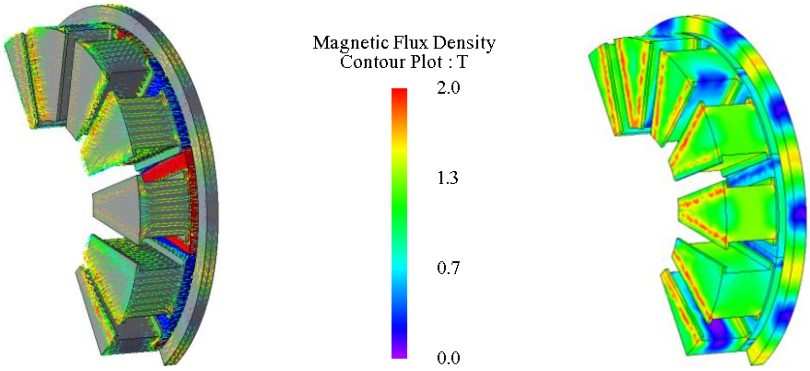

(b) YASA12/10

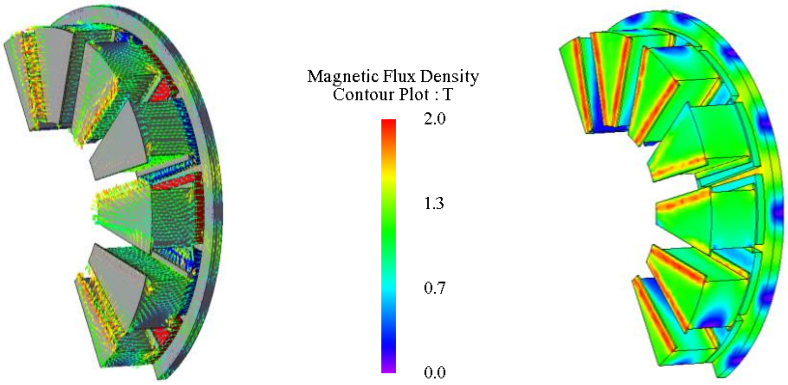

(c) YASA12/14

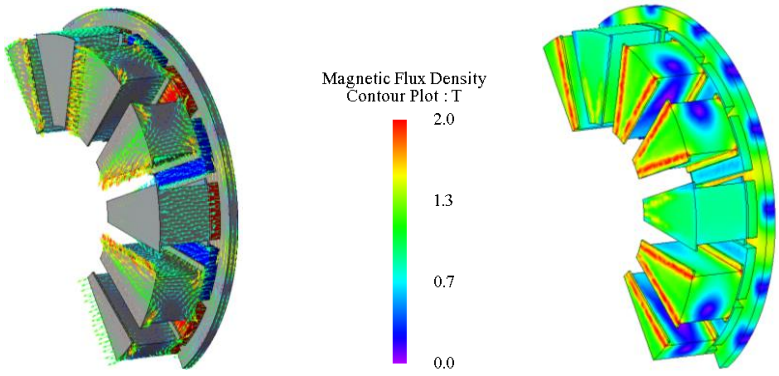

(d) YASA12/16

Fig. 2.10. Stator and rotor flux density distributions of YASA machine topologies at initial position.

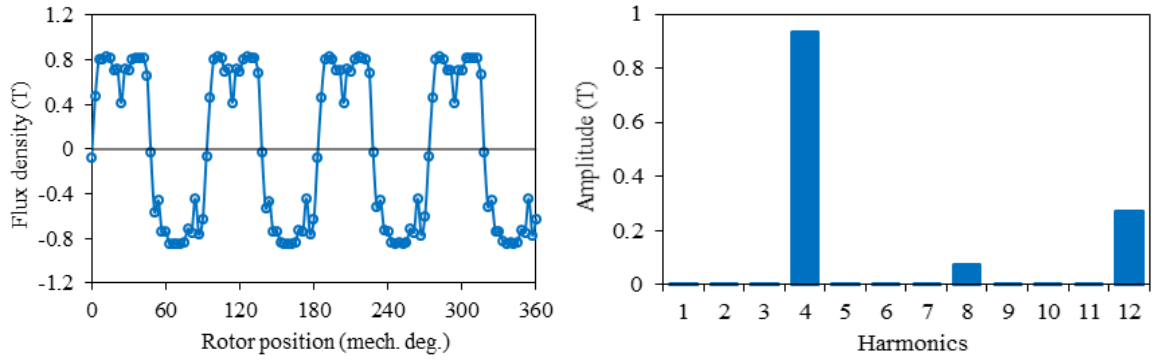

(a) YASA12/8

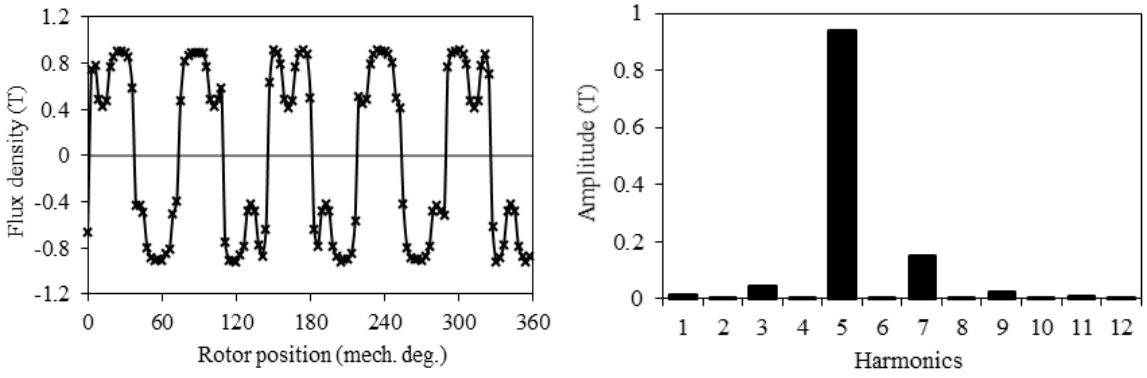

(b) YASA12/10

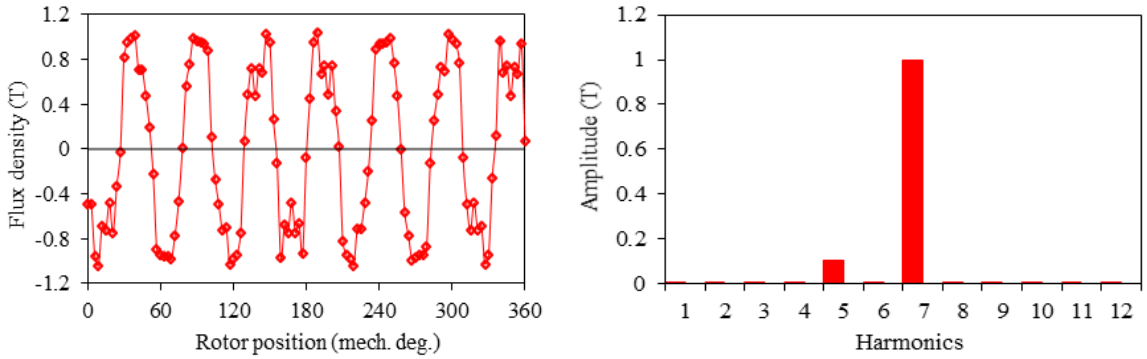

(c) YASA12/14

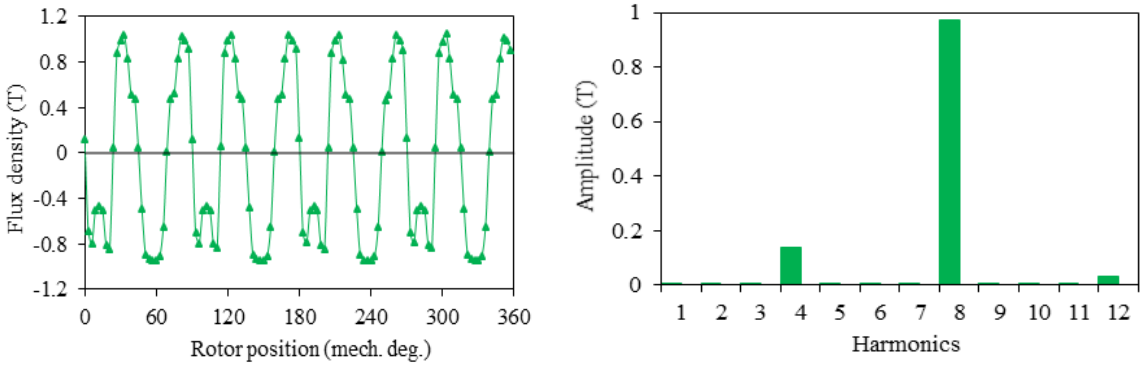

(d) YASA12/16

Fig. 2.11. Axial air-gap flux density waveforms and corresponding harmonic spectra of YASA machine topologies at mean radius of the air-gap.

2.5.3 No-load flux linkage and back EMF

The no-load phase flux linkages of YASA machine topologies are analysed and compared in Fig. 2.12. It is clear that YASA12/8 followed by YASA12/10 have the largest flux linkage amplitude while YASA12/16 has the smallest flux linkage amplitude. However, YASA12/8 flux harmonics include certain odd order harmonics, such as 3rd, 5th, and 7th, which make the flux linkage nonsinusoidal compared to the other topologies.

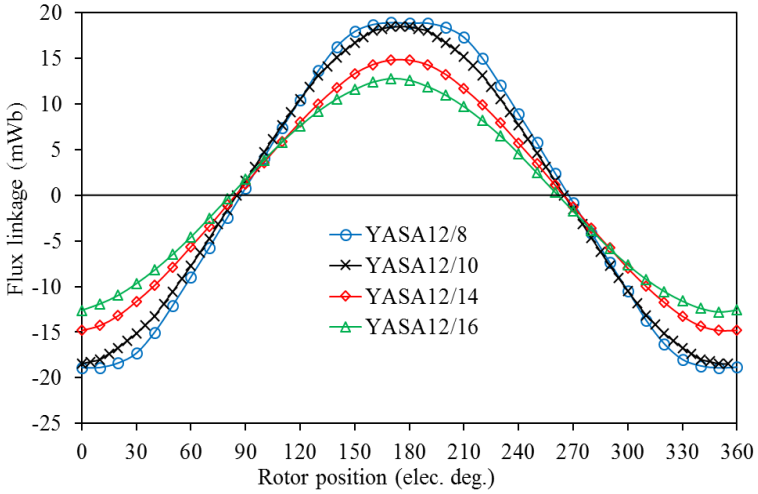

(a) Waveforms

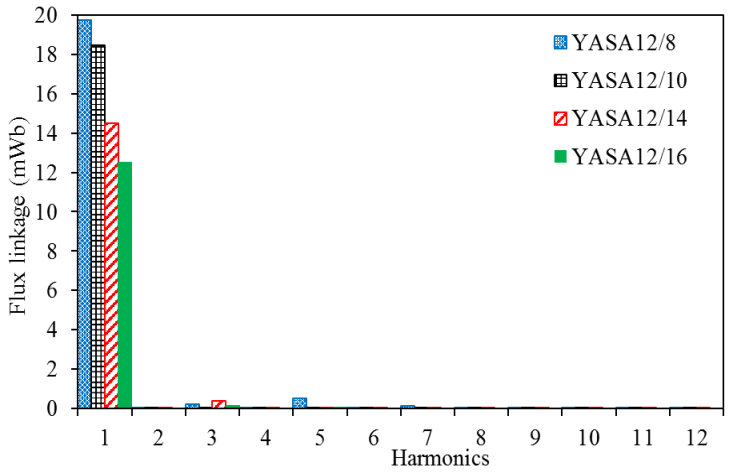

(b) Harmonic spectra

Fig. 2.12. Comparison of phase flux linkages of YASA machine topologies.

Moreover, the no-load phase back EMFs of the YASA machines are studied and compared at a rotor speed of 400 rpm. Fig. 2.13 shows the comparison of the back EMF and the corresponding harmonics for YASA topologies. YASA12/14 has the largest back EMF fundamental amplitude of approximately 4.26 V, whereas the EMF fundamental amplitude of YASA12/16 of approximately 4.25 V is just below YASA12/14. On the other hand, the amplitude of the fundamental harmonic of YASA12/10 is approximately 3.9 V, however, YASA12/8 has a non-

sinusoidal waveform and contains odd order harmonics in which the amplitude of the fundamental component is approximately 3.3 V, as can be seen in Fig. 2.13 (b).

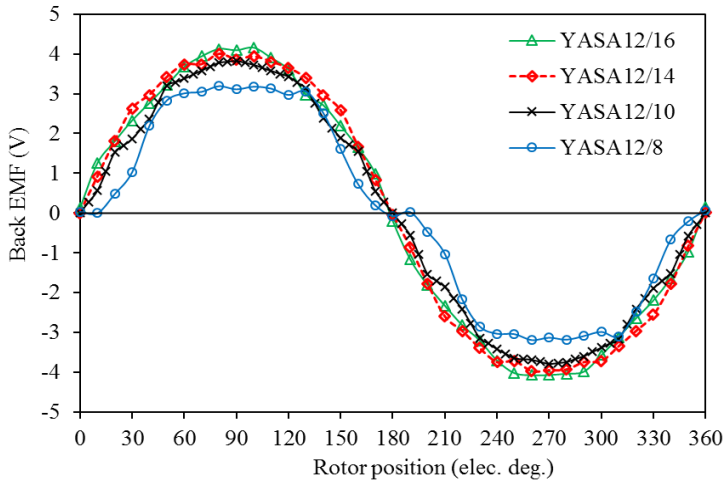

(a) Waveforms

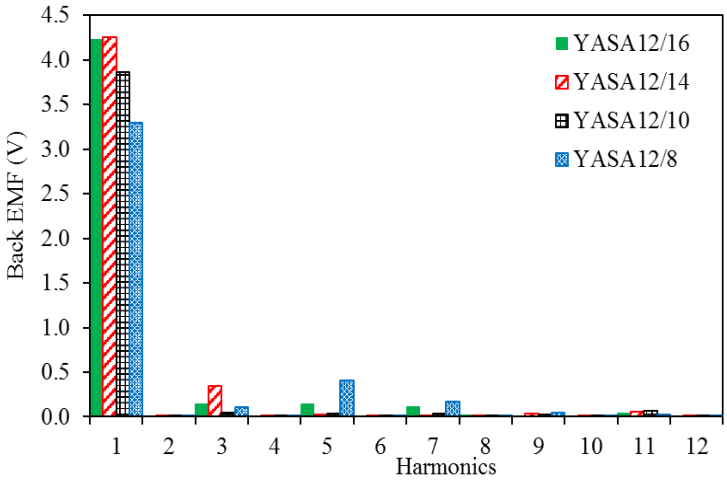

(b) Harmonic spectra

Fig. 2.13. Comparison of phase back EMFs of YASA machine topologies at 400 rpm.

2.5.4 Electromagnetic torque

The electromagnetic torque is studied and compared at rated current and the same machine speed. Fig. 2.14 shows a comparison between YASA topologies in terms of the electromagnetic torque and the current angle relation at rated current, and Fig. 2.15 compares the electromagnetic torque for YASA machines with different pole combinations. It is clear that, YASA12/16 and YASA12/14 have nearly the same highest torque while YASA12/8 has the lowest torque in which the leakage flux is high due to the magnet pitch being much bigger than the slot pole pitch. On the other hand, as can be seen in Fig. 2.15(b), YASA12/14 has the lowest torque ripple followed by YASA12/10. YASA12/8 has the highest torque ripple compared to the other topologies.

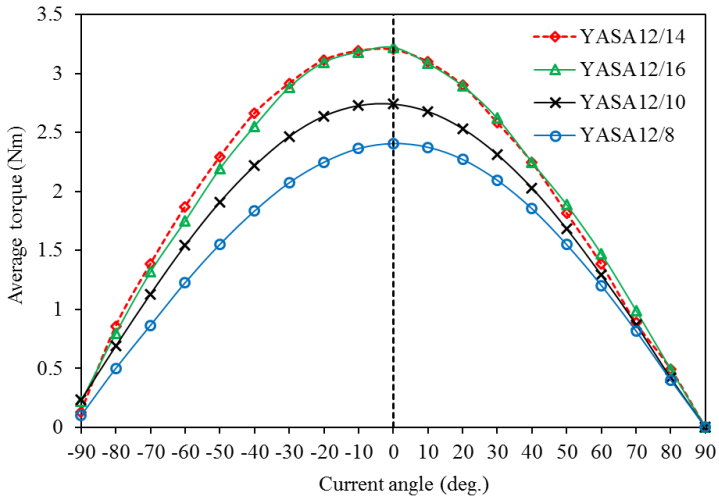

Fig. 2.14. Comparison of torque-current angle curves of YASA machine topologies.

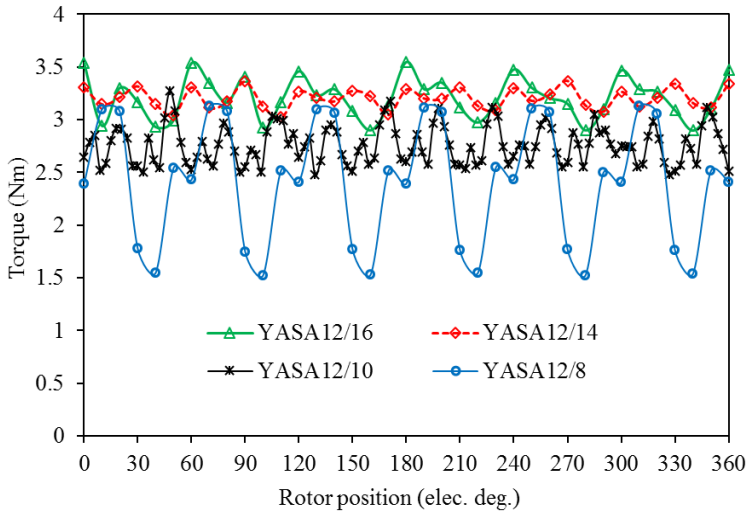

(a) Waveforms

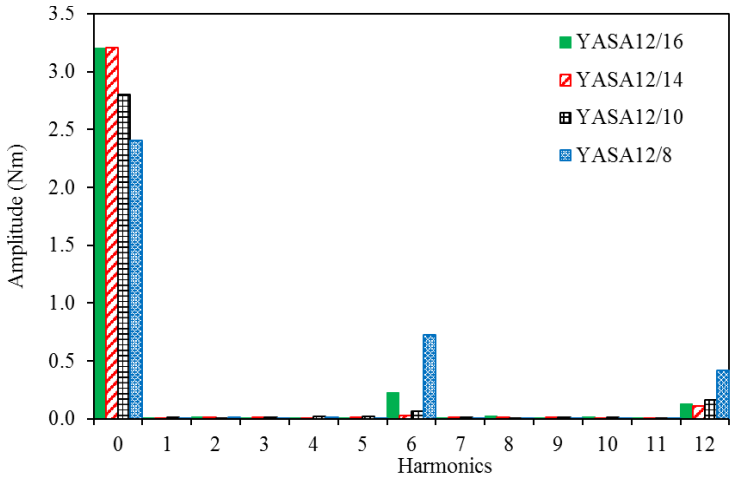

(b) Harmonic spectra

Fig. 2.15. Comparison of electromagnetic torques of YASA machine topologies.

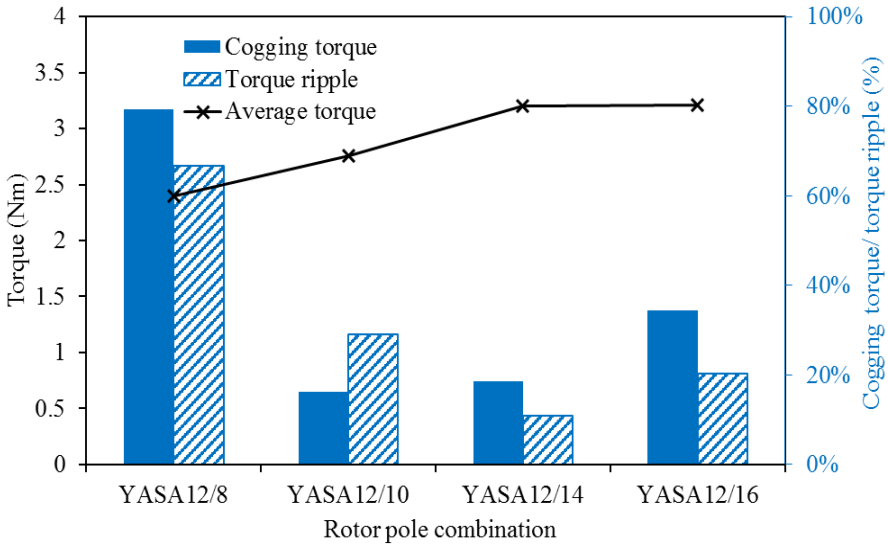

Fig. 2.16. Comparison of average torque, torque ripple and peak-peak cogging torque of YASA machine topologies.

Fig. 2.16 shows a comparison between the proposed YASA machine topologies with respect to the torque, torque ripple and cogging torque. The cogging torque and torque ripple are calculated with reference to the average torque by:

$$T_{\text{ripple}}, T_{cog} = \frac{T_{\max} - T_{\min}}{T_{\text{avg}}} \times 100 \ \% \qquad (2.11)$$

It should be noted that the preceding formula is used to calculate the cogging torque at no load and the torque ripple at load. The figure shows that YASA12/14 has a superior torque performance compared to the other topologies while YASA12/8 has high cogging torque and torque ripple.

The machine torque performance at different current, current density and copper loss was also studied. Fig. 2.17 indicates the torque – current curve while Fig. 2.18 shows the torque – current density curve. It is clear that YASA12/16 and YASA12/14 have the best performance, where at rated current, the performance is approximately the same. However, YASA12/8 has the lowest torque/current and torque/current density, the reason for which is the leakage flux being higher than with other pole combinations.

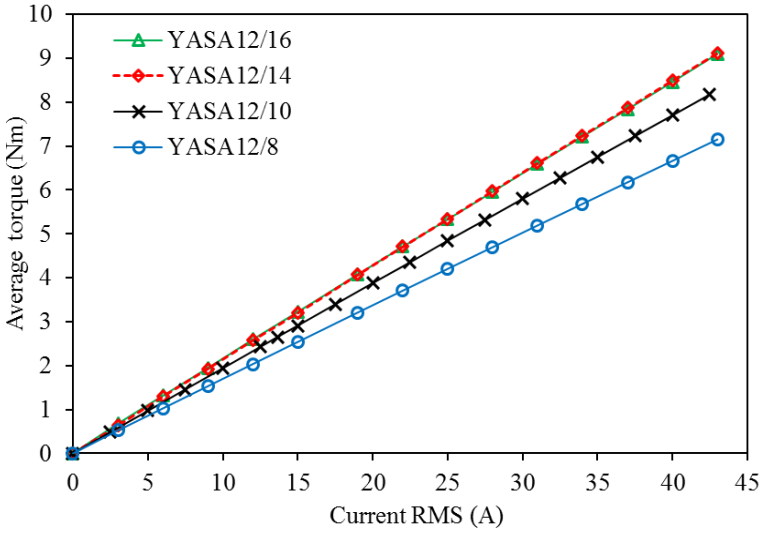

Fig. 2.17. Comparison of average torque-RMS current characteristics of YASA machine topologies.

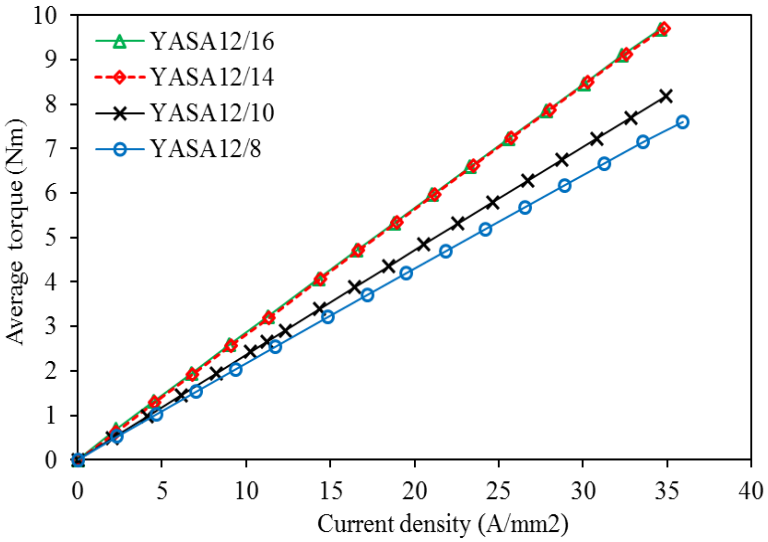

Fig. 2.18. Comparison of average torque-current density characteristics of YASA machine topologies.

Furthermore, the influence of the copper loss of windings on the machine torque was also investigated. The results are shown in Fig. 2.19. The figure shows that YASA12/16 and YASA12/14 have a high torque performance at different copper loss. However, YASA12/8 has a lower torque performance than other rotor pole topologies. Finally, the average torque per PM volume at different currents was studied and is compared in Fig. 2.20. The figure shows that YASA12/14 has the highest torque/magnet volume while YASA12/10 has the lowest performance. Moreover, both YASA12/8 and YASA12/16 have approximately the same torque per magnet volume-RMS current curve.

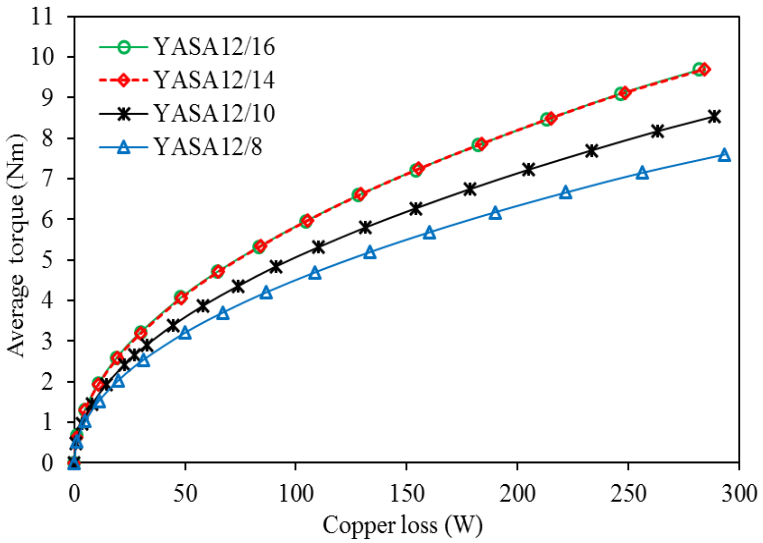

Fig. 2.19. Comparison of average torque-copper loss characteristics of YASA machine topologies.

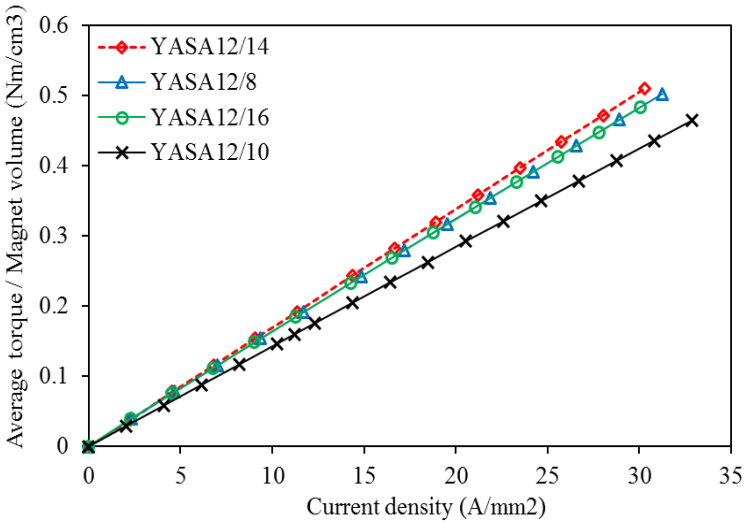

Fig. 2.20. Comparison of average torque/magnet volume-RMS current characteristics of YASA machine topologies.

2.5.5 Losses and efficiency

For the YASA topologies, SMC material is used for the machine stator and rotor back iron core. This material has the merit of flexible design, low eddy current loss [JAC98]. Several studies have been presented to predict the iron loss of YASA machines using different approaches [VAN12], [HEM14]. Moreover, it has been confirmed that YASA machines employing SMC material have a superior performance at high speed compared to YASA with electrical steel cores [KIM17]. The losses generated in PM machines can be classified as copper loss, iron loss and eddy current loss induced in the PM. The copper loss is produced by the resistive component of

the stator windings under on-load condition. The copper loss can be calculated by the classical Ohm equation when the end winding resistance is neglected. However, the copper loss in this thesis is assumed constant at all analyses of 30 W. Iron loss is generated in the machine core geometry, such as the stator pieces and the rotor back iron, due to the variation of the magnetic flux. Moreover, the intersection of the flux through the magnet generates more loss caused by the eddy current circulating in the magnet pieces. At low speed, the fundamental harmonic component of the flux is the main cause of the iron loss. Furthermore, since the flux density variation in different parts of the machine is not identical, the losses induced in the machine parts differ. However, the stator has the highest consumed loss as the flux density is high. Iron losses in PM machines, P_{Iron}, can be divided into hysteresis loss, P_h, and eddy current loss, P_e. The no-load and on-load stator iron loss in YASA machine topologies were evaluated by JMAG 3D-FE software at rated speed of 400 rpm. The iron loss was calculated based on the iron loss density (W/m^3) obtained by manufacturer's data for (GKN SMC 70H) material indicated in Appendix C, and can be estimated by:

$$P_{\text{Iron}} = P_{\text{h}} + P_{\text{e}} = \sum_{k=1}^{ne} Wh_e(B_m, f) \times V_e + \sum_{m=1}^{ne} \left(\sum_{k=1}^{N} W_e\ (|B_{mk}|, f_k) \times V_e \right) \qquad (2.12)$$

where: Wh_e is the hysteresis for each element at maximum flux density B_m and frequency f, W_e is the Joule loss for each element at maximum flux density B_{mk} and frequency of the k^{th} frequency order, V_e is the volume for each element (m^3), ne is the number of elements, and N is the maximum frequency order. A comparison of iron and PM losses of YASA machine topologies are calculated and compared in Fig. 2.21. It should be mentioned that the skin effect is not considered in this study since the machine is operating at low speed, (see Appendix A). Moreover, the eddy current loss generated in the machine iron is neglected and it only considered in the rotor PMs. It's obvious that the no-load iron and PM losses increase as the pole number increases, as illustrated in Fig. 2.21(a). Moreover, the losses increase at on-load condition due to the armature current flux. Furthermore, YASA12/16 and YASA12/14 have approximately identical on-load total losses due to the flux passing in the stator core being approximately equal as shown in Fig. 2.21(b). However, the total loss of YASA12/8 under no-load and on-load conditions is significantly lower compared with the other topologies. In addition, the efficiency of YASA topologies was predicted by accumulating the evaluated electromagnetic losses and the copper loss, as shown in Fig. 2.21(b). Since the copper loss is assumed at a constant of 30 W, and when the mechanical loss is neglected, the efficiency of all topologies at 400 RPM can be calculated from:

$$\text{Efficiency (\%)} = \frac{Output\ power}{Output\ power + Copper\ loss + Iron\ loss + PM\ loss} \times 100 \qquad (2.13)$$

The results indicate that YASA12/14 and YASA12/16 have identical superior efficiencies of approximately 80.2 %, while YASA12/10 and YASA12/8 have considerably lower efficiencies of approximately 78 % and 76 %, respectively. In fact, both YASA12/14 and YASA12/16 have high output powers at rated speed and rated current; however, more electromagnetic losses are induced due to armature current flux.

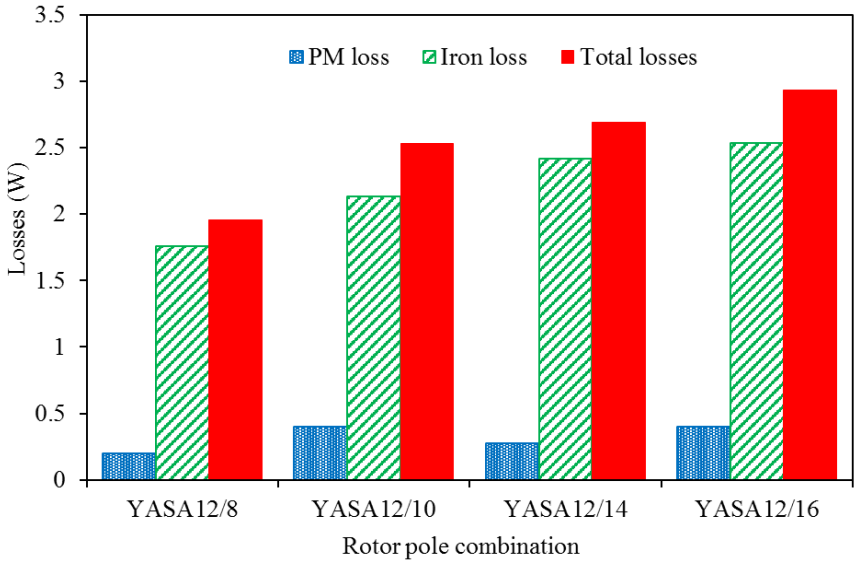

(a) No-load losses

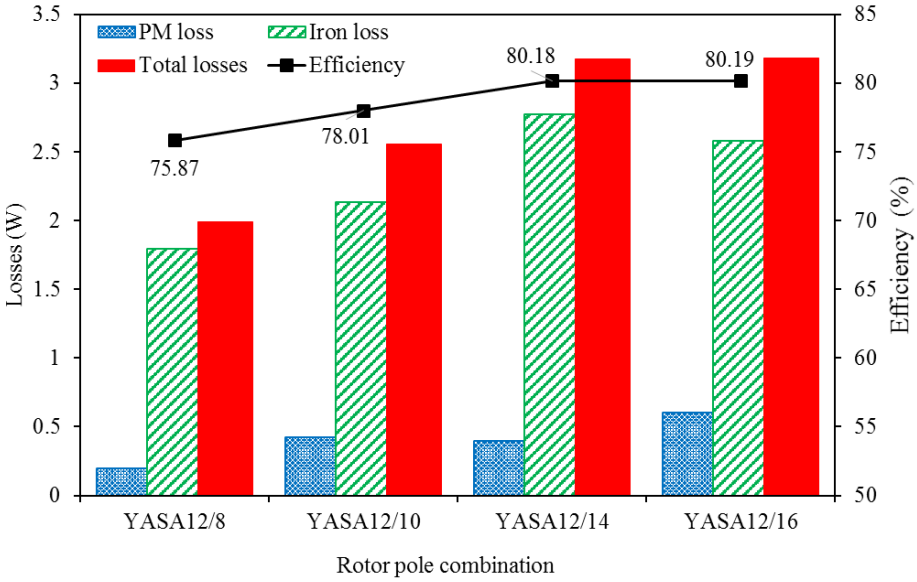

(b) On-load losses and efficiencies

Fig. 2.21. Comparison of no-load and load losses and efficiencies at rated speeds.

2.6 Summary

In this chapter, YASA machines with the same number of stator segments and different rotor pole number combinations with a high winding factor were chosen and designed with the aid of 3D-FEA. Moreover, a performance comparison between the YASA machine topologies with different rotor pole numbers has been verified. The results show that both YASA12/14 and YASA12/16 machines have higher no-load and on-load performances. Moreover, such topologies have higher back EMF and average torque; however, YASA12/16 has a noticeably higher cogging torque and torque ripple with the reference of YASA12/14. Furthermore, YASA12/8 has the smallest average torque and highest cogging torque and torque ripple compared to the other topologies. In addition, the no-load and on-load core losses for YASA topologies were examined and compared. The comparison shows that the no-load iron loss increases as the rotor pole number increases at the same speed. However, YASA12/14 has the highest on-load iron losses since it has a higher stator flux. Overall, YASA12/14 and YASA12/16 both have a higher torque density as well as higher efficiency in which both have approximately the same optimal magnet and stator active areas.

CHAPTER 3

NOVEL AXIAL FLUX MAGNETICALLY GEARED MACHINE DESIGN

3.1 Introduction

MGs are currently being developed to replace conventional mechanical gears in various electromechanical systems such as those related to renewable energy HEVs [ATA01]. Moreover, by integrating an MG into a conventional PM machine, magnetically geared machine has emerged, greatly broadening the machine topologies. A magnetically geared machine always has the merits of high torque density and reduced overall size in comparison with conventional PM machine axially combined with MGs [WAN09]. Many magnetically geared machines have been introduced for various applications. Axial flux magnetically geared machine topologies for various applications in which a conventional axial flux PM machine is combined with an MG have also been introduced and analysed. These machines have the merit of combining the advantages of conventional axial flux machines (for example, high performance, low rotor loss, and short axial length) with those of MGs in which the absence of physical contact and lubrication are the most significant features. The need for machines with superior performance in terms of reduced losses and weight has recently encouraged researchers to investigate the manufacturing and structural aspects of AFPM machines [GIU12]. However, as opposed to the relative simplicity of AFMG machines, the developed axial flux magnetically geared machine topologies have complicated mechanical structures. For example, some presented topologies have four machine parts where three air-gaps are essential [WAN13] and [KOU17], or five main parts with four gaps [TON14].

In this chapter, a novel axial flux magnetically geared machine (AFMGPM) is presented and analysed. Based on yokeless and segmented armature YASA machine, a new AFMGPM machine for low-speed and high-torque applications is designed. The topology is a combination of both YASA machine and a magnetic gear. The proposed AFMGPM offers the merit of a simple mechanical structure and is suitable for applications with limited axial space. The operating principle and the feasible stator slot/rotor pole combinations for the novel AFMGPM machine are analysed. To maximise the torque, global optimisation of the machine is conducted. By utilising ANSYS Maxwell 2D-FEA software, global optimisation based on a genetic algorithm is executed under fixed copper loss. Then, with the aid of JMAG 3D-FEA software, the influence

of individual geometric parameters is investigated. Moreover, the performance of the various stator slot and rotor pole combinations is investigated and compared using 3D-FE analysis. In addition, both no-load and on-load performance of the machines are analysed.

3.2 Proposed axial flux MG machine configuration

The proposed AFMGPM machine essentially has magnetically separated segments with windings form the machine stator [WOO07], [QIN16]. It has the same stator structure as the conventional YASA machine; however, by employing different rotor pole pairs, a new magnetically geared axial flux machine was created. The use of 2D and 3D finite element (FE) analysis allowed global and individual optimisations to be carried out to maximize the proposed machine average torque.

The 3D configuration of the proposed AFMGPM machine is shown in Fig. 1(a), with the 2D section at average diameter D_m being shown in Fig. 3.1(b). The stator of the proposed AFMGPM machine consists of ferromagnetic iron pieces (flux modulation pieces) equipped with concentrated windings and is sandwiched between two surface mounted PM rotors with different pole pairs. The ferromagnetic pole pieces have tooth tips to hold the stator windings. By utilising two rotors with different pole pair numbers - the first of which rotates at high-speed (HSR), the second at low-speed (LSR) - a magnetic gearing effect can be exerted on both rotors.

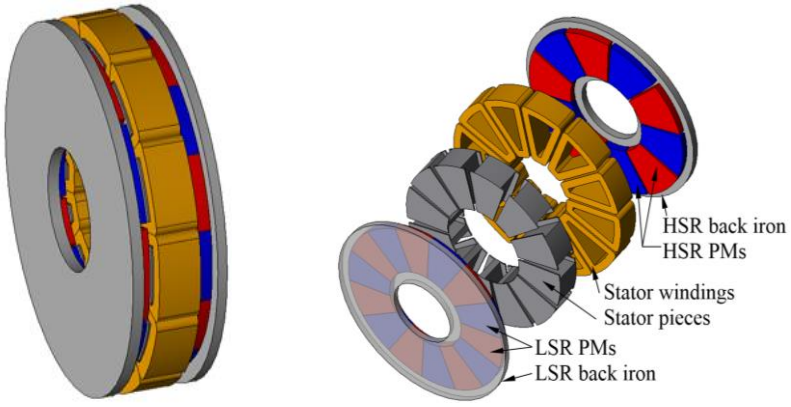

(a) 3D-model and exploded view

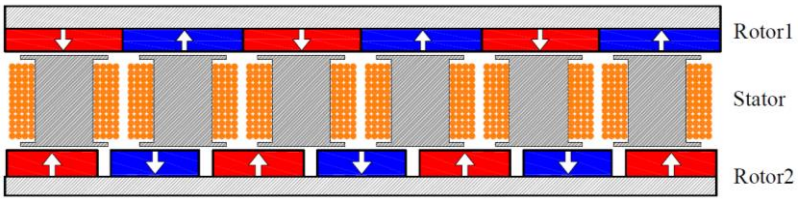

(b) 2D cross section at average diameter

Fig. 3.1 The proposed machine topology.

3.3 Principle of operation

Since the proposed AFMGPM topology is a combination of an MG and a PM machine, its operation principle will be introduced from these two perspectives. The operation principle of MGs has been thoroughly explained in [ATA04], [MEZ06]. To realise a stable electromagnetic torque transmission for conventional PM machines, the stator magnetic field harmonic and the PM flux harmonic must have the same order and speed. Therefore, the number of pole pairs of the stator windings should be equal to that of the PM rotor, and the rotational speeds of the stator flux and the PMs flux should be also equal. However, for magnetically geared machines, the pole pair number of the stator is not equal to that of the PM rotor. Therefore, to achieve stable torque transmitted to the rotor through the air-gap, the stator winding flux should have some space harmonics equal to those of the PM rotor. These harmonics can be obtained by modulating the flux to the air-gap through the modulator placed between the stator and the PM rotor. In general, in magnetic gears, one rotor is connected with an external prime-mover while the other rotor is connected with the load. The input speed and torque are transferred to the output rotor shaft with full isolation between shafts. The proposed AFMGPM machine has a modulator with windings between two different pole rotors. This modulator can modulate the flux produced by either rotors when one rotor is rotated by a specific speed. Moreover, with the presentation of the armature windings, the stator is equipped with 3–phase concentrated winding coils to create the required stator pole pairs. A magneto-motive force (MMF), which is produced by such coils, results in a multiple harmonics flux in the air-gap between the stator and the PM rotors. Moreover, based on the electromagnetic theory of conventional PM machines, the flux harmonics produced by the coil MMF must have the same pole pairs and rotation speed as the rotor's PM flux harmonics. Therefore, in addition to the torque exerted at both rotors due to the MG effect, the armature windings can produce fluxes in both air-gaps. It is important to note that the torque produced by the interaction between the armature reaction flux harmonics and PMs flux harmonics for each rotor contribute to the total torque of each rotor.

According to the theory of integer slot windings, the energy conversion is related to the fundamental component of the armature current flux density. However, for fractional slot windings, the flux density spectrum can have many even and odd harmonics which rotate at different speeds and directions. The speed and direction of the highest air-gap flux density harmonic are important to identify the machine rotor pole number and its mechanical speed with which the main harmonic order is equal to the rotor pole pairs [BIA06] [ZHU09a].

3.3.1 Magnetic gear torque

The operation principle can be deduced firstly based on MG torque transmission in which the stator winding current is not fed by 3-phase current and is assumed to be zero. When the first rotor rotates at a specific speed, the magnetic flux produced by its PMs is modulated by the ferromagnetic pieces. This results in high amplitude space harmonics in the other rotor's air-gap which has the same pole-pairs and rotational speed as the other rotor. In numerical and FE methods, the Maxwell stress tensor is utilised in the calculation of the force and the corresponding torque in the air-gap regions of PM machines. The magnetic field strength H between objects in vacuum creates a stress δ_F on the object surface and this stress can be given by:

$$\delta_F = \frac{1}{2}\mu_o H^2 \tag{3.1}$$

The flux in the air-gap is divided into two components: normal or radial and tangential fluxes. Therefore, according to the Maxwell stress tensor, the stress terms can be also divided into normal δ_{FN} and tangential δ_{FT} according to the flux density components, and can be obtained by:

$$\delta_{FN} = \frac{1}{2\mu_o}(B_N^2 - B_T^2) \tag{3.2}$$

$$\delta_{FT} = \frac{1}{\mu_o} B_N B_T \tag{3.3}$$

where B_N and B_T are the normal and tangential flux densities, respectively.

For PM machines, the flux density in the air- gap produced by the PMs of the rotor can, in general, be described as in [SPA14]:

$$B = B_\theta + jB_r \tag{3.4}$$

where B_θ and B_r are the representatives of the tangential and radial air-gap flux densities, respectively. Therefore, based on the Maxwell stress definition, the tangential average force and torque of the radial machine's rotor can be calculated as given in [LUB13]:

$$F_\theta = \delta_\theta S = \frac{r}{\mu_o}\int_0^{2\pi}\int_0^{L_m}(B_r B_\theta)\, d\theta dz. \tag{3.5}$$

$$T = rF_\theta = \frac{r^2}{\mu_o}\int_0^{2\pi}\int_0^{L_m}(B_r B_\theta)\, d\theta dz. \tag{3.6}$$

where S, r, and L_m are the surface area, the radius and the axial length of the machine rotor, respectively.

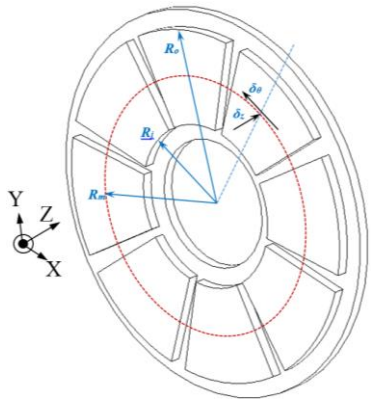

Fig. 3.2 Stresses in an axial flux PM rotor.

Similarly, for axial flux machines, the average torque obtained by the rotor disc's PM based on the tangential stress explained in Fig. 3.2, can be expressed as follows:

$$T = \frac{(R_o^3 - R_i^3)}{\mu_o} \int_0^{2\pi} (B_z B_\theta)\, d\theta. \tag{3.7}$$

In addition, the axial force F_z in the air-gap due to the axial flux density can be generally written by:

$$F_z = \frac{(R_o^2 - R_i^2)}{\mu_o} \int_0^{2\pi} (B_z^2 - B_\theta^2) d\theta. \tag{3.8}$$

where B_z is the axial flux density, R_i and R_o are the inner and outer stator radii as explained in Fig. 3.2. The torque expression in (3.7) can be used to calculate the torque produced by each rotor of the MG machine.

3.3.2 PM flux density

The air-gap flux density distribution at the axial direction produced by either rotor's PMs without modulation effect B_{pz} of axial flux topologies can be given [ZHE13]:

$$B_{pz} = \sum_{m=1,3,5,..} b_{mpz}(z) \cos(mp(\theta - \omega_r t + \theta_o)) \tag{3.9}$$

Moreover, the corresponding air-gap flux density distribution at the circumferential direction produced by either rotor's PMs without modulation effect $B_{p\theta}$ can be given as

$$B_{p\theta} = \sum_{m=1,3,5,..} b_{mp\theta}(\theta) \sin(mp(\theta - \omega_r t + \theta_o)) \tag{3.10}$$

where ω_r is the rotor flux rotational speed, and θ_o is the rotor initial position. The modulation function of the pole pieces when a rotating modulator is considered can be written as:

$$\lambda = \lambda_o + \sum_{n=1,2,3,..} \lambda_n \cos(nn_s\theta) \tag{3.11}$$

where $\lambda_o$and λ_n are the Fourier coefficients of the modulation function. However, when the pole pieces are considered, the flux density produced by the PM is distorted by the effect of such pieces, which is similar to the slotting effect in conventional PM machines. Therefore, the resulting axial and circumferential flux densities in each air-gap at a specific axial distance, due to the presence of these pieces, can be obtained by multiplying the original PM flux density with the modulating function ($B \times \lambda$), and the resulting axial flux density can be obtained as:

$$\begin{aligned} B_z &= \left\{ \sum_{m=1,3,5,..} b_{mpz}(z) \cos(mp(\theta - \omega_r t + \theta_o)) \right\} \times \left\{ \lambda_o + \sum_{n=1,2,3,..} \lambda_n \cos(nn_s\theta) \right\} \\ &= \sum_{m=1,3,5,..} \lambda_o b_{mpz}(z) \cos(mp(\theta - \omega_r t + \theta_o)) \\ &+ \sum_{m=1,3,5} \sum_{n=1,2,3,..} \frac{\lambda_n \, b_{mpz}(z)}{2} \cos\left[(nn_s + mp)(\theta - \frac{mp\omega_r}{(nn_s + mp)} \, t + \frac{mp\theta_o}{(nn_s + mp)}) \right] \\ &+ \sum_{m=1,3,5} \sum_{n=1,2,3,..} \frac{\lambda_n \, b_{mpz}(z)}{2} \times \cos\left[(nn_s - mp) \left(\theta + \frac{mp\omega_r}{(nn_s + mp)} \, t + \frac{mp\theta_o}{(nn_s + mp)} \right) \right. \end{aligned} \tag{3.12}$$

The flux density in the circumferential direction can be expressed by:

$$\begin{aligned} B_\theta &= \left\{ \sum_{m=1,3,5,..} b_{mp\theta}(\theta) \cos(mp(\theta - \omega_r t + \theta_o)) \right\} \times \left\{ \lambda_o + \sum_{n=1,2,3,..} \lambda_n \cos(nn_s\theta) \right\} \\ &= \sum_{m=1,3,5,..} \lambda_o b_{mp\theta}(\theta) \cos(mp(\theta - \omega_r t + \theta_o)) \\ &+ \sum_{m=1,3,5} \sum_{n=1,2,3,..} \frac{\lambda_n \, b_{mp\theta}(\theta)}{2} \cos\left[(nn_s + mp) \left(\theta - \frac{mp\omega_r}{(nn_s + mp)} \, t + \frac{mp\theta_o}{(nn_s + mp)} \right) \right] \\ &+ \sum_{m=1,3,5} \sum_{n=1,2,3,..} \frac{\lambda_n \, b_{mpz}(z)}{2} \times \cos\left[(nn_s - mp)(\theta + \frac{mp\omega_r}{(nn_s + mp)} \, t + \frac{mp\theta_o}{(nn_s + mp)}) \right] \end{aligned} \tag{3.13}$$

where: $b_{mp\theta}$and b_{mpz} are the Fourier coefficients of the radial and axial components of the flux density, respectively. From (3.13) the number of pole pairs of the flux density produced by the rotor in the space harmonics can be given by:

$$p_{m,k} = |mp + nn_s| \tag{3.14}$$

and the corresponding rotational speed is given by:

$$\omega_{n,m} = \frac{mp\omega_r}{(nn_s + mp)} \tag{3.15}$$
$$n = 0, \pm 1, \pm 2, \pm 3, \ldots$$
$$m = 1,3,5, \ldots$$

It can be seen that the space harmonics have more components due to the modulation effect. In addition, rotational speed (natural space harmonics) is indicated with the absence of the modulator pieces which can be obtained when *n*=0. Moreover, the amplitudes of the axial modulated space harmonics depend on the values of λ_o, b_{mpz}. It has further been proved that the maximum space harmonics of the modulated flux produced by the PM can be achieved when *n*=-1 and *m*=1. Therefore, a design with stable torque transmitted between both rotors can be achieved when the number of modulator segments is equal to the summation of pole pairs of such rotors. Hence, for high transferred torque capability of the proposed AFMGPM machine, the relationship between the numbers of pole pairs of HSR, LSR and stationary pole pieces must be satisfied by [ATA01].

$$p_l + p_h = n_s \tag{3.16}$$

From (3.15), the relationship between the HSR rotation speed (ω_h), LSR rotation speed (ω_l) and modulator pieces' speed (ω_s) can be expressed as

$$p_l\omega_l + p_h\omega_h = n_s\omega_s \tag{3.17}$$

The energy conversion relation between the input power and the output power can be given by

$$T_l\omega_l + T_h\omega_h + T_s\omega_s = 0 \tag{3.18}$$

For the stationary modulator, the above formula can be presented as

$$\frac{p_l}{p_h} = -\frac{\omega_h}{\omega_l} \tag{3.19}$$

where p_h and p_l are the numbers of pole pairs for HSR and LSR, respectively. n_s denotes the number of stationary pieces. In addition, the ratio between rotor pole pairs stated in (3.19) is the gear ratio G_r, and the negative sign indicates that two rotors will rotate at opposite directions, and the corresponding gear ratio G_r can be presented as

$$G_r = \frac{n_s - p_h}{p_h} = -\frac{p_l}{p_h} = \frac{T_l}{T_h} = \frac{\omega_h}{\omega_l} \tag{3.20}$$

For MG design, the required gear ratio can be achieved by choosing the appropriate pole pair combination of two rotors. In addition, the torque ripple in either HSR or LSR can be reduced by selecting a proper gear ratio [ABD12].

3.3.3 Armature current flux density

With the presence of the stator winding, the air-gap flux density produced by a stator only which adopts three-phase concentrated windings can be given by:

$$B_s = \sum_i b_{is}(z)\cos(ip(\theta - \frac{\omega_s}{i}t)) + \sum_j b_{js}(z)\cos(jp(\theta + \frac{\omega_s}{j}t)) \tag{3.21}$$

The modulated armature reaction air-gap flux density in the axial direction due to the slotting effect can be obtained by multiplying the flux density obtained by the stator current B_s presented by (3.21), by the modulation operator $\lambda_s(\theta)$ presented by (3.11) which can be expressed by:

$$\begin{aligned} B_s(z) &= B_s\,\lambda_s(\theta) \\ B_s(z) &= \sum_{i=0,1,2,.} \lambda_o b_{is}(z)\cos(ip(\theta \pm \frac{\omega_s}{i}t)) \\ &+ \sum_{n=1,2,.}\sum_{i=0,1,2,.} \frac{\lambda_n b_{is}(z)}{2}\cos((ip \pm nn_s)(\theta - \frac{ip}{(ip \pm nn_s)}\omega_s t)) \\ &+ \sum_{n=1,2,.}\sum_{j=0,1,2,..} \frac{\lambda_n b_{js}(z)}{2}\cos((jp \pm nn_s)(\theta + \frac{jp}{(jp \pm nn_s)}\omega_s t)) \end{aligned} \tag{3.22}$$

where b_{is} and b_{js} are the Fourier coefficients of the axial components of the flux density produced by the armature windings. It can be seen that the air-gap flux density due to the armature windings has harmonics with the number of pole pairs given by:

$$p_{i,j} = (ip \pm nn_s) \text{ or } (jp \pm nn_s) \tag{3.23}$$

and the corresponding rotational speed is given by:

$$\omega_{i,j} = \text{of } \frac{ip}{(ip \pm nn_s)}\omega_s \text{ or } \frac{jp}{(jp \pm nn_s)}\omega_s \tag{3.24}$$

$$i, j = 0, \pm1, \pm2, \pm3, \ldots$$

$$n = 1,3,5, \ldots$$

Therefore, comparing (3.14) and (3.23), and if *i or j* are assumed to be equal to *m*, this results in the two magnetic fields including harmonics that have the same pole pairs. When comparing (3.15) and (3.24), it is clear that the two magnetic fields have the same speed as the rotor. In this case they can produce steady torque in addition to the MG effect torque.

3.4 Stator/rotor pole number combination of the proposed magnetically geared machine

Magnetically geared machines are subject to the restraints of both PM machines and the magnetic gears. In other words, the number of rotor poles and slots of magnetically geared machines cannot be freely chosen. For the proposed magnetically geared machine, the stationary pole pieces n_s is preferred as 12. Therefore, according to the magnetic gear principle given in (3.16), four rotor pole combinations can be considered for n_s=12. Moreover, for PM machines, the relation between the stator slots n_s and rotor pole pairs p can be obtained by (2.1). It is evident that maximum flux linkage can be obtained when the stator slots n_s and rotor pole $2p$ combinations differ by the smallest integer which are obtained when $k = 1$ and 2 [ISH05] [WAN08]. Therefore, by considering both (3.16) and (2.2), possible rotor pole combinations of the machine can be determined for n_s of 12 and are listed in Table 3.1.

However, balanced concentrated windings are normally adopted when S_{pp} ≤0.5 [CRO02]. Therefore, for the proposed AFMGPM machine, the concentrated winding can only be used for two rotor pole combinations which listed in Table 3.1. The first combination is known as (MG12/5-7), in which HSR pole pairs p_h equals 5 and LSR pole pairs p_l equals 7. The second combination is known as (MG12/4-8), in which p_h=4 and p_l=8. The remaining pole combinations in Table 3.1 are not convenient for the proposed topology since the S_{pp} of HSR is an integer, thus resulting in a low winding factor which causes a non-sinusoidal phase back EMF for concentrated windings.

Table 3.1 Rotor pole combinations for 3-phase concentrated windings.

n_s	p_l	p_h	G_r	K_{w1}		S_{pp}	
				LSR	**HSR**	**LSR**	**HSR**
12	7	5	1.4	0.933	0.933	2/7	2/5
	8	4	2	0.866	0.866	1/4	1/2
	10	2	5	0.50	0.50	1/5	1
	11	1	11	0.25	0.25	2/11	2

Furthermore, the variable combinations of stator slots and rotor poles are responsible for the distribution of the machine windings. For the selected rotor pole combinations, the phase winding has 4 coils are connected in series, the winding layout and the EMF phasors for both rotor pole combinations are depicted in Fig. 3.3.

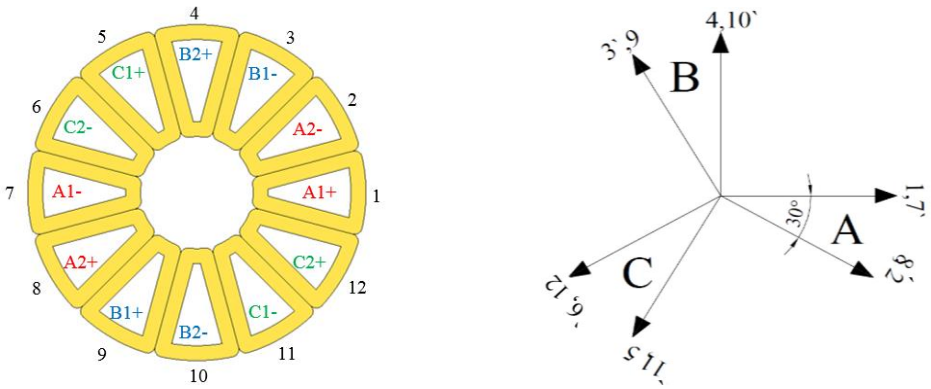

(a) MG12/5-7.

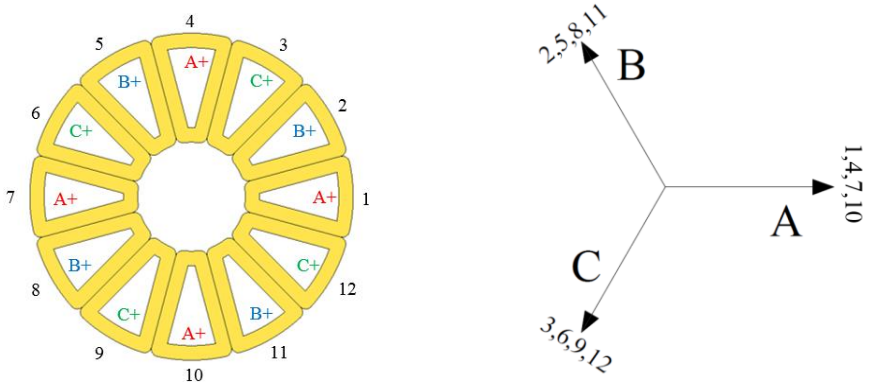

(b) MG12/4-8.

Fig. 3.3 Coil distribution and the EMF phasors for proposed topologies.

3.5 Global optimisation of AFMGPM machine.

With the aim of obtaining the maximum torque transmission capability, the proposed AFMGPM machine is globally optimised by utilising 2D-FE software method described in Appendix A. For this study, the machine is operated as a magnetically geared motor. Since the MG has input and output shafts, the LSR is assumed to be the output rotor which is connected to the drive, and the HSR is assumed as being connected to an external prime-mover. Moreover, it has been stated that the maximum torque can be produced by MG effect when the relative angle between both rotors is adjusted at 90 elec. deg. [FRA09], before starting the study procedure, the relative initial position between two rotors must be adjusted at maximum torque position as explained in Fig. 3.4. The relative angle position δ in electric degrees can be calculated by

$$\delta = p_h \theta_H + p_l \theta_L \tag{3.25}$$

Where θ_H and θ_L are the HSR and LSR axes positions in mechanical degrees, respectively. The maximum relative position angle is obtained by fixing the LSR pole axis at zero initial position,

whereas the HSR axis position is rotated over 90 elec. deg. (18 mech. deg. of MG12/5-7, and 22.5 mech. deg. of MG12/4-8) with the reference of LSR position, as explaind in Fig. 3.4. Moreover, the stator winding is supplied by 3-phase current. The LSR pole axis position is aligned with the d-axis position of phase A to maximize the LSR torque in which the torque produced by armature current is added to the LSR MG torque. Furthermore, the HSR speeds of both topologies are assumed as 400 rpm, therefore, the LSR speeds are calculated according to (3.20). In this case, both rotors contribute for the stator flux, the frequency of the no-load and on-load stator fluxes f can be obtained by

$$f = \frac{n_h p_h}{60} = \frac{n_l p_l}{60} \tag{3.26}$$

The stator flux frequency of the proposed MG12/5-7 is calculated to be a 33.33 Hz and a 26.66 Hz for MG12/4-8.

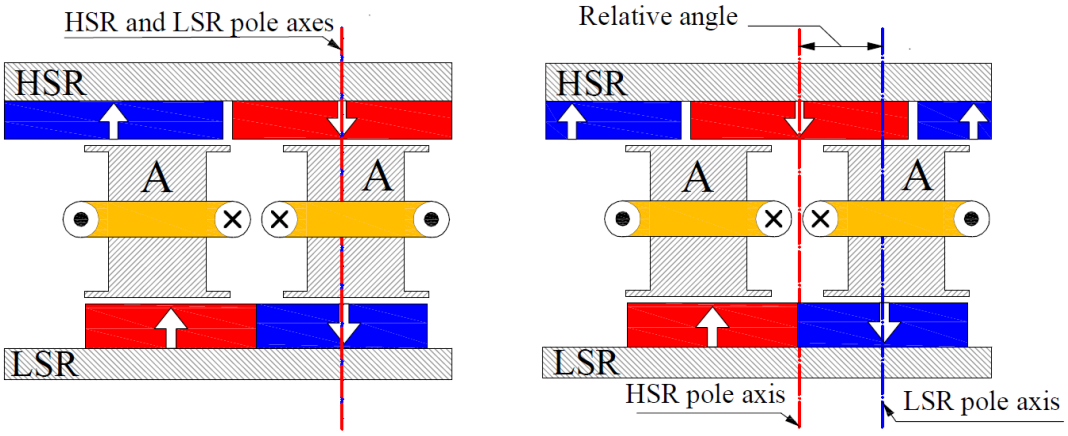

(a) Minimum relative angle (Zero elec. deg.)

(b) Maximum relative angle (90 elec. deg.)

Fig. 3.4 Identify of the relative angle between HSR and LSR.

During the study process, the machine's constant parameters and dimensions are obtained and are provided in Table 3.2. Meanwhile, the variable parameters are indicated in Fig. 3.5 and identified in Table 3.3.

Table 3.2 Constant parameters of the machine.

Parameter	MG 12/5-7	MG 12/4-8
HSR rated speed (rpm)	400	400
LSR rated speed (rpm)	285.7	200
HSR pole pair no. (p_h)	5	4
LSR pole pair no. (p_l)	7	8
Stator slot number (n_s)	12	12
Machine outer diameter (mm)	90	90
Axial length (mm)	25	25
Air-gap length (mm)	0.5	0.5
Number of turns /phase	80	80
Packing factor	0.5	0.5
Copper loss (W)	30	30
Gearing ratio G_r	1.4	2
PM remanence B_r (T)	1.2	
Iron material	GKN SMC 70H	

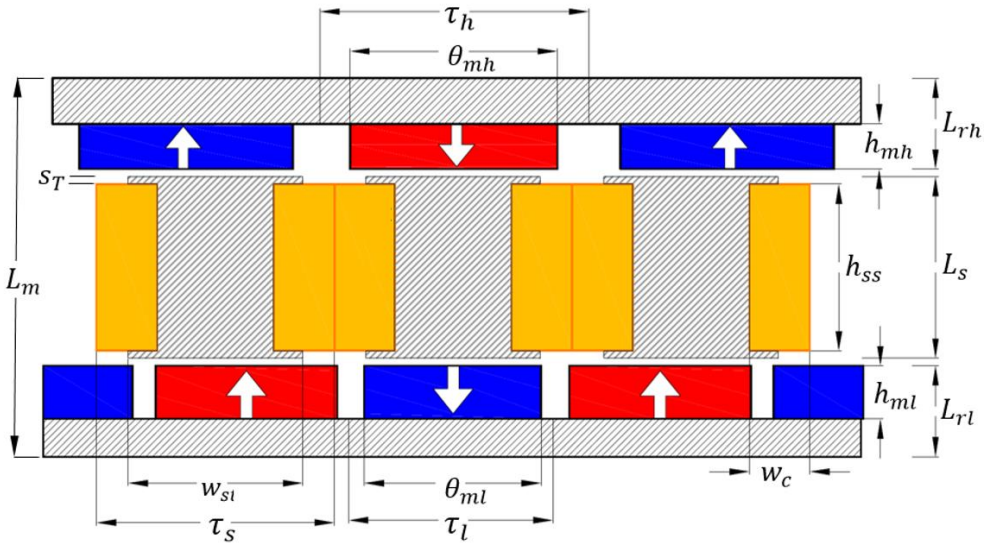

Fig. 3.5 Machine topology dimensions.

Table 3.3 Variable parameters of the machine

Parameter	Symbol	Definition
HSR magnet angle ratio	r_{hp_ratio}	$\frac{\theta_{mh}}{\tau_h}$
LSR magnet angle ratio	r_{lp_ratio}	$\frac{\theta_{ml}}{\tau_l}$
HSR magnet thickness ratio	r_{ht_ratio}	$\frac{h_{mh}}{L_{rh}}$
LSR magnet thickness ratio	r_{lt_ratio}	$\frac{h_{ml}}{L_{rl}}$
Stator slot depth ratio	s_{p_ratio}	$\frac{w_c}{\tau_s}$
Stator slot tips thickness ratio	s_{T_ratio}	$\frac{s_T}{L_s}$
Stator tooth width ratio	s_{so_ratio}	$\frac{w_{st}}{\tau_s}$
Rotor thickness ratio	$R_{\_ratio}$	$\frac{L_{rl}}{L_m}, \frac{L_{rh}}{L_m}$

Global optimisation is carried out by utilising 2D-FE analysis for the proposed topologies. During the machine optimisation process, the machine's outer diameter and the axial length are fixed. The parametric global optimisation constraints and results were obtained and are listed in Table 3.4.

Table 3.4 Proposed Topology Optimal Parameters

Parameters	Restrictions	Optimal value MG12/5-7	Optimal value MG12/4-8
HSR PM angle ratio	[0.7-1]	0.95	0.87
LSR PM angle ratio	[0.7-1]	0.99	1
HSR magnet thickness ratio	[0.4-0.6]	0.56	0.50
LSR PM thickness ratio	[0.4-0.6]	0.57	0.50
Stator slot depth ratio	[0.1-0.3]	0.24	0.23
Stator tip thickness ratio	[0.04-0.25]	0.04	0.04
Stator tooth width ratio	[0.5-0.95]	0.57	0.62
Rotor thickness ratio	[0.2- 0.3]	0.24	0.20

3.6 Influence of critical parameters on machine performance

With the optimal dimensions, the influence of each parameter on torque performance is studied with the aid of 3D-FEA software. Since the output torque of the AFMGPM has two torque parts; magnetic gear effect and armature reaction electromagnetic torques, the influence of each parameter is being on the total torque. The sequence of the influence of the PM dimensions, slot width, tooth tip thickness, slot opening width, and the ratio between the inner and outer diameters on the machine torque is considered. Moreover, under the investigation of each individual parameter, the optimal values of other parameters will be fixed. The influence of each parameter on average torque is explained in the following section.

3.6.1 Influence of PM dimensions

As can be seen in Fig. 3.5, the AFMGPM machine has high and low-speed rotors. By keeping other parameters constant, the influence of the LSR PM dimensions on the LSR average torque of MG12/5-7 and MG12/4-8 are illustrated in Fig. 3.6. It is obvious that the maximum output torque is sensitive to the PM dimensions of both machines. A maximum LSR torque of MG12/5-7 can be obtained when the PM angle ratio of the LSR r_{lp_ratio} is designed between (0.98-1) and the magnet thickness ratio r_{lt_ratio} is approximately 0.58, Fig. 3.6(a). On the other hand, the output torque of MG12/4-8 can be maximised when the LSR PM angle ratio is approximately 1 and the thickness ratio is approximately 0.5, Fig. 3.6(b).

Moreover, with optimal dimensions of LSR PM, the variation of the PM dimensions of the HSR on the output torque of two machine models is shown in Fig. 3.7. For MG12/5-7, the LSR torque reaches maximum value when the HSR PM thickness ratio r_{ht_ratio} and magnet angle ratio r_{hp_ratio} are designed at approximately 0.5 and 0.94, respectively, as can be seen in Fig. 3.7(a), whereas the torque of MG12/4-8 reaches maximum value when the HSR PM thickness ratio r_{ht_ratio} is approximately 0.5 and magnet angle ratio r_{hp_ratio} is approximately 0.87, Fig. 3.7(b). According to the obtained performances of two topologies, the torque always reaches its maximum value when the rotor pole arc and the stator pole arc are approximately the same. The effect of leakage flux in this case is decreased in which the MG torque is highly affected by the magnet angle.

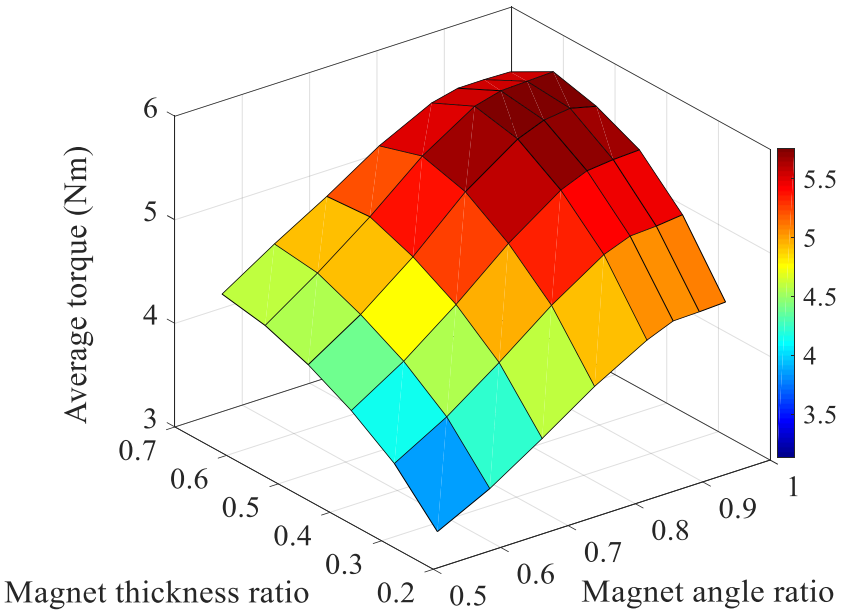

(a) MG.12/5-7

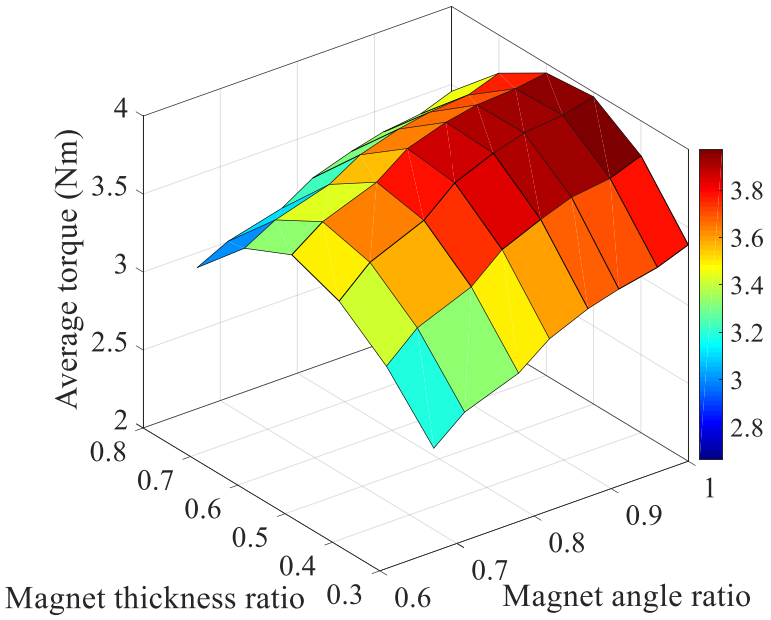

(b) MG12/4-8.

Fig. 3.6 Influence of the LSR magnet dimensions on LSR output torque.

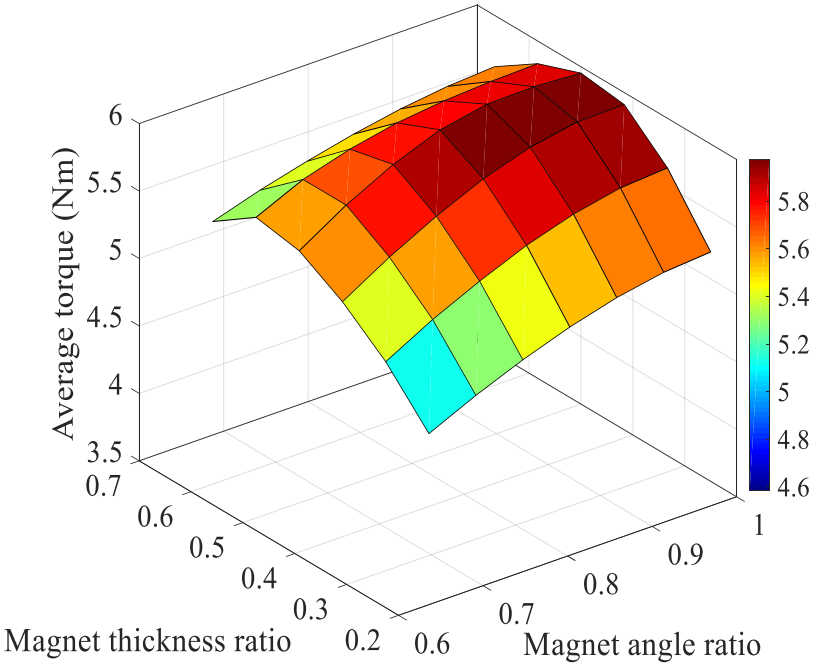

(a) MG12/5-7

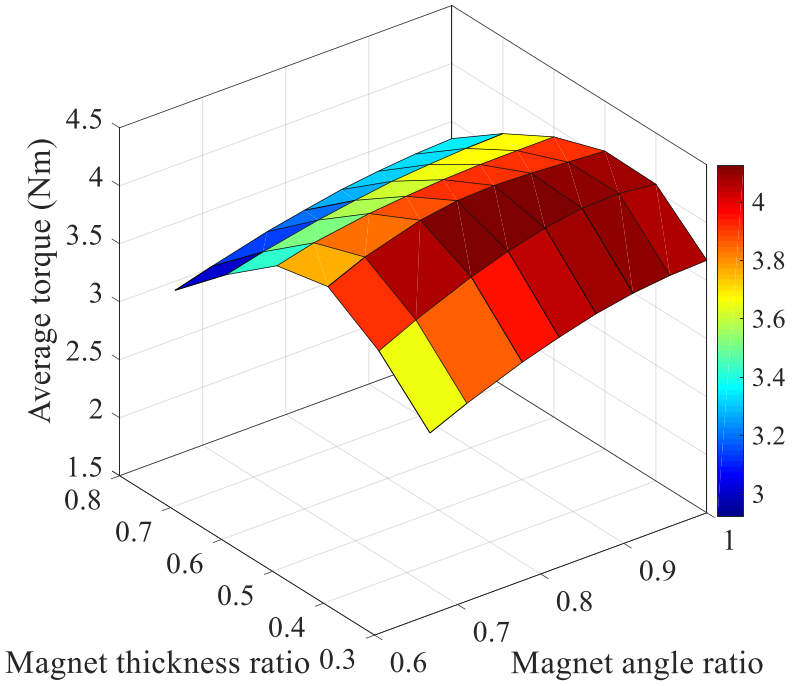

(b) MG12/4-8

Fig. 3.7 Influence of the HSR magnet dimensions on LSR output torque.

3.6.2 Influence of slot depth

The influence of the stator slot depth was investigated, with the armature reaction at rated current is being considered. The phase winding resistance and the copper loss when the end winding is neglected can be calculated utilising (2.7) and (2.8), respectively. Therefore, the rated current at fixed copper loss of 30 W, can be calculated by (2.9).

Fig. 3.8 indicates the effect of the slot depth on the average torque for the considered models. It can be seen that the two topologies have optimal LSR average torque when the slot depth ratio s_{p_ratio} is approximately 0.24. At fixed machine outer diameter, and by considering the end winding thickness, the machine active length in the radial direction is changed with the stator slot. The slot width in this case affects the torque produced by the armature current and MG effect.

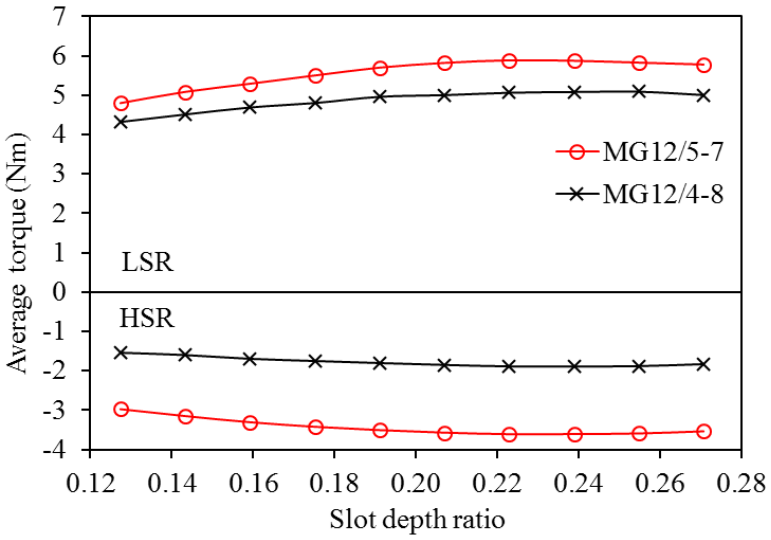

Fig. 3.8 Influence of the slot depth on the average torque.

3.6.3 Influence of slot tips thickness

At fixed stator width L_s, the average output torque for different tooth tips thickness is presented in Fig. 3.9. It can be seen that the average torque is sensitive to the stator slot width in which the torque decreases as the tooth tips thickness increases. That due to the increases of leakage flux and decreases of the slot area as well as the armature current capability. The shape of the stator slot has a critical impact on the MG effect as well as the armature current torque.

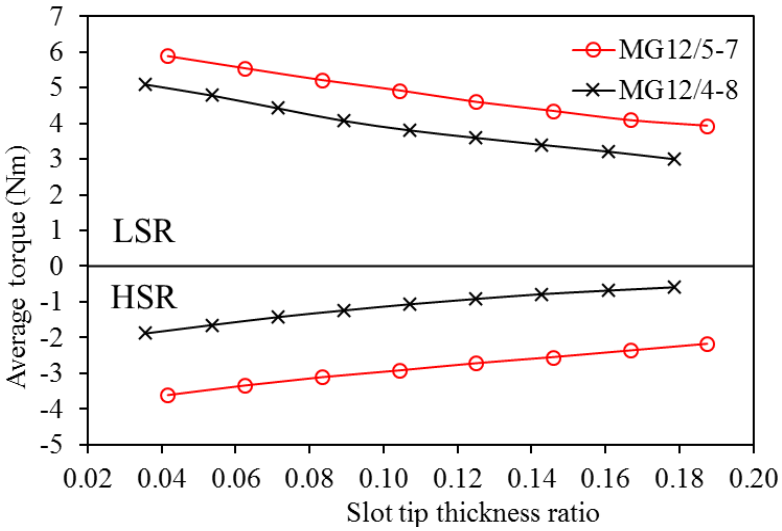

Fig. 3.9 Influence of slot tips thickness on the average torque.

3.6.4 Influence of slot opening width

The influence of the slot opening on the average torque is obtained by studying the changing of the ratio of the stator pole width w_{st} to the stator pole pitch τ_s. Fig. 3.10 indicates the effect of slot opening width on both machines torque performance. It can be noted that the machine torque of the two models reaches its maximum value when the slot opening width ratio is approximately 0.38. For surface mounted PM machines, slot opening has significant impact on the machine performance. It has been shown that PM and armature leakage fluxes share the tooth tips, a fact which increases the local saturation [ZHU15]. However, the influence of slot opening on the AFMGPM machine torque is inconsequential. This is because of the optimal tooth tip thickness is very slight (0.5 mm): small tooth tips reduce the leakage flux and increase the local saturation.

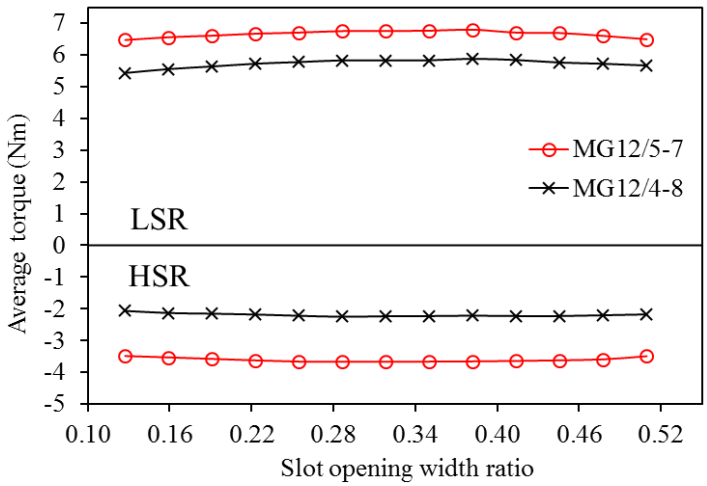

Fig. 3.10 Influence of slot opening on average torque.

Therefore, to reveal the effect of the slot opening on the proposed MG12/5-7, the machine torque is investigated for thicker tooth tip thickness. Fig. 3.11 indicates the effect of slot opening on the average torque at no-load and on-load when the tooth tip thickness is doubled (to 1 mm). It is clear that the machine torque significantly increases with the increase of the slot opening. The effect of the local saturation is effectively eliminated in this case since a larger tip thickness results in more flux passing through the area of the tooth tips. However, the behaviour of both no-load and on-load torques are approximately equal at all slot opening values. Therefore, since the LSR torque has two torque components, the influence of the slot opening on the MG and armature current torques is indicated in Fig. 3.12. It is obvious that, with the increase of slot opening width, the torque contributed by the armature current slightly increases, before decreasing when the slot opening width is larger than 5 mm. Additionally, the gearing effect torque is significantly affected by the slot opening when the tips saturation is considered. Fig. 3.13 plots the machine flux density distribution on the stator poles for different tooth tip thicknesses in which the local saturation can be clearly seen on the tooth tips.

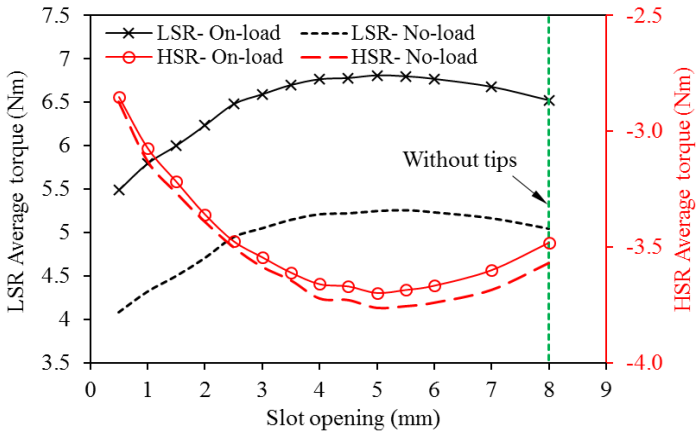

Fig. 3.11 Influence of slot opening on average torque at 1 mm tip thickness for MG12/5-7.

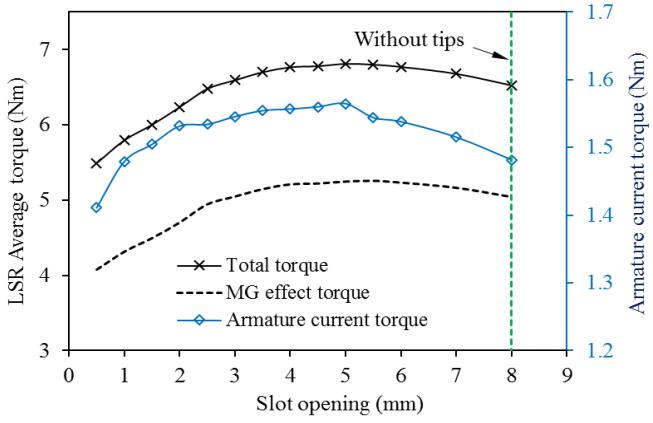

Fig. 3.12 Influence of slot opening on the LSR torque components for 1 mm tip thickness of MG12/5-7.

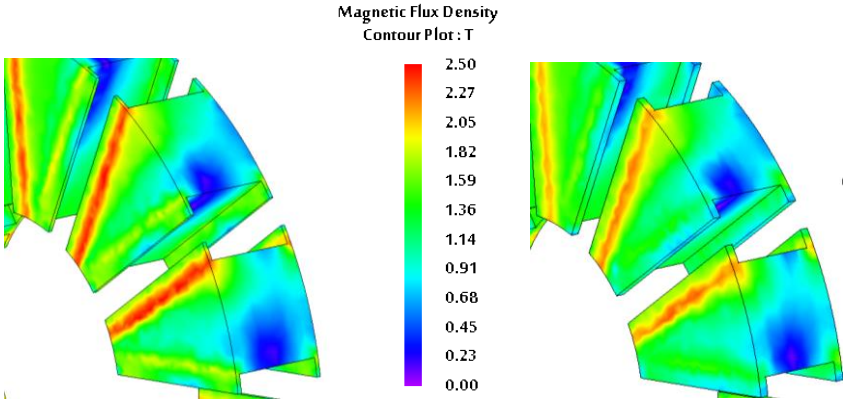

(a) 0.5mm (b) 1 mm

Fig. 3.13 On-load stator pole flux density distribution for different tip thicknesses at initial position.

3.6.5 Influence of the ratio between outer and inner machine diameters

The influence of the ratio of the machine inner diameter, D_i with respect to the machine outer diameter, D_o was also studied. The inner diameter is changed at different values, whereas the outer diameter is kept constant. Fig. 3.14 indicates the influence of inner to outer diameter variation on the machine torque performance. It is obvious that the average torque of two topologies increases as the ratio decreases. On the other hand, when the ratio increases, the machine active length decreases, which results in decreasing of the stator coil and the magnet active lengths.

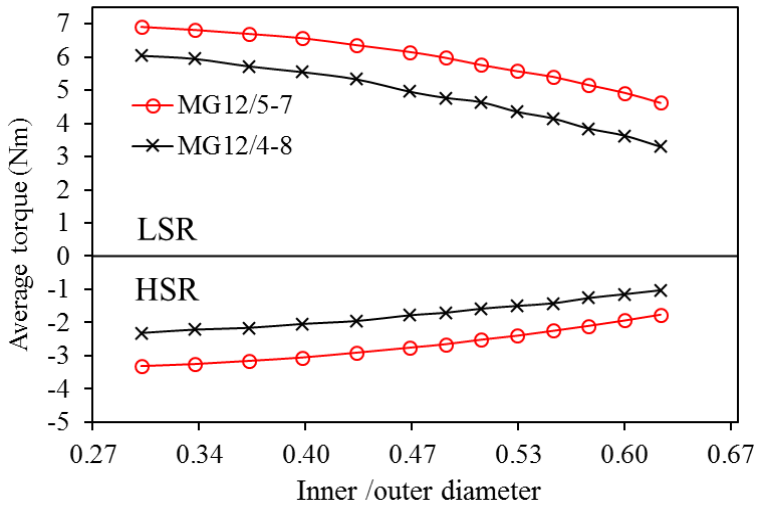

Fig. 3.14 Influence of inner diameter on the average torque.

3.7 Performance analysis of proposed optimised AFMGPM machine

As has been shown, during machine optimisation, the dimensions were chosen to maximize the output torque. The optimal parameters and dimensions of the proposed AFMGPM machine were chosen according to 3D FE analysis results listed in Table 3.5. By considering two load conditions, i.e. no - load condition, in which the winding current is zero and the machine works as MG, and on - load condition, in which the rated current is applied to the winding and the machine works as magnetically geared motor, the optimised topology was analysed and studied by utilising 3D - FE analysis.

Table 3.5. Machine optimal dimensions and rated parameters

Parameter	**MG 12/5-7**	**MG 12/4-8**
High speed (RPM)	400	400
Low speed (RPM)	285.5	200
High speed rotor pole No. (P_h)	10	8
Low speed rotor pole No. (P_l)	14	16
Stator Pole Number (St)	12	12
Machine Inner Diameter (mm)	30	30
Machine Outer Diameter (mm)	90	90
Axial Length (mm)	25	25
Air gap Length (mm)	0.5	0.5
Number of turns of armature coil/phase	80	80
Packing factor	0.5	0.5
High speed rotor pole arc (degree)	34	39
High speed rotor PM Thickness (mm)	3	2.5
Low speed rotor pole arc (degree)	25.4	22.5
Low speed rotor PM Thickness (mm)	3.5	2.5
Slot Area (mm^2)	44	52
Armature stator Axial Length (mm)	12	14
Rotor Axial Length (mm)	6	5
I_{rms} (A)	13.5	14.8
PM volume (mm^3)	26263.6	19348

3.7.1 No-load flux density

Fig. 3.15 plots the no-load flux density distribution of both machine geometries at initial position. Moreover, the flux density adjacent to HSR and LSR for both proposed topologies at no-load were also analysed and obtained. The flux density is examined in the middle of the gap between the stator and each rotor in the axial direction. Fig. 3.16 shows the air-gap axial components of PM flux density variation and their space harmonic spectra for MG12/5-7 topology. It is evident that the largest harmonic components at HSR and LSR air-gaps are the 5^{th} and the 7^{th} respectively, which are the same as the number of pole pairs of HSR and LSR. Moreover, the 5^{th} harmonic component exists at LSR air-gap flux density while the 7^{th} harmonic is also present at HSR air-gap flux density due to the modulation effect caused by the presence of stator segments [ATA01].

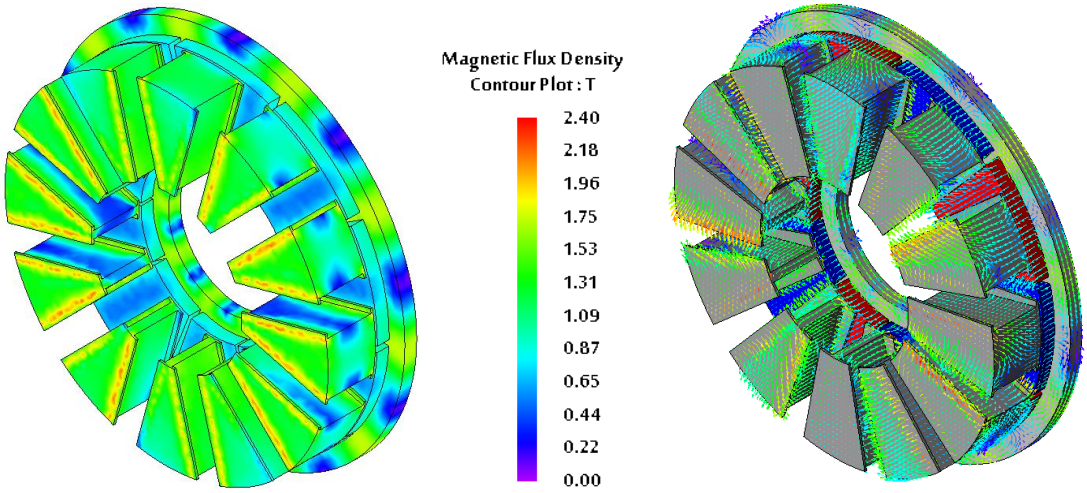

(a) MG12/5-7

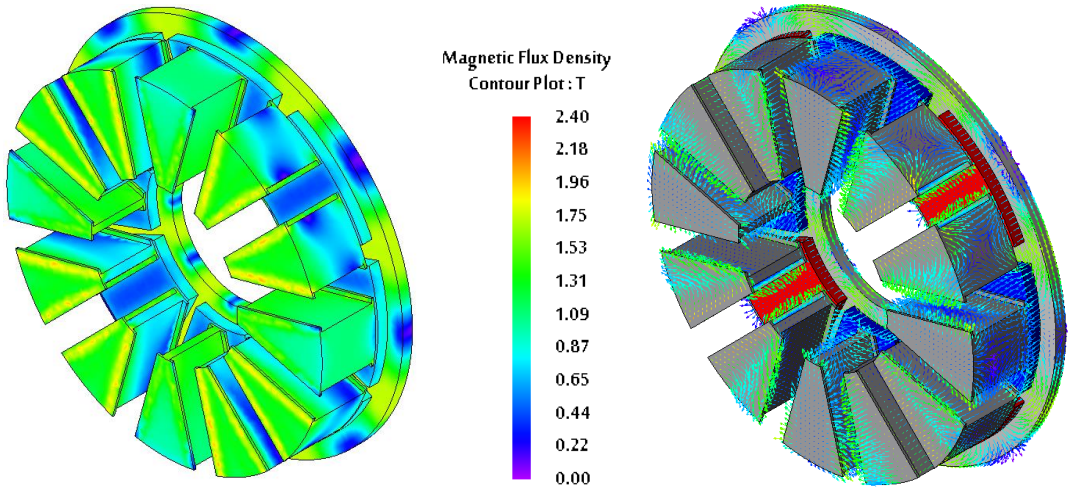

(b) MG12/4-8

Fig. 3.15 No-load flux density distribution at initial position.

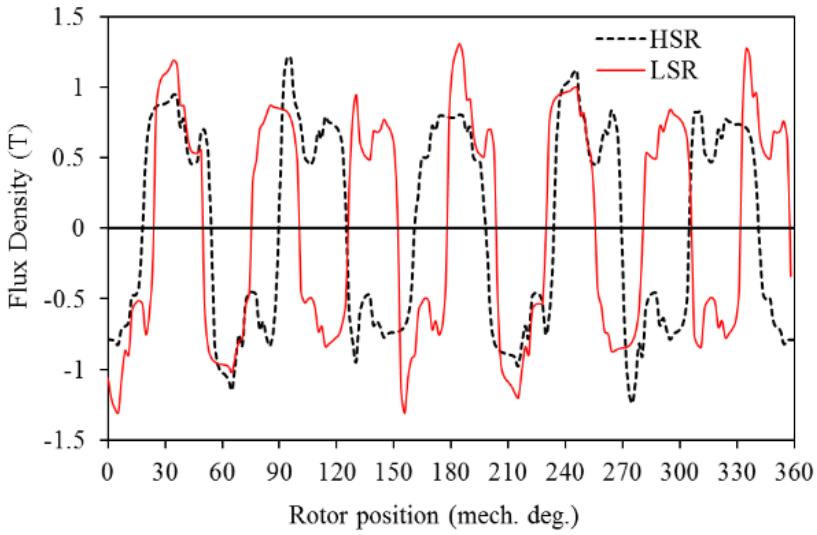

(a) Waveforms

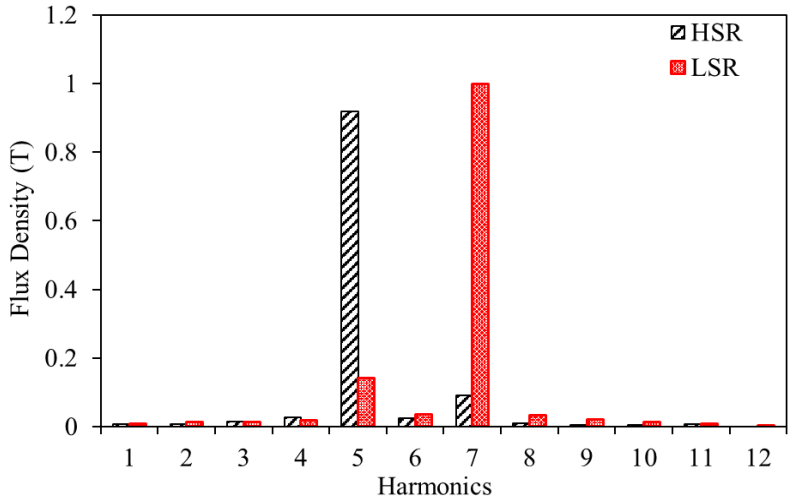

(b) Harmonic spectra

Fig. 3.16 Comparison of no-load flux density in the middle of HSR and LSR air-gap at mean radius for MG12/5-7 topology.

On the other hand, Fig. 3.17 shows the variation of axial component of PM flux density and the corresponding space harmonic spectrum in the MG12/4-8 air-gaps. It can be noted that the flux density contains many harmonics in which the largest harmonics components at HSR and LSR air-gaps are the 4^{th} and the 8^{th}, which are the same as the numbers of pole pairs of HSR and LSR, respectively.

Moreover, Fig. 3.18 depicts the axial component of flux density in the MG12/5-7 air-gap produced by the armature windings only. It can be performed when rated current is applied to the stator windings while the machine magnets are assigned as vacuum. It is revealed that the

armature field includes many space harmonics. However, the harmonics contain higher order of the 5th and the 7th harmonics rotate at opposite directions.

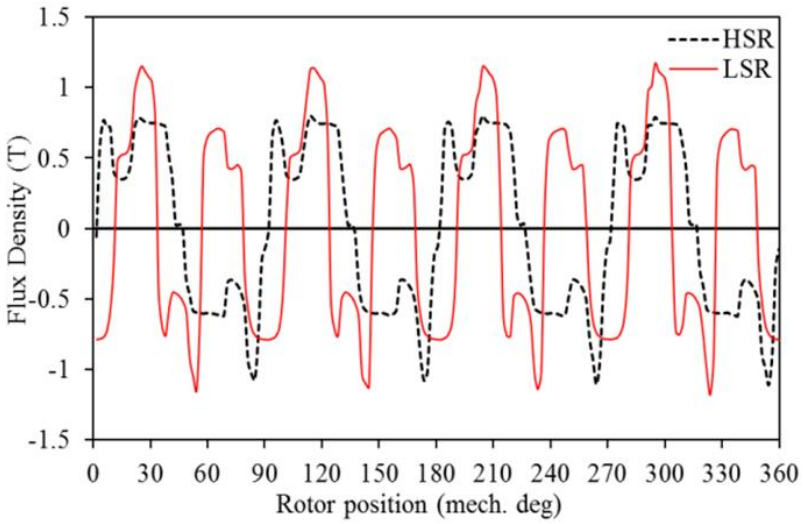

(a) Waveforms

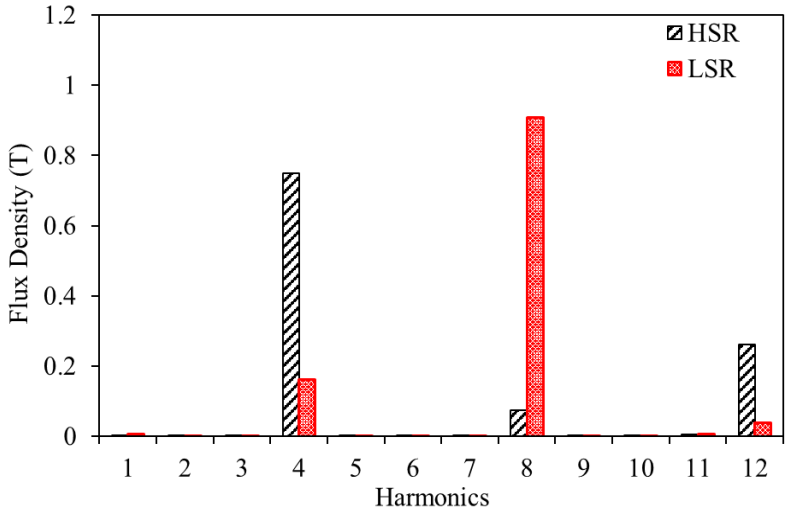

(b) Harmonic spectra

Fig. 3.17 Comparison of no-load flux density in the middle of HSR and LSR air-gap at mean radius for MG12/4-8 topology.

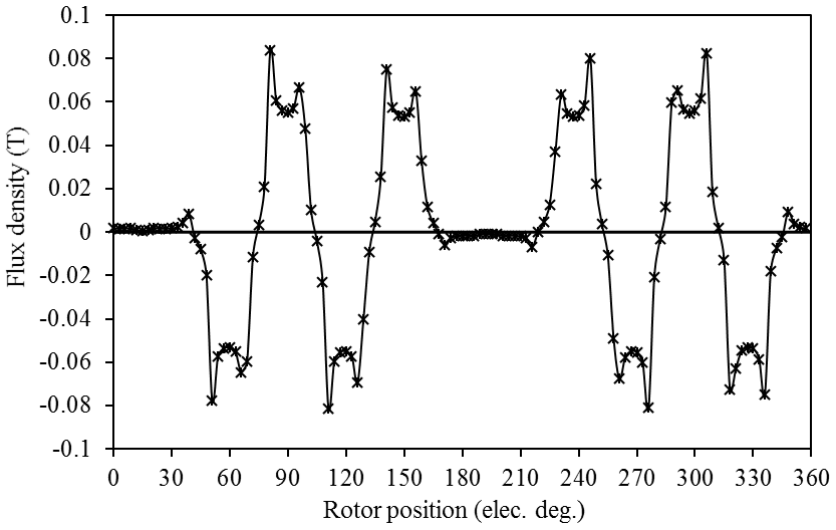

(a) Waveform

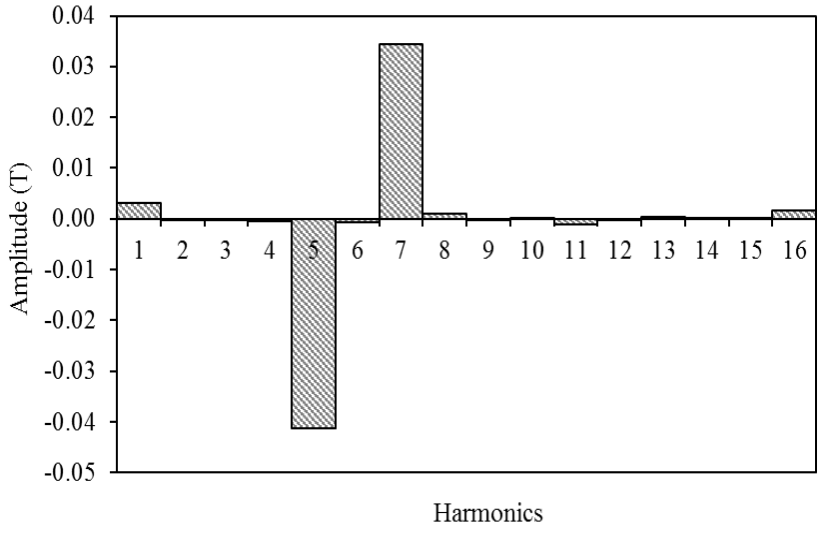

(b) Harmonic Spectra

Fig. 3.18 Armature flux density in the middle of the LSR air-gap at mean radius for MG12/5-7 at rated current.

Similarly, Fig. 3.19 shows the axial air-gap armature flux density of MG12/4-8. It is clear that the 4^{th} and the 8^{th} harmonic orders are the highest amplitudes of the armature current flux density. Therefore, since the HSR and the LSR of two machines rotate in different directions to realise the MG function, the positive and negative armature flux harmonics and the harmonics of each rotor flux share the same order and speed of rotation, which can then interact with each other and contribute extra torque.

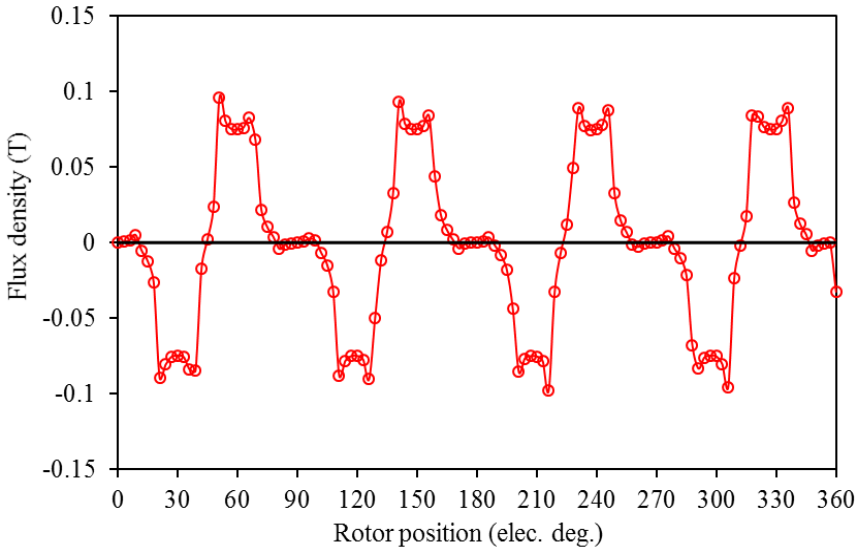

(a) Waveform

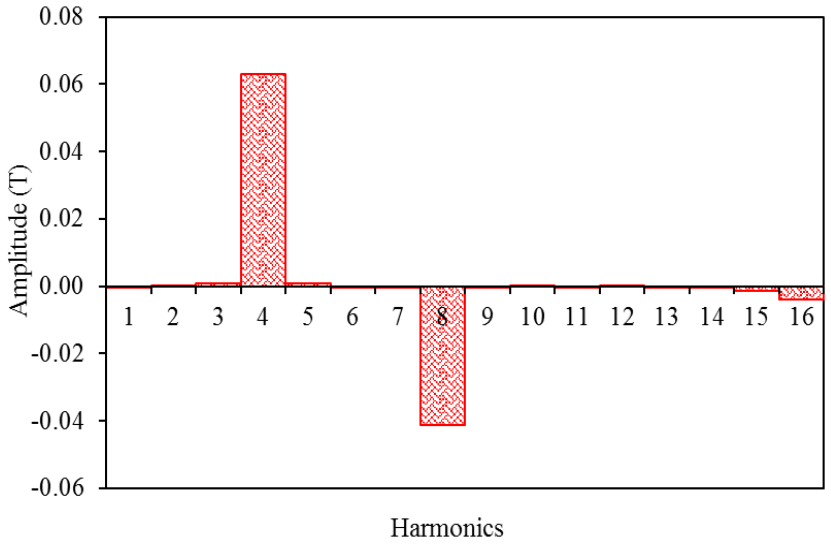

(b) Harmonic Spectra

Fig. 3.19 Armature flux density in the middle of the LSR air-gap at mean radius for MG12/4-8 at rated current.

3.7.2 No-load flux linkage and back EMF

The machine topologies are simulated at open circuit and both rotors are rotating at their rated speeds. The no-load performance is calculated at an initial relative angle between HSR and LSR of zero, in which the d- axes of HSR and LSR poles are aligned. Fig. 3.20 and Fig. 3.21 indicate the 3 phase flux linkages and the corresponding harmonic spectra of MG12/5-7 and MG12/4-8 respectively. It can be observed that the phase flux linkage waveforms of the two machines are sinusoidal and symmetrical. Also, MG12/5-7 has a higher flux linkage magnitude of

approximately 17.2 mWb whereas MG12/4-8 has flux linkage magnitude of approximately 15.9 mWb.

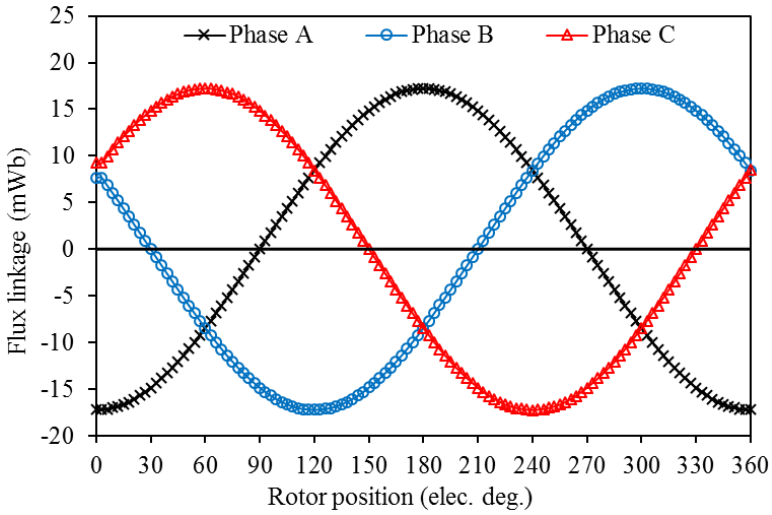

(a) Wavforms

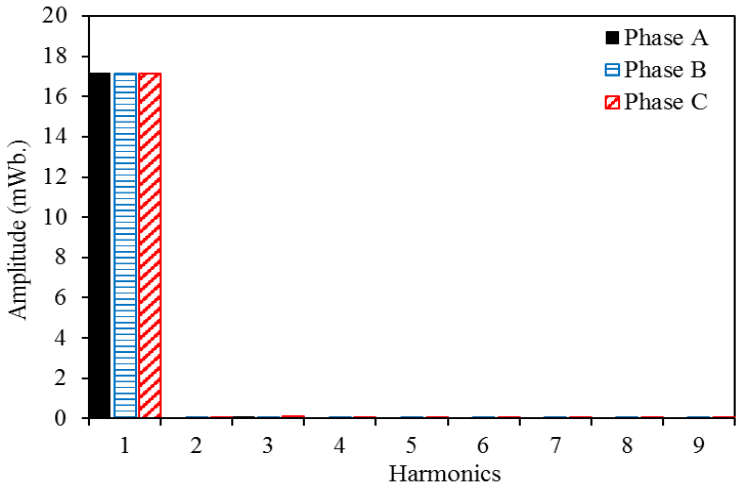

(b) Harmonic spectra

Fig. 3.20 3-phase flux linkage waveforms of the MG12/5-7 machine at relative angle of zero elec. degrees.

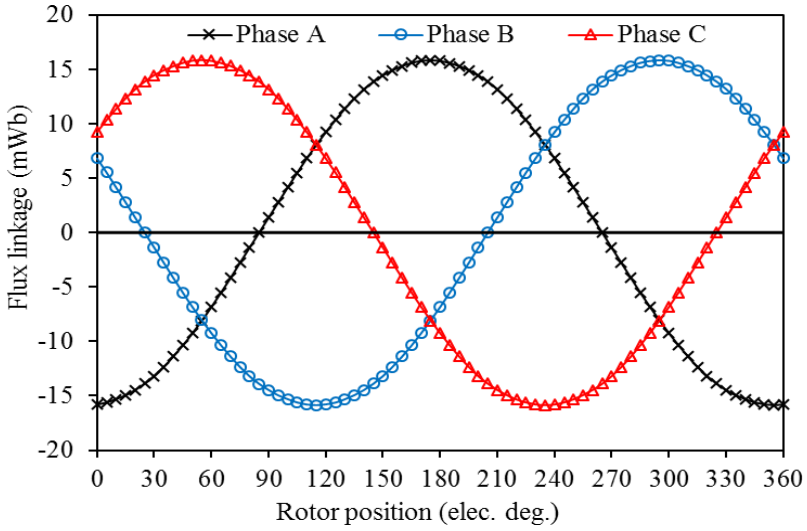

(a) Waveforms

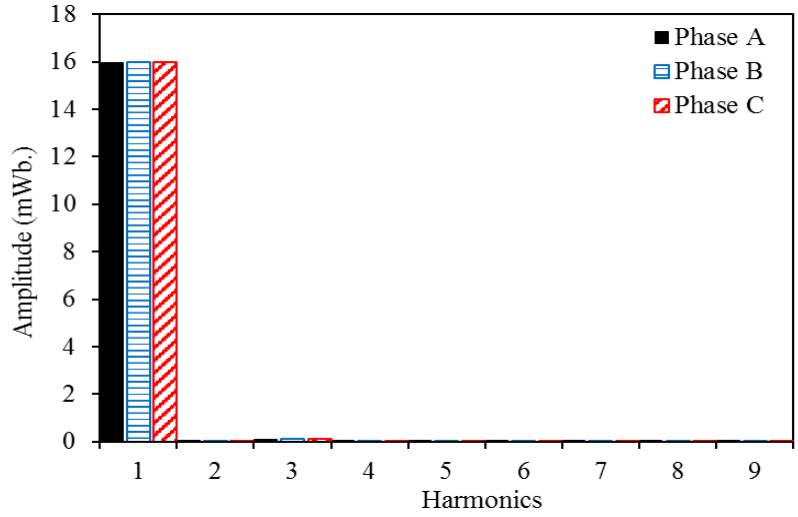

(b) Harmonic spectra

Fig. 3.21 3-phase flux linkage waveforms of the MG12/4-8 machine at relative angle of zero elec. degrees.

The 3-phase back EMFs and the corresponding spectra of the proposed MG12/5-7 and MG12/4-8 topologies are illustrated in Fig. 3.22 and Fig. 3.23 respectively. Both topologies back EMF waveforms contain slight 3rd and 5th harmonics. On the other hand, the back EMF induced in the stator windings is a result of the summation of the back EMF produced by both rotors. The back EMF amplitude values of MG12/5-7 and MG12/4-8 are approximately 3.6 and 2.6 V, respectively. Moreover, it can also be notice that MG12/5-7 has a significant higher EMF amplitude in that the machine back EMF amplitude is proportional to the winding factor which is higher than MG12/4-8 as evidenced in Table 3.1.

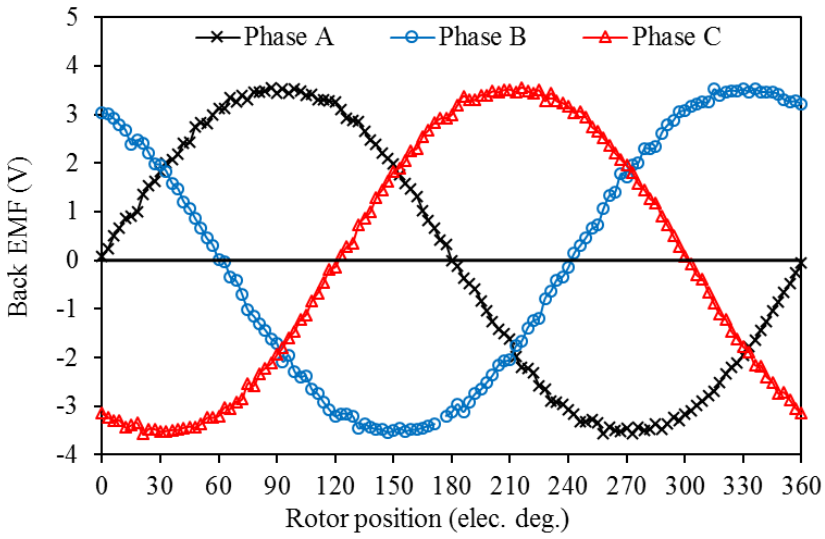

(a) Waveforms

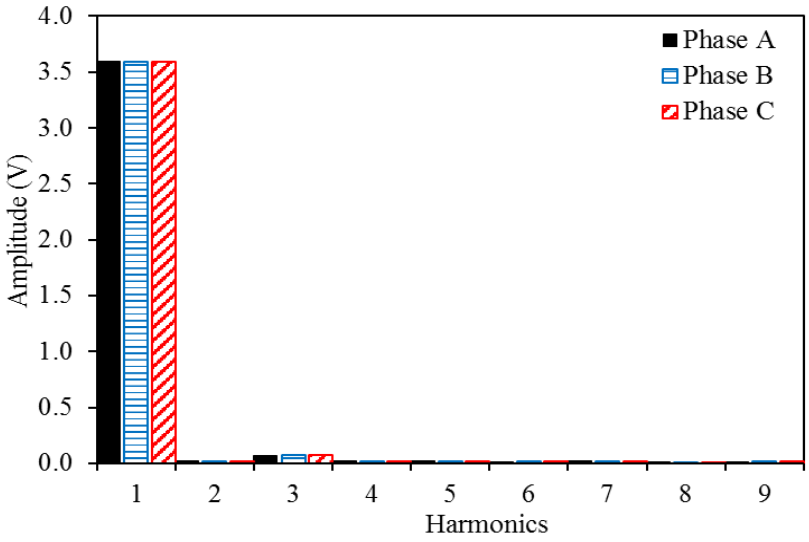

(b) Harmonic spectra

Fig. 3.22 3-phase back EMFs and the corresponding harmonics of MG12/5-7 at relative angle of zero elec. degrees.

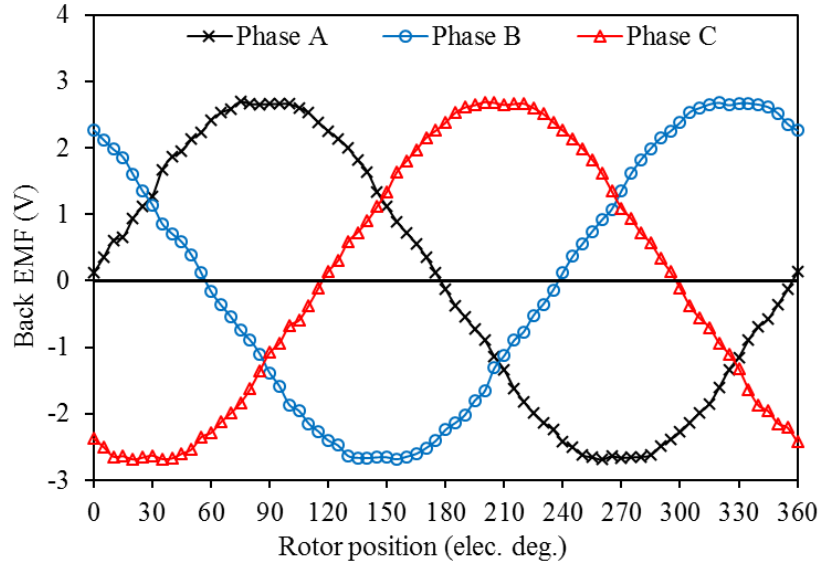

(a) Waveforms

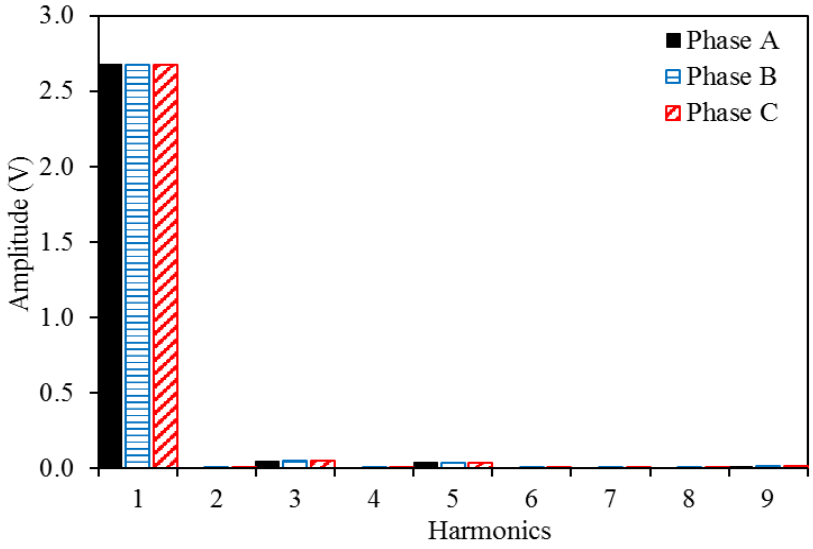

(b) Harmonic spectra

Fig. 3.23 3-phase back EMFs and the corresponding harmonics of MG12/4-8 at relative angle of zero elec. degrees.

3.7.3 Cogging torque

In conventional PM machines, the cogging torque exists because of the interaction between the magnet MMF harmonics and the stator slot permanence harmonics. Cogging torque can cause speed ripple and vibration which must be practically considered. However, MG machines always have two or three components which can rotate independently. A detailed analysis of cogging torque for the radial MG was described in [NIG12b]. However, the magnetic gearing effect was considered, and the study presented the transferred torque ripple instead of cogging torque. Moreover, the cogging torque of axial MG has been studied in [AFS15]. It has been stated that, when the modulator is considered as the stationary part, the total cogging torque of each rotor consists of the cogging torque from the interaction of the rotor flux with the stationary part and the cogging torque from the other rotor PMs caused by the modulation of the magnetic flux density (imaginary PM). Therefore, to examine the cogging torque of the proposed machine, the relative angle between both rotors should be zero. This can be obtained by aligning one LSR pole with one HSR pole. Consequently, the average torque obtained from the magnetic gearing effect is always zero. Moreover, the machine HSR is driven with a constant rated speed of 400 rpm whereas the LSR speed is 285.5 rpm.

Fig. 3.24 indicates the cogging torques of HSR and LSR of MG12/5-7 for one electrical cycle and Fig. 3.25 plots both rotor cogging torques of MG12/4-8. It can be found that the fundamental harmonic of both HSR and LSR of MG12/5-7 is the 12^{th} while that of MG12/4-8 is mainly the 6^{th} harmonic. A relatively high cogging torque is produced by the LSR of MG12/5-7. Moreover, the amplitude of cogging torque of HSR for MG12/4-8 is significantly higher than that of LSR, as can be seen from the Fast Fourier transform (FFT) results indicated in Fig. 3.25(b). Therefore, as can be clearly seen in Fig. 3.15, severe leakage flux occurs in the airgap in which the magnet flux is coupling to the stator pole, returns to the same rotor and does not pass through it, Fig. 3.15(b). Therefore, high leakage flux adversely affects the machine performance and increases the cogging torque. Obviously, for any combination of slot and pole numbers, the cogging torque level can be estimated by calculating the cogging torque factor C_T. It is obvious that C_T is 2 for both HSR and LSR of MG12/5-7, and, similarly, C_T factors of MG12/4-8 for both rotors are 4.

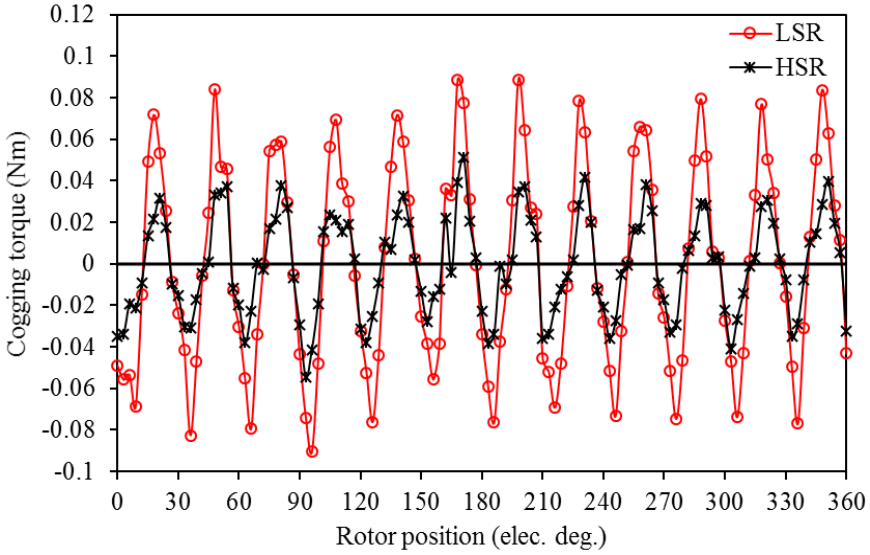

(a) Waveforms

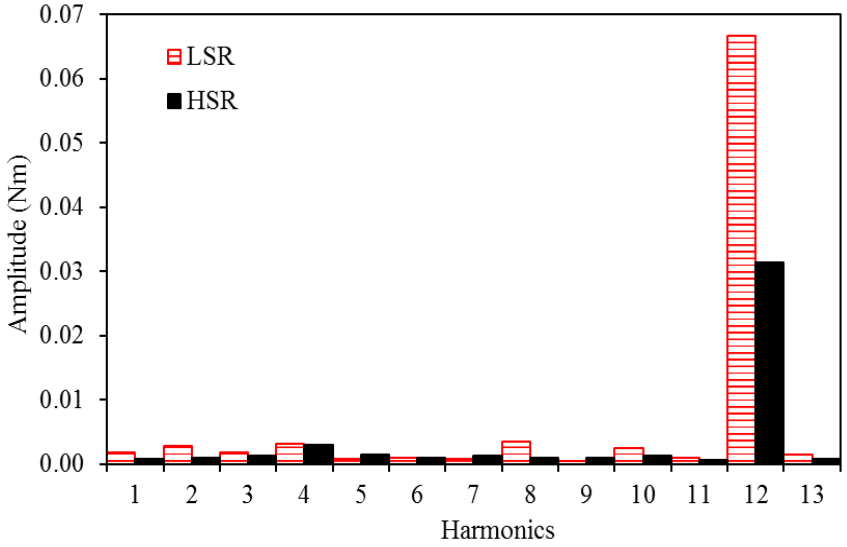

(b) Harmonic spectra

Fig. 3.24 Cogging torque waveforms and the corresponding harmonics of MG12/5-7.

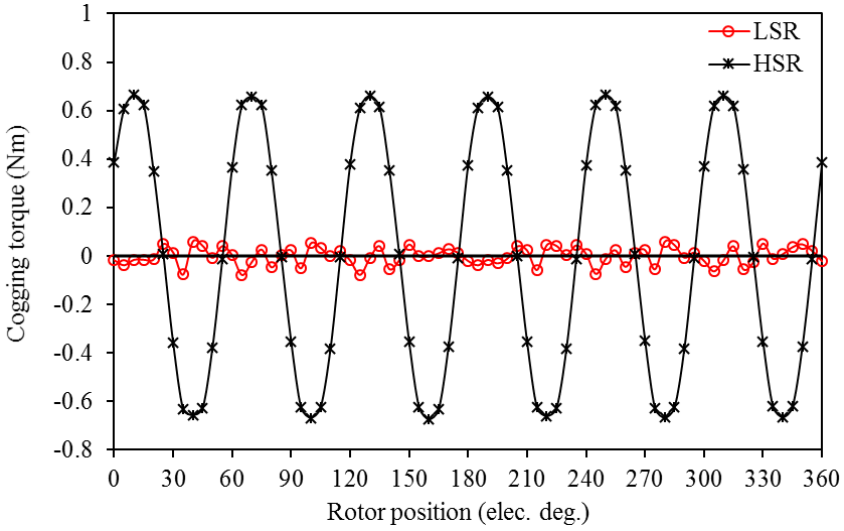

(a) Waveforms

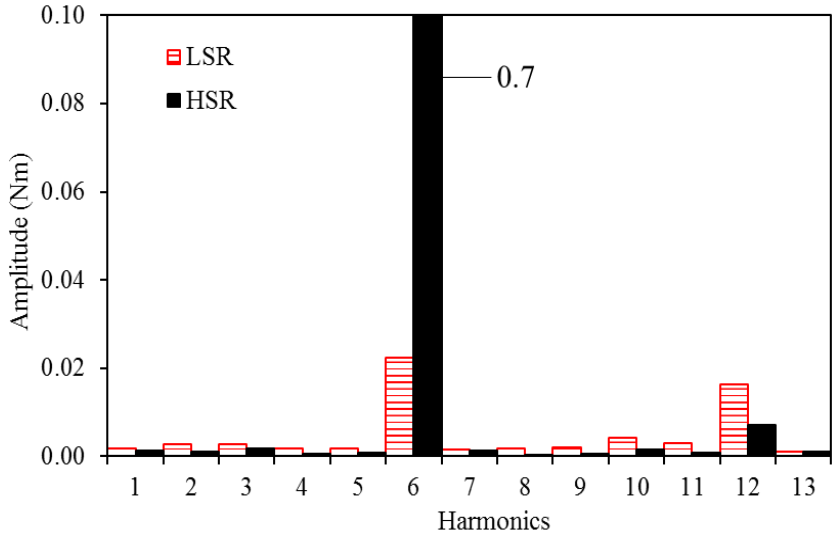

(b) Harmonic spectra

Fig. 3.25 Cogging torque waveforms and the corresponding harmonics of MG12/4-8.

3.7.4 Torque

The torque of the proposed machine consists of two parts: torque produced by MG effect, which is a function of the relative position between HSR and LSR, and electromagnetic torque produced by the interaction of armature field and PM field. Fig. 3.26 shows the torque angle characteristics for the proposed machine which can be obtained by blocking the LSR at initial position of $\theta_l = 0^o$ whereas the HSR is incrementally rotated with the reference of the LSR position. It is clear that the torque of both rotors increases as the relative angle increases and reaches its maximum value when δ is 90 elec. deg., in which the corresponding mechanical angles of HSRs θ_h of MG12/5-7 and MG12/4-8 are 18° and 22.5°, respectively. Similarly, by holding the HSR still at

$\theta_h = 0^o$ and rotating the LSR with reference of the HSR initial position, the torque reaches its maximum value when the corresponding mechanical angle of LSRs θ_l of MG12/5-7 and MG12/4-8 are 12.85° and 11.25°, respectively. It can also be seen that maximum torques of 5.34 Nm and 3.83 Nm for HSR and LSR, respectively, can be gained by the MG effect of MG12/5-7. The resulting magnetic gear ratio is approximately 1.40. Moreover, for the proposed MG12/4-8, a maximum torque of approximately 2.24 Nm and 4.49 Nm can be obtained by HSR and LSR respectively, in which the gear ratio is approximately 2.0.

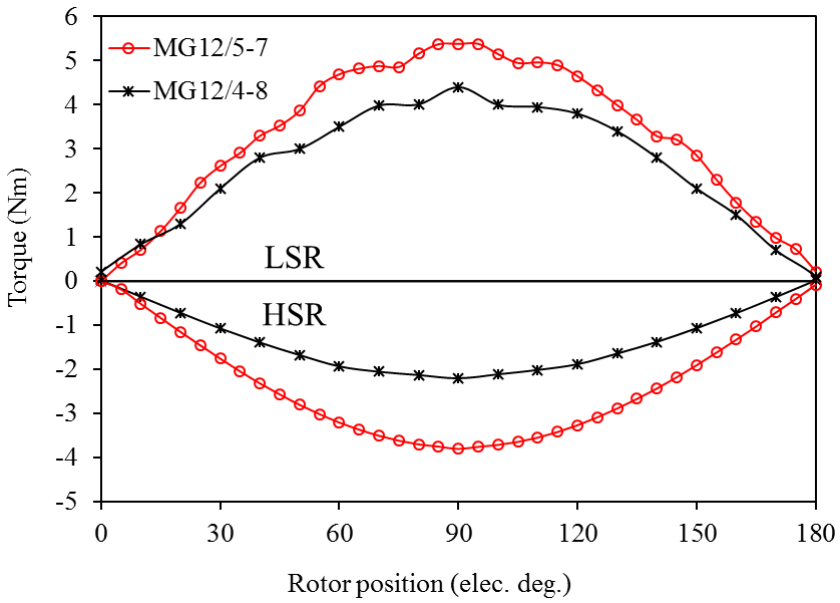

Fig. 3.26 MG effect torque-relative angle characteristics for HSR and LSR.

Additionally, the torque performance over the rotor position obtained by 3D-FE model for the two topologies are performed. Fig. 3.27 and Fig. 3.28 compare the torque performance of both topologies at no-load and on-load conditions, respectively. It should be mentioned that, the difference between the machine performance at no-load and on-load conditions is the absence or presence of the armature current, respectively. On other words, the no-load condition is the performance of the machine when the relative angle δ is at its maximum value and the armature winding current is zero (open circuit), while the on-load condition is the performance when the rated current is applied to the armature current at maximum relative angle. It is clear that the proposed MG12/5-7 machine has low torque ripple. Furthermore, at the rated current, the LSR torque is amplified to reach just below 7.0 Nm, while the HSR torque remains the same value as no-load condition of 3.83 Nm. Similarly, for the proposed MG12/4-8, a maximum torque of approximately 6 Nm can be obtained by the LSR while the HSR torque remains the same value as no-load condition of 2.24 Nm. This phenomenon is due to the alignment of LSR pole axis with

the d-axis of phase (A) as explained in Fig. 3.4(b), and thus the armature current flux and LSR flux will be matched and the LSR MG torque will be amplified by the armature current torque. Nevertheless, the HSR flux will be shifted from the d-axis armature current flux by a specific angle depending on the relative angle between two rotors, which at relative angle of approximately 90°, results in zero torque being produced by the armature current on the HSR.

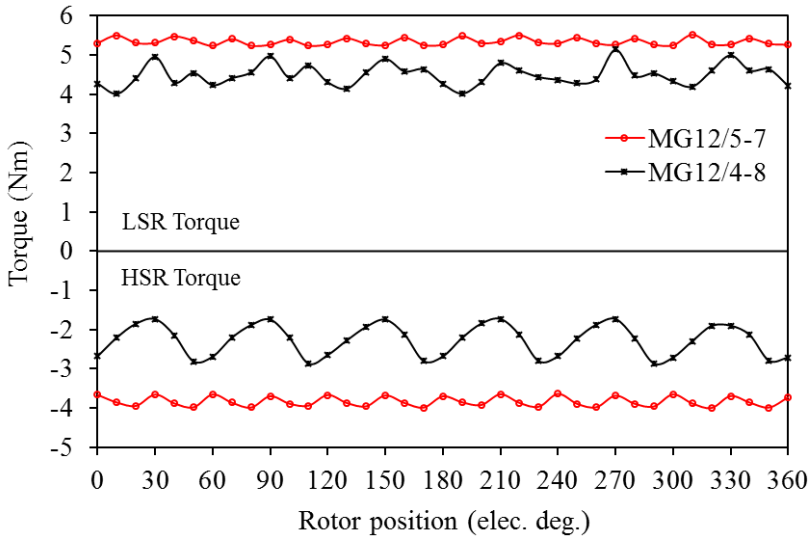

(a) Waveforms

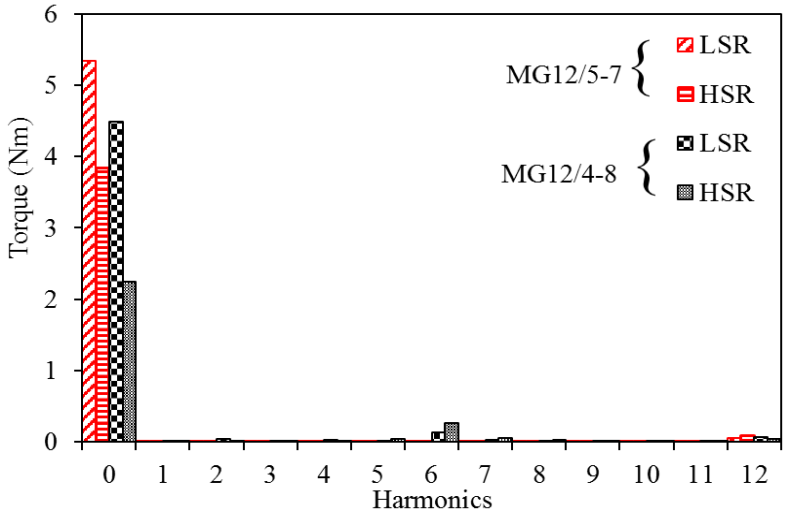

(b) Harmonic spectra

Fig. 3.27 Comparison of no-load torques of HSR and LSR for different rotor pole combinations (δ =90 elec. degrees and I_{rms}=0 Amp.).

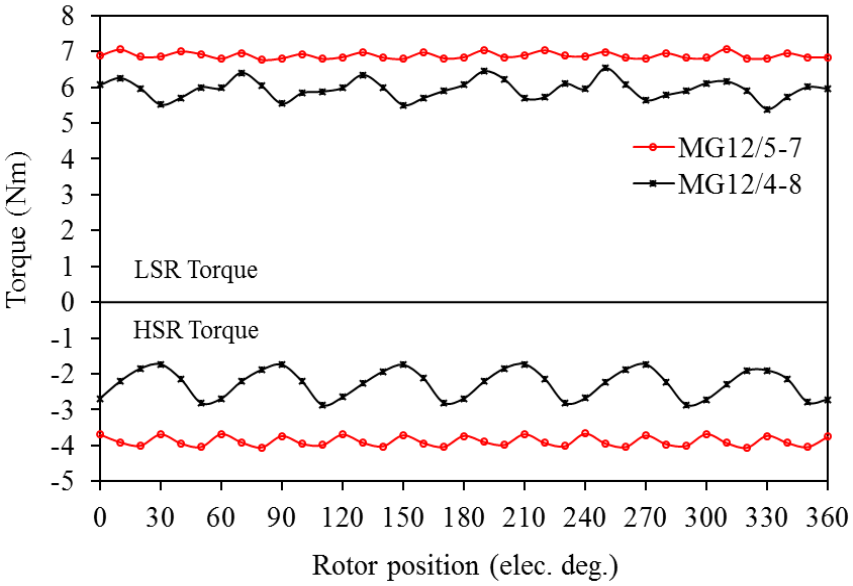

(a) Waveforms

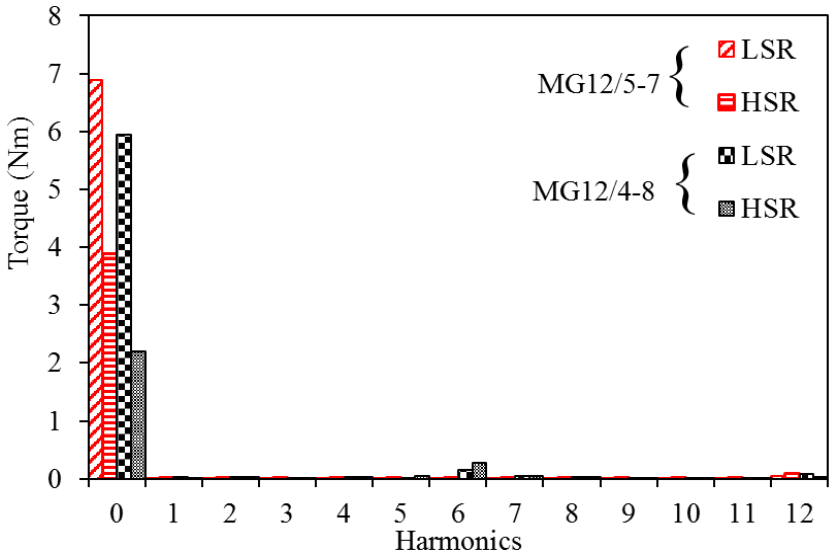

(b) Harmonic spectra

Fig. 3.28 Comparison of the on-load torques of HSR and LSR for different rotor pole combinations when the LSR is the output rotor (δ =90 elec. degrees., I_{rms} at rated values. and current angle 0^o).

Moreover, Fig. 3.29 compares the torque performance of both topologies at on-load when the d-axis of phase (A) is aligned to the HSR pole axis. In this case, the MG torque of the HSR will be amplified by the armature current torque. It can be obviously seen that the HSR torque of the proposed MG12/5-7 is increased from 3.83 Nm at no-load to 5.1 Nm at the rated current, while the LSR torque remains the same value as no-load condition of 5.34 Nm. Similarly, the HSR of

MG12/4-8 is amplified to reach a maximum torque of approximately 4.5 Nm and the LSR torque remains the same value as no-load condition of 4.49 Nm.

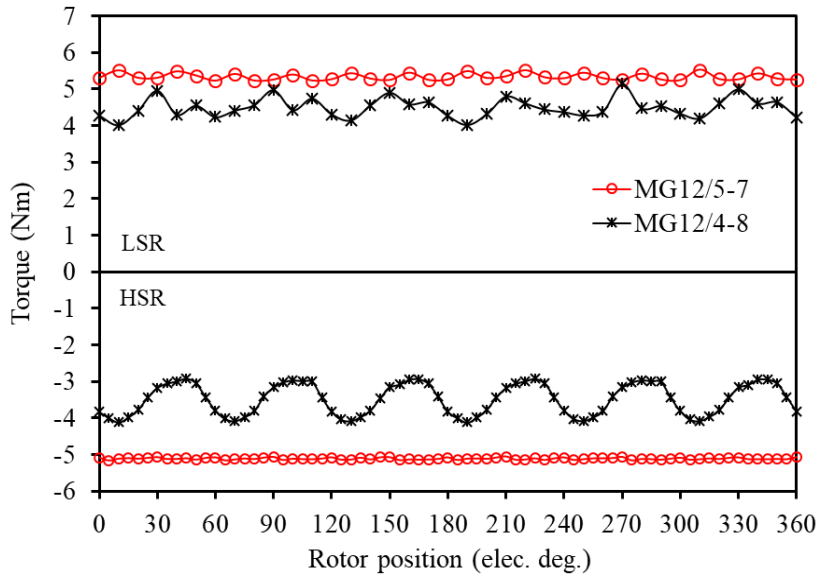

(a) Waveforms

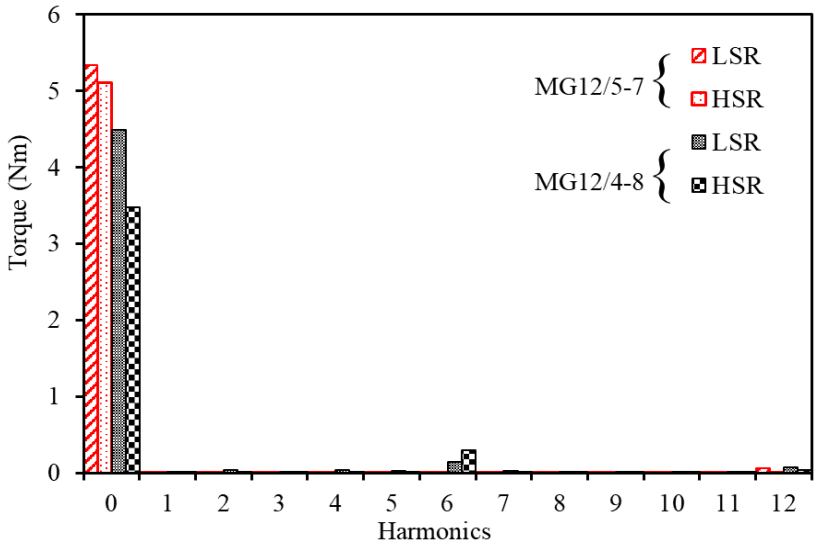

(a) Harmonic spectra

Fig. 3.29 Comparison of the on-load torques of HSR and LSR for different rotor pole combinations when the HSR is the output rotor (δ =90 elec. degrees, I_{rms}= at rated values and current angle 90^o).

In conclusion, the results indicated that the proposed machine topologies can be operated at no-load conditions in which the machine works as MG and generator. However, at motoring mode, the matching between the armature reaction flux and the output rotor PM flux is the most important concern and must be accurately controlled.

3.8 Performance comparison of axial flux magnetically geared machine and YASA machine

With the aid of 3D-FE analysis, the 3-phase AFMGPM machine and the 3-phase YASA machine are analysed and compared. By considering no-load conditions, in which the winding current is zero, and on-load condition, in which the winding is applied with a specific current, a performance comparison between the proposed machine and YASA machine topologies i.e. flux linkage, back EMF and torque is performed. Moreover, a complete performance comparison of both machines with different operation conditions is indicated in Appendix B.

3.8.1 No-load flux linkage and back EMF

To calculate the no-load flux linkage and back EMF of the AFMGPM machine, the initial relative angle between both rotors is adjusted to zero elec. deg. Moreover, since the proposed machine has two rotors with two different speeds, the back EMF of the YASA machine is presented at the same speeds as the AFMGPM machine rotors. On the other hand, YASA12/14 back EMF is presented at the same speed as LSR (285.7 rpm), and similarly for YASA12/10 at the same speed as HSR (400 rpm).

Fig. 3.30 shows the phase flux linkages of the MG12/5-7 compared with YASA12/10 and YASA12/14 at rated speeds. The flux linkage of YASA12/10 has the highest amplitude value of approximately 18.4 mWb. MG12/5-7 and YASA12/14 have amplitude values of 17.2 and 14.8 mWb, respectively. In addition to the low rotational speed, YASA12/14 has smaller rotor pole pitch compared with the stator pole-pitch. This results in lower flux passing to the stator pole. However, since the proposed machine has a combination of two YASA topologies in which both rotors contribute to the total flux linking the stator windings, the flux linkage amplitude is between both YASA machine flux linkages.

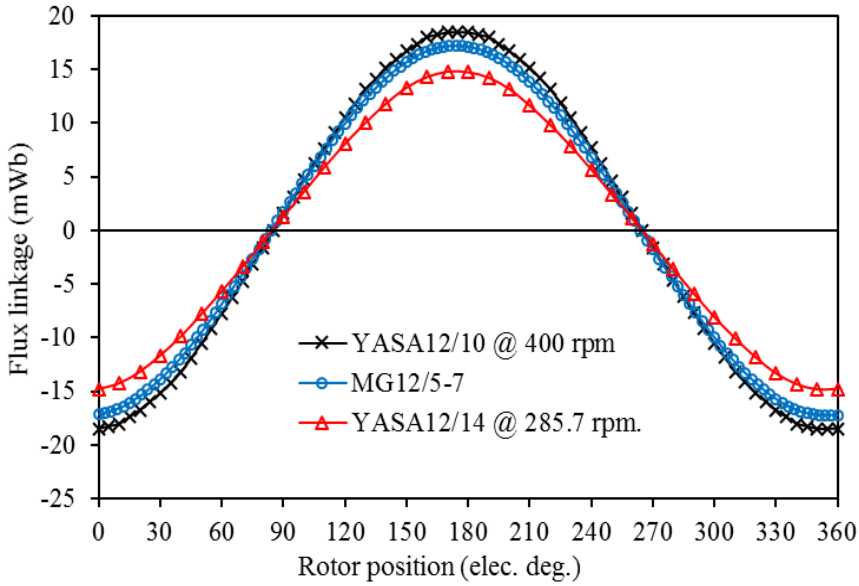

(a) Waveforms

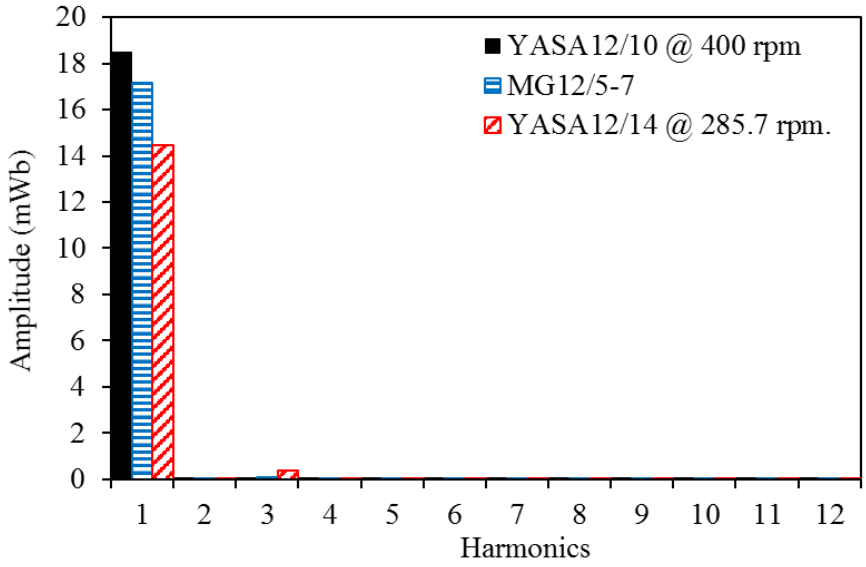

(b) Harmonic spectra

Fig. 3.30 Comparison of no-load flux linkage waveforms at rated speeds.

In addition, the phase back EMFs and the corresponding harmonics are also compared and plotted in Fig. 3.31. The graph indicates that the amplitude of the phase back EMF is approximately 3.80 for YASA12/10 at 400 rpm. Moreover, a maximum back EMF of approximately 3.0 V can be gained by YASA12/14 at 285.7 rpm. Furthermore, for MG12/5-7, both HSR and LSR PMs contribute to the total back EMF: at 400 rpm HSR speed and a 285.7 rpm LSR speed, the amplitude of the phase back EMF is approximately 3.67 V.

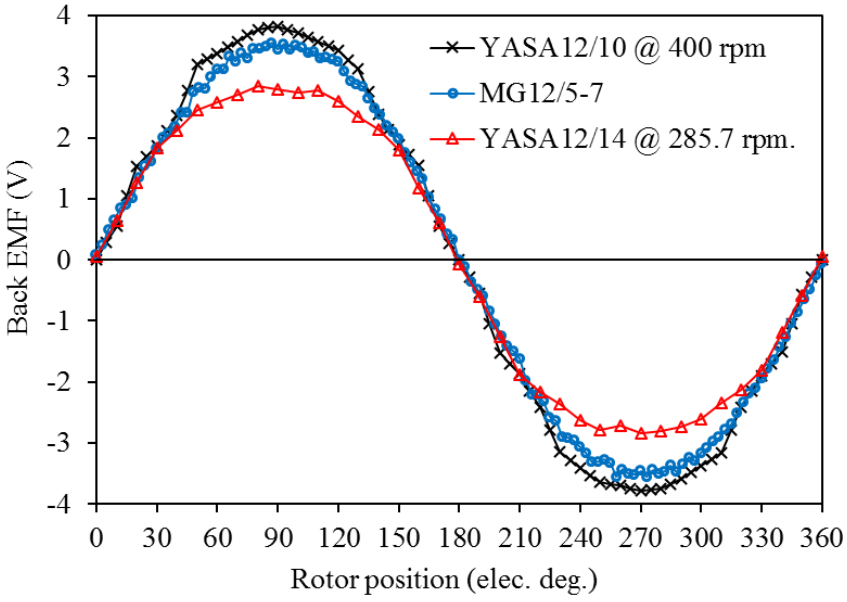

(a) Waveforms

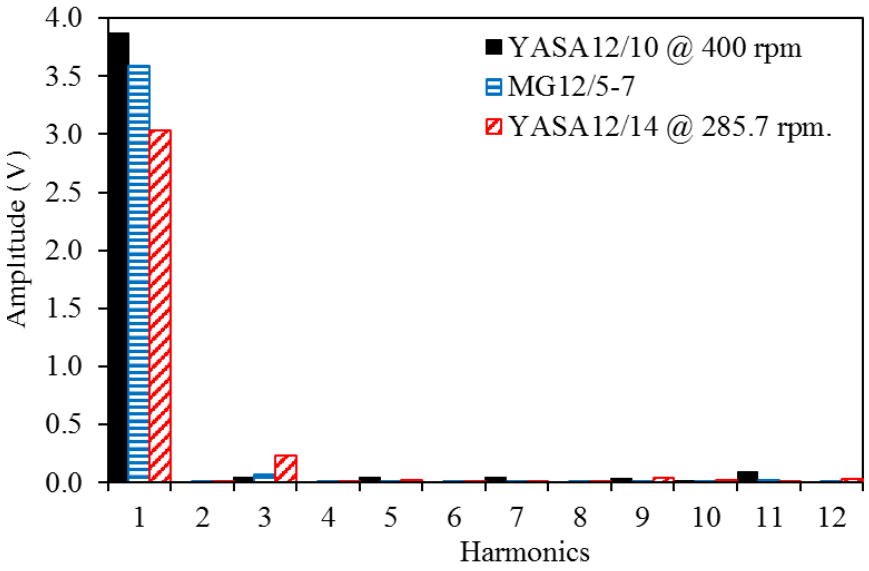

(b) Harmonic spectra

Fig. 3.31 Comparison of no-load phase back EMF waveforms of MG12/5-7 with YASA12/10 and YASA12/14 at rated speeds.

Fig. 3.32 shows the phase flux linkages of the MG12/4-8 compared with YASA12/8 and YASA12/16 machines at rated speeds. It is clear that the flux linkage of YASA12/8 has the highest amplitude value of approximately 18 mWb. MG12/4-8 and YASA12/16 have amplitude values of approximately 15 and 12 mWb, respectively.

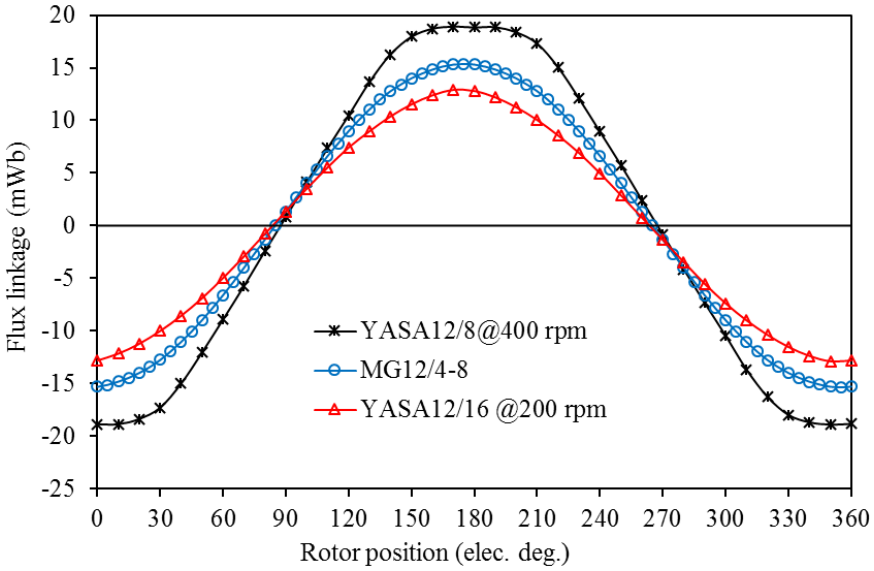

(a) Waveforms

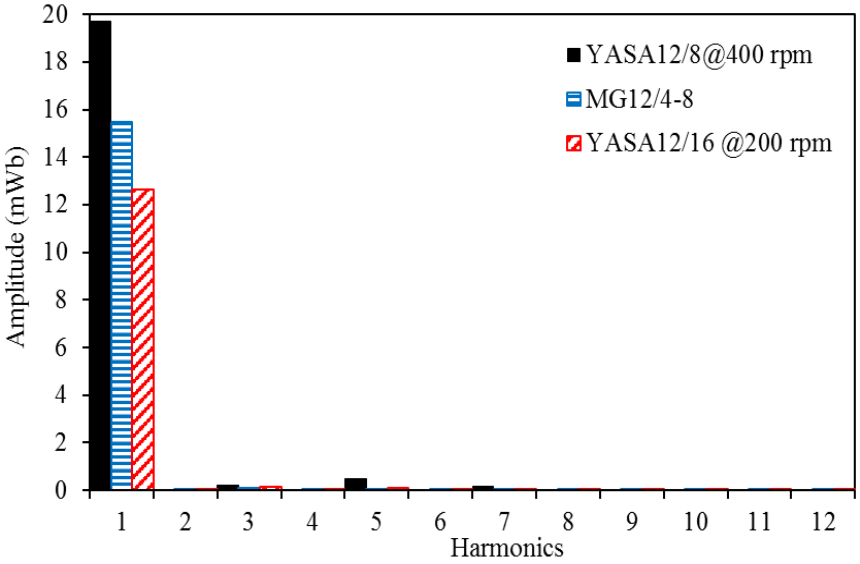

(b) Harmonic spectra

Fig. 3.32 Comparison of flux linkage waveforms at rated speeds.

Moreover, a comparison between the phase back EMFs of MG12/4-8, YASA12/8 and YASA12/16 is illustrated in Fig. 3.33. It should be mentioned that the back EMF of the YASA12/8 is presented at the same speed of HSR (400 rpm) and for YASA12/16 at the same speed of LSR (200 rpm). The comparison indicates that an amplitude of approximately 3.3 V can be obtained for YASA12/8 at 400 rpm. The amplitude of the phase back EMF of MG12/4-8 at rated speeds of both rotors is approximately 2.55 V. Moreover, at 200 rpm a maximum back EMF of approximately 2.2 V can be gained by YASA12/16. Nevertheless, YASA12/8 has a trapezoidal phase back EMF waveform. Therefore, the machine has a small winding factor since there is a

large difference between the pole number and the stator pole number. A comparison of the harmonic spectra of phase back EMF is shown in Fig. 3.33(b).

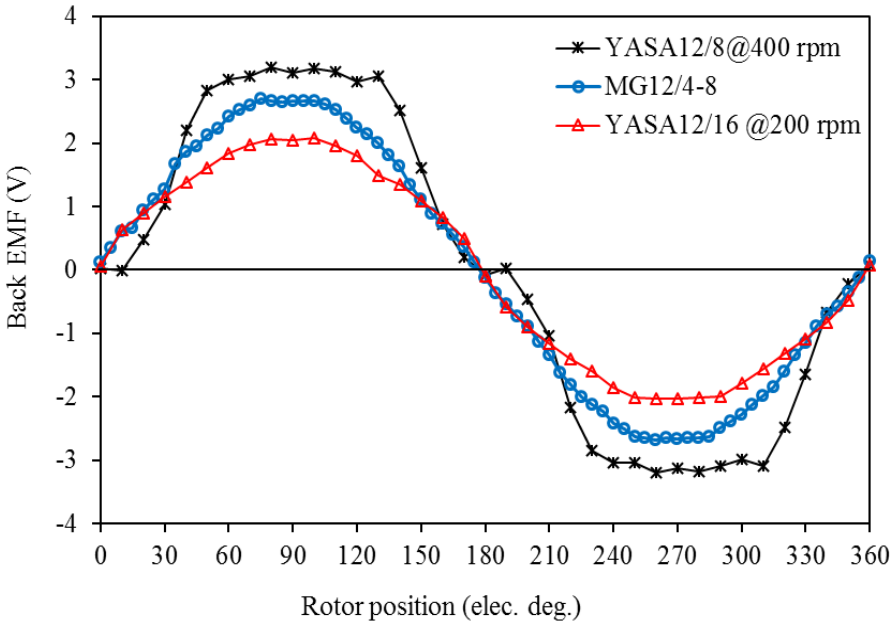

(a) Waveforms

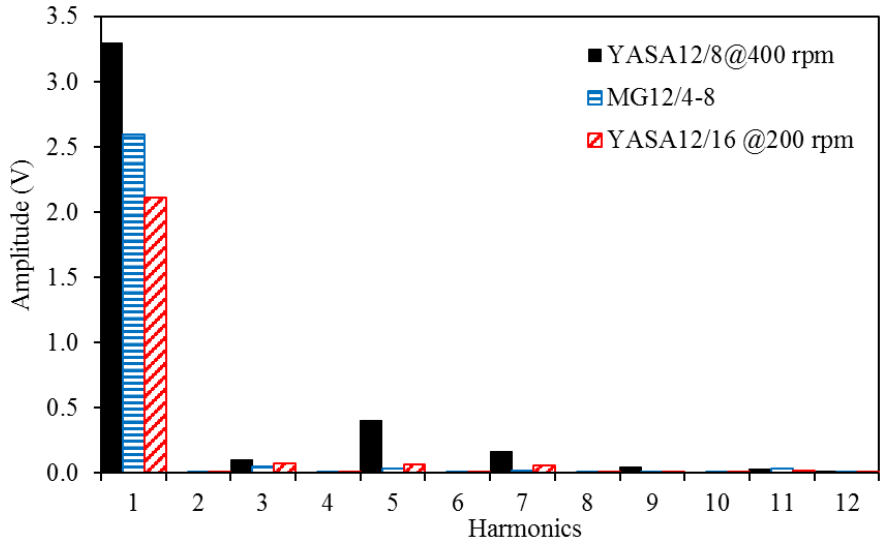

(b) Harmonic spectra

Fig. 3.33 Comparison of back EMF waveforms and corresponding harmonics.

3.8.2 Torque

The torque performance of different load conditions of the proposed machine is investigated and compared with YASA machine torque. Fig. 3.34 shows a comparison between the no-load and on-load LSR torques of MG12/5-7 and the electromagnetic torque of the YASA12/14 machine. It should be mentioned that the no-load torque of AFMGPM machine is calculated at initial

relative angle position of 90 elec. deg. When the LSR is considered as an output rotor, the no-load LSR average torque is significantly higher than the on-load average torque of YASA12/14: 5.30 Nm and 3.2 Nm, respectively. Moreover, the LSR average torque increases further to reach just below 7 Nm when rated current is applied to the machine windings. Similarly, when HSR is considered as an output rotor, a comparison of HSR and YASA12/10 average torques is illustrated in Fig. 3.35. It can be evidenced that maximum average torques of approximately 3.8 Nm and 5.1 Nm can be obtained by HSR at no-load and on-load, respectively. Both torques are also higher than YASA12/10 machine torque at rated current of approximately 2.8 Nm.

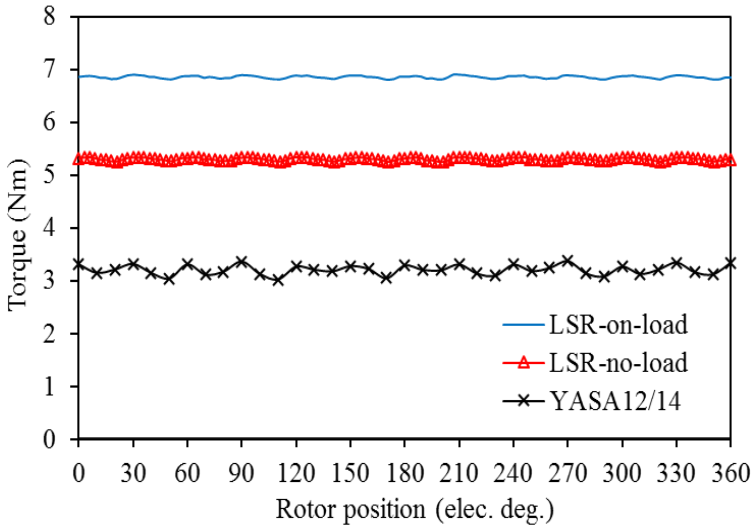

(a) Waveforms

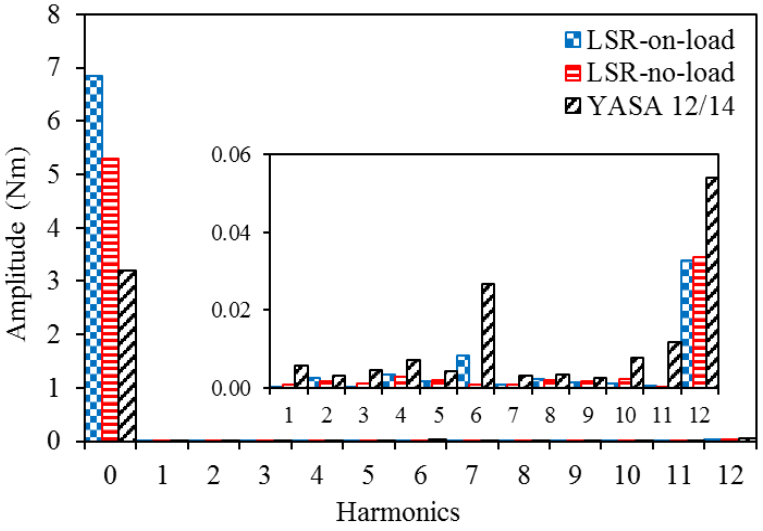

(a) Harmonic spectra

Fig. 3.34 Comparison of LSR and YASA12/14 torques.

Moreover, the torque ripple of the proposed machine is significantly lower when compared to YASA topologies, as can be seen in Fig. 3.34(b) and Fig. 3.35(b). It is clear that the LSR and

HSR at no-load have the approximately the same torque ripple of 1.7 %. The torque ripples of HSR and LSR at on-load are approximately 2 % and 1.5 %, respectively. However, the torque ripple of YASA12/14 is 10 %, while YASA12/10 shows the higher value of approximately 25%.

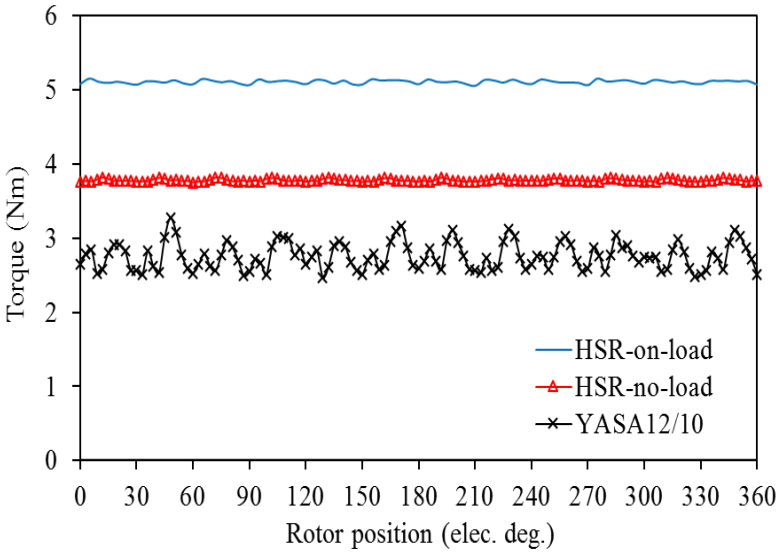

(a) Waveforms

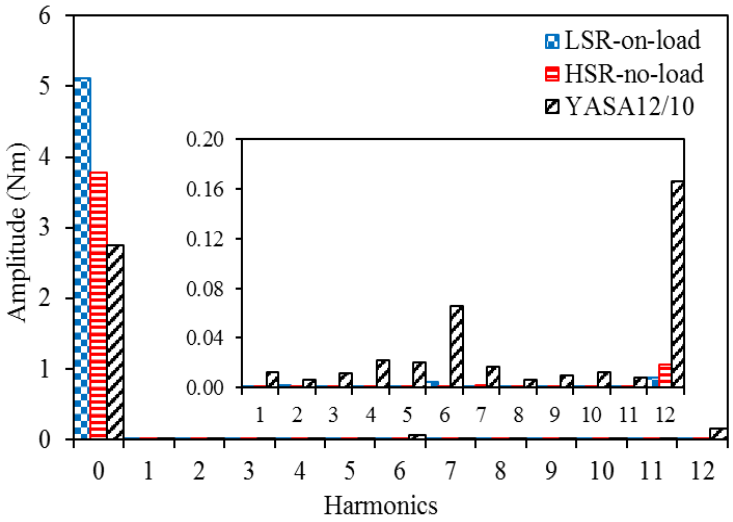

(a) Harmonic spectra

Fig. 3.35 Comparison of HSR and YASA12/10 machine torques.

Fig. 3.36 provides a comparison of the electromagnetic torque of YASA12/8 and the no-load and on-load torques of the HSR at a relative angle of 90°. Moreover, Fig. 3.37 compares the torque of the YASA12/16 machine with the torque of the LSR at different load conditions. It can be concluded that the no-load and on-load of LSR torques have higher values of 4.5 Nm and approximately 6 Nm, respectively while the torque obtained by YASA12/16 is approximately 3.2 Nm. On the other hand, when the HSR is considered as an output rotor, a no-load torque of 2.25

Nm and an on-load torque of 3.5 Nm can be obtained by the HSR. However, the torque of YASA12/8 is significantly lower than on-load torque of HSR of 2.4 Nm, which is slightly higher than the no-load torque. Moreover, the torque ripples of YASA12/16 and the LSR at no-load are approximately the same, at 25 %, while the on-load torque ripple of the LSR has the least value of approximately 20%. However, YASA12/8 and the HSR at no-load have significantly higher torque ripples of 66% and 50 %, respectively, whereas the HSR at on-load has a relatively low torque ripple of approximately 35 %.

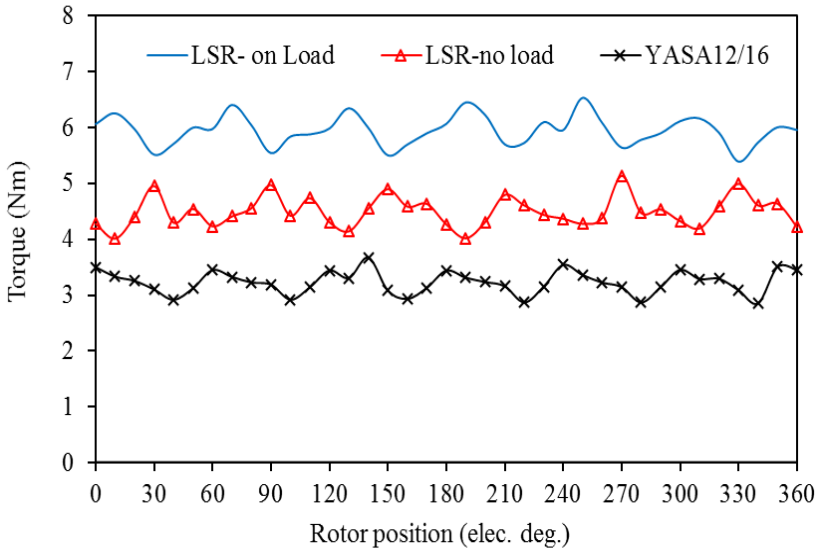

(a) Waveforms

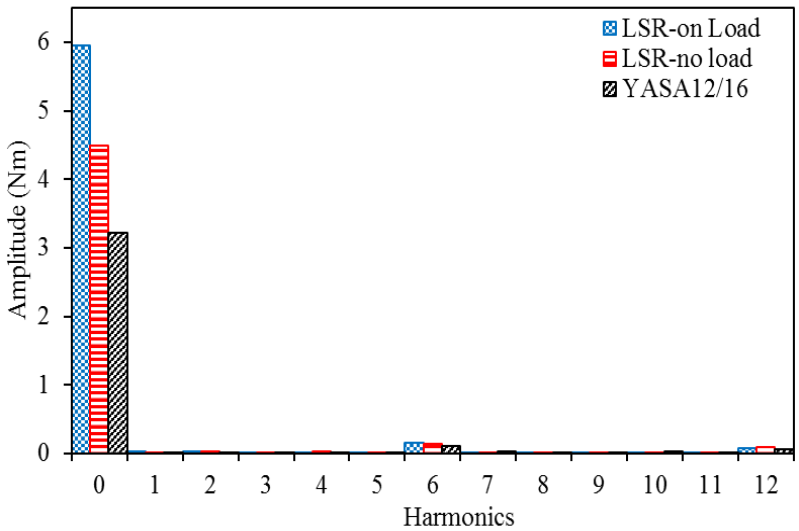

(a) Harmonic spectra

Fig. 3.36 Comparison of no-load and on-load LSR and YASA12/16 machine torques.

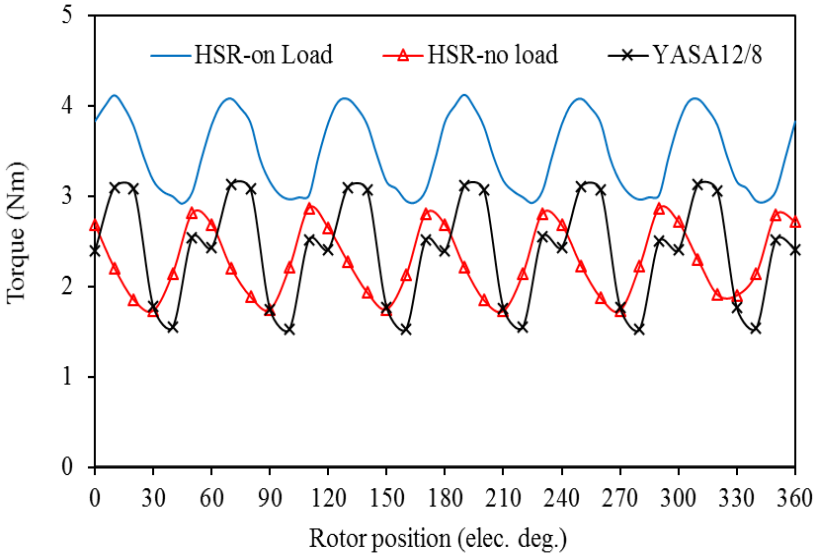

(a) Waveforms

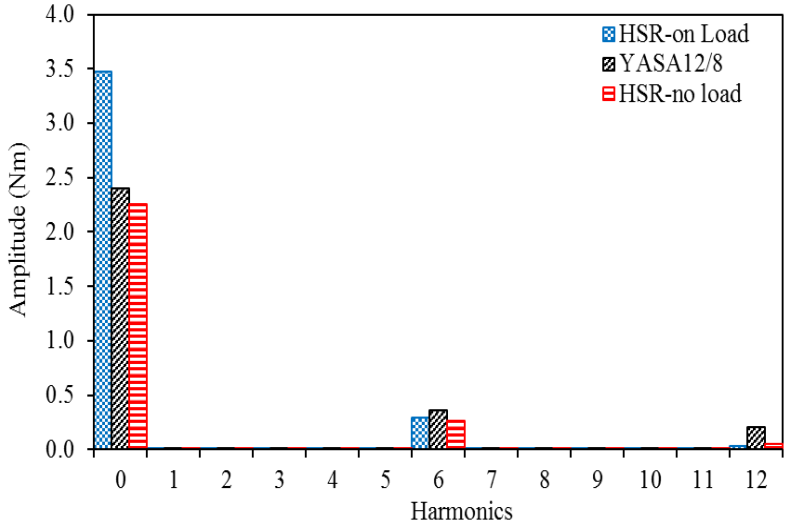

(a) Harmonic spectra

Fig. 3.37 Comparison of no-load and on-load HSR and YASA12/8 machine torques.

3.9 Summary

A novel axial flux magnetically geared machine has been presented in this chapter. The new topology is developed by combining the YASA PM axial field machine with an axial MG. 12 pole pieces are chosen for the machine stator and the possible rotor pole number combinations are investigated. It has been found that magnetically geared machines are subject to the restraints of both PM machines and the magnetic gears. Two pole number combinations have been selected for such a machine. To maximise the machine torque, the proposed topologies are first globally optimised with the aid of 2D-FEA. Then, by using 3D-FEA, the influence of critical machine parameters on the machine torque is investigated. It has been found that at constant machine volume, the PM dimensions, slot opening and inner diameter have significant impacts on the torque performance. Moreover, both topologies have been analysed to investigate the machine performance at no-load. It has been concluded that both topologies have approximately sinusoidal back EMF waveforms. However, compared with MG12/5-7 topology, MG12/4-8 has higher HSR cogging torque as well as torque ripple due to the higher slot leakage flux. Moreover, the torques at no-load and on-load of the proposed machine have been analysed. It is shown that MG12/5-7 has a significant torque quality as well as torque density at all conditions. Furthermore, by adjusting the initial position of the output rotor pole axis, the armature current torque can be added to the transferred MG torque with no effect on the input torque. In addition, the no-load performance (i.e. flux linkage and back EMF) of the proposed machine have been compared to the YASA machine. The torque performance of the AFMGPM machine at different load conditions is also compared to the torque of YASA topologies. The simulation results show the back EMF amplitude of MG12/5-7 is higher than YASA12/14 and slightly lower than YASA12/10 when calculated at rated speeds. Moreover, compared with the YASA machine the proposed machine can obtain a significantly higher torque density at no-load and on-load conditions.

CHAPTER 4

AXIAL FLUX MAGNETICALLY GEARED MACHINE FOR POWER SPLIT APPLICATION IN HEVS

4.1 Introduction

With the merit of high efficiency, fuel economy and low emission, HEVs have been regarded as the most realistic substitute for conventional fuel vehicles [MIL06]. In HEVs, a mechanical planetary gear is normally used to transmit and split the power produced by an internal combustion engine (ICE). However, planetary gears have the same problems as conventional mechanical gears; namely, lubrication and mechanical loss [NIU13a]. To overcome these drawbacks, magnetically geared machines have been introduced to realise a power split function.

Many radial magnetically geared machines have been introduced for various applications such as HEVs [CHA07], [ATA08], wind power generation [JIA09], [JIA11] and so on. For HEVs, these machines have the merit of smooth power flows from the engine to the driven wheels without torque interruption caused by mechanical transmissions and are suitable to achieve power split [JIA10], [NIU13b]. In general, only two AFMG machine topologies have been proposed for power split applications in HEVs. In [TON14], an axial field magnetically geared machine has two identical electrical ports and two different rotor constructions. Moreover, in [LAI16], an axial magnetically geared machine with two different mechanical ports and two electrical ports with different winding sets was also presented. Moreover, in [NIU14] an axial flux variable speed – constant frequency (VSCF) is presented for power split in wind power application. The machine has a stator of two primary and secondary windings with different distribution and different pole numbers. The presented topologies suffer from inherently complex mechanical constructions as well as dual inverters and controllers are required to control each stator individually.

In this chapter, the proposed 3-phase AFMGPM machine topologies introduced in Chapter 3 will be analysed and studied to realise power split function in HEVs. The conventional HEV system was described. Subsequently, the structure of the HEV system based on the proposed AFMG machine is explained. Moreover, by utilising 3D-FE analysis, the proposed topologies are analysed and compared at different operation modes. The machine performance at no-load and on-load is investigated and compared.

4.2 Proposed system of axial flux magnetically geared machine.

The power split system in HEVs has three main power components: the conventional ICE, the electrical motor and the generator. A planetary gear is used to connect the power components together (Fig. 1.3). The presented machine is proposed for variable speed HEV systems. The machine can realise the function of planetary gear and conventional synchronous motor/generator in conventional hybrid electric traction systems as clarified in Fig. 4.1. The proposed machine operating condition can be classified into three operating modes, as can be seen in Fig. 4.2.

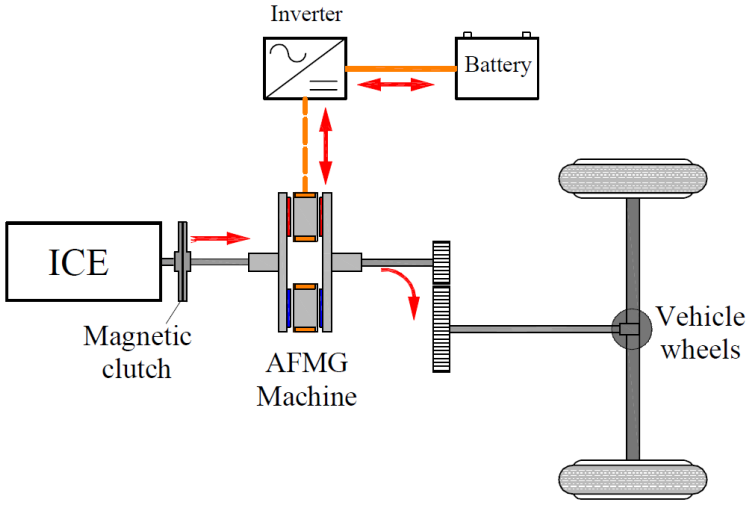

Fig. 4.1 Power split configuration in HEVs based on the proposed AFMGPM.

4.2.1 Power split mode (Mode 1)

In this case, either LSR or HSR is connected to the load, which is driven by the torque transferred due to the magnetic gearing effect from the input mechanical torque. The MG machine in this case operates as an MG to scale up/down the torque/speed of the prime-mover. Moreover, the machine also operates as a generator due to the induced EMF on the stator windings (Fig. 4.2(a)).

4.2.2 Magnetically geared motor mode (Mode 2)

In this operating mode, the load is driven by the torque transferred from the mechanical prime-mover utilising a magnetic gearing effect. In addition, the machine torque can be amplified by the electric torque produced by the armature current flux when the rated current is injected into the machine windings (Fig. 4.2(b)).

4.2.3 Pure electric drive mode (Mode 3)

In this case, the relative angle between two rotors is zero. Moreover, the load will be driven by injecting the rated current to the electric machine windings in which the machine works as a PM machine to drive the demanded load (Fig. 4.2(c)).

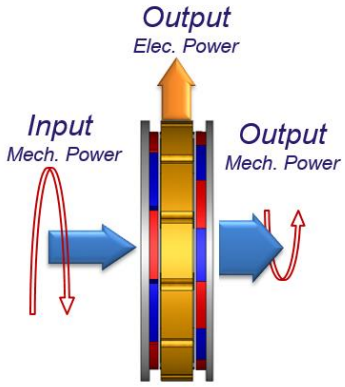

(a) Power split

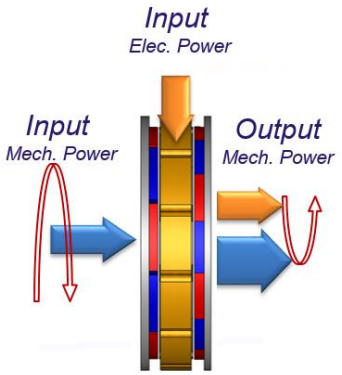

(b) Magnetically geared motor

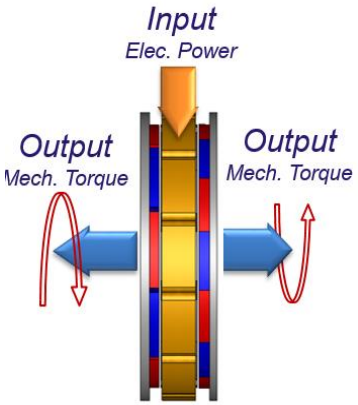

(c) Pure electric drive

Fig. 4.2 Proposed machine operating modes.

4.3 Performance analysis of the proposed magnetically geared machine at different operation modes.

In order to verify the proposed machine operation under the proposed applications, both MG12/5-7 and MG12/4-8 should be analysed and studied at maximum relative angle between HSR and LSR of 90 elec. deg. However, practical limitations have an effect here, since at 90 elec. deg. the operation point at this angle is critical and is located at the end of the stable operation region, as indicated in Fig. 3.26. Therefore, for HEV applications, the MG effect torque of the rotor connected to the load (operation torque) must not reach its maximum value. For the proposed application, the operation torque must always be located in the stable operation region. Therefore, with the aim of obtaining maximum MG torque in the stable operation region, both rotors should

be placed to have a relative angle between both rotors' pole axes at value less than 90 elec. deg.(in this case chosen to be 80 elec. deg). By utilising JMAG-3D FE analysis, the performance of the machine was verified and compared at no-load and full-load conditions at the selected relative angle.

4.3.1 Flux linkage and back EMF

The no-load performance relative angle of 80 elec. deg. was firstly obtained and compared between the two machines. The machine was simulated at open circuit and both rotors were rotated at their rated speeds. It should be mentioned that the flux linkage and back EMF results presented in Chapter 3 were obtained when the relative angle between HSR and LSR positions is zero elec. deg. Fig. 4.3 shows the comparison of phase flux linkages between the two AFMGPM machines when the relative angle is at its maximum value of 80 elec. deg. It can be observed that the proposed MG12/5-7 has higher fundamental flux linkage amplitude of 13.5 mWb since it has a higher winding factor, while the flux linkage magnitude of MG12/4-8 is approximately 12 mWb. Apparently, the phase flux linkage waveforms of the two machines are almost sinusoidal and symmetrical and include a 3^{rd} harmonic component included as shown in Fig. 4.3(b).

The phase back EMFs and the spectra for the proposed topologies are compared in Fig. 4.4. Both topologies have quasi-sinusoidal back EMF waveforms in which the 3^{rd} harmonic exists. However, the back EMF of MG12/4-8 contains more harmonics (the 5^{th} and the 7^{th} harmonics).

The back EMF induced in the stator windings is a result of the summation of the back EMF produced by both rotors. This can be clearly explained by examining the back EMF contributed by each individual rotor. Fig. 4.5 shows the back EMF induced in the machine windings due to individual HSR and LSR for MG12/5-7. With the aid of 3D-FEA, the back EMF of the individual rotors was calculated by examining the winding EMF induced by one rotor while the PM of the other rotor was assigned as a vacuum. Meanwhile, each rotor is kept at the same initial position as the maximum MG torque position. It is obvious that the angle between both back EMFs of the individual HSR and LSR is 90 elec.deg, which is the same as the relative angle. The back EMF amplitude of MG12/5-7 is approximately 2.6 V. Moreover, since both rotors' EMFs contribute to the total back EMF, Fig. 4.5 shows a comparesion between the simulated total EMF and that calculated by the summation of the individual rotor EMFs of MG12/5-7. A good agreement was found between both waveforms in which the difference is due to the saturation effect for the simulated result.

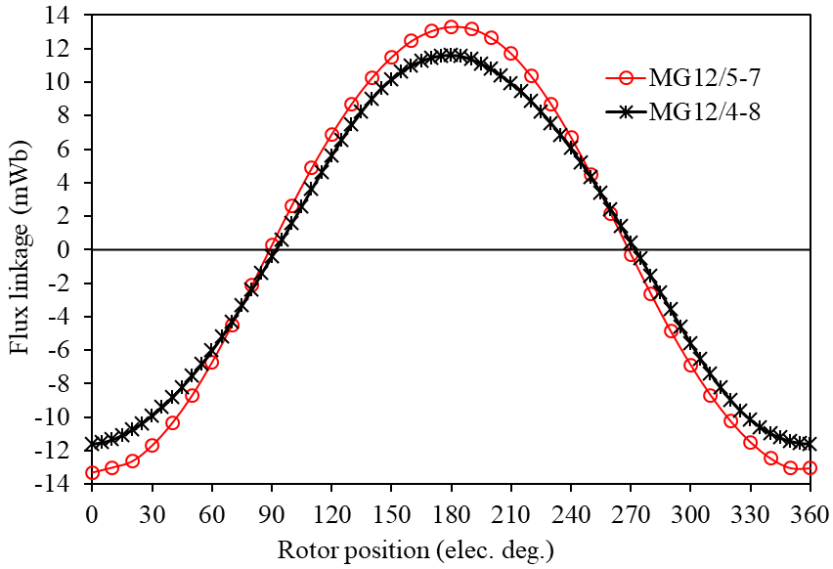

(a) Waveforms

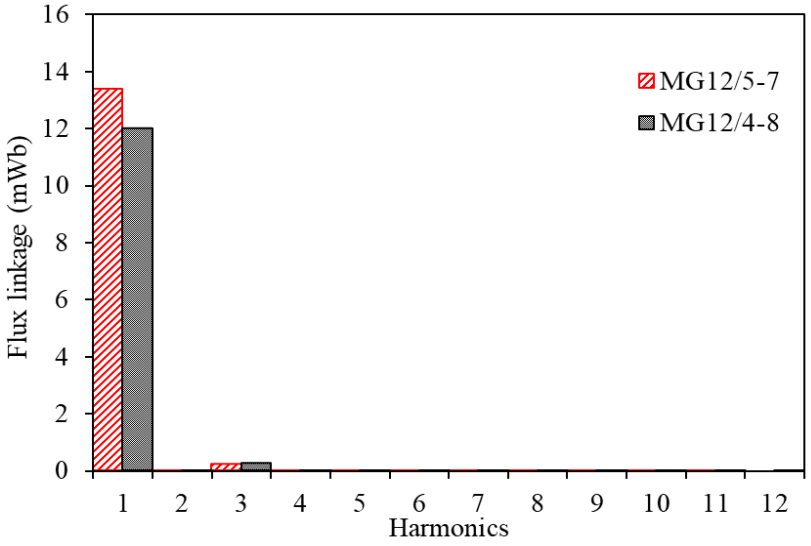

(a) Harmonic spectra

Fig. 4.3 Comparison of flux linkages for different rotor pole combinations at relative angle of 80 elec. degrees.

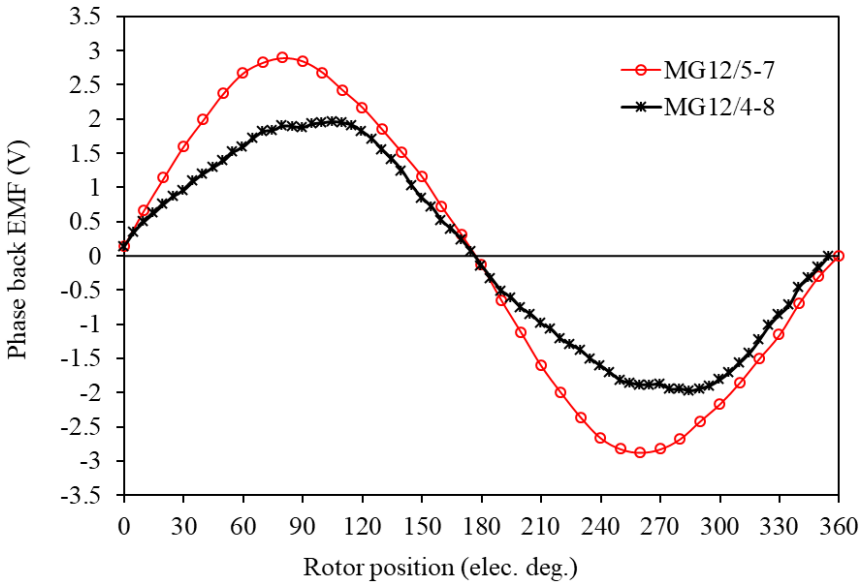

(a) Waveforms

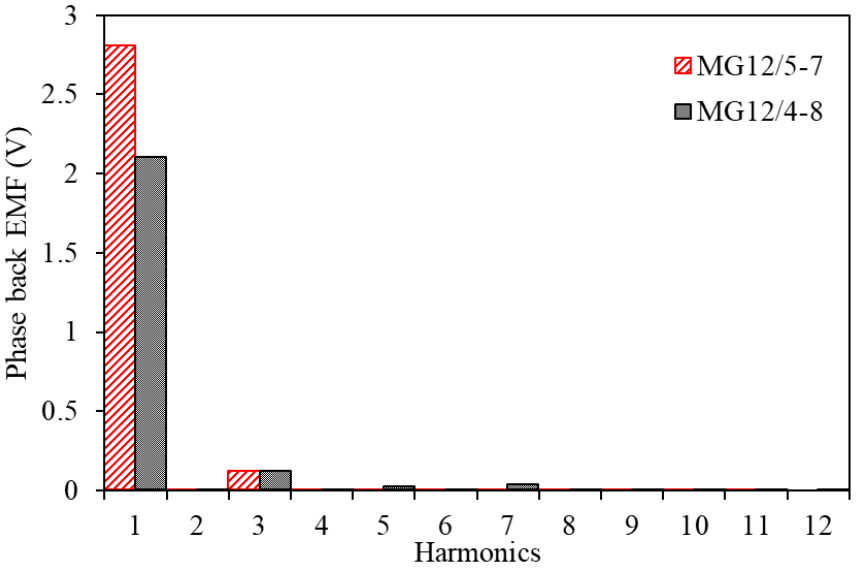

(b) Harmonic spectra

Fig. 4.4 Comparison of phase back EMFs and corresponding harmonics for different rotor pole combinations at relative angle of 80 elec. degrees.

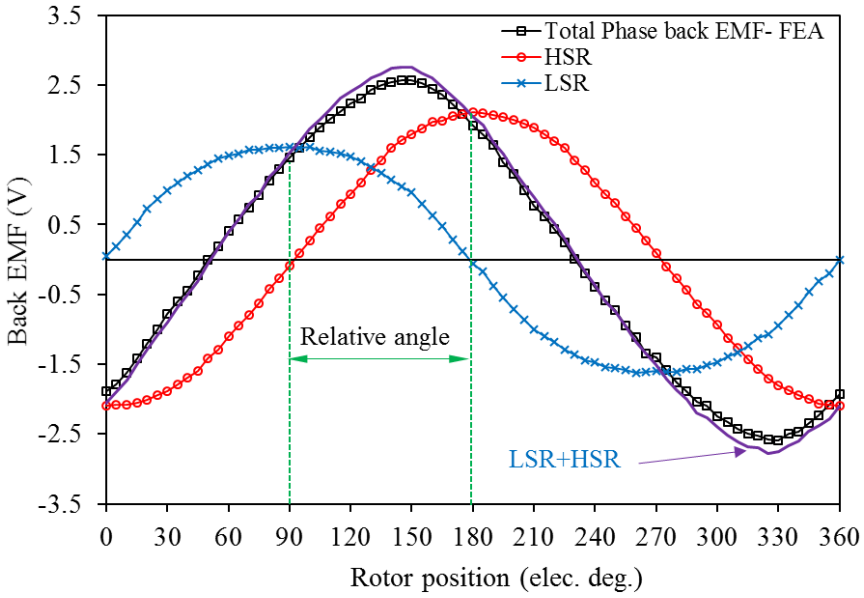

Fig. 4.5 Back EMF waveforms for individual rotors of MG12/5-7 at maximum relative angle.

It can be concluded that, practically, the relative angle between HSR and LSR depends on the load driven by the magnetic gear. In other words, at light or no applied load, a relative angle of approximately zero elec. deg. can be obtained. In this case, the flux linkage and the back EMF amplitudes are maximised. However, the relative angle is increased with the load applied to the output shaft. Therefore, since both rotors contribute to the total phase back EMF, the machine back EMF decreases with the relative angle, as illustrated in Fig. 4.6.

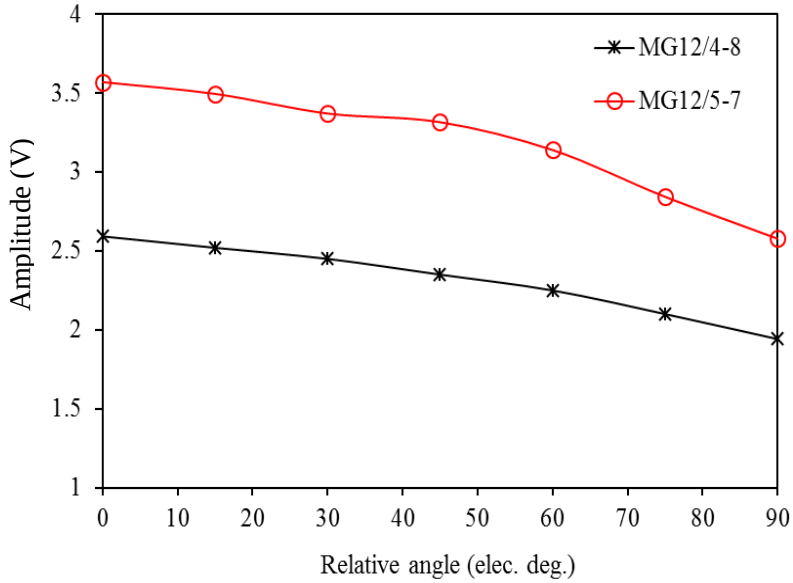

Fig. 4.6 Fundamental amplitude of phase back EMF variation against the relative angle.

Moreover, the fundamental phase back EMF waveforms dominated by LSR (E_L) and HSR (E_H) can be expressed as

$$E_L(\theta) = E_{Lm} \sin(\theta - \theta_L) \tag{4.1}$$

$$E_H(\theta) = E_{Hm} \sin(\theta - \theta_H) \tag{4.2}$$

where, θ, θ_L and θ_H are the rotor position, LSR and HSR initial positions in electrical degrees, respectively. E_{Lm} and E_{Hm} are the amplitudes of LSR and HSR EMFs, respectively. Therefore, since the total back EMF is contributed by both rotors, the total back EMF e_t can be obtained by the summation of (4.1) and (4.2)

$$e_t(\theta) = E_{tm} \sin(\theta - \alpha) \tag{4.3}$$

where, E_{tm} is the amplitude of the fundamental total back EMF and α is the phase shift which both can be obtained as

$$E_{tm} = \sqrt{E_{Lm}^2 + E_{Hm}^2 + 2E_{Lm}E_{Hm}Cos(\theta_L - \theta_H)} \tag{4.4}$$

$$\alpha = tan^{-1}\left(\frac{E_{Lm}\, sin(\theta_L) + E_{Hm}\, sin(\theta_H)}{E_{Lm}\, cos(\theta_L) + E_{Hm}\, cos(\theta_H)}\right) \tag{4.5}$$

It can be deduced that the maximum back EMF is obtained when the relative angle δ is zero, in which the total back EMF waveform is in phase with HSR and LSR EMFs. However, when the LSR initial position is assumed to be zero elec. deg., and with $\delta = \theta_H = 90^o$, the total back EMF has the lowest amplitude and the waveform is shifted by $\alpha = \tan^{-1}\left(\frac{E_{Hm}}{E_{Lm}}\right)$ elec. deg. Therefore, when the EMF harmonics are ignored, according to (4.4) and (4.5), the total back EMF amplitudes and phase shift of MG12/5-7 are approximately 2.6V and 52^o respectively, whereas the amplitude and the phase shift of MG12/4-8 are approximately 2.1V and 56^0 respectively, in which the angle value α results are in good agreement with the results obtained from Fig. 4.5.

4.3.2 Torque

As explained earlier, the angle between the HSR and the LSR is determined by the applied load. However, when the load exceeds the maximum torque value, both rotors will slip, and the machine performance will be unstable. Moreover, when the load torque increases higher than the MG operation torque, the machine output torque is amplified with the aid of armature current torque to boost the machine operation point to the stable area, as explained in Section 4.4.

The machine current is calculated by utilising (2.9).However, for the proposed application, the end winding is considered for the winding length as well as the winding resistance at copper loss of 30 W. The winding length can be calculated by the coil approximate dimensions as indicated in Fig. 4.7. As can be seen in the figure, the mean winding length L_a can be approximately calculated by

$$L_a = 2L_c + \tau_o + \tau_i \tag{4.6}$$

where L_c is the coil active length, and τ_o and τ_i are the lengths of the outer and inner end winding, respectively.

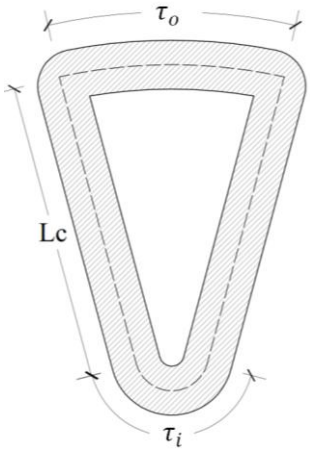

Fig. 4.7 Stator coil diagram and dimensions.

Fig. 4.8 shows the proposed MG12/5-7 machine torque produced by MG effect at relative angle of 80 elec. deg., and the harmonic spectra (Mode 1) as well as the maximum torque when the rated current is injected to the stator winding at the same relative angle, (Mode 2). Similarly, Fig. 4.9 shows the proposed MG12/4-8 torque performance at the same conditions.

According to Fig. 4.5, the LSR position is placed where the d- axis of its pole is aligned with the axis of phase A. Therefore, according to the operation principle of synchronous machines, the armature field only interacts with the PM field of LSR, which results in extra torque and torque being transferred from HSR due to the gearing effect.

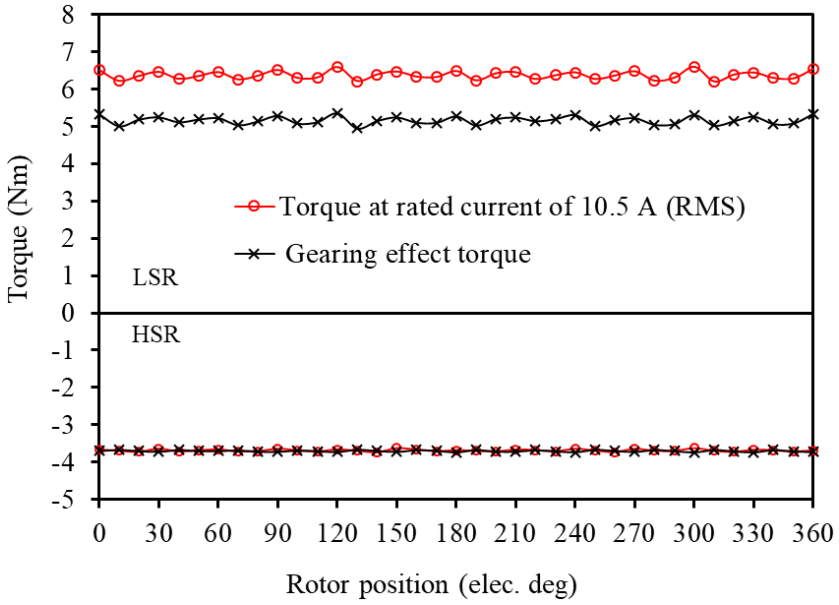

(a) Waveforms

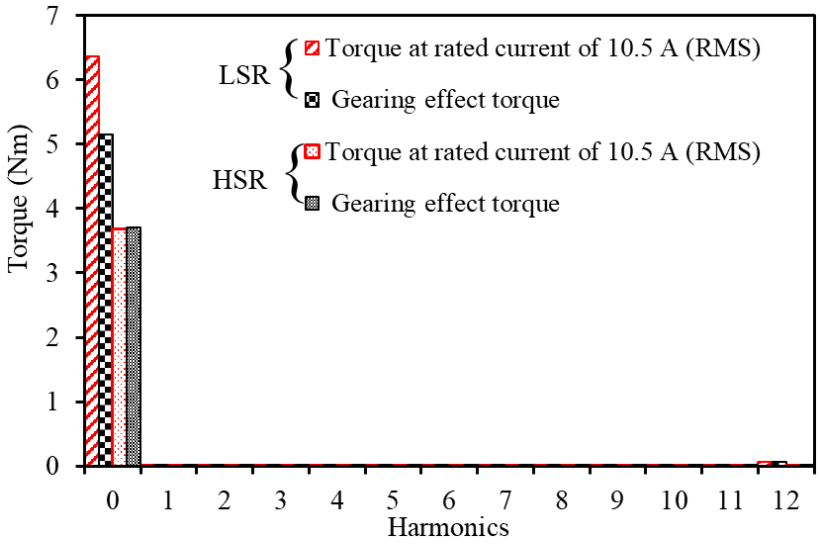

(b) Harmonic spectra

Fig. 4.8 MG and on-load torques of MG12/5-7 at relative angle of 80 elec. degrees.

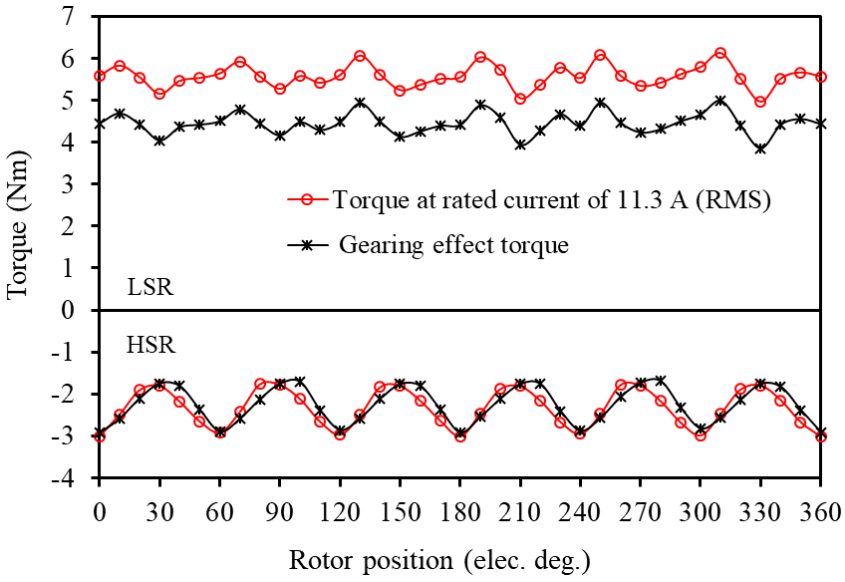

(a) Waveforms

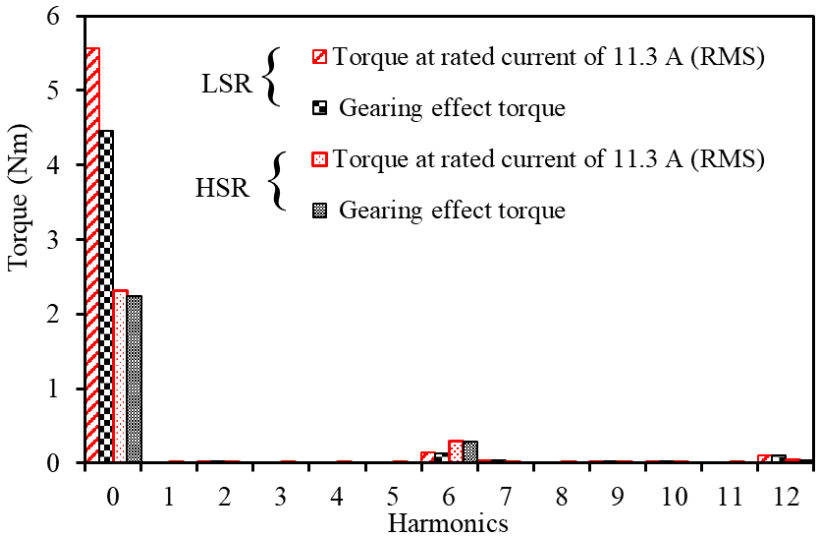

(b) Harmonic spectra

Fig. 4.9 MG and on-load torques of MG12/4-8 at relative angle of 80 elec. degrees.

Fig. 4.10 shows the relation between the machine average torque and the current angle at the maximum relative angle. It is obvious that the torque produced by armature reaction can be controlled by the current angle. On the other hand, the power or the torque produced by the armature current can be split between the high and low-speed rotors by changing the current angle between (0 to 90) elec. deg. Moreover, assuming that the d-axis of LSR in phase with the d-axis of phase A, therefore, at the preferred relative angle, the torque can be added to LSR magnetic gear torque when the current angle is 0^{o}. In this case, the current is aligned with LSR EMF waveform. In addition, by changing the current angle to its optimal value of 90 elec. deg., the armature current torque will be added to HSR torque. Furthermore, at maximum torque exerted

on a specific rotor, the armature reaction effect on the other rotor is negligible. In general, the matching between MG torque of either HSR or LSR and armature current torque can be obtained by the accurate choice of the relative angle and the stator's current angle.

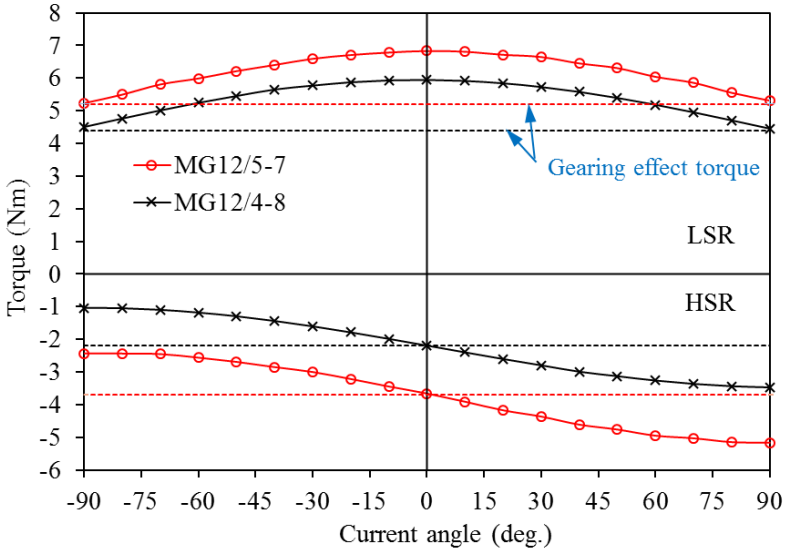

Fig. 4.10 Torque – current angle curves for proposed topologies at maximum MG torque.

Fig. 4.11 shows the machine electromagnetic torque due to the armature current and without magnetic gearing effect for both topologies (Mode 3). Magnetic gearing effect can be cancelled when the relative angle between both rotor poles is zero. On the other hand, the axes of both rotors are placed to be aligned with the axis of phase A. This shows that the proposed machine works as a conventional AFPM without utilising a magnetic gearing effect.

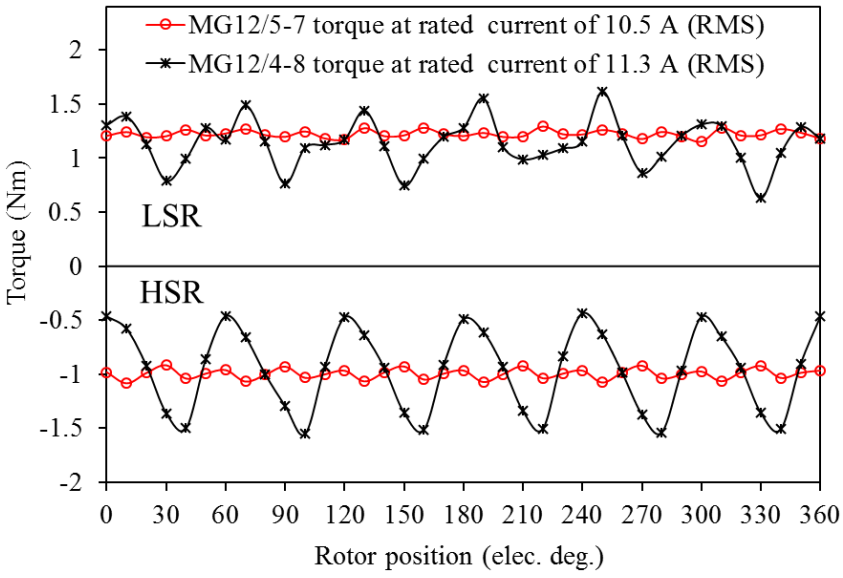

(a) Waveforms

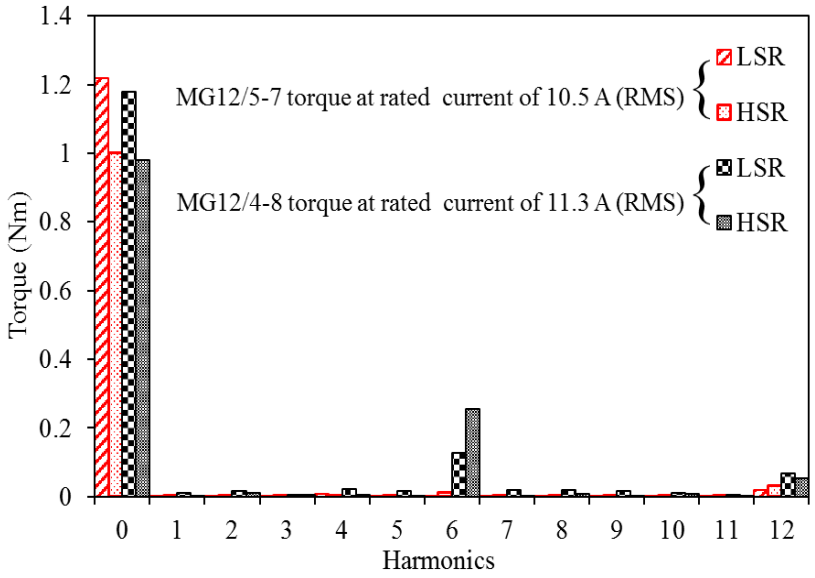

(a) Harmonic spectra

Fig. 4.11 Comparison of armature current torques of the proposed machine at no MG effect and at rated currents.

In addition, more investigations were carried out for the performance of the proposed machine when two current angles are considered (0 and 90 elec. deg.). At optimal relative angle, the current angle is adjusted to maximise the LSR torque when it is assumed to be output torque. The LSR torque of the topologies is studied when the current angle is adjusted at zero elec. degrees in which the armature current torque is added to the LSR MG torque. The output torques of the proposed topologies with respect to current density were obtained. Fig. 4.12 shows the comparison of the produced optimal torque against armature current density. Both topologies

have liner versus current density relations. Moreover, there is a miner effect of armature reaction on the HSR torque of both topologies.

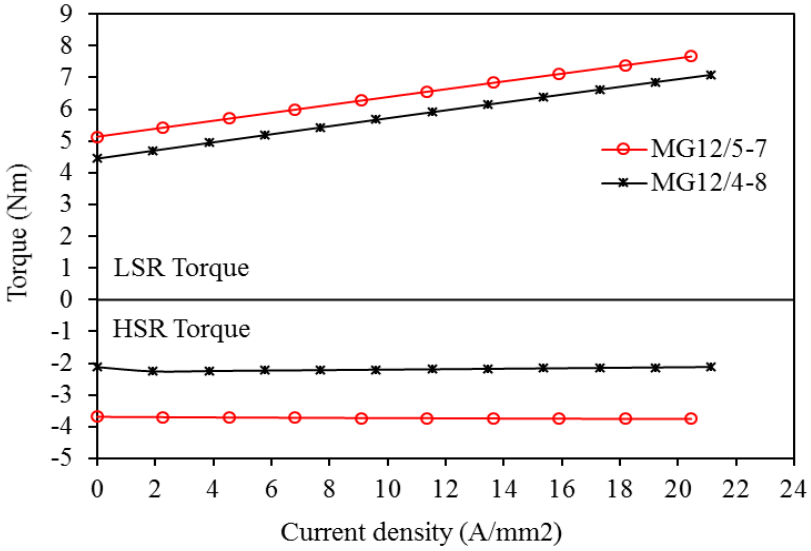

Fig. 4.12 Comparison of torque – current density relation for the proposed rotor pole combinations.

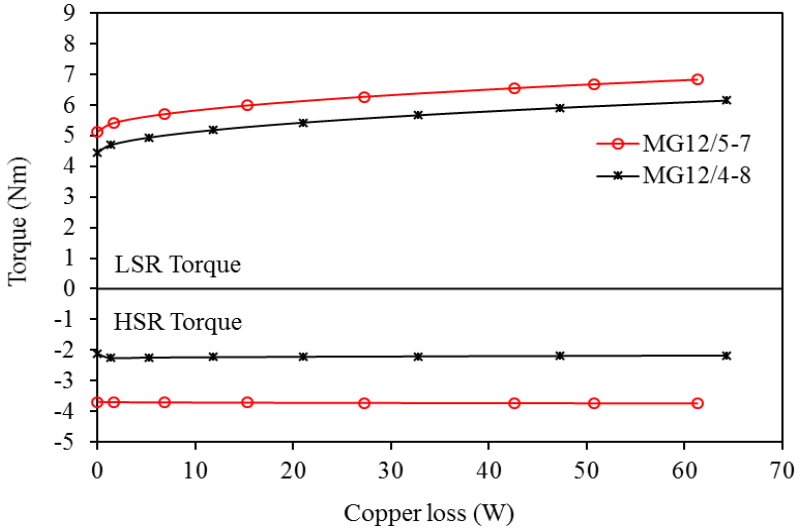

Fig. 4.13 Comparison of torque- copper loss relation for different rotor pole combinations.

Moreover, the relation between the machine torque and the machine copper loss was analysed and compared, as shown in Fig. 4.13. Clearly, MG12/5-7 has higher torque compared to MG12/4-8 over the copper loss range. The torque per total magnet volume with respect to the machine current density is compared in Fig. 4.14, indicating that MG12/4-8 has higher LSR torque per magnet volume than MG12/5-7 since more magnet volume has been used for MG12/5-7 with shorter stator thickness, which was obtained through the machine's optimisation.

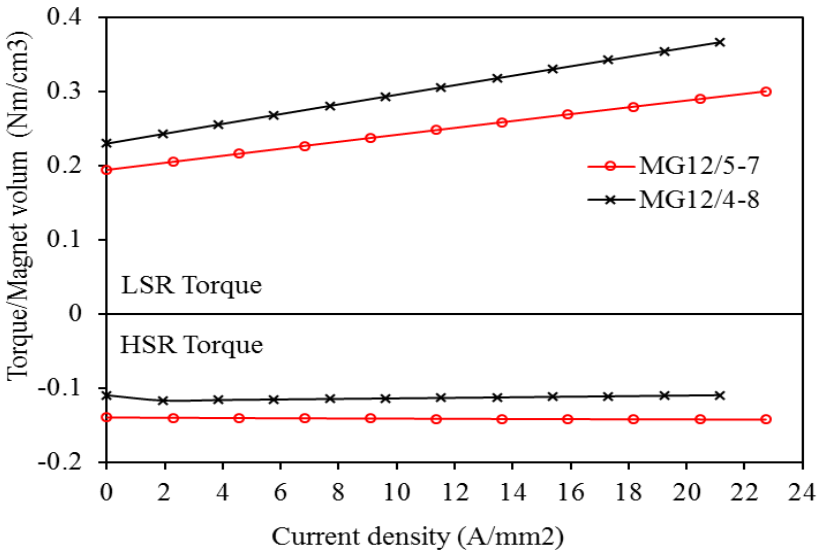

Fig. 4.14 Comparison of torque/magnet volume – current density relation for different rotor pole combinations.

Similarly, the torque performance of the machine topologies is also studied when the current angle is adjusted at 90 elec. deg. In this case, the armature current torque is added to the MG torque of the HSR. The output torque of the proposed topologies as a function of current density and copper loss were obtained and compared in Fig. 4.15 and Fig. 4.16, respectively. It is obvious that the HSR torques are linearly proportional to the current density for both topologies. Moreover, MG12/5-7 has higher torque over the copper loss range compared to MG12/4-8. Fig. 4.17 indicates the comparison of the torque per magnet volume as a function of current density of both machines. It can be noticed that both topologies have approximately the same performance when the HSR is assumed as output torque. MG12/5-7 has superior torque per magnet volume performance over the current density less than 20 A/mm^2 while MG12/4-8 has greater performance after such current density point. Moreover, there is no effect of armature current on the LSR torque of both topologies when the current angle is adjusted to 90 elec. deg.

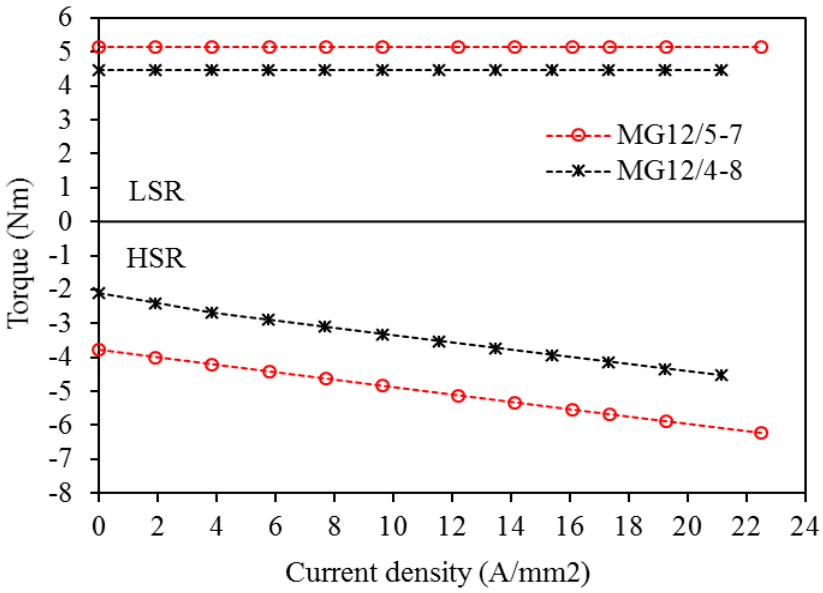

Fig. 4.15 Comparison of torque – current density relation for the proposed rotor pole combinations.

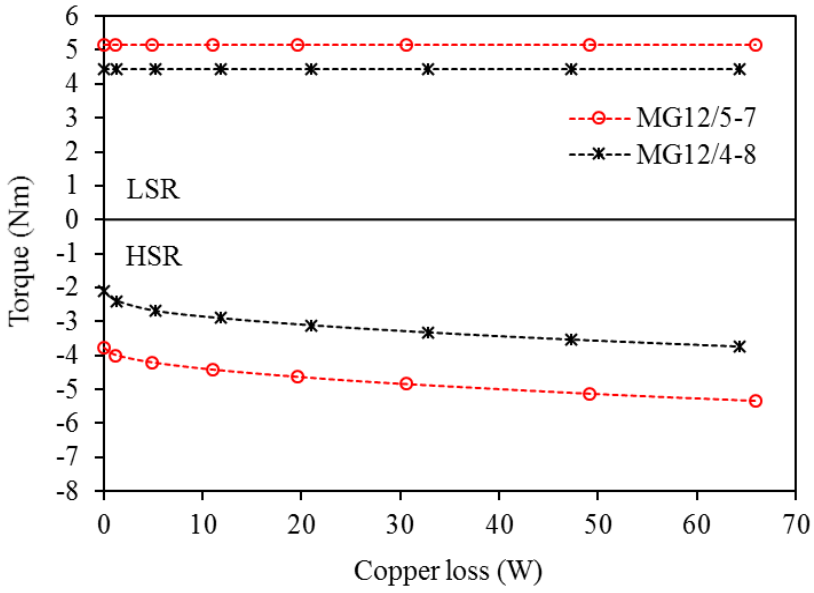

Fig. 4.16 Comparison of torque-copper loss relation for different rotor pole combinations.

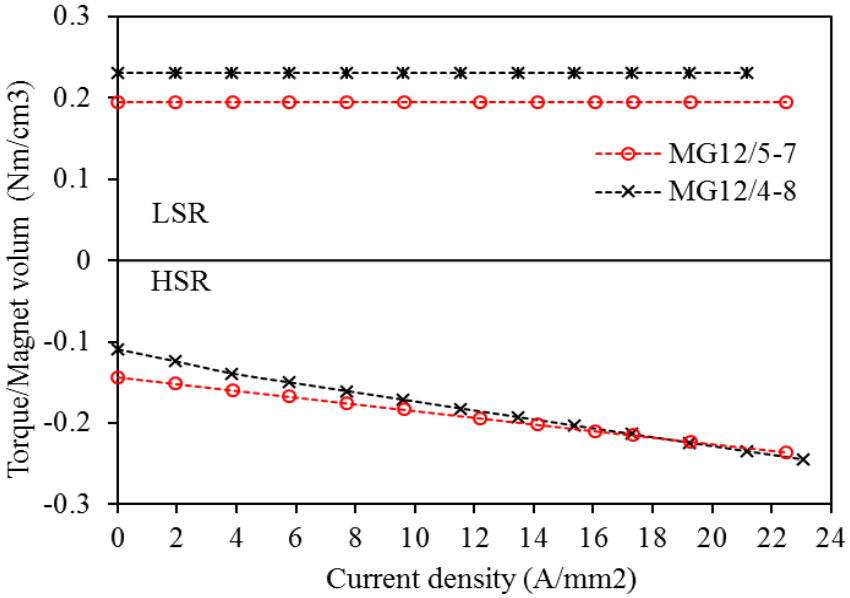

Fig. 4.17 Comparison of torque/magnet volume – current density relation for different rotor pole combinations.

It can be clearly seen that the relation between the machine torque and the current density is linear. Therefore, a general equation for the machine torque can be expressed. The machine total torque . consists of two torque components. The first is no-load magnetic gear torque, which can be expressed by

$$T_L = T_H\, G_r \sin(\delta) \tag{4.7}$$

The second torque component is the torque produced by the armature current and can be expressed according to (A.12) as

$$T_e = K_T\, I \cos(\beta) \tag{4.8}$$

where K_T is the torque constant which depends on the machine dimensions and parameters and β is the current angle. Therefore, when the MG torque is reached to its maximum value (relative angle δ = 80 elec. deg.) the machine torque can be maximised by applying current into the stator windings. The total average torque of the magnetically geared machine can be presented as the combination of (4.7) and (4.8) when the mechanical loss is ignored. Thus, at maximum angle δ, and d- axis of the LSR pole is aligned with the axis of phase A ($\beta = 0$), the total average output torque amplitude can be written as

$$T_o = K_T\, I + T_H\, G_r \tag{4.9}$$

By considering HSR as output torque, the equation can be written by

$$T_o = K_T I + \frac{T_L}{G_r} \quad (4.10)$$

It can be concluded that at maximum MG effect torque (relative angle $\delta \approx 90$ elec. deg.) the machine torque can be maximised by matching the armature reaction torque with the MG torque utilising the current angle.

4.3.3 Axial force

The major force which should be considered in the machine analysis is the attractive force between the rotor PMs and the stator core (the axial force). Fig. 4.18 compares the axial forces exerted on the machine rotors at no-load and on-load conditions. It is worth mentioning that the force is calculated at relative angle between HSR and LSR of 80 elec. deg. In this case, the d-axis of the LSR and the d-axis of phase A are aligned, whereas the HSR is adjusted at 80 elec. deg. with the reference of the LSR.

It can be seen that the average magnetic forces of HSR and LSR are unequal due to the unequal number of rotor poles and hence different air-gap flux density. Moreover, the magnetic forces applied on the HSRs are slightly increased at on-load condition due to the armature current flux density, whereas the forces applied on the LSRs are approximately the same as that at no-load condition since the d-axis of the LSR and the axis of phase A are aligned. Moreover, as can be seen in Fig. 4.19, an unbalanced force exists on the machine stator since the force on the stator is the sum of both rotor forces, but in opposite directions.

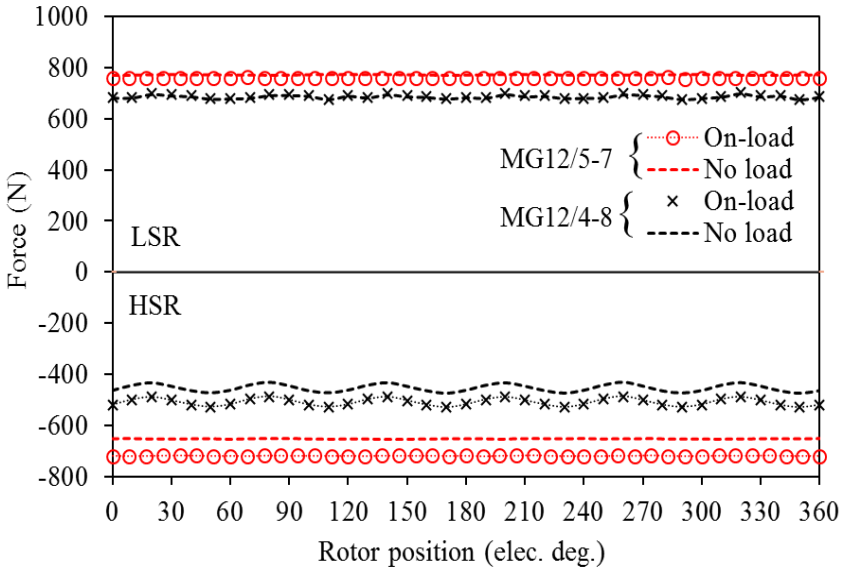

(a) Waveforms

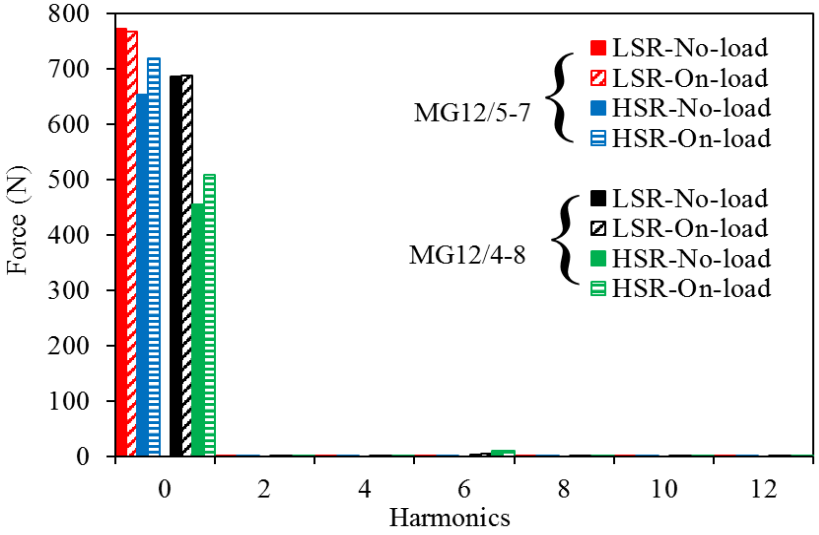

(b) Harmonic spectra

Fig. 4.18 Comparison of high and low speed rotor axial forces for different rotor pole combinations at no-load and on-load.

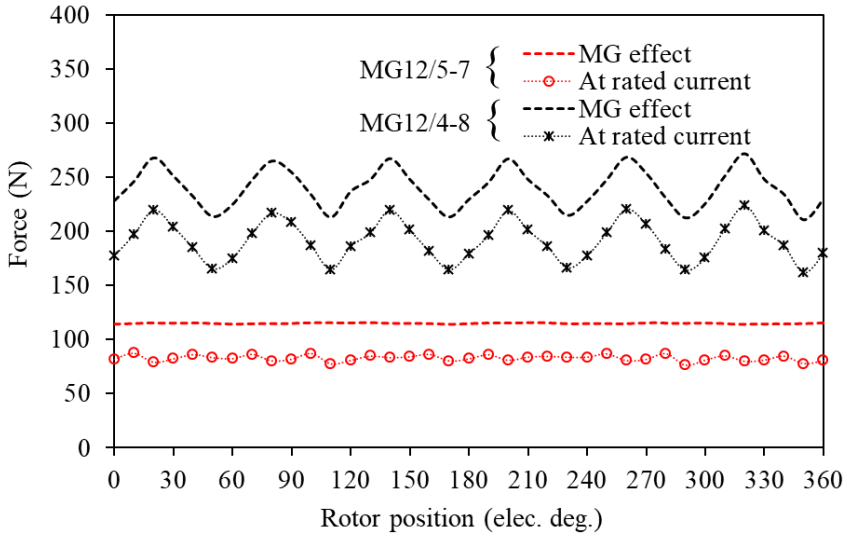

(a) Waveforms

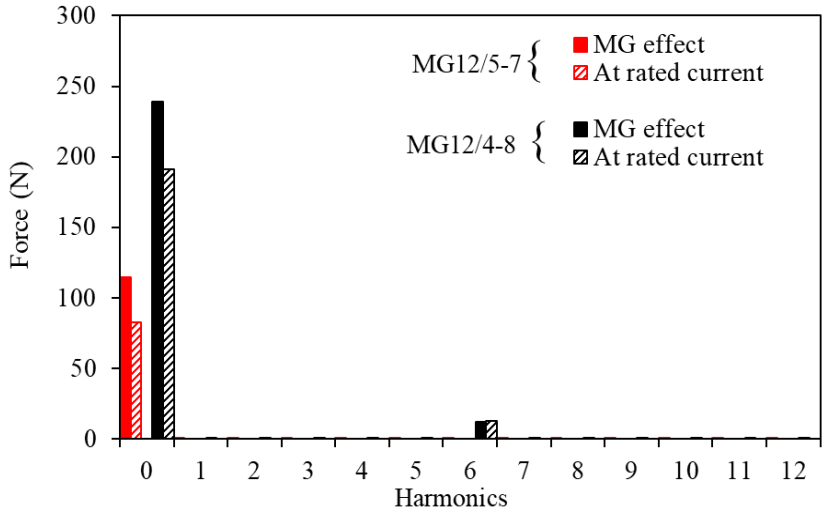

(b) Harmonic spectra

Fig. 4.19 Comparison of axial forces applied on stators for different rotor pole combinations at no-load and on-load.

4.3.4 Losses and efficiency

With the aid of 3D-FEA and by utilising GKN SMC70H material for the stator and both rotor cores, the loss within the stator and rotor of the proposed machine is analysed. Assuming constant rotor rated speeds, and the relative angle at maximum value of 80°, the iron loss is evaluated based on the equation (2.12). Moreover, in order to estimate the magnet eddy current loss, the magnet characteristics of NdFeB are assumed to be linear. A magnet permeability (μ_r) of 1.05, a remnant flux density (B_r) of 1.2 T and a magnet resistivity of 1.4×10^{-6} (Ωm) are assigned to the magnet. Moreover, the skin effect of the eddy current passing in the magnet is ignored since the magnet skin depth is always higher than the magnet dimensions at the studied frequencies (see

Appendix A). Fig. 4.20 shows the iron loss density distributions of both topologies at no-load. It is evident that the stator poles have higher loss compared to the rotor back iron. The iron loss in the rotor back iron of internal stator axial flux machines is always low since the flux passing through the rotor core is DC. Therefore, the majority of rotor loss is contributed by eddy current losses whilst the hysteresis loss is almost insignificant. In contrast, the iron loss is higher in MG12/5-7 since the flux density of the stator pole and tooth tips are higher, as can be seen in Fig. 3.16. Moreover, eddy current loss distributions in the HSR and LSR magnets of MG12/5-7 and MG12/4-8 topologies at no-load are plotted in Fig. 4.21 and Fig. 4.22, respectively. The majority of PM eddy current losses are generated by the fundamental frequency of the magnetic flux due to the slot opening of the stator. It can be concluded that LSRs of both topologies have higher eddy current losses compared with HSRs.

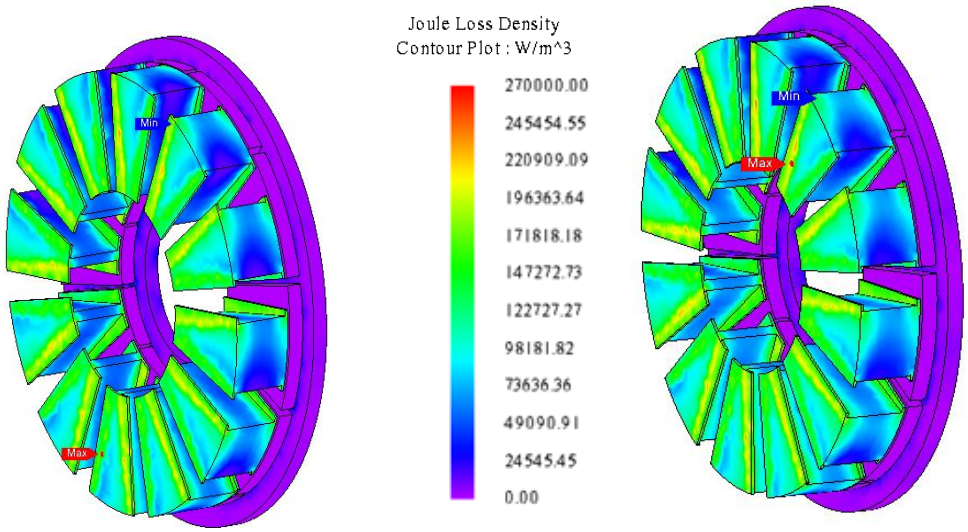

(a) MG12/5-7 (b) MG12/4-8

Fig. 4.20 No-load iron loss distribution for the proposed topologies.

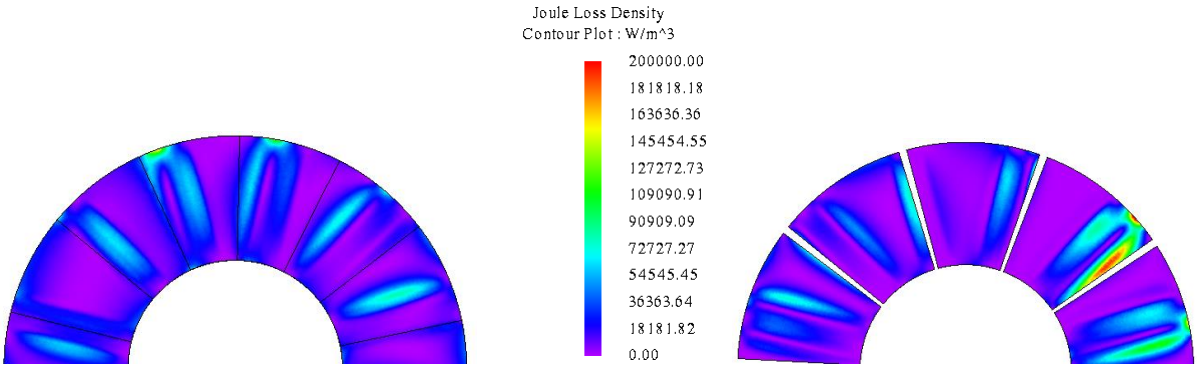

(a) LSR (b) HSR

Fig. 4.21 No-load PM eddy current loss distributions of MG12/5-7.

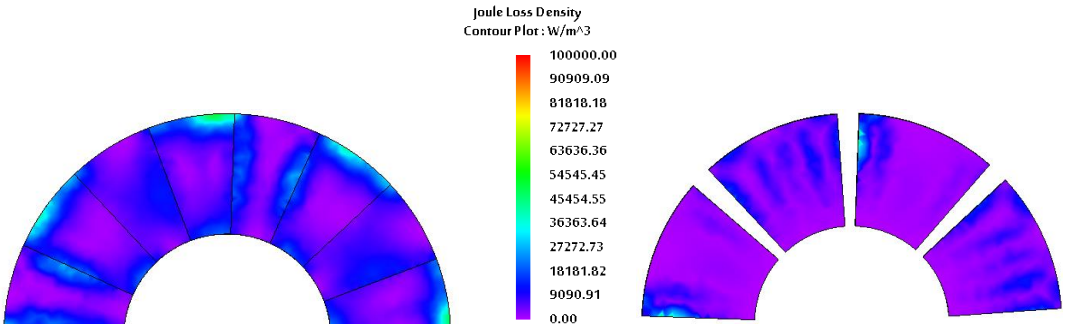

(a) LSR (b) HSR

Fig. 4.22 No-load PM eddy current loss distributions of MG12/4-8.

Moreover, the iron and PM losses in AC machines are mainly caused by the flux fundamental frequency variation. However, many of higher order frequency components must be considered, which are more significant at higher speeds. The losses at different HSR speeds for MG12/5-7 and MG12/4-8 at no-load and on-load are calculated. It should be mentioned that since the machine has two rotors with two different speeds, the losses are obtained with respect to the HSR speed, which is the same for both topologies. Moreover, a constant copper loss of 30 W is considered through the on-load loss calculation. Fig. 4.23 indicates the iron and PM losses generated in MG12/5-7 machine at no-load and on-load conditions over the HSR speed. The losses of MG12/4-8 are also illustrated in Fig. 4.24. It is clear that the stator iron loss rapidly increases while the rotor iron loss slightly increases with the rotor speed. However, the stators generate considerably higher iron losses compared with both rotor iron losses. The iron losses somewhat increase at on-load condition since SMC is used for stator and rotor cores in which the eddy current loss of such material is low. It can also be seen that eddy current loss generated within the PMs increases with the rotor speed and further increases can be noticed at on-load condition. The figures also show that the PM eddy current losses generated in the LSRs are higher than those of the HSRs. In addition to the leakage flux between the magnets, more high order sub-harmonics of the armature flux exist and rotate in the opposite direction of the LSR, which generates more losses within the LSR magnets.

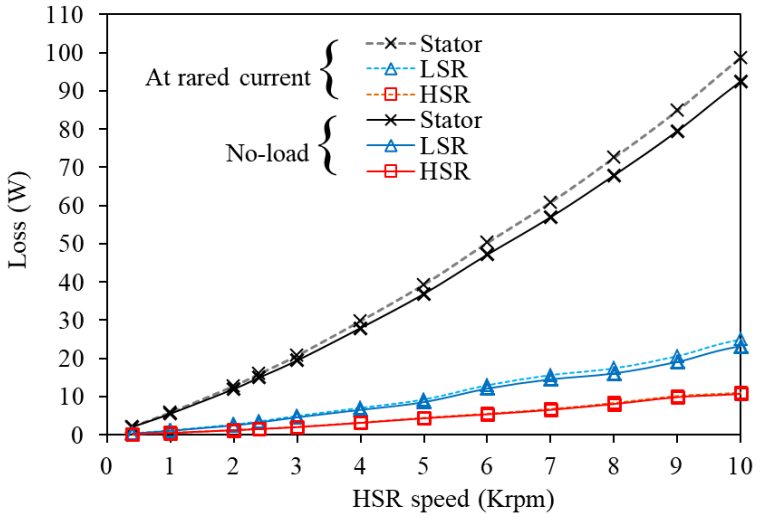

(a) Iron loss

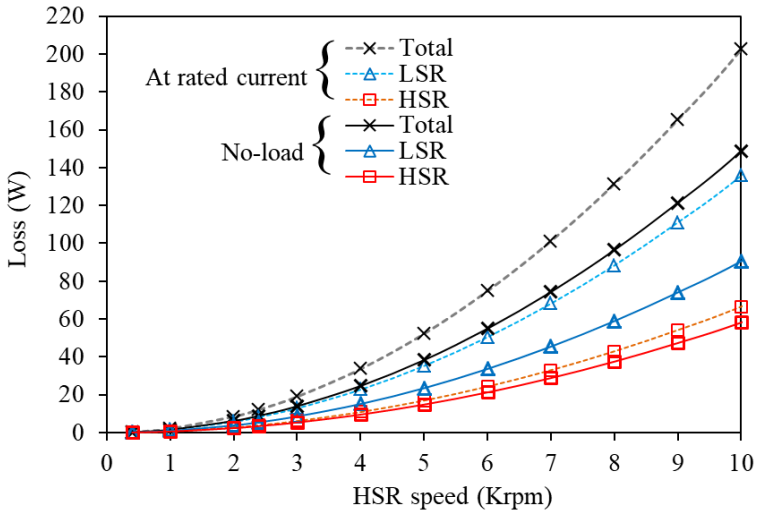

(b) PM eddy current loss

Fig. 4.23 Comparison of no-load and on-load loss components of MG12/5-7 at different HSR speeds.

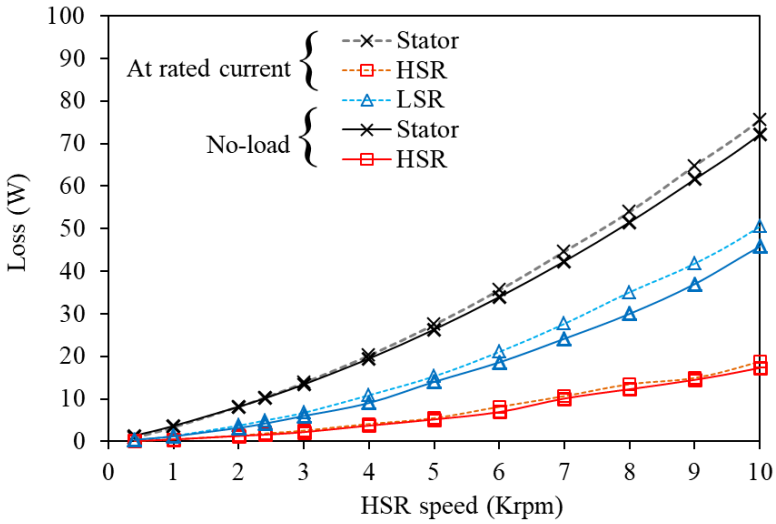

(a) Iron loss

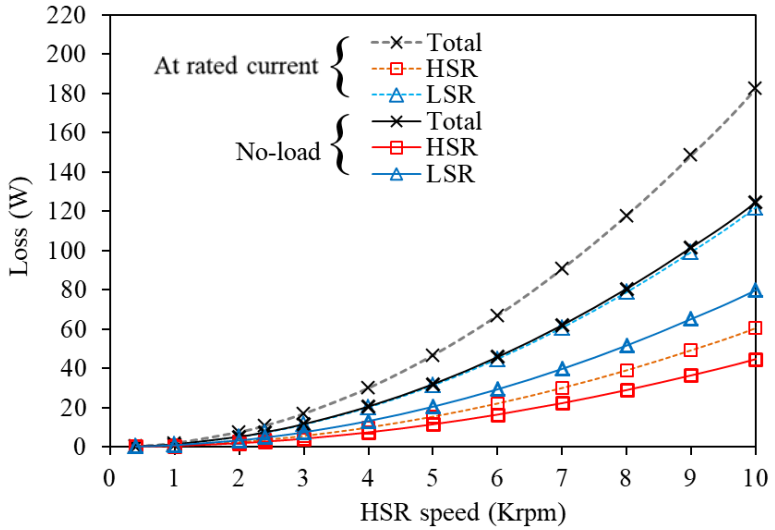

(b) PM Eddy current loss

Fig. 4.24 Comparison of no-load and on-load loss components of MG12/4-8 at different HSR speeds.

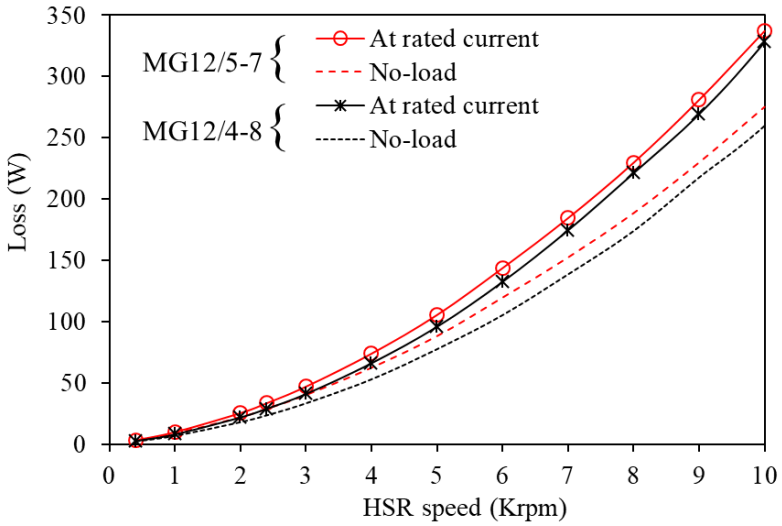

Fig. 4.25 Comparison of total losses in the proposed topologies against frequency at different load conditions.

Fig. 4.25 shows a comparison of no-load and on-load total losses as a function of the machine HSR speed of both topologies. It can be noticed that the total losses for both topologies become significantly high under high speed and on-load conditions. Moreover, the loss of MG12/5-7 is slightly higher than MG12/4-8 over the HSR speed and all load conditions. The no-load flux passing through the stator pole of MG12/5-7 is higher, as indicated earlier. Moreover, the currents applied to the windings increase the magnet eddy current as well as iron losses since more flux passes through the iron and also interacts with the magnet poles.

In addition, assuming constant copper loss of 30 W and constant rated rotor speeds at the maximum relative angle of 80 elec. deg. and when the mechanical loss is ignored, the efficiencies of both topologies are calculated and compared. Table 4.1 compares and summarise the obtained losses, torque densities, efficiencies and power factors of the two topologies at rated speeds. It is evident that the PM and iron losses are higher in MG12/5-7 since both the flux density and the output torque are higher. However, MG12/5-7 has higher efficiency compared with MG12/4-8 at the given copper loss. Moreover, the current densities of MG12/5-7 and MG12/4-8 are approximately 9.5 A/m^2 and 8.5 A/m^2, respectively. Therefore, the machine current density values are in the range of forced air-cooled topologies. However, according to the machine structure, air-cooled system may be difficult to set up since the air cooling system has thermal limitations and the machine has a segmented stator. The design of YASA machine enables it to be cooled by liquid passing through a series of pipes directly over the stator coils as indicated in [CAM12]. Moreover, in [ZHA16], a water-cooled YASA machine topology was analysed and a prototype designed. In order to enable a higher electrical loading, a water-cooled system was

designed for the prototype of the machine, as shown in Fig. 4.26. The cooling system consists of copper pipes placed near the stator windings and surrounded by epoxy to improve the robustness of the stator. Therefore, this cooling system is preferred and could also be used for the proposed AFMGPM machine since it has the same structure as YASA machine.

Table 4.1 Comparison of machine losses and efficiency at rated current and speed

Parameters	MG 12/5-7	MG 12/4-8
LSR speed (rpm)	285.7	200
Torque density (kNm/m^3)	40	35
Mechanical output power (W)	195	119
Copper loss (W)	30	30
Rated current density (A/mm^2)	9.5	8.5
PM eddy current loss (W)	0.30	0.26
Iron loss (W)	2.8	2.16
Power factor	0.7	0.54
Efficiency (%)	85.2	78.3

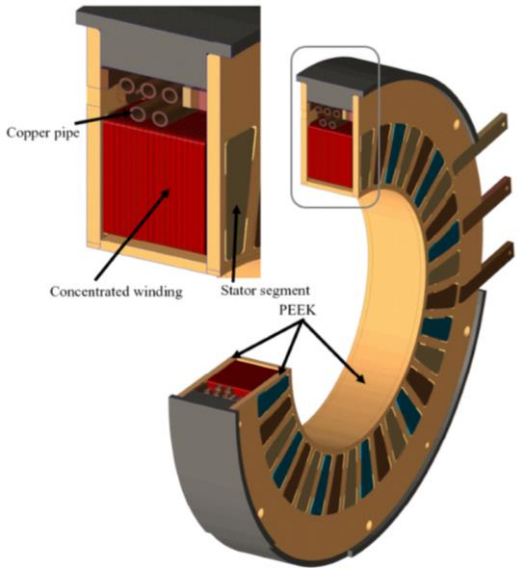

Fig. 4.26 YASA machine topology and its cooling system presented in [ZHA16].

4.3.5 Influence of machine size on power output

In addition to HEVs, the presented machine in this study is also suitable for other low speed high torque applications, such as wind power generation. Several magnetically geared topologies have been presented for such application, in which there wind turbine systems are convenient for the proposed AFMGPM machine [SUN08], [LUO17]. In [SUN08], for wind power generation applications, a magnetically geared machine with two mechanical ports and one electric port was presented to replace the mechanical gear-box between an electrical excited generator and the wind turbine. The primary shaft of the magnetically geared machine is connected to the wind turbine while the generator shaft is connected to the secondary magnetically geared shaft. The input power produced by the wind turbine could be split between the output shaft and the electrical port which is connected to the power storage device by a converter. The power storage is connected to the generator rotor by utilising an inverter and slip rings. In this case, when more power is needed by the generator and the grid power is higher than the generator power, its power can be regulated and boosted by the field current through the slip rings obtained by the power storage device. In [LUO17], a magnetically geared topology with two rotors and a stator with two winding sets was presented. Both rotors were connected to two blades rotating in opposite directions. It has main and axillary windings to control each rotor individually to maximise the generator power. Therefore, these methods is more suitable and can be utilised for the proposed AFMGPM machine.

For the proposed machine, the output power at rated speed is quite low since its outer diameter is very small. Therefore, the influence of the machine size and the possibility for higher power applications will be discussed in this sub-section. From the conventional AFPM machine point of view, it is evident that the outer diameter has a significant impact on the machine torque/power at a constant speed since they are proportional with the cube of the outer diameter ($T \propto {D_O}^3$) [WOO06]. In addition, it is obvious that with the increase of the machine size, the optimal modular (slot)/rotor pole number combination and geometrical structure for largest output power changes. However, for the sake of simplicity and discussion, the proposed MG12/5-7 machine is simply scaled up since it has a larger output power than the MG12/4-8. The optimized topology of MG12/5-7 is scaled in both radial and axial directions with the same scale factor as explained in Fig. 4.27. Fig. 4.28 indicates the powers of the HSR and LSR and the corresponding machine volume at different scale factors at the rated speeds. It is clear that the machine volume linearly increases with the scale factor, and power significantly increases as the machine is scaled up. Therefore, according to the obtained results, when the outer diameter and the axial length are

scaled by 10, (i.e. D_o=900 mm and L_x=250 mm), the output and the input power of 206 kW and 157 kW can be predicted, respectively.

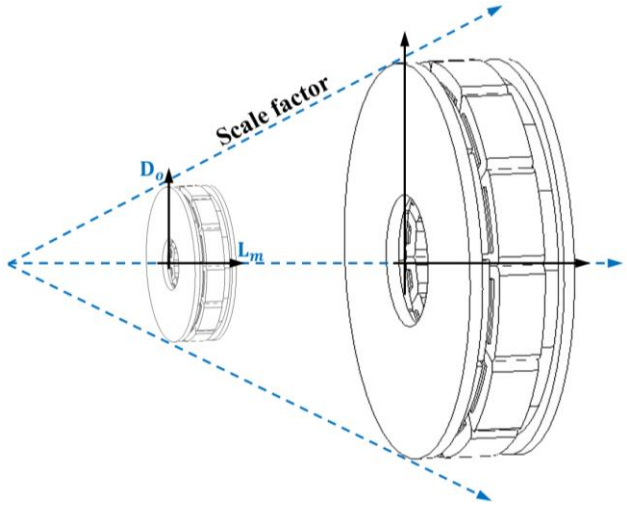

Fig. 4.27 Volume scale method of the proposed topology.

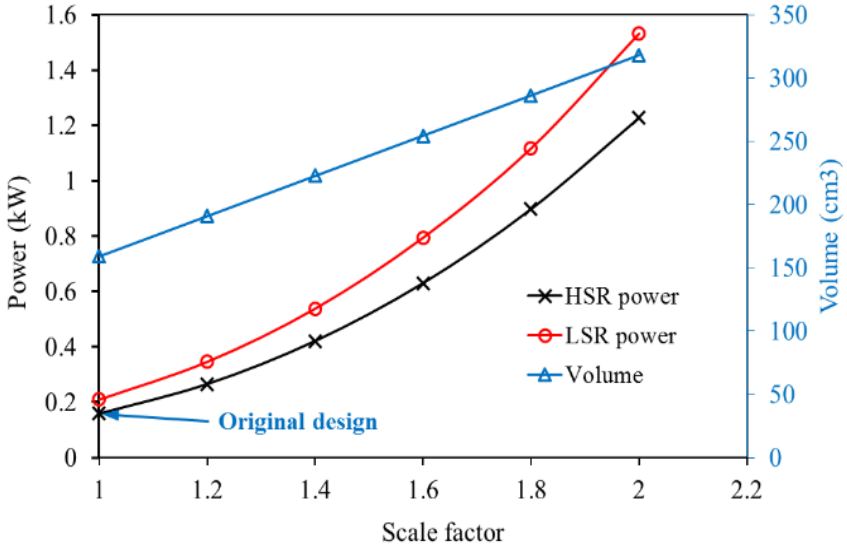

Fig. 4.28 Influence of machine volume on output power at rated speed.

4.4 Proposed control method of AFMGPM machine

For conventional magnetically geared machines with one stator located between two rotors, a 3-phase distributed winding is always utilised. The windings have the same pole as the output rotor to match the electromagnetic torque produced by the armature winding with the output MG torque. However, concentrated windings are considered for the proposed topology and the LSR is assumed as an output rotor which is connected to the drivetrain.

To investigate the control method of the proposed machine, the machine operation mechanism needs to be explained with the aid of the relationship between the machine output torque and the

relative angle between HSR and LSR as indicated in Fig. 3.26, which is represented in Fig. 4.29. In order to ensure a stable operation of the machine at all loads, the maximum relative angle is set at 80^0. As described earlier, in the first operation mode, in which the machine functions as a generator and an MG has the HSR handled by the ICE. The average output torque can be explained by

$$T_o = (T_{ICE} - T_{Hloss})\, G_r \sin(\delta) - T_{Lloss} \tag{4.11}$$

where T_{ICE}, T_{Lloss} and T_{Hloss} are the engine torque, and LSR and HSR mechanical losses, respectively. At light load applied to the output shaft, most of its power is converted to electrical output power by the armature windings installed in the stator and the rest of the power is directly transmitted through the output rotor shaft to overcome the mechanical losses and propel the vehicle's wheels. Moreover, with rising of the output power due to the wheel load torque, the relative angle between both rotors increases and the machine MG torque follows the load torque while the electric output power decreases. When the load torque reaches the maximum of MG torque, the machine torque performance approaches the unstable operation area (Operation point A), as explained in Fig. 4.29. In this case, the armature current torque is utilised to boost the output torque and maintain the machine operating in the stable zone. In other words, as explained in the figure, when the load torque increases to reach a value higher than the maximum MG torque, (Point B), the armature current must be injected and follow the increase of the load torque. However, the load torque must not exceed the machine rated torque (Point C) which is considered in the design process. In this case, the output torque can be expressed as:

$$T_o = \frac{3}{2}\frac{E_{Lm} I_m \cos(\beta)}{\omega_l} + (T_{ICE} - T_{Hloss})\, G_r \sin(\delta) - T_{Lloss} \tag{4.12}$$

where I_m,is the amplitude of the stator current.

Therefore, according to the machine operation mechanism, the control strategy of the proposed machine can be explained as indicated in Fig. 4.30. For conventional PM machines, the rotor d-axis can be defined as the position where the fundamental component of the flux reaches the maximum. However, since the proposed machine has two rotors, the main objective is the accurate estimation of the rotor initial position and the location of the d-axis of the output rotor flux in the d-axis of the armature current flux. Therefore, according to the experimental methodology applied and indicated in Chapter 6, there is a practical method of defining the initial d-axis position of the rotor. It involves injecting direct current into the stator winding of phase A while both rotors are free. In this case, both rotors are dragged to a position where the d-axes of

the rotor and phase A are aligned. This position can be recorded by the controller as a reference for rotor position estimation during normal operation.

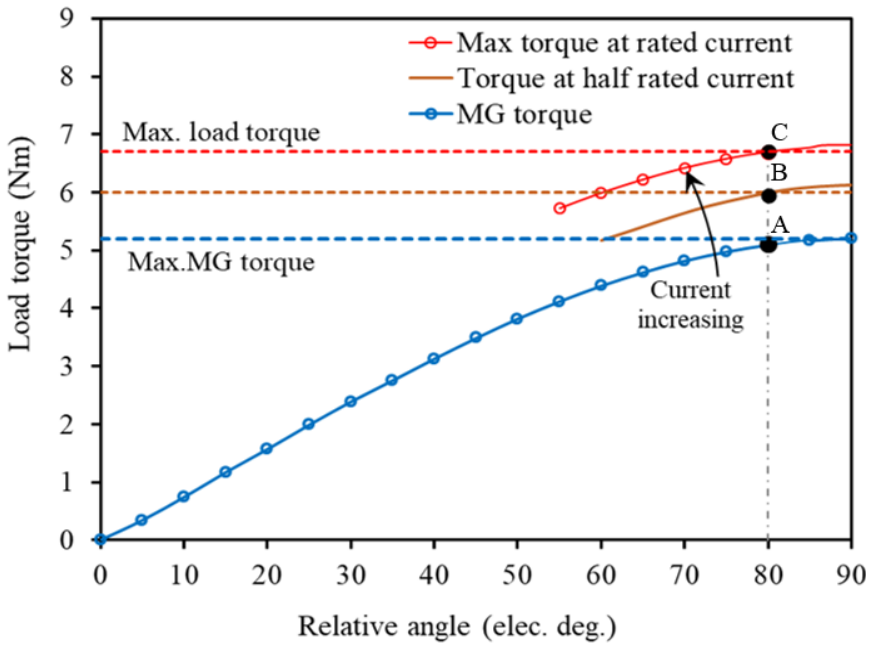

Fig. 4.29 Torque – relative angle limits of the proposed machine.

As the ICE is operating, its power is delivered to the wheels through the MG. During which operating mode the battery can be charged by the back EMF induced in the stator windings. Moreover, the HSR and LSR positions can be measured by resolvers to determine the relative angle during the machine operation. However, when the wheels' torque increases and reaches the maximum limit of the MG, which can be also estimated by the relative angle (i.e. 80 elec. deg.), a current is applied to the stator winding to overcome the load torque (Motoring mode). In other words, the current obtained by the inverter is utilised to maintain the operation point at the maximum relative angle. Therefore, the current is increased and decreased to keep the operating point moving between points A and C according to the load torque, as indicated in Fig. 4.29. The alignment between the d-axis of the armature current flux and the d-axis of the LSR PM can be obtained by adjusting the current angle to be the same as the LSR angle obtained by the resolver. In the last operating stage, when the torque applied to the wheels decreases under point A. In this case, the stator current is reduced by the current controller to zero and the machine returns to the MG and generation operating mode.

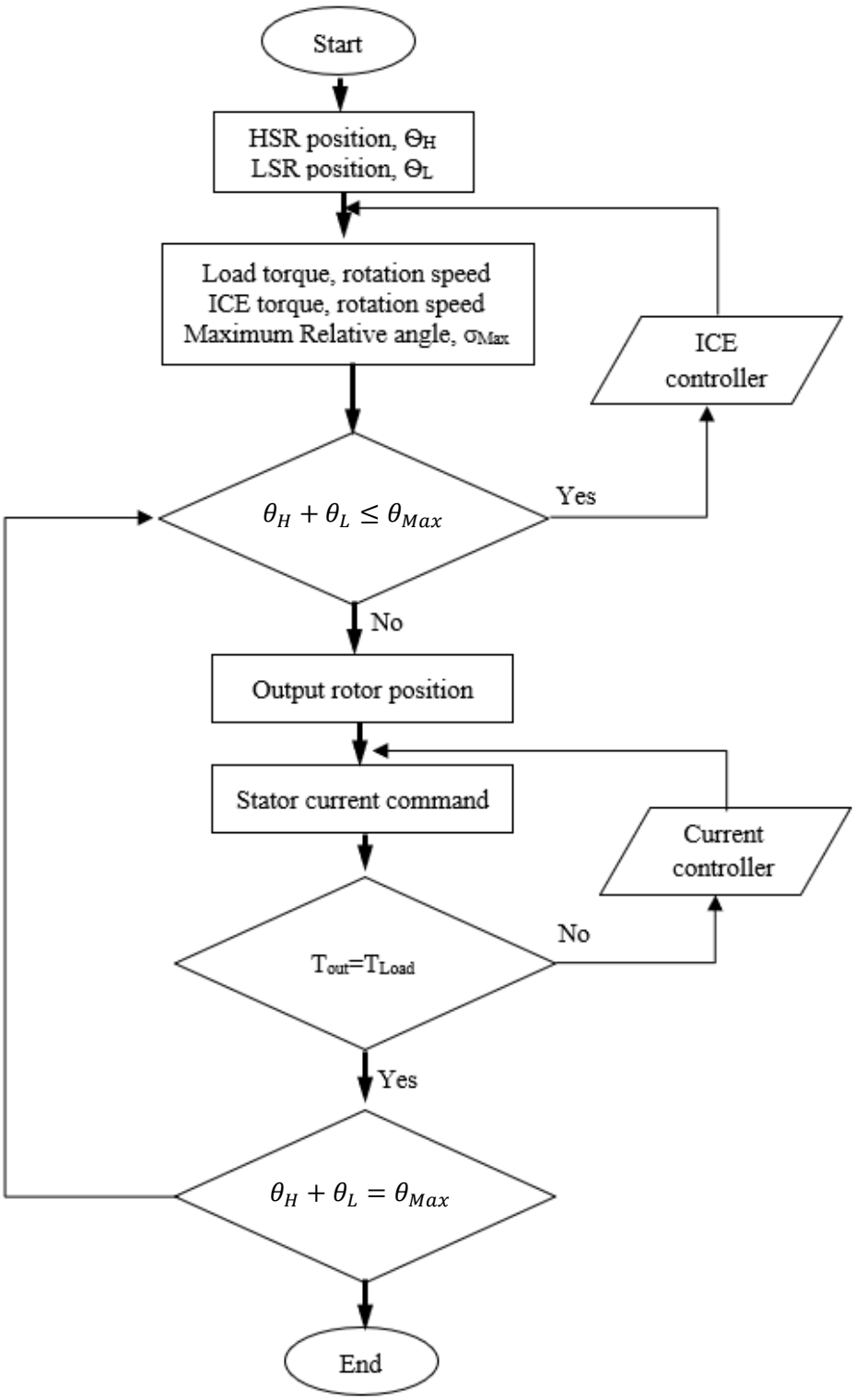

Fig. 4.30 Control scheme of AFMGPM machine.

4.5 Summary

In this chapter, the new axial flux magnetically geared machine for power split applications is investigated. Combining an axial magnetic gear with a PM machine results in a new magnetically geared machine which is capable of splitting or mixing the machine input power. Furthermore, various operating modes of the proposed topologies were studied and investigated. It has been shown that the mechanical input torque applied on either HSR or LSR can be scaled up or down by utilising the proposed AFMGPM. Moreover, the output torque transferred by magnetic gearing effect can be increased by the armature current torque. Furthermore, the electric input power can be split into two mechanical output torques. The performance comparisons between MG12/5-7 and MG12/4-8 under different operation modes show that both topologies have significant torque density at no-load and full-load conditions. Nevertheless, MG12/4-8 has lower torque and higher torque ripple compared to MG12/5-7. Moreover, regarding iron losses and PM losses, a comparison between both topologies at no-load and on-load at different rotor speeds is also performed. It has been found that MG12/5-7 has trivially higher core losses as well as PMs eddy current losses. More stator flux and greater magnet volume are the main reasons for the extra losses generated within MG12/5-7 geometry. Furthermore, with the rise of the machine load, the output torque can be amplified by the armature current torque with the aid of the current angle control which can be estimated from the output rotor position. In general, both topologies have high torque densities, and both can realise the power split function in HEVs whereby the proposed machine is capable of decoupling torque and speed between the conventional ICE and the drive. The developed torque can be maximised by controlling the phase difference between the armature current and the LSR back EMF waveforms to be zero.

CHAPTER 5

INFLUENCE OF STATIC AND DYNAMIC ROTOR/STATOR MISALIGNMENTS IN AXIAL FLUX MAGNETICALLY GEARED MACHINES

5.1 Introduction

Axial flux PM machines have a unique shape in which the small separation between the rotor plate and the stator face can be adjusted by an accurate bearing manufacturing. However, manufacturing faults must be considered in axial machines assembling process [GUO17]. Similar to conventional PM machines, axial flux magnetically geared machines are more susceptible to manufacturing imperfections and structural deformations which may deteriorate the machines' electromagnetic performance such as output torque, and introduce vibration and noise [GAS09]. Therefore, it is necessary to investigate the influence of manufacture tolerances on the performance of this type of machine.

For most PM machines, rotor eccentricity is the most common issue, and can be classified into static, dynamic (rotating) or combined eccentricity. Taking a radial flux PM (RFPM) machine as an example, static eccentricity exists when the rotating axis of the rotor is shifted from the axis of the stator and the smallest air-gap is fixed at one specific position. If dynamic eccentricity exists in the machine, however, the position of the smallest air-gap changes as the rotor rotates [ZHU13a].

The influence of rotor eccentricity in RFPM machine has been widely investigated in recent years. In [ZHU13b], its influence on back-EMF and torque of a PM brushless machine is analysed. The study indicates that static and dynamic eccentricities result in unbalanced three phase back-EMFs without affecting their harmonics. In [ZHU14], the impact of static and dynamic eccentricities on RFPM machines with different slot/pole combinations is examined. The study states that machines with closely similar numbers of stator slots and rotor poles are more sensitive to the effects of eccentricity than those with a larger difference between stator slot and rotor pole numbers. In [WU13], unbalanced magnetic force (UMF) caused by rotor eccentricity in radial PM machines has been investigated. It shows that, PM machines having

asymmetrical stator windings, the magnitude of UMF increases with the pole number due to static-dynamic rotor eccentricities.

In addition to rotor eccentricity and due to their unique geometry, AFPM machines have more possible types of manufacture tolerances, such as rotor/stator axis misalignment, since the stator and rotor are axially arranged. Rotor eccentricity in AFPM machines can be defined as angular rotor misalignment in which the rotor tilts with respect to the stator. On the other hand, when the rotor axis is shifted radially with respect to the stator reference axis, the rotor eccentricity can be defined as rotor/stator axis misalignment [THI12]. With reference to AFPM machines, the influence of rotor eccentricity has also been investigated in a number of papers [MIR12a], [MIR12b]. The influence of rotor/stator axis misalignment on AFPM machines was initially investigated in [MIR12a]. In [MIR12b], the effect of static rotor angle misalignment on air-gap flux density, back-EMF and the force of a single sided AFPM machine is investigated. The study shows that rotor angular misalignment leads to distorted air-gap flux density distribution, unbalanced back-EMF and uneven force. The effect of rotor/stator misalignment on the cogging torque of a single-sided AFPM machine is discussed and experimentally verified in [THI16]. The results reveal that rotor misalignment creates more cogging torque harmonics, which are sidebands of the fundamental harmonic. Furthermore, in [GER14], the influence of rotor imperfections on the forces and torques acting on the YASA machine is briefly investigated. The study and experimental results show that the rotor angular and axis misalignments significantly affect the rotor force and torque. Moreover, rotor defects increase the force on the machine stator due to the unbalanced force produced by the rotors. Furthermore, in terms of the YASA machine, the impacts of static and dynamic rotor angular and axis misalignments on no-load performance are investigated in [GUO17]. An analytical method and experimental test are utilised to analyse the machine back-EMF under rotor misalignments. The study indicates that angular misalignment has a minor effect on the machine back-EMF. However, static and dynamic axis misalignments change the amplitude and the phases of the machine back-EMF.

The possible rotor/stator misalignments for the magnetically geared machine are obtained in Fig. 5.1. In this Chapter, only LSR/stator axis and angular misalignments are considered. Since rotor misalignment has not been investigated for AFMG machines, the influence of static and dynamic LSR/stator misalignments on machine performance is investigated using 3-D FEA. The cogging torques of HSR, LSR, and air-gap flux densities as well as back-EMFs are studied. Performance comparisons of the machine under healthy, static and dynamic misalignment conditions are

conducted. Additionally, the influence of LSR /stator misalignment on the transferred MG and on-load torques are studied and compared with the healthy condition. Finally, the force exerted in the machine parts is investigated and compared.

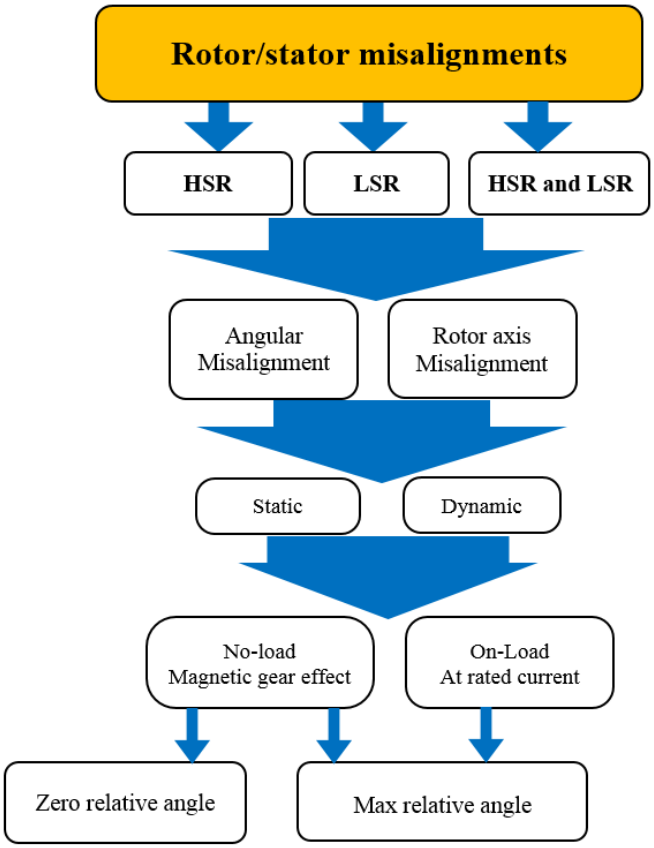

Fig. 5.1 Rotor misalignment categories of AFMG machines.

5.2 Static and dynamic LSR/stator misalignments

In general, there are two potential types of rotor/stator misalignments in axial flux machines. The first is axis misalignment, which occurs when the rotor center line is offset from the center line of the stator [MIR12b]. The second is angular misalignment, in which the rotor and stator are un-parallel. In this case, the rotor axis is angularly deviated with respect to the center of the stator, and the air-gap width is uneven Fig. 5.2. The two types of misalignment are further categorised into the following: static misalignment and dynamic misalignment. The static axis misalignment may occur when the rotor bearing housing flange is defected; therefore, the LSR shaft geometry center is offset in relation to the stator geometry center. In this case, the LSR rotates on its shaft's reference axis, as shown in Fig. 5.2 (a, b). Moreover, dynamic misalignments may occur, in which the LSR geometry center is offset with reference to the center of the stator's geometry and rotor shaft. In this case, the LSR rotates around the stator geometry center (reference axis) due to a

failed connection between the rotor disk geometry and its own shaft, as shown in Fig. 5.2 (c,d) [LI16].

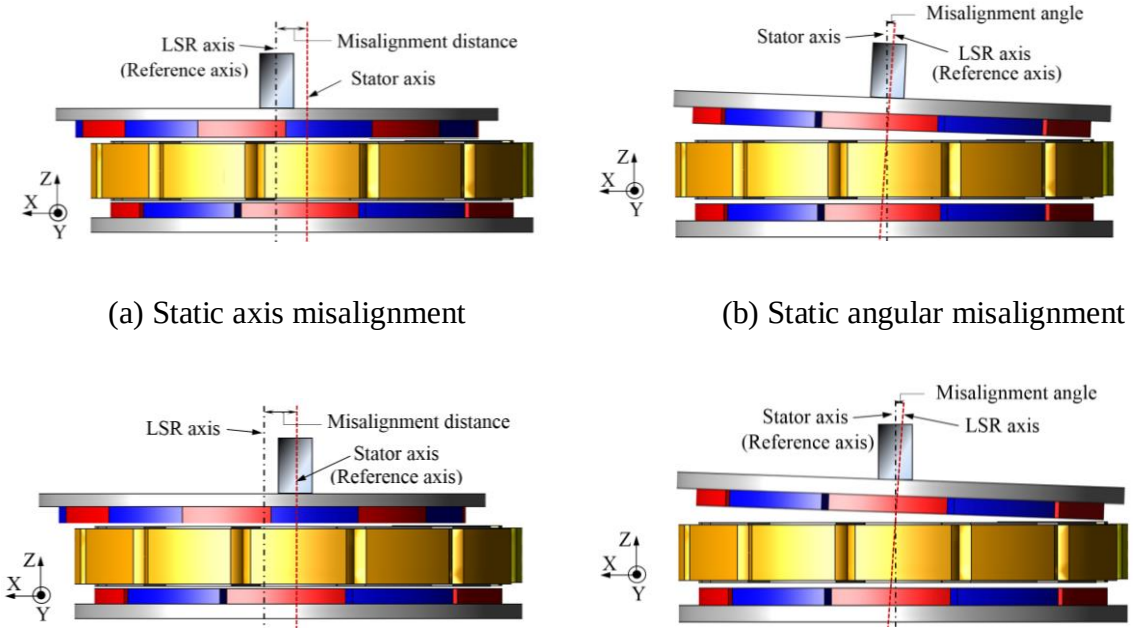

(a) Static axis misalignment (b) Static angular misalignment

(c) Dynamic axis misalignment (d) Dynamic angular misalignment

Fig. 5.2 Models of LSR/stator misalignment.

5.3 Influence of LSR/stator axis misalignment on machine performance

With the aim of investigating the influence of LSR/stator axis misalignment on machine performance, 3-D FEA is usually used. The LSR is offset by 2 mm in the x-axis, the LSR magnet is offset over the stator outer diameter on one side and the stator outer diameter is offset over LSR PMs on the opposite side. The machine performance (i.e. cogging torque, flux density, back EMF and torque) is investigated under static and dynamic misalignments with reference to the normal, healthy condition.

5.3.1 Cogging torque.

One of the decisive factors, which should be studied in the analysis and design of PM machines, is cogging torque. The cogging torque T_C exists in PM machines due to the interaction between the PM magnetic flux harmonics and the angular variations of stator slots' reluctance and can essentially be described as in [AYD03].

$$T_C(\theta_m) = -\frac{1}{2}\emptyset_g^2 \frac{dR}{d\theta} \tag{5.1}$$

where $\emptyset_g$ and R are the flux and reluctance of the air-gap, respectively, and θ is the rotor position. In addition, the cogging torque waveform of a PM machine can be expressed as in [ZHU00].

$$T_C = \sum_{k=1}^{\infty} T_{mk} \sin(kN_c\theta + \varphi_k) \tag{5.2}$$

where T_{mk} and φ_k are the magnitude and phase of the k^{th} harmonic component, respectively. The cogging torque amplitude differs depending on the stator and rotor pole combinations. It has been shown that PM machines with rotor pole and stator slot numbers differing by one have significantly smaller cogging torque compared to those differing by two at normal condition [ZHU13a]. Moreover, numerous methods have been investigated for cogging torque minimisation in axial flux machines [AYD07]. However, the cogging torque is significantly exacerbated by the unavoidable manufacturing tolerance [GAS09]. For the introduced magnetic geared machine, the impact of static and dynamic LSR/stator axis misalignments on two rotors' cogging torque is investigated. To calculate the cogging torque, the magnetic gear average transferred torque between both rotors should be zero. This can be achieved by aligning one LSR pole with one HSR pole (whereby the relative angle between HSR and LSR is zero). Moreover, the HSR is driven with a constant speed of 400 rpm while the LSR speed is 285.5 rpm. As such, the average torque produced from the magnetic gearing effect between both rotors is always zero. Furthermore, it should be noted that since the machine has two rotors, the LSR and HSR cogging torque periods are calculated with respect to their individual mechanical cycles.

Fig. 5.3 and Fig. 5.4 show the LSR and HSR cogging torques at static and dynamic misalignments with the reference to the healthy condition, respectively. It is clear that LSR and HSR cogging torques for the healthy model have periodic components with fundamental harmonics of 84th and 60th order, respectively, which can also be estimated by calculating the smallest common multiple between n_s and the rotor pole $2p$ [ZHU00]. However, misalignment of the LSR/stator results in LSR and HSR cogging torque modulation in which additional cogging torque harmonics are created. It can also be noticed that native harmonics of the 14th order for LSR and of the 10th order for HSR appear due to static rotor misalignment (the multiple of rotor poles) while the native harmonics of the 12th order for LSR and the 9th order for HSR appear due to dynamic rotor misalignment, as shown in Fig. 5.3(b) and Fig. 5.4(b).

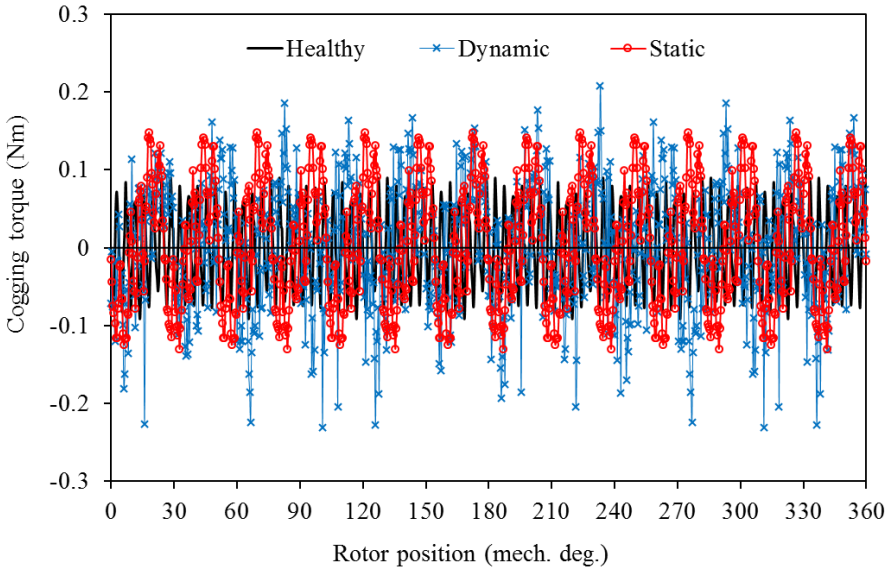

(a)) Waveforms

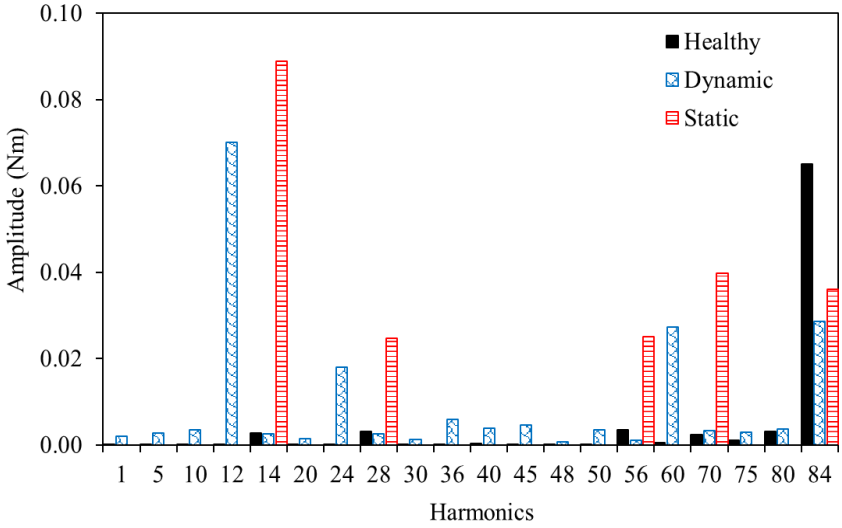

(b) Harmonic spectra

Fig. 5.3 Comparison of LSR cogging torques at different LSR misalignment cases.

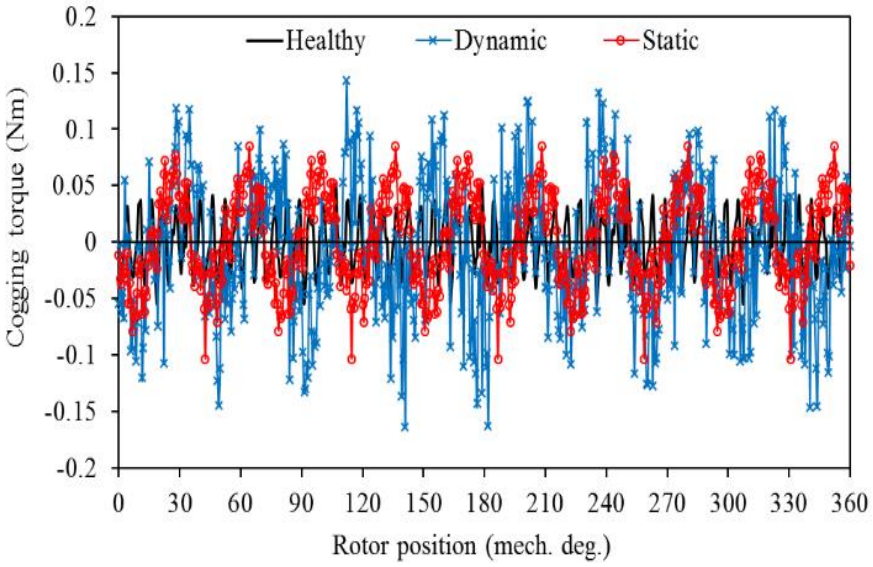

(a) Waveforms

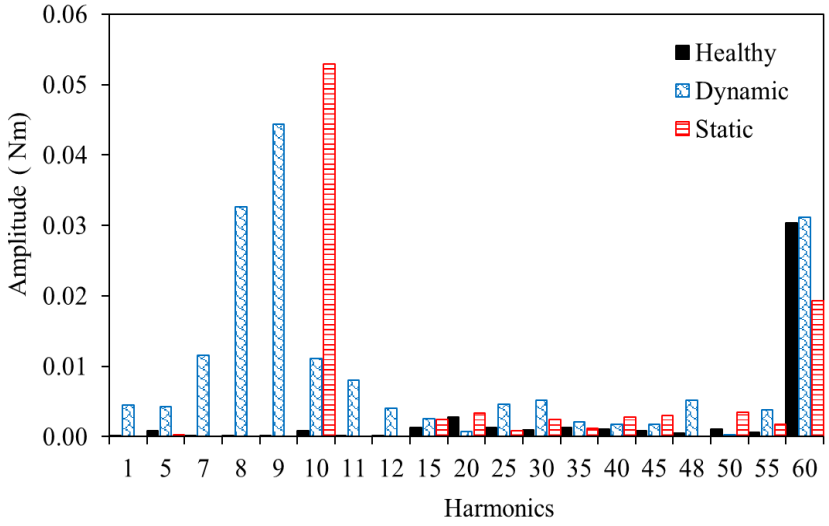

(b) Harmonic spectra

Fig. 5.4 Comparison of HSR cogging torques at different LSR misalignment cases.

The cogging torque amplitudes for LSR and HSR at healthy conditions are different due to different number of rotor poles and hence differing air-gap flux, as stated by (5.1) . On the other hand, in terms of rotor misalignment, during the rotation of the HSR and LSR, the timing of LSR pole/slot intersection is not symmetrical due to the shifted position of the rotor axis. Moreover, in terms of dynamic LSR misalignment, the torque arms for each rotor pole vary as the rotor changes its position [THI16]; therefore, the cogging torque waveform is distorted and the amplitudes of the existing harmonics are changed, which results in additional harmonics. According to (5.2), the additional harmonics are added to the existing harmonics, which results in obvious changes in the waveform of the cogging torque.

5.3.2 Air-gap flux density

To reveal the reason for the cogging torque being affected by rotor misalignment, the flux densities at initial rotor position over the circumferential path of the middle air-gap corresponding to LSR and HSR for all conditions are calculated and compared in Fig. 5.5 and Fig. 5.6, respectively. It can be seen that the flux density of the healthy condition machine evidences odd harmonics in addition to the fundamental order, e.g. 5^{th}, 9^{th}, 17^{th} and 19^{th} harmonics for LSR air-gap and 7^{th}, 15^{th}, 17^{th} and 19^{th} harmonics for HSR. When LSR misalignment exists, the non-uniform reluctance is greater on the side at which the rotor pole is offset over the stator's outer diameter and smaller at the opposite side as a consequence of the fringing effect, (Fig. 5.7). Therefore, the non-uniform reluctance results in air-gap flux distortion. The amplitudes of the fundamental harmonics of LSR flux (7^{th}) and HSR (5^{th}) are obviously reduced due to the fringing effect. Moreover, the number of additional field harmonics is increased due to static and dynamic LSR misalignments, as can be seen in Fig. 5.5(b) and Fig. 5.6 (b). The additional flux sideband harmonics around the LSR flux fundamental harmonics (i.e. 6^{th}, 8^{th}) are significantly increased. Moreover, the air-gap flux density waveform shown in Fig. 5.5(a) is shifted due to the rotor shifting with respect to the circumferential middle circle over the air-gap. On the other hand, the change in the HSR flux density is slighter compared to that of LSR flux density. The fundamental sideband harmonic orders (4^{th}, 6^{th}) are marginally increased, as can be seen in Fig. 5.6 (b). Therefore, it can be concluded that for PM machines, the flux distribution in the air-gap is essentially non-uniform, which is the reason for cogging torque production. However, the air-gap flux distortion caused by rotor misalignment contributes more undesired harmonic contents, ultimately resulting in an increase in the machine cogging torque.

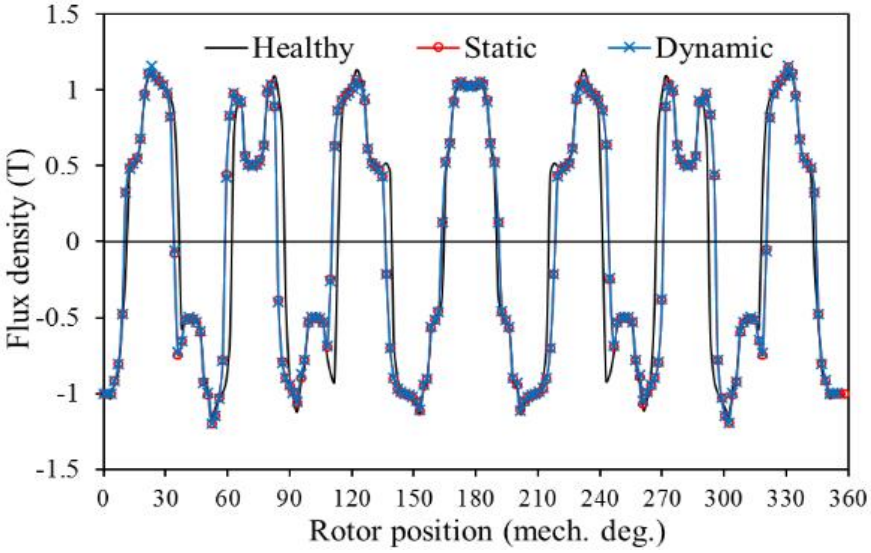

(a) Waveforms

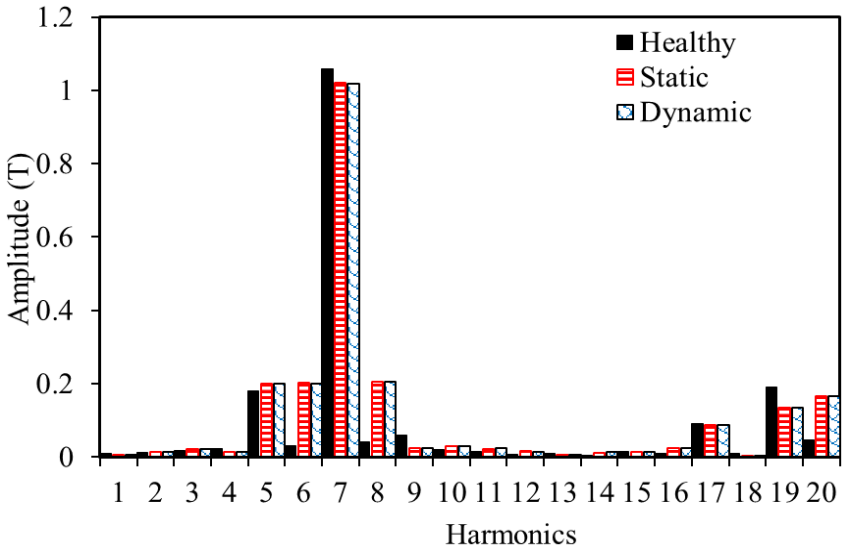

(b) Harmonic spectra

Fig. 5.5 Comparison of flux density in the middle of the LSR air-gap at initial position for different LSR axis misalignment cases.

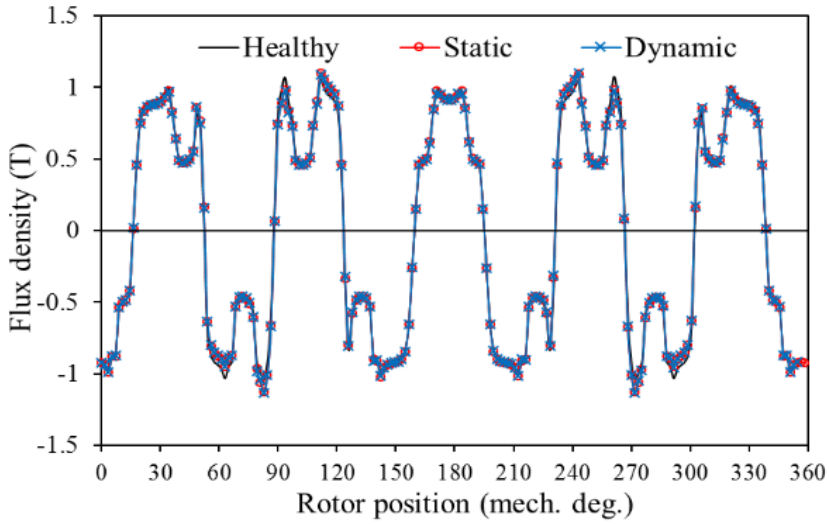

(a) Waveforms

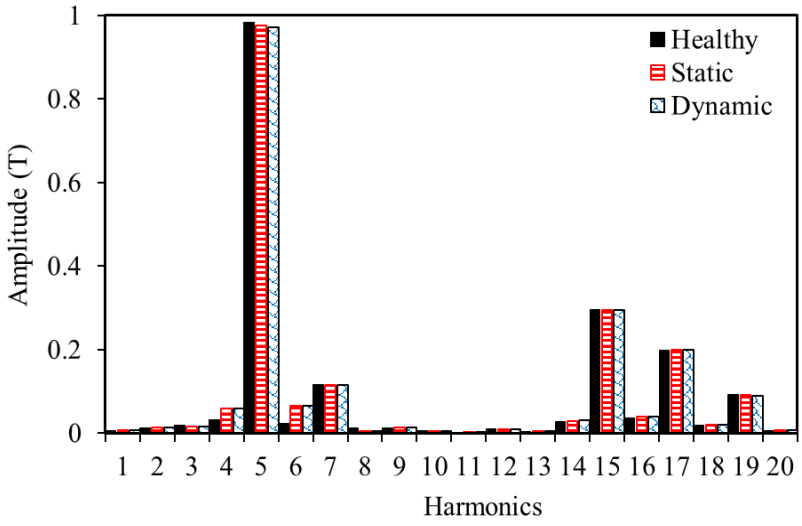

(b) Harmonic spectra

Fig. 5.6 Comparison of flux density in the middle of HSR air-gap at initial position for different LSR axis misalignment cases.

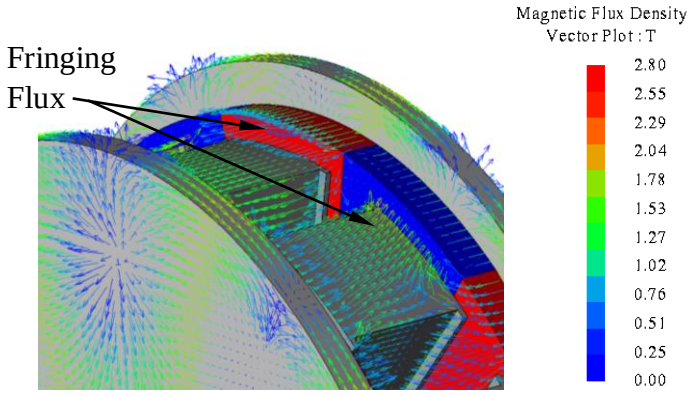

Fig. 5.7 Fringing flux due to shifting of the LSR.

5.3.3 Back EMF

The influence of both static and dynamic LSR axis misalignments on the machine back EMF is also investigated. Fig.5.8 indicates the calculated 3-phase back EMF waveforms and their spectra in the static misalignment case. The back EMF waveform at static misalignment is slightly changed compared to healthy back EMF. Static misalignment results in slightly unbalanced 3-phase back EMF waveforms. More specifically, the amplitudes of 3-phase EMFs are unequal: the back EMF of phase A has the largest amplitude: the largest amplitude phase depends on the direction of rotor/stator misalignment. Unbalanced back EMF is due to unbalanced flux distribution over the LSR air-gap attributable to rotor misalignment. Moreover, as can be shown in Fig.5.8 (b), static axis misalignment only changes the harmonic component amplitude of the back EMF with no changes to the harmonic contents. On the other hand, for dynamic LSR misalignment, the 3-phase back EMF waveforms are slightly modulated: unbalanced for a full electrical cycle, but balanced with respect to one mechanical cycle in which the 3-phase EMF fundamental harmonic amplitudes are equal, as shown in Fig.5.9 (a). From Fig. 8 (b), it can be seen that dynamic axis misalignment affects the harmonic amplitude and contents since more harmonics (i.e. 5^{th} and 9^{th}) appear due to rotor rotation at dynamic misalignment. In general, the decreases in 3-phase back EMF amplitudes are slight; therefore, more significant decreases are expected in the case of higher rotor misalignment levels.

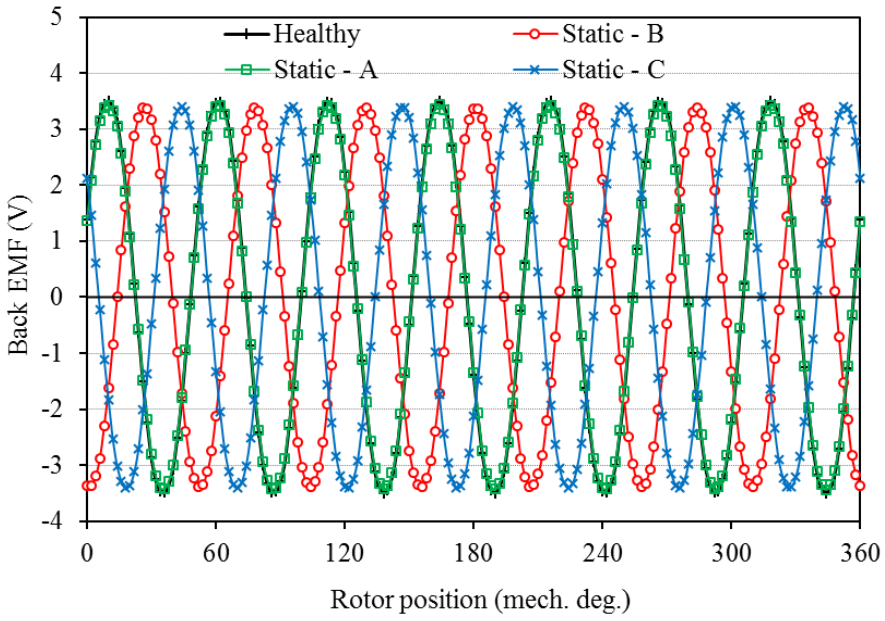

(a) Waveforms

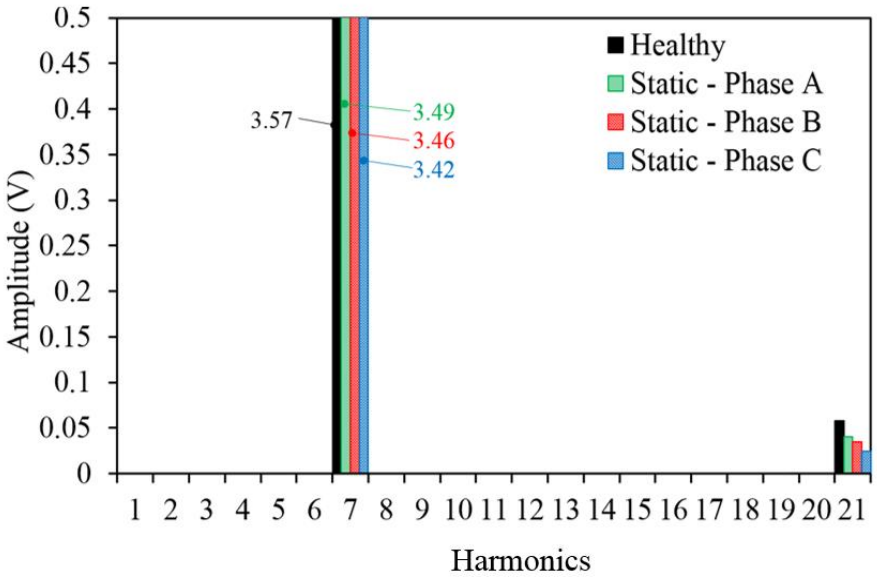

(b) Harmonic spectra

Fig.5.8. 3-phase back EMFs at static LSR axis misalignment.

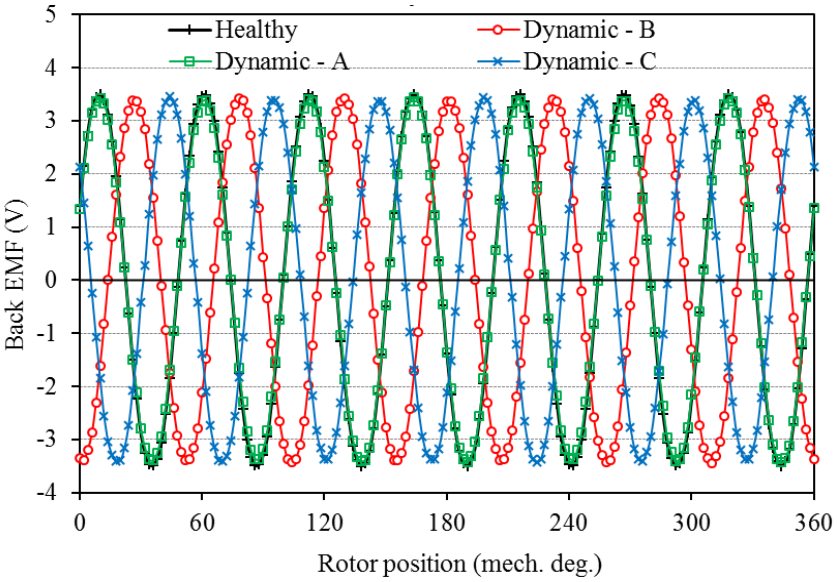

(a) Waveforms

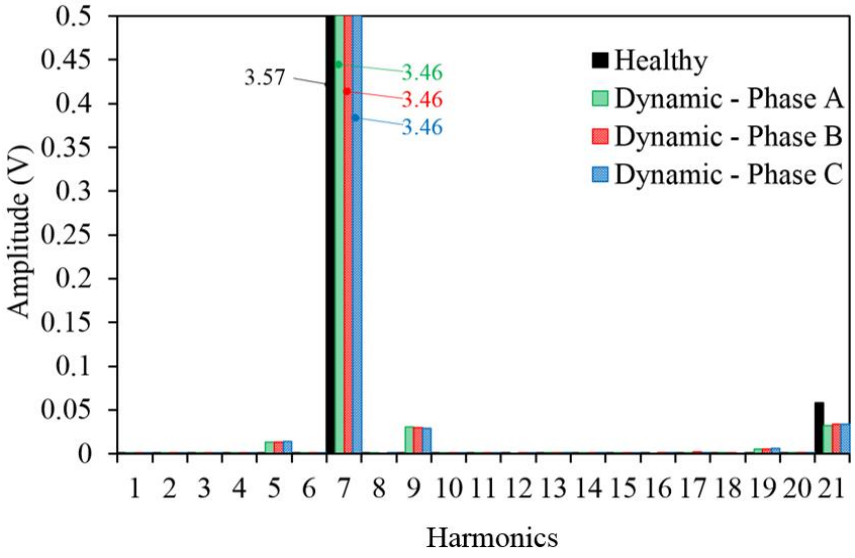

(b) Harmonic spectra

Fig.5.9 3-phase back EMFs at dynamic LSR misalignment cases.

5.3.4 Torque

The HSR and LSR torques produced by both gearing effect and armature current of the proposed machine at static and dynamic LSR/stator axis misalignments are studied and compared. The torque transferred by the magnetic gear is calculated at maximum relative angle between both rotors (90 elec. deg.) at no current. Moreover, the machine on-load torque can be obtained when rated current is applied to the stator winding at maximum relative angle between both rotors. Fig. 5.10 shows the no-load magnetic gear torque response for static and dynamic LSR misalignments

compared to the healthy torque performance. When LSR/stator axis misalignment exists, the gearing effect torque of both rotors is significantly decreased, as shown in Fig. 5.10(a). Moreover, the static and dynamic misalignments have the same effect on the torque performance. The decrease in machine torque is due to the decrease in the flux density of the LSR air-gap. Furthermore, the torque ripple for the healthy condition of both rotors is relatively small (i.e. 2%); nevertheless, LSR static and dynamic misalignments increase the torque ripple of both rotors (LSR 4%, HSR 6%), as shown in Fig. 5.10(b). On the other hand, the LSR misalignments have the same effect on machine on-load torque as no-load torque. The change in the machine torque here occurs for the same reason as the no-load case, as can be seen in Fig. 5.11.

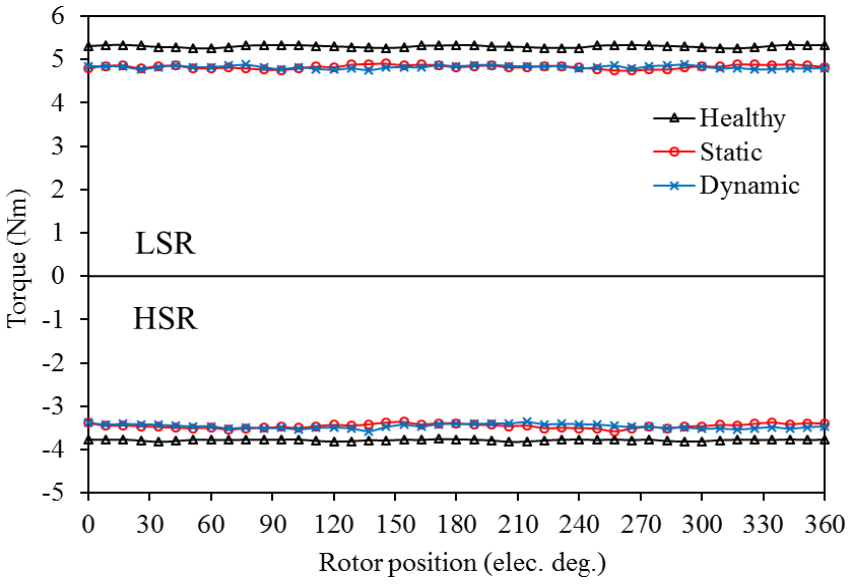

(a) Waveforms

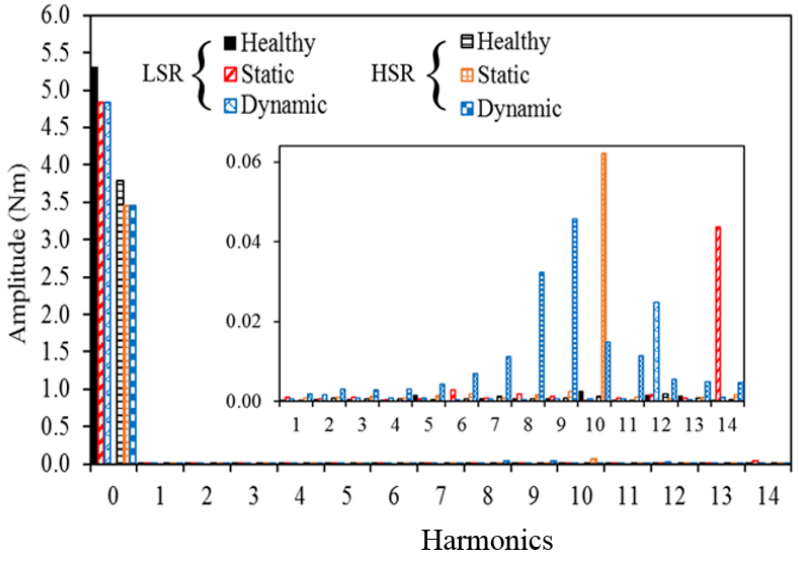

(b) Harmonic spectra

Fig. 5.10 Comparison of no-load magnetic torques at different LSR misalignment cases.

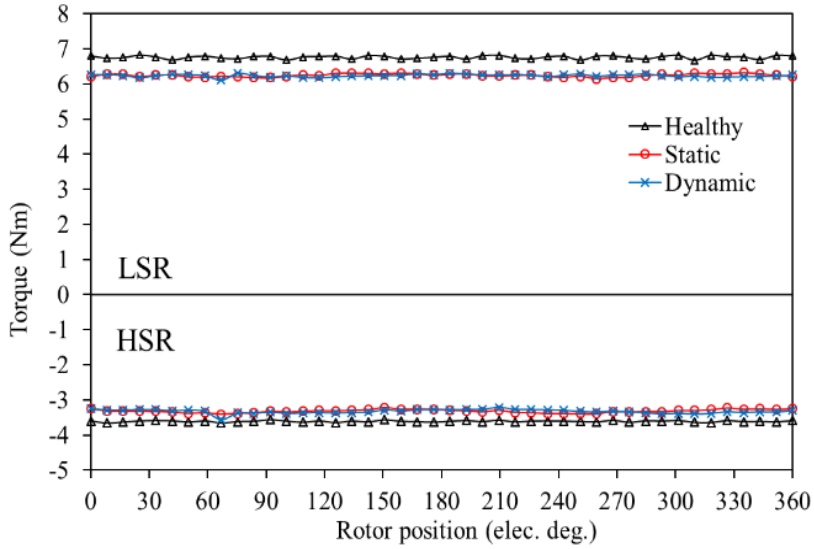

(a) Waveforms

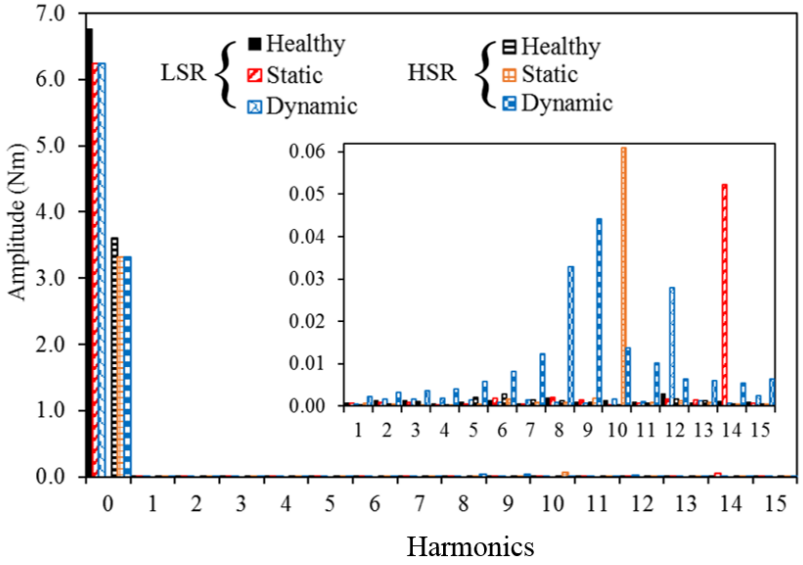

(b) Harmonic spectra

Fig. 5.11 Comparison of on-load torques at different LSR misalignment cases.

5.3.5 Unbalanced force

The magnetic force affecting the machine parts at LSR/stator axis misalignment is studied. The no-load magnetic force affecting the machine parts at LSR/stator axis misalignment is studied. The major force which should be considered in the machine analysis under rotor / stator misalignment is the attractive force between the rotor PMs and the stator core (the axial force). The resultant air-gap magnetic force, F_{axial}, that acts in the axial direction on the rotor due to the magnetic field distribution in the air-gap can be expressed as [HUA00]

$$F_{axial} = \frac{\alpha_p \, S_g \, B_g^2}{2\mu_o} \tag{5.3}$$

where α_p is the ratio of the magnet surface area with respect to the air-gap area, and S_g is the air-gap's surface area. For conventional internal stator axial flux machines, the magnetic forces between the stator and both rotors are equal due to the equal distribution of air-gap flux density. The force on one rotor is applied in the opposite direction to the other rotor. This results in an equivalent and approximately zero force being applied on the stator. However, since the proposed AFMGPM machine has two rotors with different pole numbers, an unbalanced force on the machine parts is inevitable. As a result, the unbalanced magnetic force applied on the stator is nonzero and has a specific value. Fig. 5.12 shows the comparison of the axial forces exerted on the machine rotors for one mechanical cycle at healthy, dynamic and static misaligned LSR conditions. It is worth mentioning that the force at no-load is calculated at maximum MG torque, with the relative angle between HSR and LSR being (90 elec. deg.). It can be seen that the average magnetic forces of HSR and LSR for the healthy model are unequal due to the unequal number of rotor poles. Moreover, the magnetic forces applied on the LSR are slightly decreased compared to the healthy topology due to the LSR axis misalignment. Moreover, as can be seen in Fig. 5.13, the force applied on the machine stator decreases since the force on the stator is the sum of both rotor forces, which are applied in opposite directions. Furthermore, the waveforms of the forces of the machine parts are slightly modulated due to the distorted flux distribution in the air-gaps.

The X-Y forces exerted on all parts of the topology at different misalignment conditions are calculated and compared in Fig. 5.14. It is clear that the forces in the x-direction applied on both rotors increase and the LSR force has one x-direction: the same direction as the LSR shifting. Moreover, the forces in the Y direction of all parts alternate over the rotor position and dramatically increase compared to the healthy topology. Furthermore, the force behaviour at dynamic axis misalignment for all parts is basically a repetition of the force behaviour at the static condition whereby the misalignment direction changes at each rotor position.

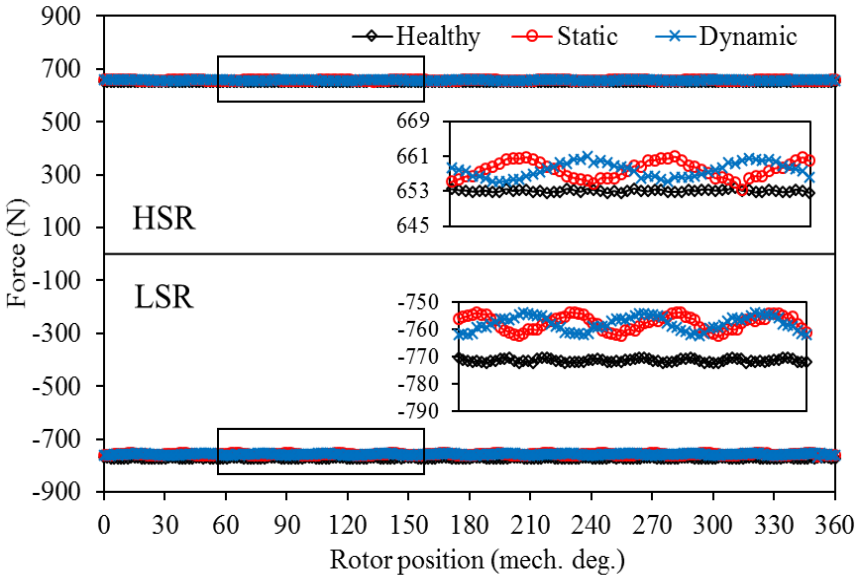

(a) Waveforms

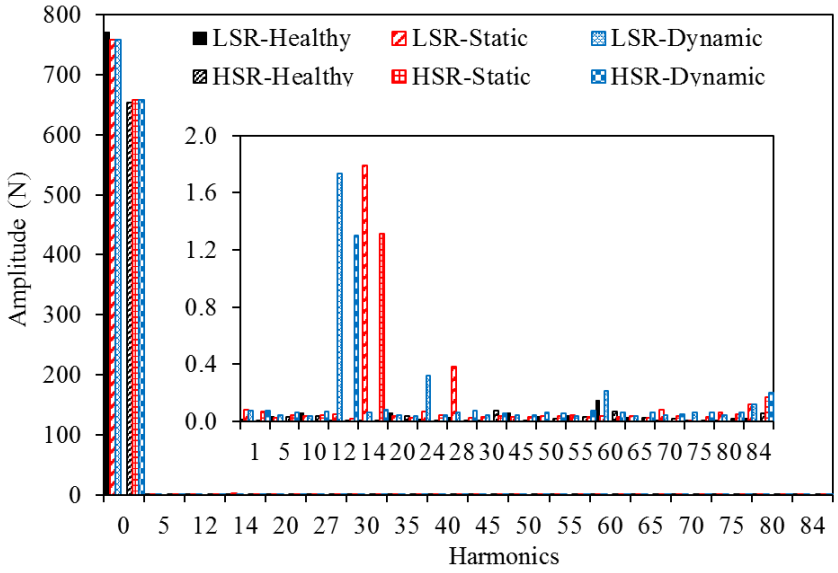

(b) Harmonic spectra

Fig. 5.12 Comparison of no-load magnetic axial forces exerted on the machine HSR and LSR at LSR axis misalignment.

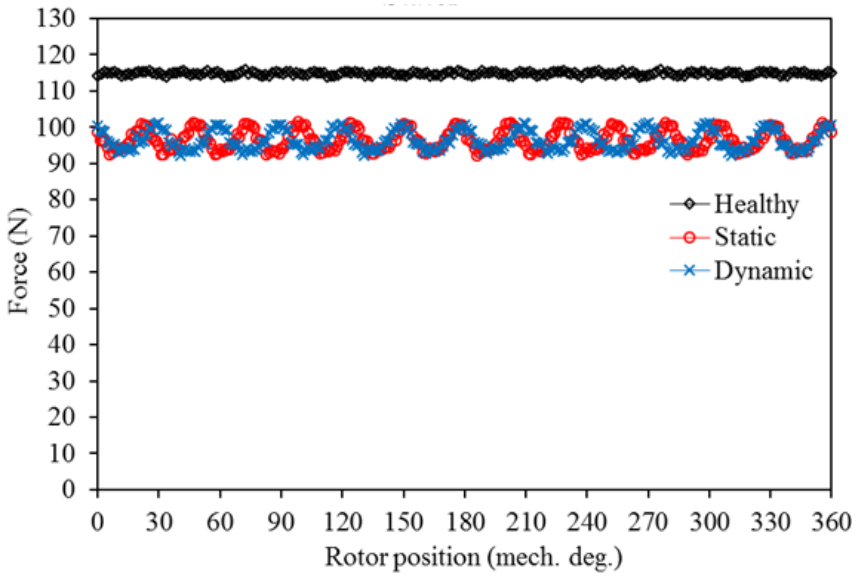

(a) Waveforms

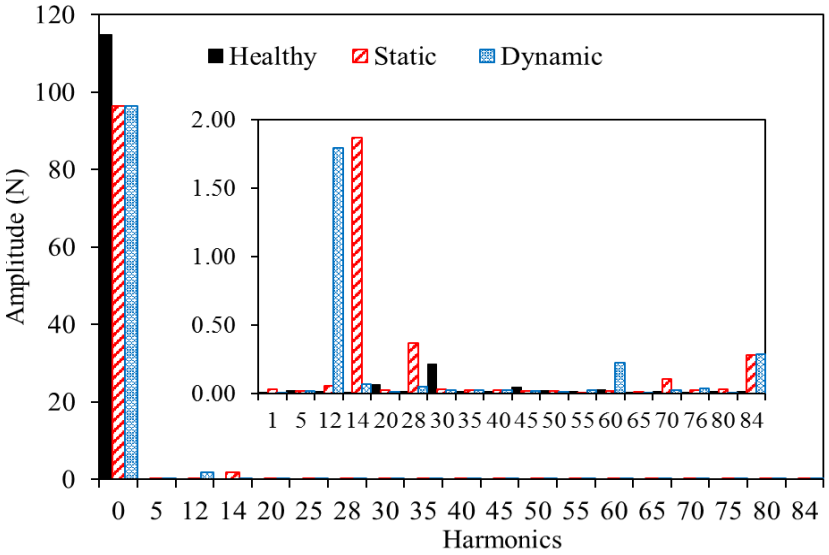

(b) Harmonic spectra

Fig. 5.13 Comparison of no-load magnetic axial forces exerted on the machine stator at LSR axis misalignment.

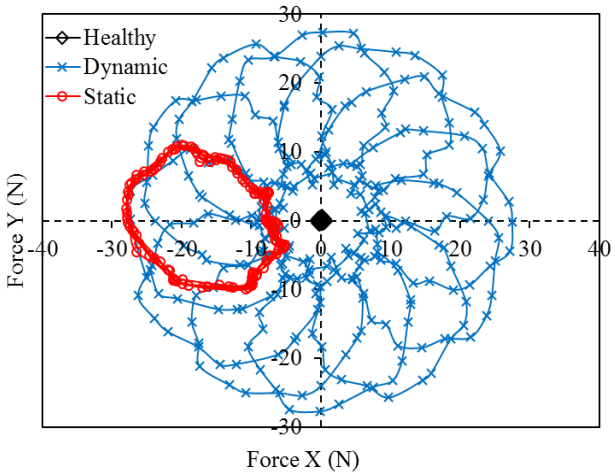

(a) LSR forces

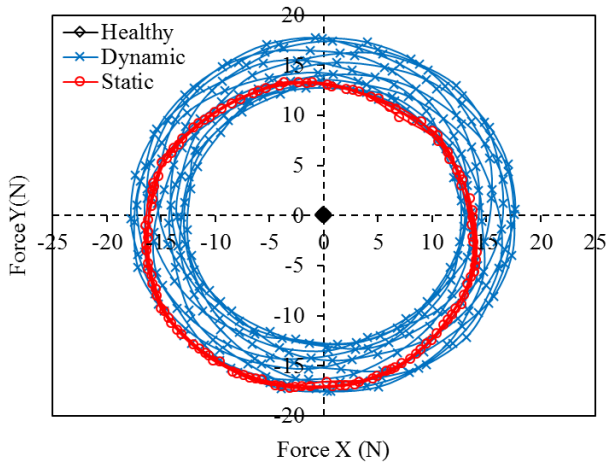

(b) HSR forces

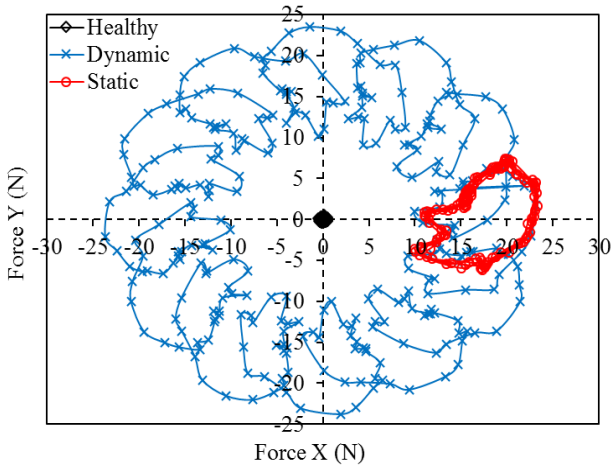

(c) Stator forces

Fig. 5.14 Comparison of no-load (x-y) magnetic forces exerted on the machine parts at LSR axis misalignment.

In addition, the forces on the machine parts are studied at on-load when the rated current is applied to the machine stator windings. Fig. 5.15 plots the on-load axial force applied on the machine rotors whereas Fig. 5.16 indicates the axial force exerted on the machine stator. It is clear from the results that static and dynamic axis misalignments at on-load have the same effect on the machine forces at no-load. In general, the force applied on the machine parts at healthy condition decreases due to the armature current flux. Fig. 5.17 indicates the x-y force components on the machine parts. It is evident that the x-y forces applied on the HSR and stator change slightly due to the LSR misalignment. In addition, the force variation on the LSR is of minor increment compared to the force at no-load condition.

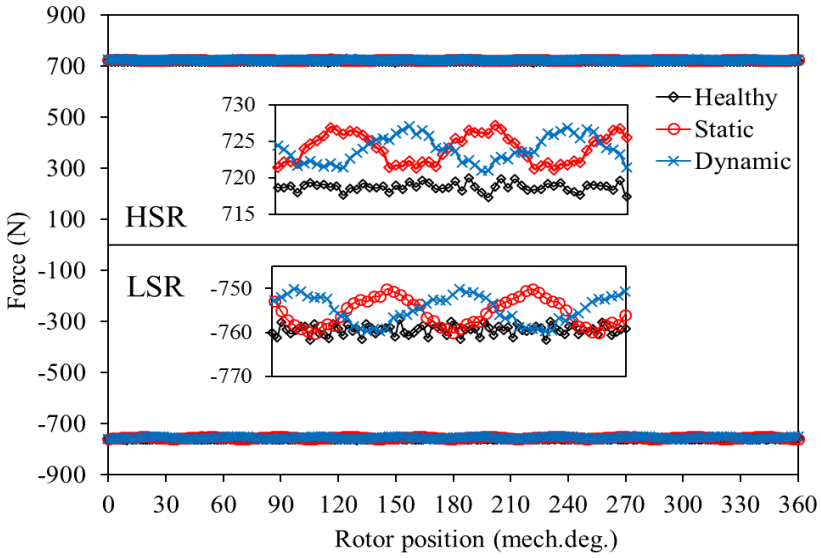

(a) Waveforms

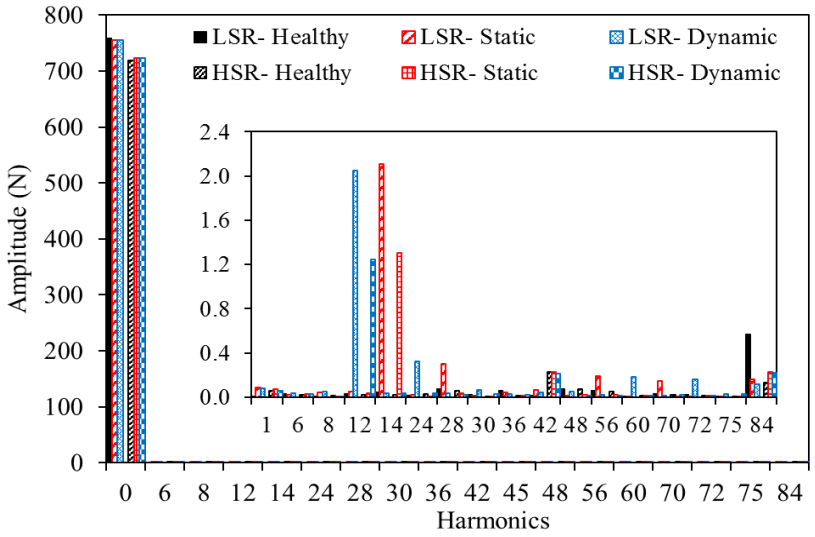

(b) Harmonic spectra

Fig. 5.15 Comparison of on-load magnetic axial forces exerted on the machine parts.

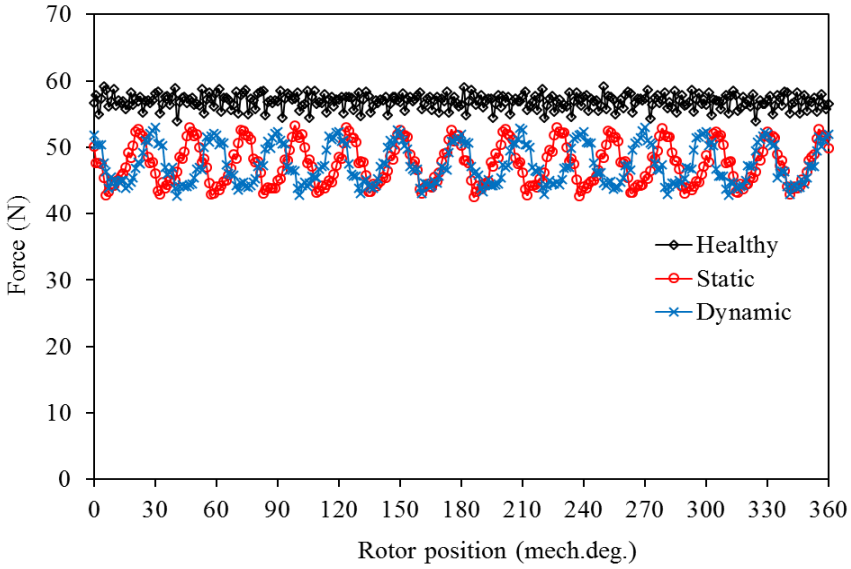

(a) Waveforms

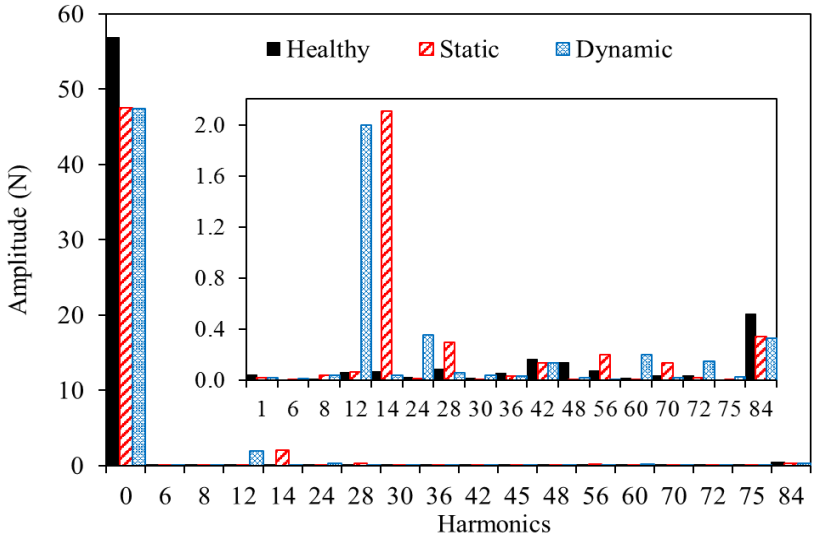

(b) Harmonic spectra

Fig. 5.16 Comparison of on-load axial forces exerted on the machine stator.

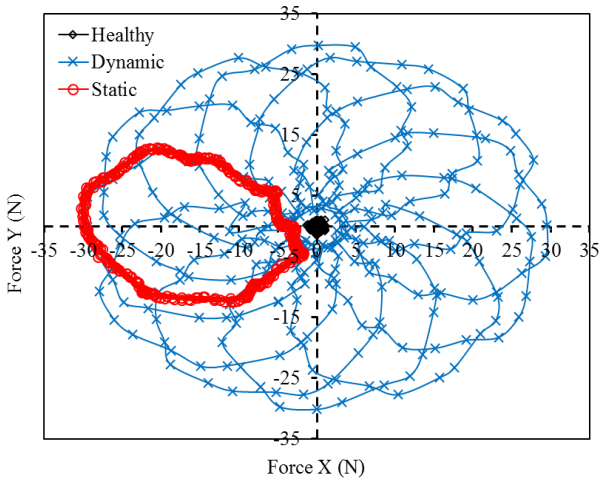

(a) LSR forces

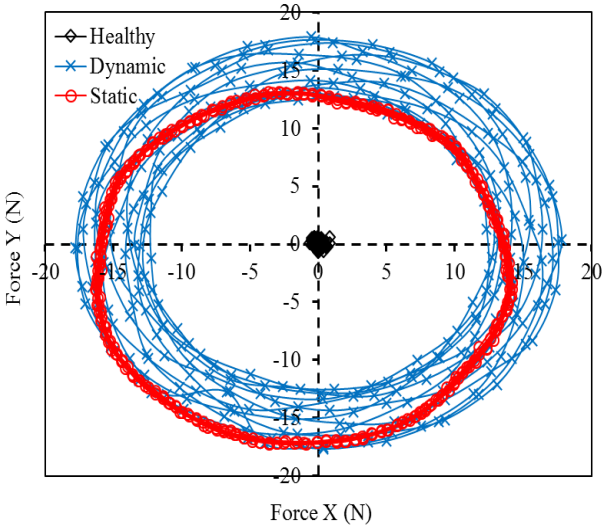

(b) HSR forces

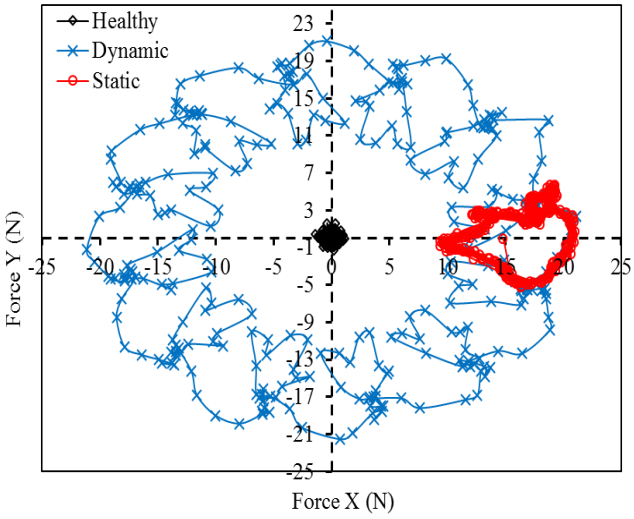

(c) Stator forces

Fig. 5.17 Comparison of on-load (x-y) forces exerted on the machine parts.

5.4 Influence of LSR/stator angular misalignment on machine performance

For axial flux machines, angular misalignment occurs when the machine rotor is nonparallel to the stator by a specific angle, as shown in Fig. 5.2. In this case, the air-gap thickness is non-uniform over the circumferential rotor direction. The minimum and maximum air-gap thicknesses are fixed over different rotor position at static angular misalignment, Fig. 5.2(b), while at dynamic angular misalignment, the gap thickness changes according to the rotor position, Fig. 5.2(d). Therefore, as can be seen in Fig. 5.18, the air-gap thickness G_o is uneven. Thus, the air-gap maximum thickness G_{max} and the minimum air-gap thickness G_{min} are exist due to LSR angular misalignment.

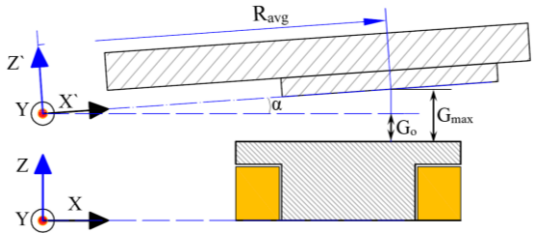

Fig. 5.18 Rotor angular misalignment.

In general, the angular misalignment factor of axial flux machines can be calculated as [MIR12a]:

$$\text{Misalignment factor} = \frac{G_{max} - G_{min}}{2G_0} \times 100\% \tag{5.4}$$

Therefore, the rotor misalignment angle α can be calculated as

$$\alpha = \sin^{-1}\left(\frac{G_{max} - G_o}{R_{avg}}\right) \tag{5.5}$$

In this study, the influence of LSR angular misalignment is investigated at LSR deviated by angle α of 0.5 degrees. Since the air-gap thickness and the average radius of 0.5 mm and 30 mm, respectively, are considered, the machine performance is studied at a misalignment factor of approximately 50%.

5.4.1 Cogging torque

Fig. 5.19 and Fig. 5.20 show the effect of LSR angular misalignment on the LSR and HSR cogging torques with reference to the healthy condition, respectively. It is clear that modulation appears on the LSR cogging torque in which additional cogging torque harmonics of the 14th order and of the 12th order are created due to static and dynamic LSR angular misalignments,

respectively. Moreover, the fundamental harmonic amplitudes of the LSR cogging torques decrease at static and dynamic LSR / stator angular misalignments. Nevertheless, the fundamental harmonic of the 60th order of HSR cogging torque increases at static angular misalignment and increases further due to dynamic misalignment. In general, static and dynamic angular misalignments have a minor effect on the machine HSR and LSR cogging torques compared to the cogging torque of the healthy condition.

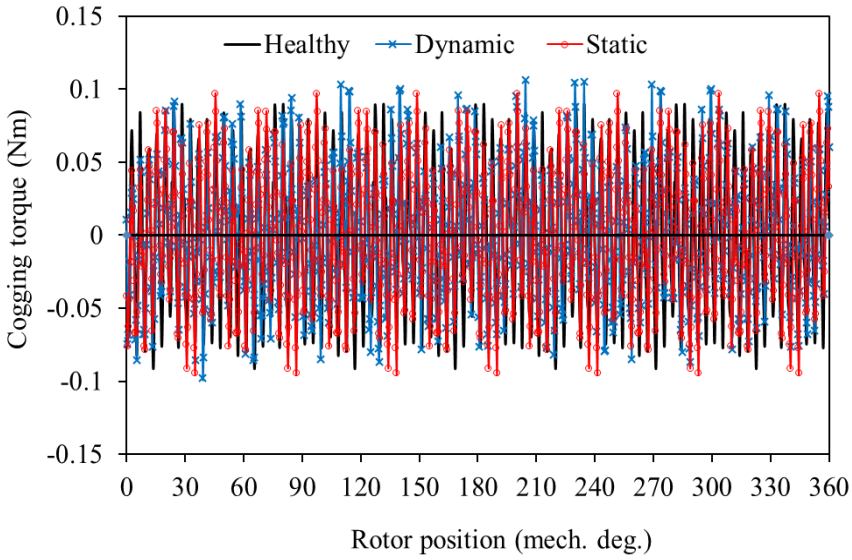

(a) Waveforms

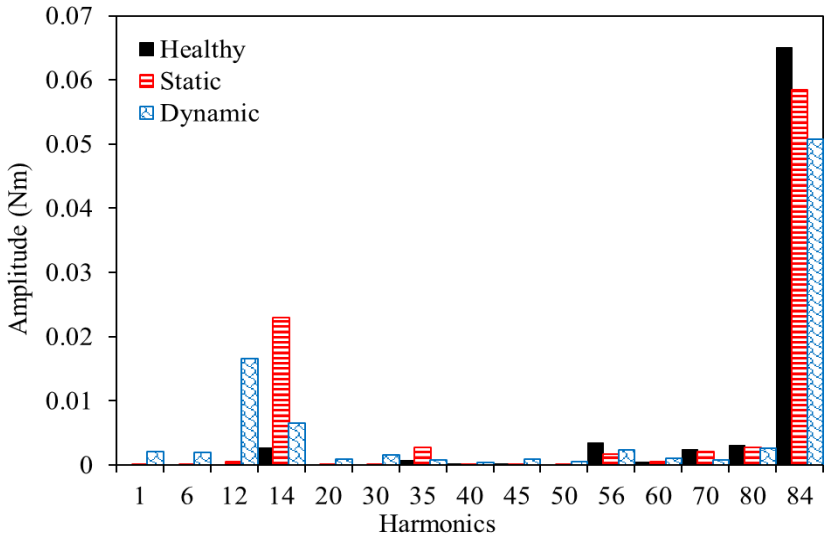

(b) Harmonic spectra

Fig. 5.19 Comparison of LSR cogging torques.

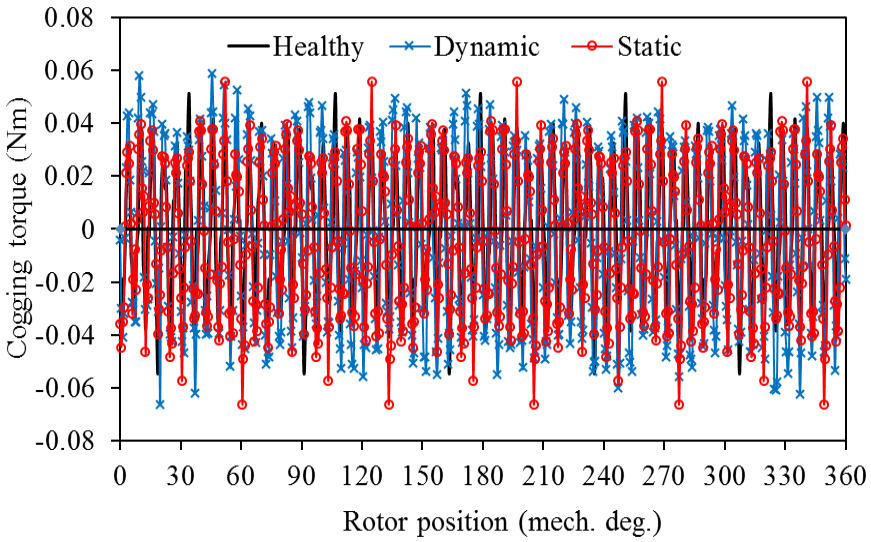

(a) Waveforms

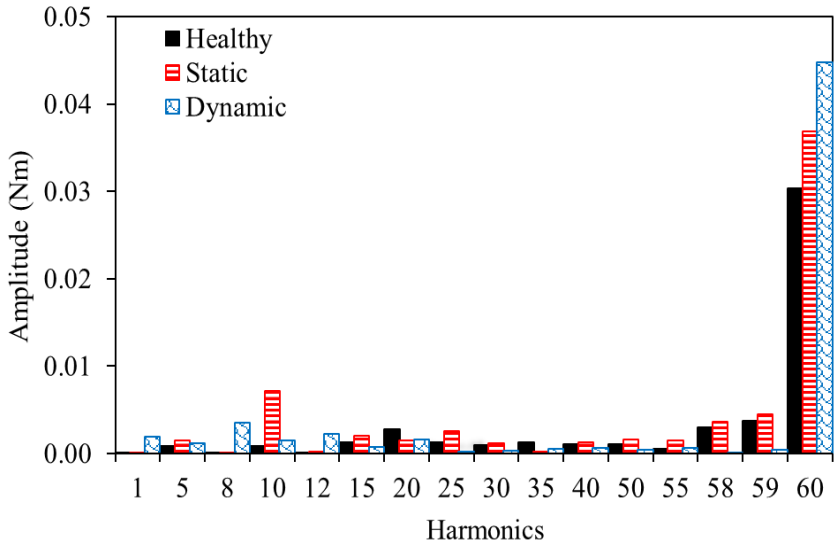

(b) Harmonic spectra

Fig. 5.20 Comparison of HSR cogging torques.

5.4.2 Air-gap flux density

Fig. 5.21 presents a comparison of axial flux densities at the LSR air-gap at static and dynamic angular misalignments. It should be noted that the flux density is measured over a circumferential path at mean air-gap radius and in the middle of the minimum air-gap thickness parallel to the stator geometry. Fig. 5.22 indicates the influence of LSR angular misalignment on the HSR air-gap flux density with reference to the healthy condition. It is clear that static and dynamic angular misalignments have insignificant effect in terms of changing the LSR flux density profile. Moreover, LSR angular misalignment has almost no effect on HSR air-gap flux density when compared to the healthy condition.

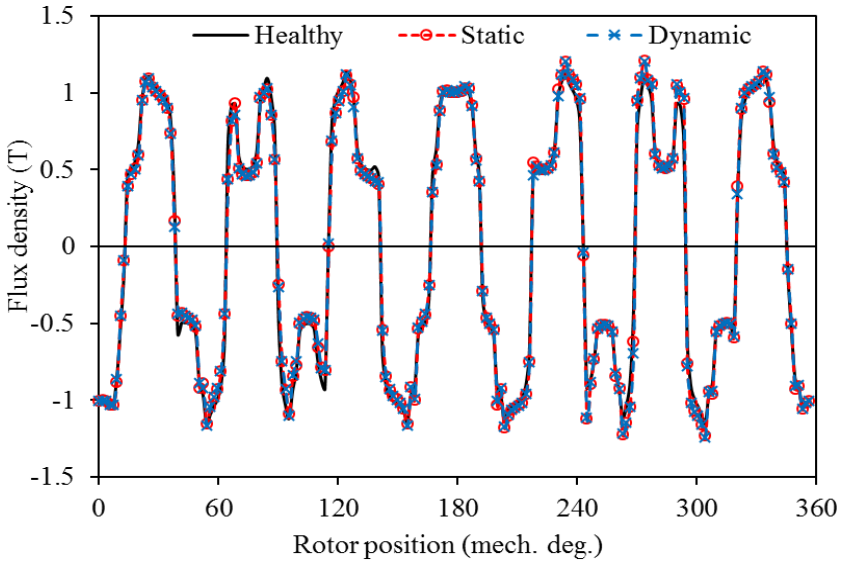

(a) Waveforms

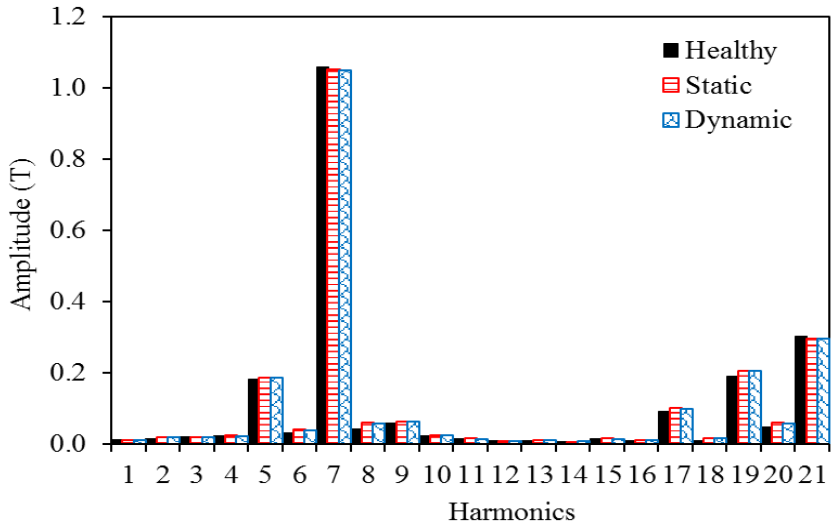

(b) Harmonic spectra

Fig. 5.21 Comparison of flux density in the middle of the LSR air-gap at initial position for different LSR angular misalignment cases.

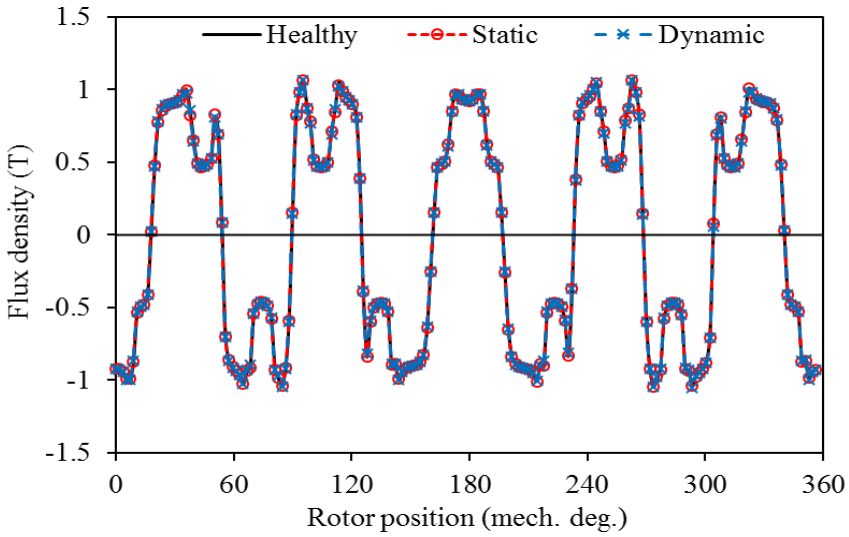

(a) Waveforms

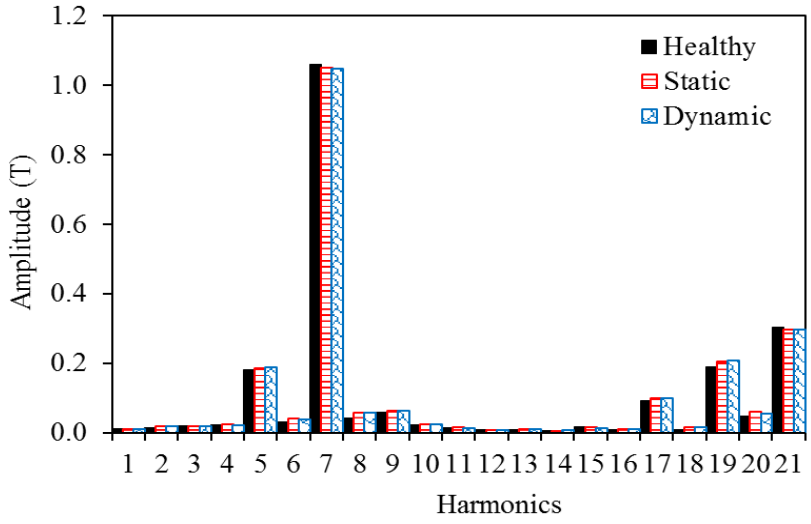

(b) Harmonic spectra

Fig. 5.22 Comparison of flux density in the middle of the HSR air-gap at initial position for different LSR angular misalignment cases.

5.4.3 Back EMF

The influence of static and dynamic LSR/stator angular misalignments on the back EMF is investigated and compared with the healthy condition in Fig. 5.23 and Fig. 5.24, respectively. It can be clearly seen that the influence of static angular misalignment on the 3-phase back EMF waveforms is minor. More specifically, the amplitudes of 3-phase EMFs are slightly unequal over one electrical cycle. Moreover, as shown in Fig. 5.24, the dynamic angular misalignment over a mechanical cycle has almost no effect on the back EMF amplitude for 50% angular misalignment compared with the healthy condition. Generally, higher flux linkages are linked to the phase coils

since the rotor is close to the centre of the phase coils on one side. In addition, fewer flux linkages are present in the phase coils on the other side. This results in a slight change in the total back EMF since the drop in the back EMF on one side is compensated by the rise of the coils' phase EMF on the other side, as clearly indicated in Fig. 5.25 and Fig. 5.26.

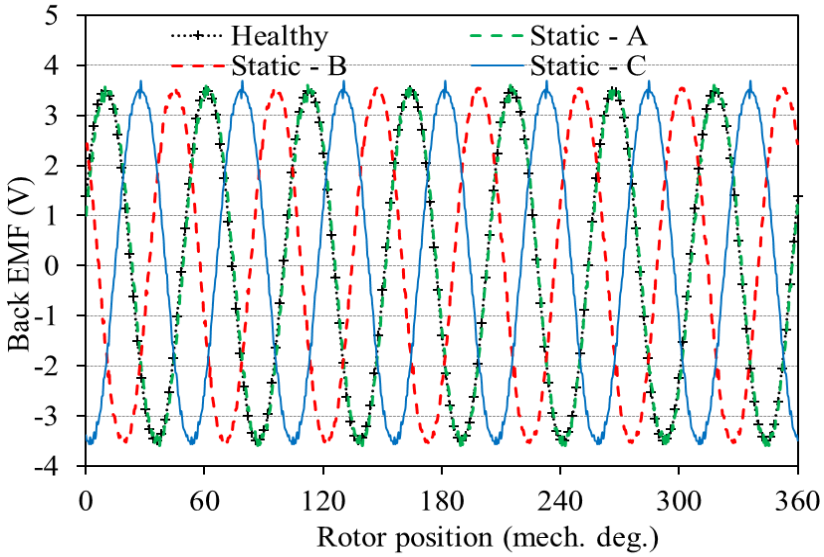

(a) Waveforms

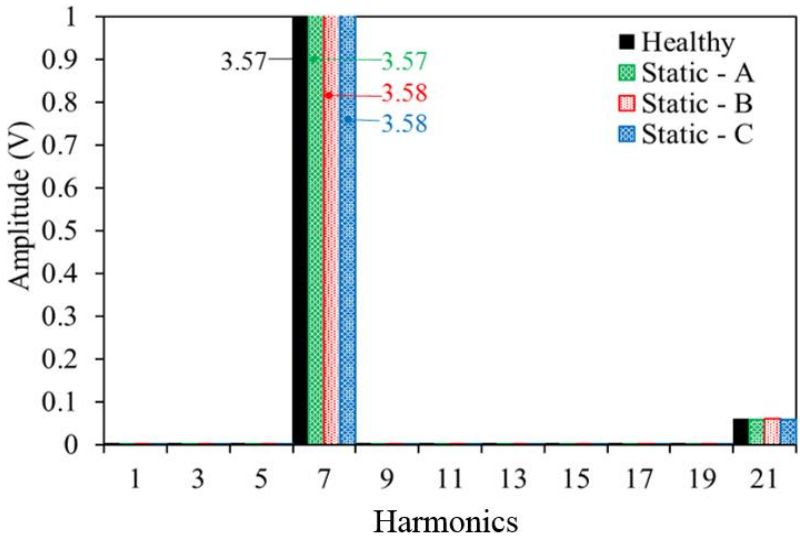

(b) Harmonic spectra

Fig. 5.23 3 phase back EMFs at LSR static angular misalignment cases.

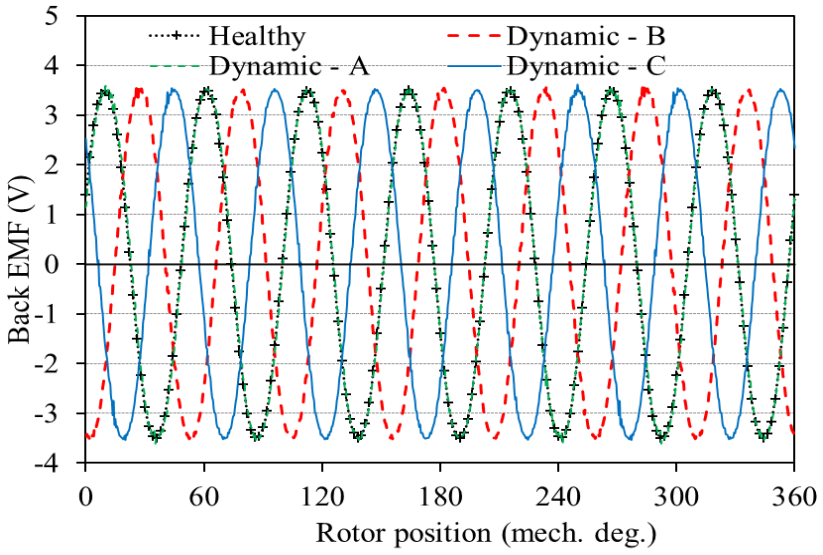

(a) Waveforms

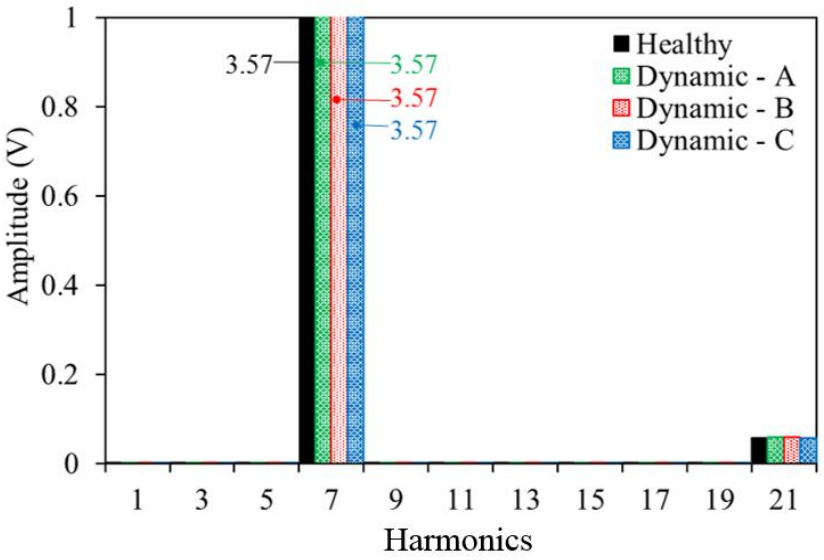

(b) Harmonic spectra

Fig. 5.24 3 phase back EMFs at LSR dynamic angular misalignment cases.

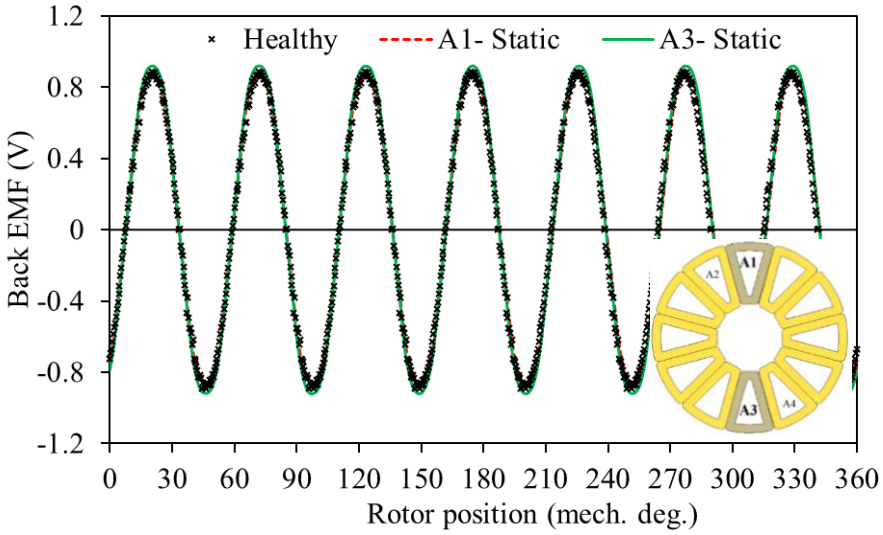

(a) Waveforms

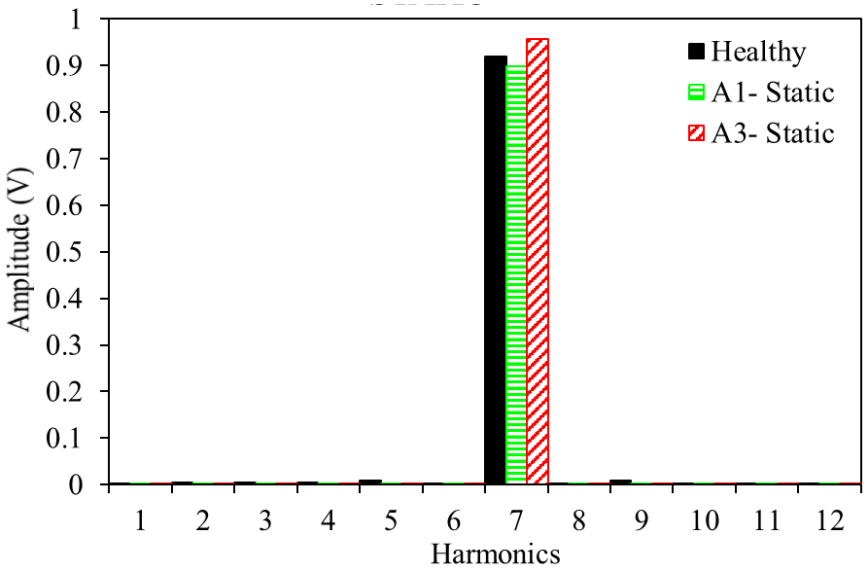

(b) Harmonic spectra

Fig. 5.25 Comparison of coil phase back EMFs at LSR static angular misalignment.

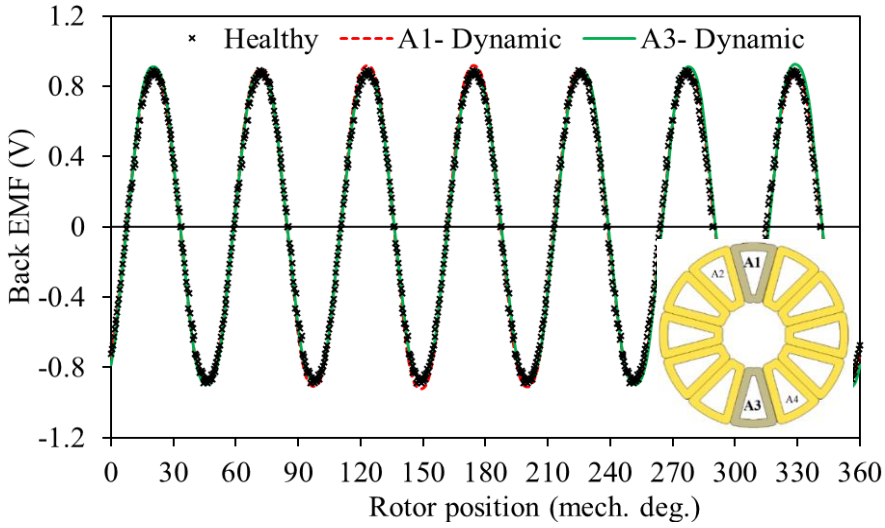

(a) Waveforms

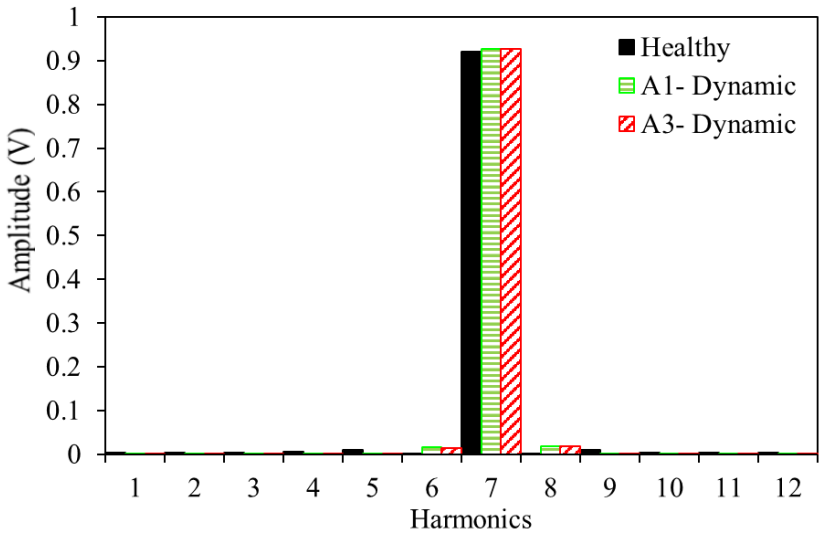

(b) Harmonic spectra

Fig. 5.26 Comparison of coil phase back EMFs at LSR dynamic angular misalignment.

5.4.4 Torque

Fig. 5.27 and Fig. 5.28 show the effect of the LSR/stator angular misalignment on the torques at no-load and on-load conditions, respectively. It is obvious that the average torque of all conditions is slightly affected by static and dynamic angular misalignments. However, Fig. 5.27 (b) and Fig. 5.28 (b) confirm that the rotor angular misalignment distorts the profile of output torque and inherently results in slightly higher torque ripple compared with the healthy condition. Overall, the static and dynamic angular misalignments have a trivial effect on the machine HSR and LSR torques at no-load and on-load conditions.

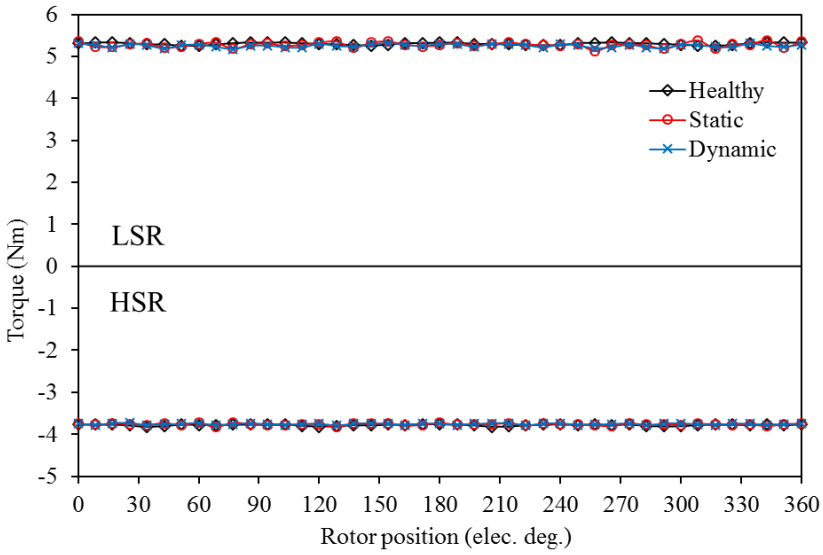

(a) Waveforms

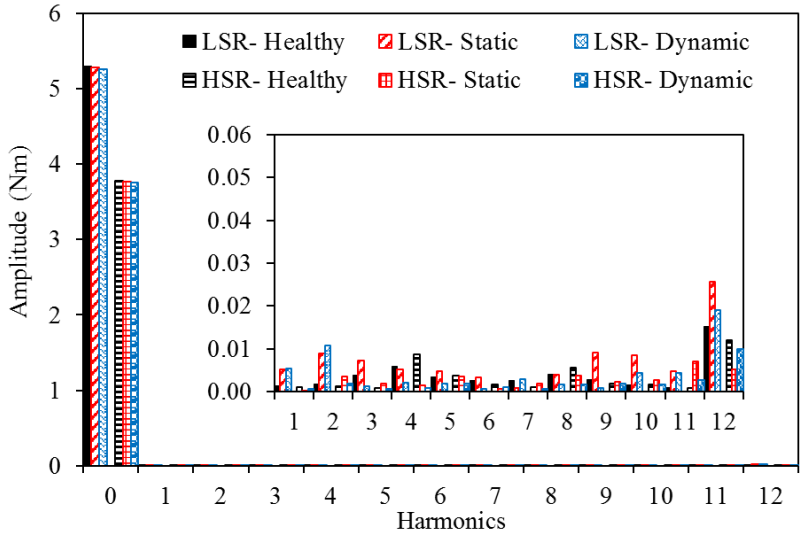

(b) Harmonic spectra

Fig. 5.27 Comparison of magnetic torques exerted in the machine rotors at LSR angular misalignment.

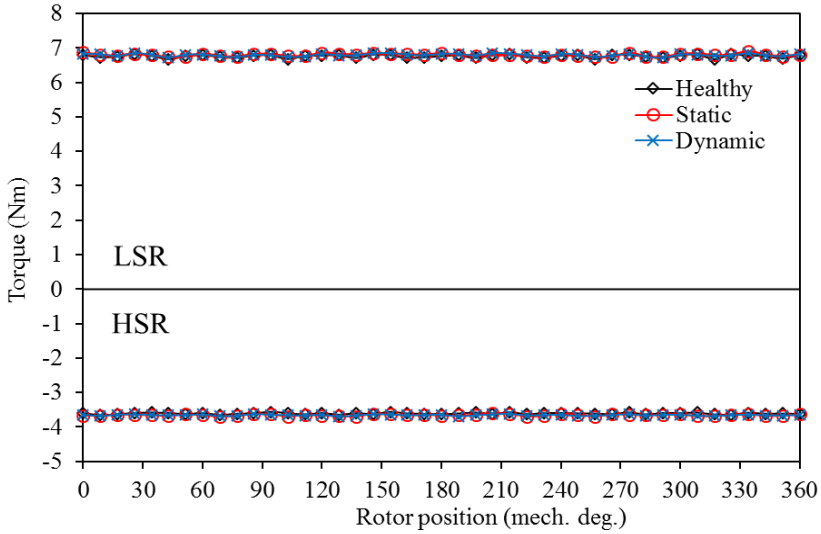

(a) Waveforms

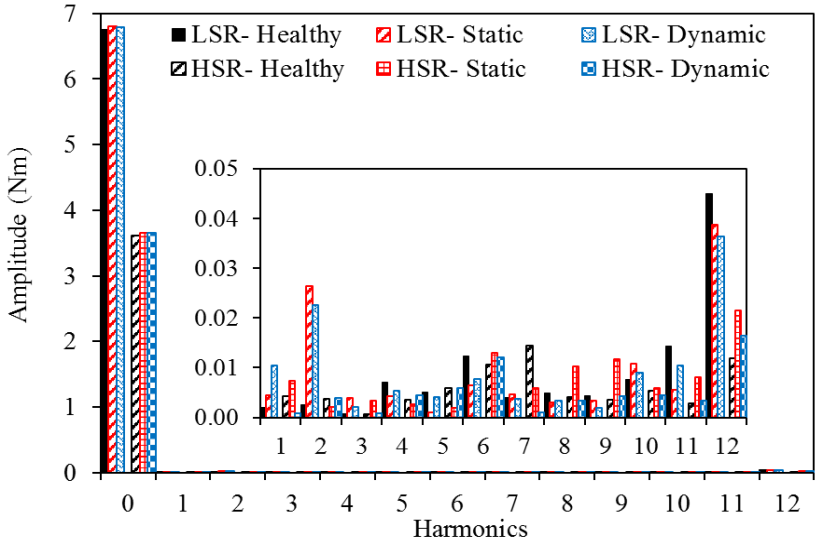

(b) Harmonic spectra

Fig. 5.28 Comparison of the on-load torques exerted on the machine rotors at LSR angular misalignment.

5.4.5 Unbalanced force

The no-load magnetic force is examined at maximum relative angle between HSR and LSR. Fig. 5.29 indicates the axial force applied on both HSR and LSR, and Fig. 5.30 plots the axial force performance applied on the stator at static and dynamic angular misalignments with reference to the healthy condition. It can be noticed that there are no significant changes to the total average force affecting the machine parts since the change in flux density is negligible. However, the axial force at static angular misalignment slightly decreases for all parts. In addition, the angular misalignments excite a lower order of the forces (frequency subharmonics) whose frequency orders are the same as the pole numbers and slot numbers. Moreover, Fig. 5.31 shows the x-y

forces affecting the machine HSR, LSR, and the stator. It is clear that the force applied on the machine parts rises negligibly compared to the force at healthy condition.

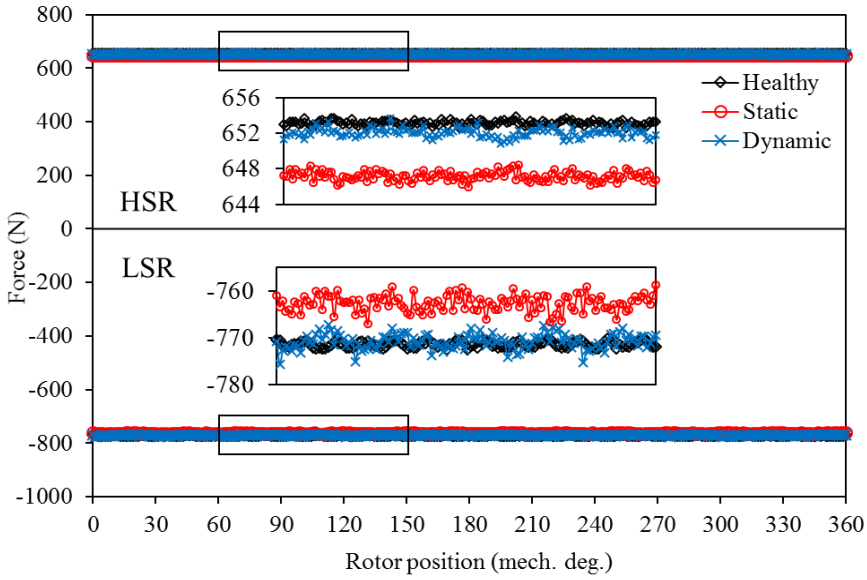

(a) Waveforms

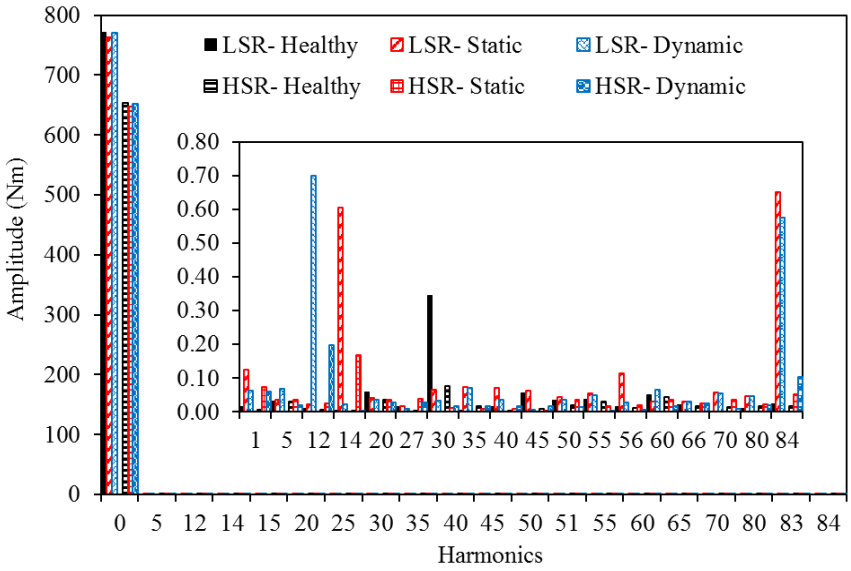

(b) Harmonic spectra

Fig. 5.29 Comparison of the no-load axial forces exerted in the machine rotors.

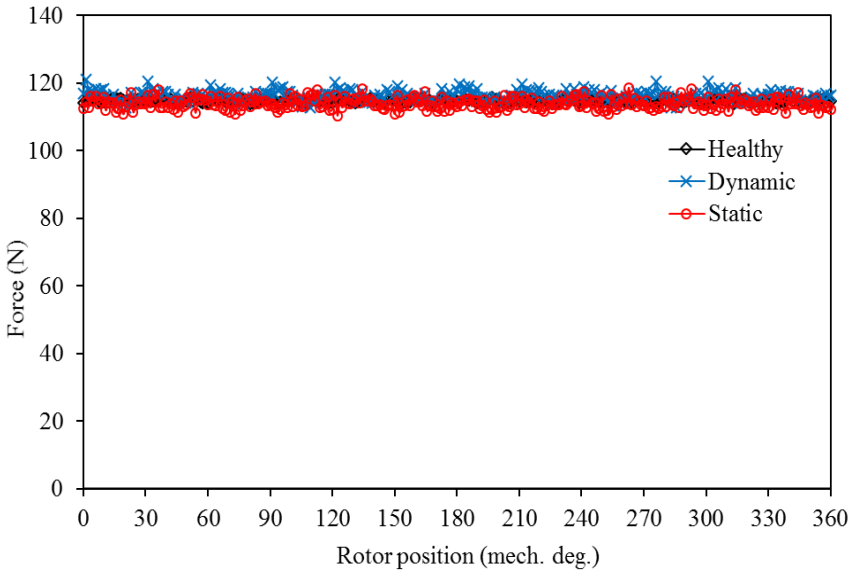

(a) Waveforms

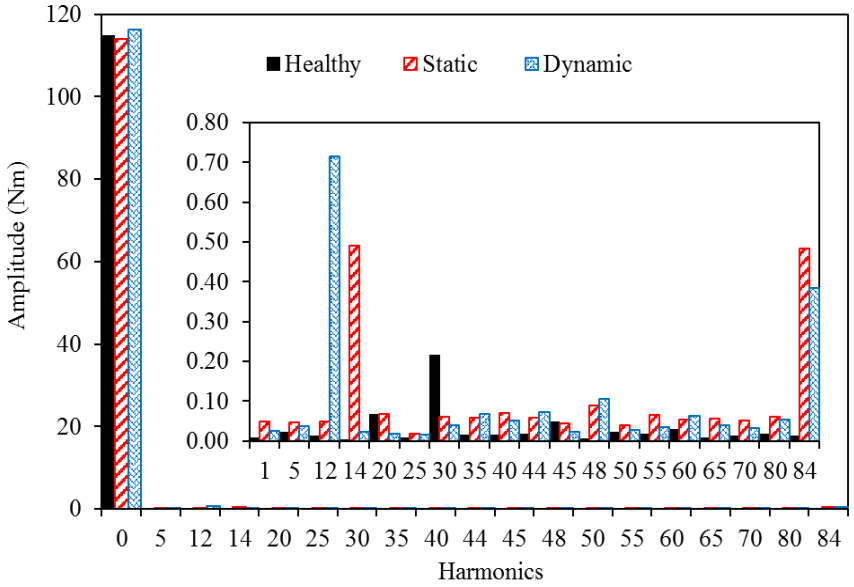

(b) Harmonic spectra

Fig. 5.30 Comparison of no-load axial force exerted on the stator.

Similarly, the predicted on-load force performance applied on HSR and LSR at different angular misalignment modes is compared in Fig. 5.32. It can be seen that the HSR forces of static and dynamic angular misalignments remain relatively unchanged, whereas the LSR forces have a relative increase and their ripples increase, whereby more low frequency subharmonics are created, as shown in Fig. 5.32 (b). Moreover, Fig. 5.33 illustrates the force applied on the stator at different LSR angular misalignments at on-load. It is obvious that both static and dynamic LSR angular misalignments affect the profile of the force applied on the stator compared with the healthy mode. This is due to the force applied on the LSR increasing due to the angular

misalignment, since the force applied on the stator is the summation of both rotors' attractive forces.

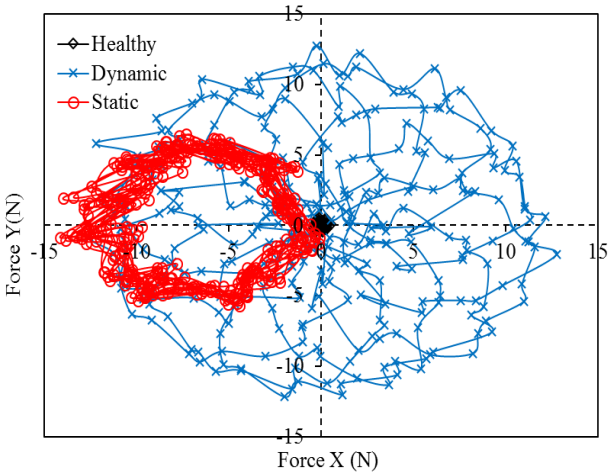

(a) LSR forces

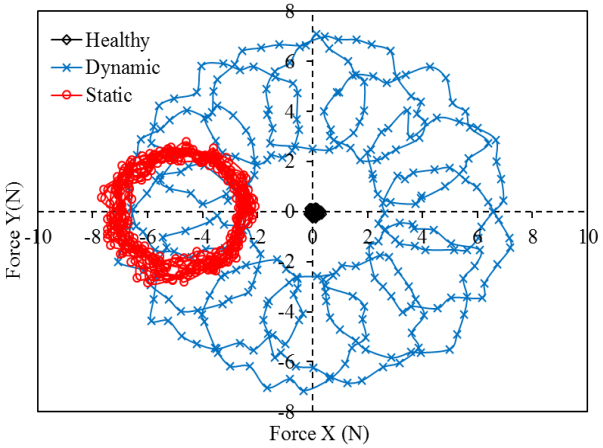

(b) HSR forces

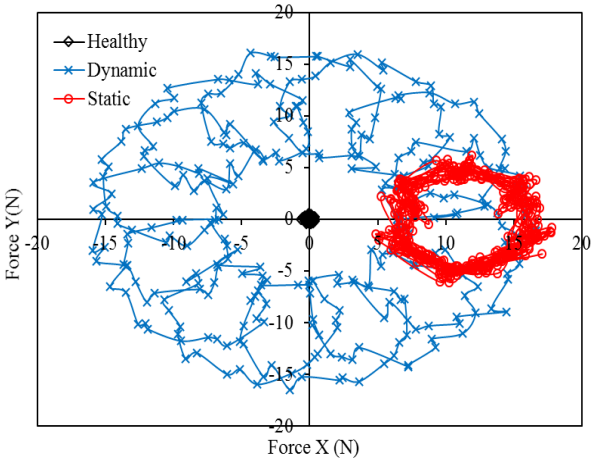

(c) Stator forces

Fig. 5.31 Comparison of no-load (x-y) forces exerted on the machine parts.

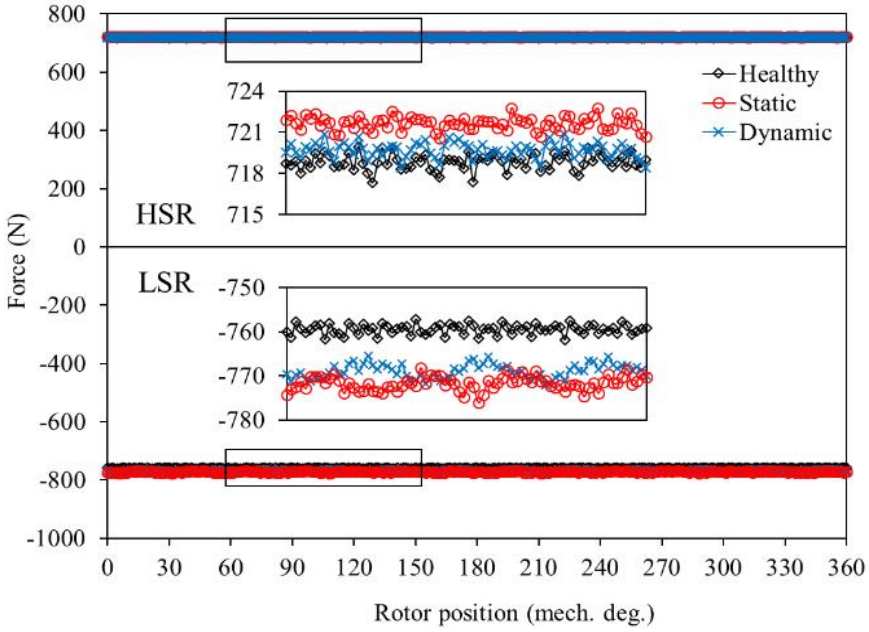

(a) Waveforms

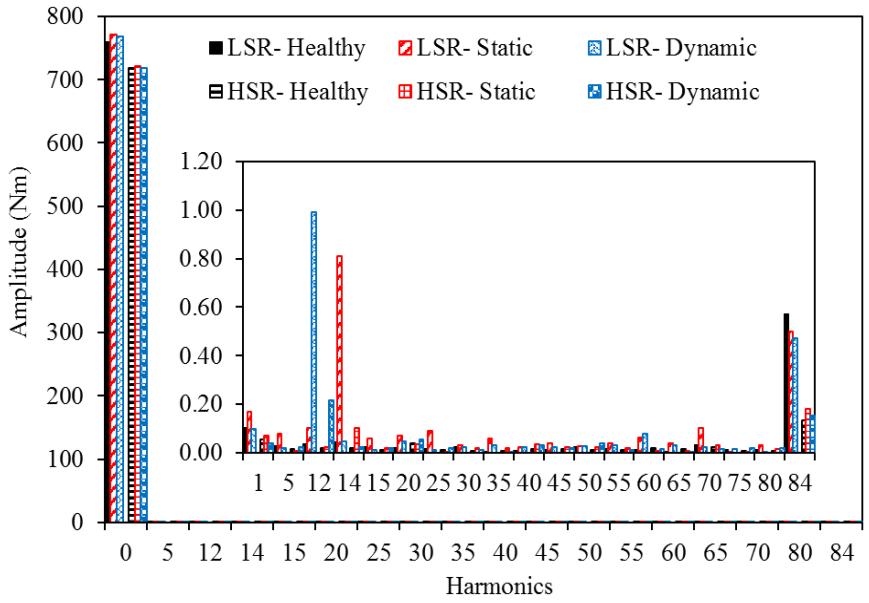

(b) Harmonic spectra

Fig. 5.32 Comparison of the on-load axial forces exerted on the machine rotors.

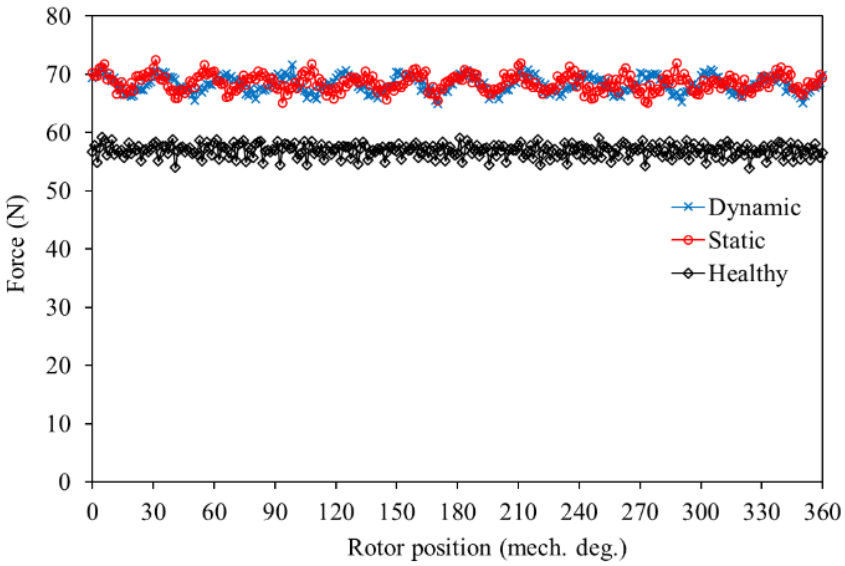

(a) Waveforms

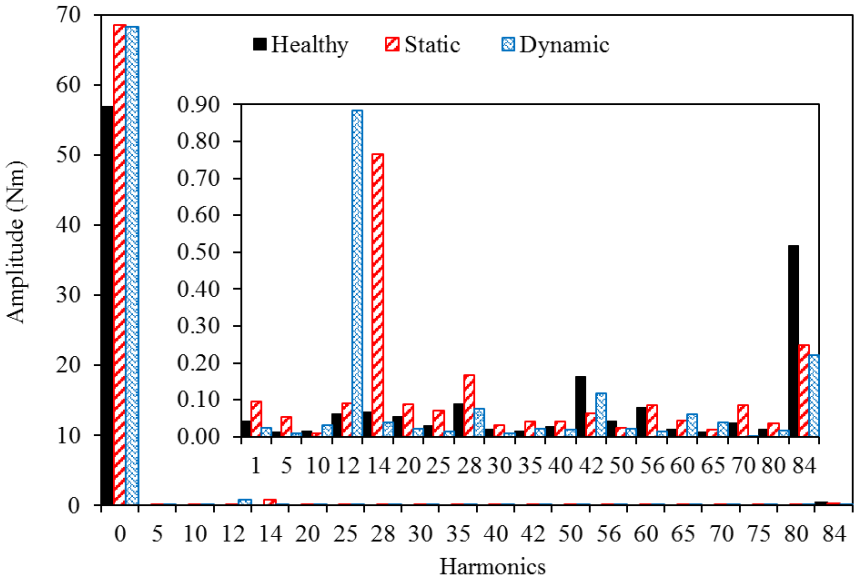

(b) Harmonic spectra

Fig. 5.33 Comparison of the no-load axial forces exerted on the stator.

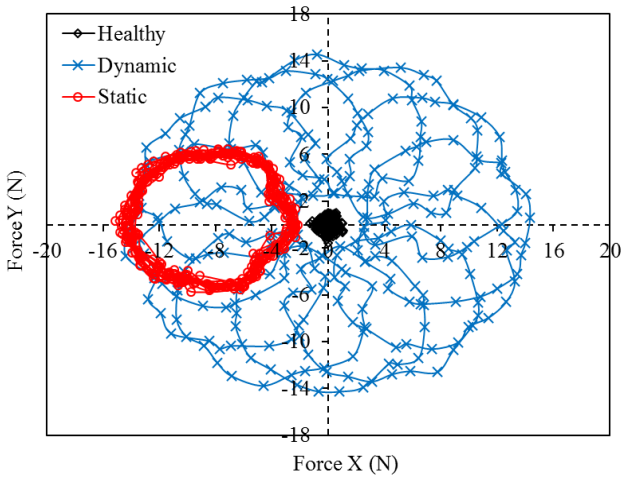

(a) LSR forces

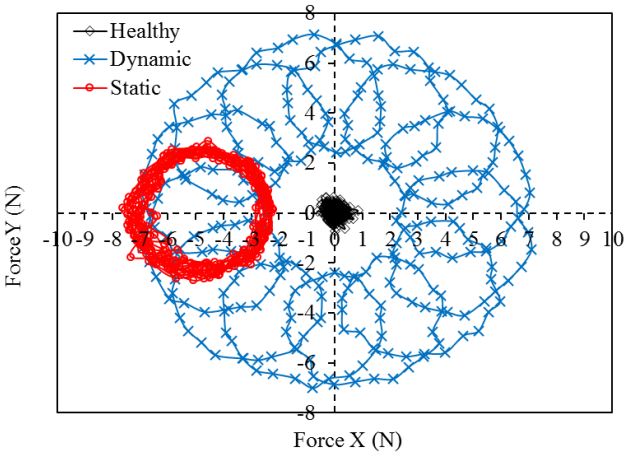

(b) HSR forces

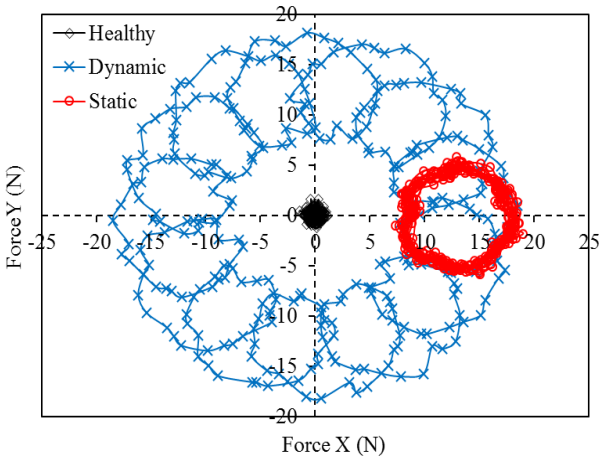

(c) Stator forces

Fig. 5.34 Comparison of electromagnetic (x-y) forces exerted on the machine parts.

Table 5.1 summarises a comparison of the simulation results between the effects of LSR axis and angular misalignments under different load conditions on the machine performance which

indicates that, the LSR/stator axis misalignment has a significant effect on the performance of the axial flux magnetically geared machine compared with angular misalignment.

Table 5.1 Comparison of machine performances with and without LSR eccentricity.

(a) No- load (Relative angle =0^o)

	Healthy		**Stator/rotor Misalignment**				**Angular misalignment**			
	HSR	LSR	HSR		LSR		HSR		LSR	
			Static	**Dynamic**	**Static**	**Dynamic**	**Static**	**Dynamic**	**Static**	**Dynamic**
Cogging torque native harmonic order	60	84	10	9	14	12	60	84	60	84
Cogging torque native harmonic amplitude (Nm)	0.03	0.06	0.053	0.044	0.088	0.072	0.037	0.045	0.058	0.056
EMF amplitude (V)	3.59		3.5	3.47	-	-	3.58	3.59	-	-

(b) No- load (Relative angle =90^o)

	Healthy		**Stator/rotor Misalignment**				**Angular misalignment**			
	HSR	LSR	HSR		LSR		HSR		LSR	
			Static	**Dynamic**	**Static**	**Dynamic**	**Static**	**Dynamic**	**Static**	**Dynamic**
Average torque (Nm)	3.78	5.30	3.45	3.45	4.83	4.83	3.76	3.75	5.25	5.24
X Force amplitude (N)	0.14	0.53	14.08	17.65	4.95	27.47	2.28	7.12	1.15	11.80
Y Force amplitude (N)	0.33	0.53	13.43	17.75	11.04	27.36	2.65	26.50	5.67	29.24
Z Average force (N)	653.9	770.2	660.94	661.10	753.49	753.62	656.14	654.30	772.56	769.54

(c) On-load (Relative angle =90^o)

	Healthy		**Stator/rotor Misalignment**				**Angular misalignment**			
	HSR	LSR	HSR		LSR		HSR		LSR	
			Static	**Dynamic**	**Static**	**Dynamic**	**Static**	**Dynamic**	**Static**	**Dynamic**
Average torque (Nm)	3.68	6.85	3.32	3.32	6.25	6.24	3.65	3.66	6.80	6.80
X Force amplitude (N)	0.19	0.53	14.19	17.84	1.75	29.51	2.22	7.09	2.16	14.33
Y Force amplitude (N)	0.44	0.56	13.14	17.87	12.95	29.77	2.89	7.15	6.48	14.55
Z Average force (N)	719.53	767.00	723.83	723.87	754.87	754.88	721.58	719.65	771.83	768.83

5.5 Summary

The influence of static and dynamic LSR/stator misalignments on the performance of axial flux magnetically geared machine has been analysed using 3-D FEA with reference to the healthy case. Two misalignments types in which axis LSR misalignment and angular LSR misalignment are considered. It is found that rotor/stator axis misalignment results in additional cogging torque harmonics due to the additional air-gab flux density harmonics. Moreover, air-gap flux density is sensitive to rotor/stator axis misalignment. Furthermore, the amplitude and the harmonic components of the back-EMF are slightly changed, in which the degree of such change depends on the stator/rotor axis misalignment distance. In addition, the effect of the LSR misalignment on the magnetic gear torque and on-load torque has been studied. It is shown that the machine torque is obviously decreased by static and dynamic LSR/stator axis misalignments. Also, the attractive force applied on the machine HSR, LSR and stator is sensitive to all conditions of axis misalignment. In addition, the influence of static and dynamic LSR/stator angular misalignments on the performance is also examined for the proposed machine. It is clear that, the angular misalignment has insignificant effect on the machine performance. In contrast, the performance at no-load and load conditions under axis and angular LSR/stator misalignments can be summarised as follows:

1- The HSR cogging torque fundamental harmonic orders significantly increase by approximately 70 % at static axis misalignment and 50 % at dynamic axis misalignment whereas the HSR cogging torques at static and dynamic angular misalignments increase by approximately 20% and 50 %, respectively.

2- The LSR cogging torque increases by approximately 40 % at rotor static axis misalignment; however, the cogging torque for LSR decreases at dynamic axis misalignment and angular misalignment. In these cases more low order sub harmonics (i.e. 12^{th} and 14^{th}) are created.

3- The three phase back EMFs slightly unbalance at static rotor axis misalignment and negligibly change at dynamic axis misalignment and angular misalignment. The unbalanced phase back EMFs depend on the misalignment level in which the unbalance is increased when the rotor axis shifting increases.

4- The torques at no load and on-load at maximum relative angle decrease due to static and dynamic LSR axis misalignments. However, the effect of LSR angular misalignment on the average torque is negligible with reference to the healthy condition.

5- The no-load and on-load axial forces due to LSR axis and angular misalignments have the same performance whereby the change is insignificant.

6- The X and Y forces applied on all machine parts are sensitive to the LSR axis misalignment. However, angular misalignment has a lower effect compared with axis misalignment.

Finally, since a proportion of the rotor PMs are overhung relative to the stator poles when axis misalignment exists. This results in the flux density decreasing in addition to the leakage and fringing flux which occur with such overhung magnets. However, angular misalignment has insignificant effect on the machine performance. This is due to the air-gap flux density being fairly changed since the air-gap flux density at the position of the minimum air-gap length increases and decreases at the other side. This results in a uniform phase flux linking the windings and hence insignificant effect on the back EMF.

CHAPTER 6

PROTOTYPE MACHINE DESIGN AND VALIDATION OF EXPERIMENTAL RESULTS

6.1 Introduction

Using the principles outlined in the theory of axial flux machines and axial flux magnetically geared machines elucidated in the previous chapters, a prototype machine was designed and fabricated. The constructed prototype is a modification of the optimised model. Due to mechanical constraints, several dimensions of the prototype machine were modified (i.e. stator tip thickness and inner diameter). Moreover, due to manufacturing difficulties, the machine stator and both of the rotors pole were designed to be rectangular. The manufactured machine allows reassembly and modification of the main components of the machine's structure. Since the proposed axial flux magnetically geared and conventional YASA machines are similar in structure, the prototype was designed so that the magnetically geared machine with two different rotor poles and the conventional YASA machine with two identical rotor poles could be assembled by sharing the same stator. Moreover, with the same dimensions as the prototype machines, FE models were established utilising 3D-FE software for validation of experimental results.

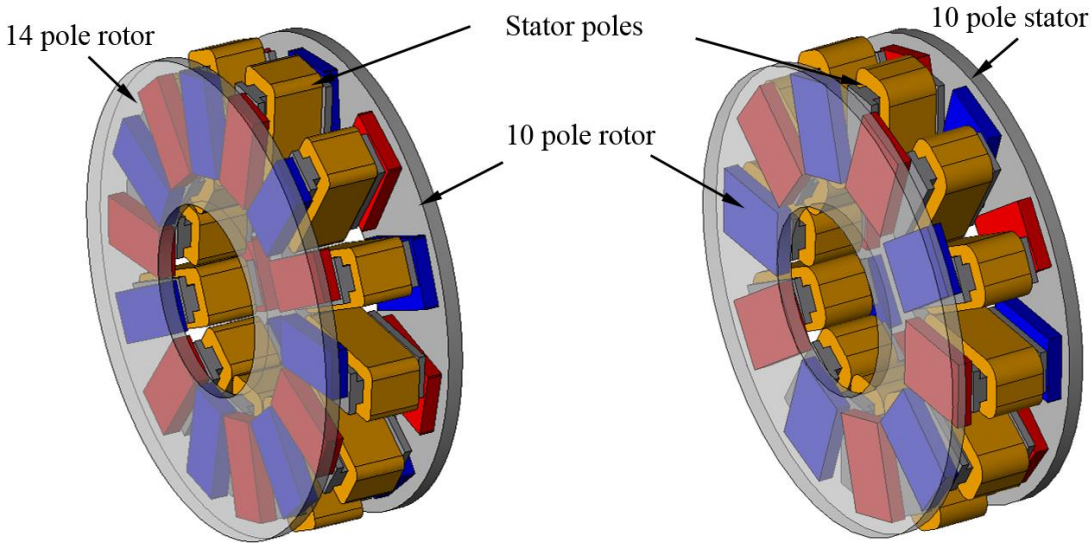

(a) Magnetically geared machine (b) YASA machine

Fig. 6.1. Prototype machines: 3D-views.

This chapter firstly presents the manufacturing process of prototype machines, and then the experiment results and the corresponding analyses of the proposed magnetically geared prototype and YASA machines. Fig. 6.1 shows the 3D model views of the final designs of the proposed magnetically geared and YASA machine prototypes. The conventional YASA machine (YASA12/10) was assembled and tested, with two 10 pole identical rotors of which were physically connected to each other. By replacing one rotor of the YASA machine with 14 poles, the proposed magnetically geared machine (MG12/10-14) was also assembled and tested. Finally, a performance comparison of the proposed machine and the conventional YASA machine was performed.

6.2 Prototype dimensions and manufacturing process

The prototype machine is an axial flux permanent-magnet machine with two surface-mounted PM rotors and one stator configuration. Fig. 6.2 shows the full-scale prototype machine parts before and after assembly. Table 6.1 presents the dimensions and parameters of the proposed magnetically geared and conventional YASA prototypes. The stator pole is comprised of stacked laminated steel sheets. A concentrated winding was placed over each individual stator segment, as shown in Fig. 6.2(a). The segments were combined with high strength fibreglass material to form the machine stator, as shown in Fig. 6.2(b). In addition, the phase stator winding has four coils connected in series and the three phase windings are connected in a star formation. The rotor is a disk type iron rotor made of non-laminated mild steel with a set of N35SH magnets arranged on the surface utilising a tufnol sheet holder and adhesive glue, as can be seen in Fig. 6.2(c) and (d). The rotor disk was placed in an aluminium holder connected by a sliver steel shaft via a set of screws to allow the rotor disk to be changed if needed. Both rotor shafts were adjusted on two holder frame disks with two ball bearings on each side. By assembling the stator and both rotors using an aluminium outer frame, the magnetically geared and conventional YASA machine could be individually assembled sharing the same stator and one rotor. The main parts and the complete structure of the prototype are shown in Fig. 6.2(e) and (f), respectively. Moreover, the prototype design diagram can be examined in detail in Appendix D.

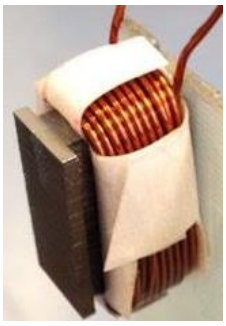

(a) Stator pole with and without coils

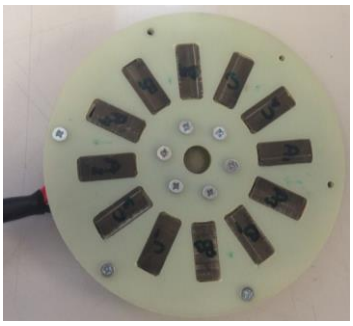

(b) Stator

(c) MG machine rotors

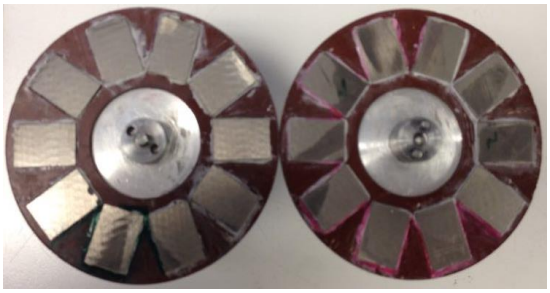

(d) YASA machine rotors

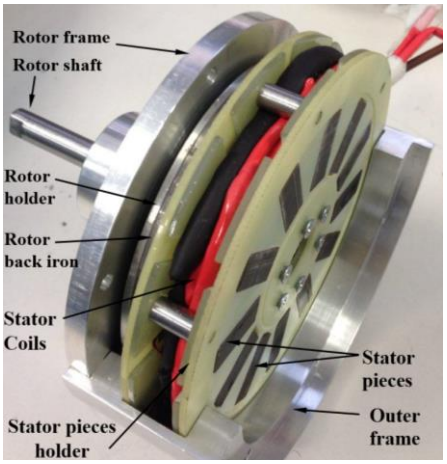

(e) Prototype's main components

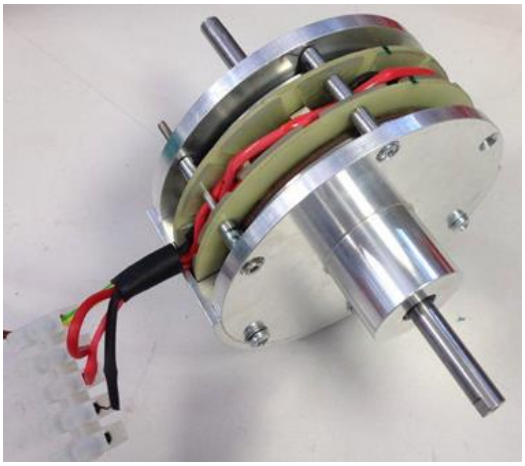

(f) Complete prototype structure

Fig. 6.2. Prototype machines.

Table 6.1. Prototype machine dimensions and parameters

Parameter	Value	Parameter	Value
HSR pole pair no. (p_h)	5	LSR pole width (mm)	10
LSR pole pair no. (p_l)	7	LSR pole height (mm)	20
No. of stator slots (n_s)	12	Rotors back iron thickness (mm)	3
No. of coils /phase	4	Stator pole height (mm)	20
No. of turns /phase	168	Conductor diameter (mm)	0.71
Air-gap width (mm)	0.5	Winding resistance /phase (Ω)	0.5
Axial length (mm)	30	Winding inductance /phase (mH)	0.54
Stator (D_i) (mm)	48	Packing factor	0.5
Stator (D_o) (mm)	88	Max. rated current (A)	6
HSR pole thickness (mm)	3	AFMGPM gearing ratio (G_r)	1.4
HSR pole width (mm)	14	Magnet material	N35SH
HSR pole height (mm)	20	PM remanence B_r (T)	1.21
LSR pole thickness (mm)	3.5	Iron material	Mild steel

6.2.1 YASA machine design and validation of test results

A prototype of the YASA machine was firstly assembled for experimental tests; specifically, the no-load and on-load tests. The machine was assembled with a 3-phase 12-pole concentrated winding stator and two identical 10 pole rotors physically connected to each other.

6.2.1.1 Cogging torque

The cogging torque of the prototyped YASA machine was measured and compared to the predicted results obtained by FEA by adopting the measuring method described in [ZHU09b] and with the aid of the test rig displayed in Fig. 6.3. The rotor shaft was connected to a balance beam to measure the force produced by the prototype with the aid of a digital weight scale. In this case, the rotor was stationary whereas the stator was fixed to the jaws of the lathe machine which could be freely rotated to vary the rotor position. Moreover, a pre-load weight was located on the beam above the digital scale to keep continuous attachment with the digital scale when the position was changed. This method allowed for measuring of different weights on the digital weight scale as

the stator position was changed. Subsequently, the torque was measured using the following equation:

$$Torque\ (Nm) = ([\text{Scale reading}] - [\text{pre-load weight}]\ (Kg) \times \text{Beam length}\ (m) \times 9.81(m/s^2) \quad (7.1)$$

Fig. 6.4 shows a comparison between measured (MEA) and predicted (FEA) cogging torques of the YASA prototype machine for half electric cycle. It should be noted that the measured cogging torque was slightly modulated due to manufacturing tolerances. Additionally, misalignment between the machine stator and rotors was identified which might be the most influential manufacturing tolerance on the measured results as explained in CHAPTER 5. As can be seen in Fig. 6.4(b), according to the results obtained from the FEA of the prototype model, the rotor/stator misalignment can be predicted as approximately 0.7 mm.

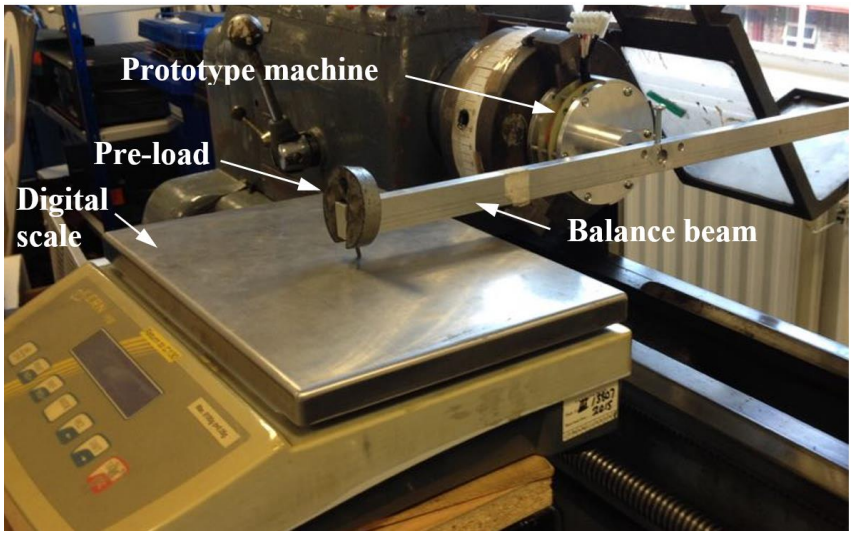

Fig. 6.3. Prototype test rig.

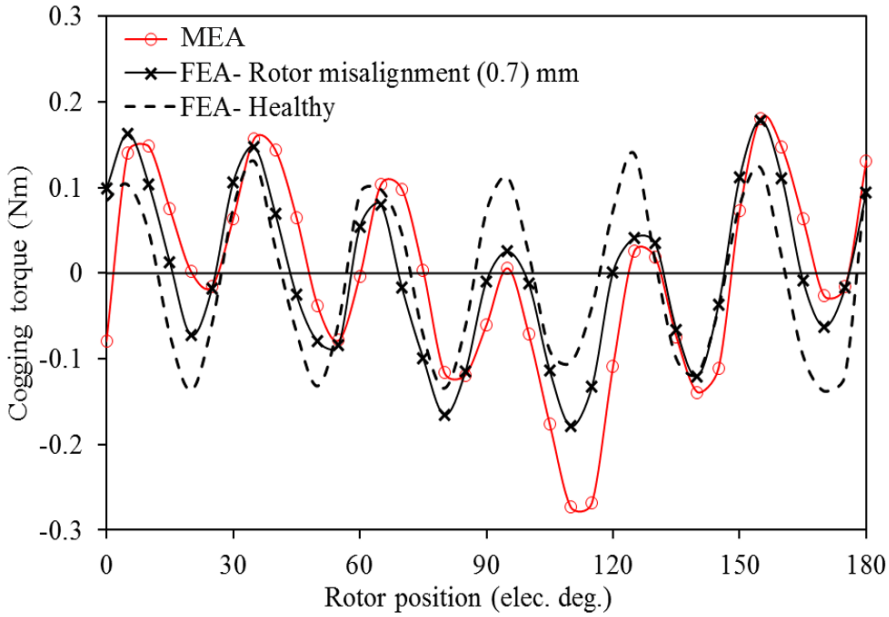

(a) Waveforms

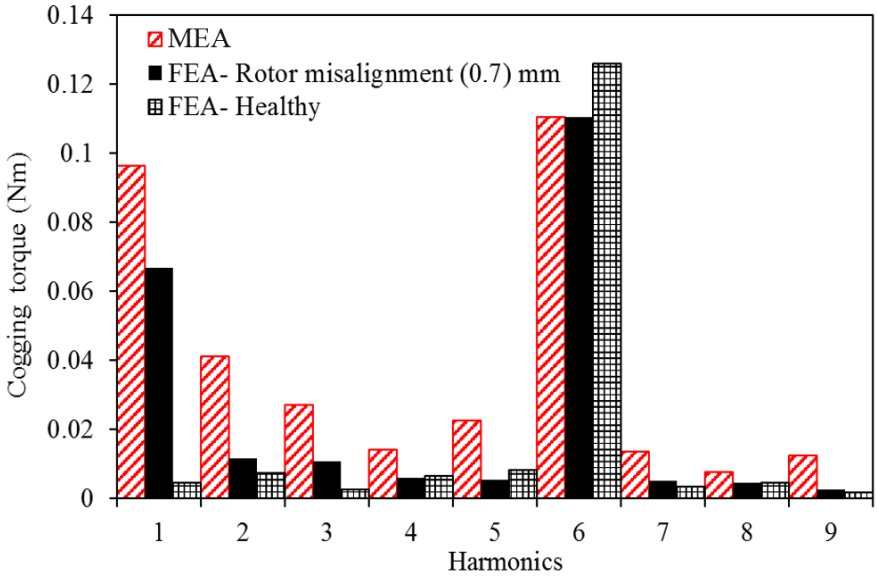

(b) Harmonic spectra

Fig. 6.4. Comparison of predicted and measured cogging torques of YASA machine for half electrical cycle.

6.2.1.2 Back –EMF

The phase back EMF of the YASA prototype was measured at the rated speed at 400 rpm by utilising an external prime-mover. Fig. 6.5 shows a comparison between the obtained three-phase back EMF of the prototype, and the predicted result. It is clear that the amplitude of the measured back EMF waveform of approximately 6.7 V is slightly lower than the predicted value of approximately 7.0 V, in which the difference between the peak values is approximately 5%.

Moreover, the three-phase measured back EMF waveforms are approximately symmetrical, as shown in Fig. 6.5 (b). Furthermore, the back EMF for each coil of phase (A) was also measured and compared (see Fig. 6.6). It obvious that the phase back EMFs of the coils are slightly different amplitudes, possibly due to manufacturing tolerance (see Fig. 6.6(b)). However, the difference between the back EMFs of the coils has only a minor effect on the total phase back EMF.

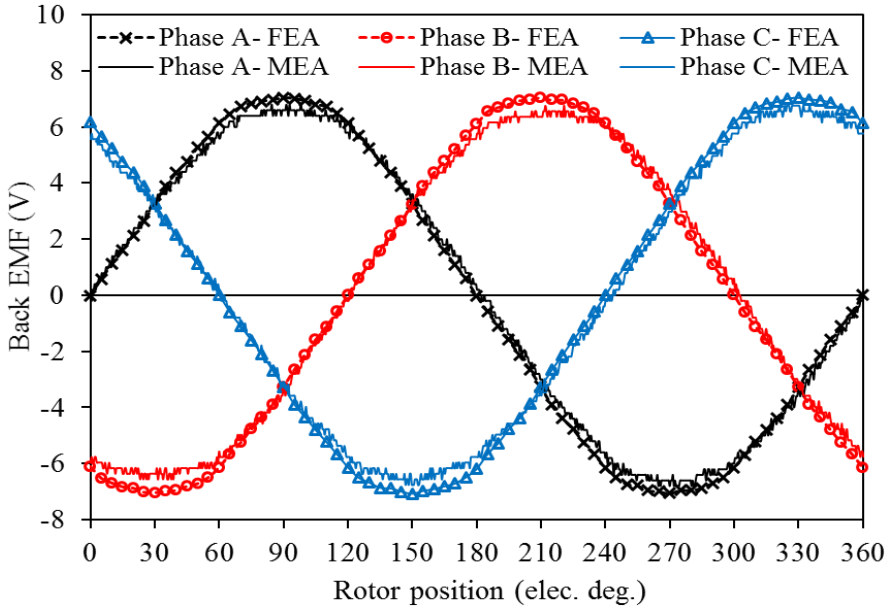

(a) Waveforms

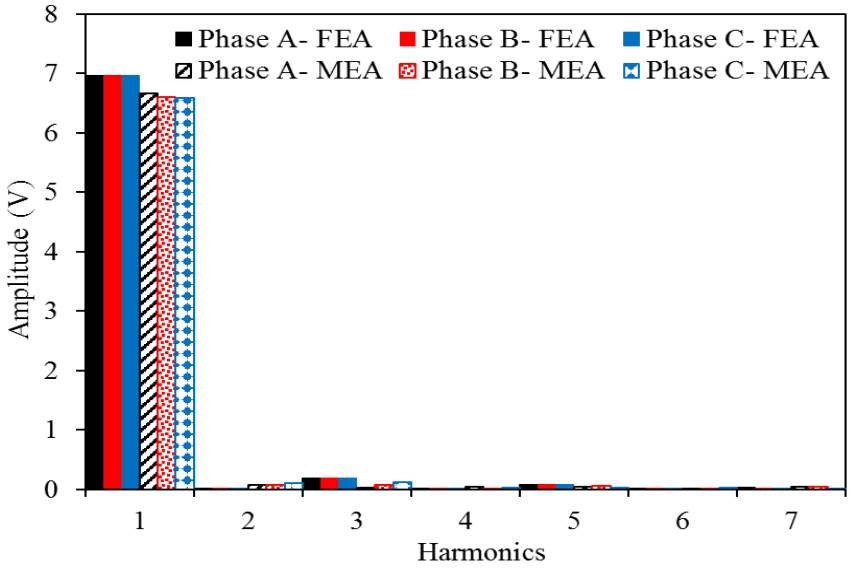

(b) Harmonic spectra

Fig. 6.5. Comparison of the predicted and measured phase back EMF of the YASA machine at 400 RPM.

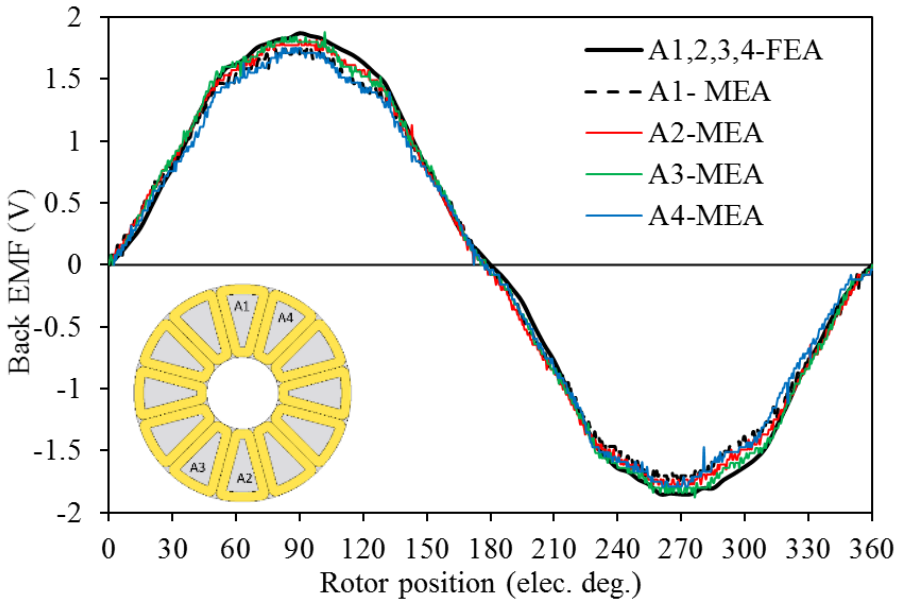

(a) Waveforms

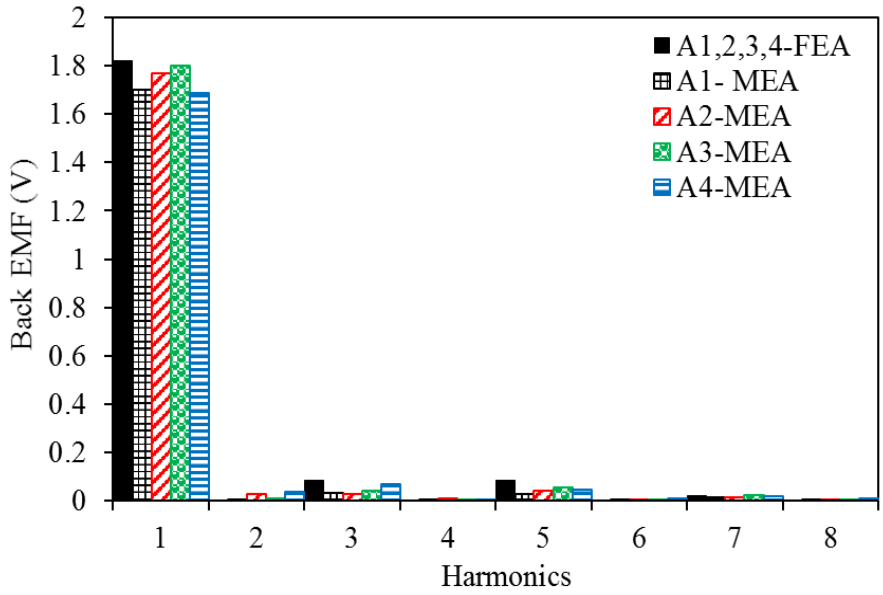

(a) Harmonic spectra

Fig. 6.6. Comparison of the predicted and the measured phase back EMF waveforms of phase (A) coils at 400 RPM.

6.2.1.3 Static torque

The prototype static torque was also measured and compared with the FEA result. The prototype on-load static torque was measured using the same method described for cogging torque. The only difference between static torque and cogging torque measurement is the presence or absence of current during excitation, respectively. However, by supplying the stator windings with DC currents in which ($I_a=I$, $I_b=I_c=-½I$), the static electromagnetic torque can be measured. Fig. 6.7(a)

shows the comparison of the predicted and measured static torque at different currents. Moreover, the relationship between the stator current and the measured maximum torque is plotted in Fig. 6.7 together with the corresponding FE result. A good match between the measured and predicted results was clearly obtained in which the measured and predicted torque constants are approximately 0.36 and 0.37, respectively.

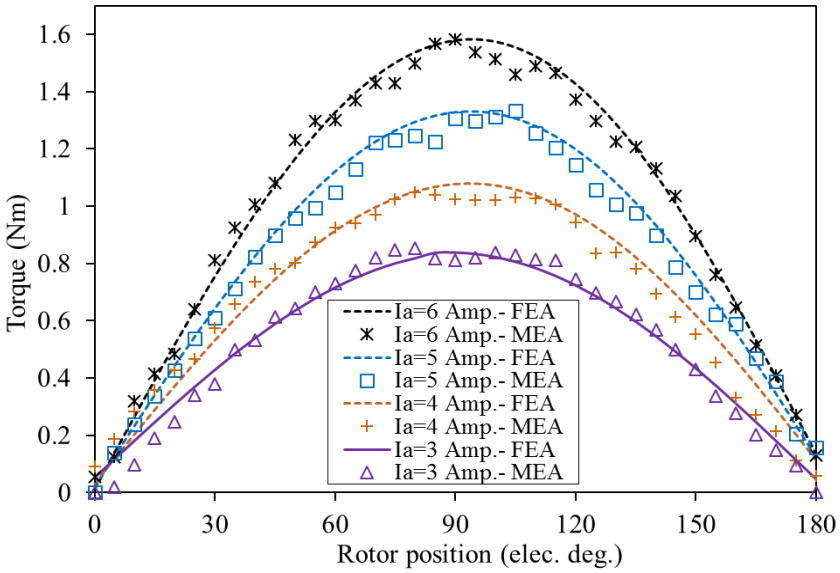

(a) Static torque curves at different maximum currents

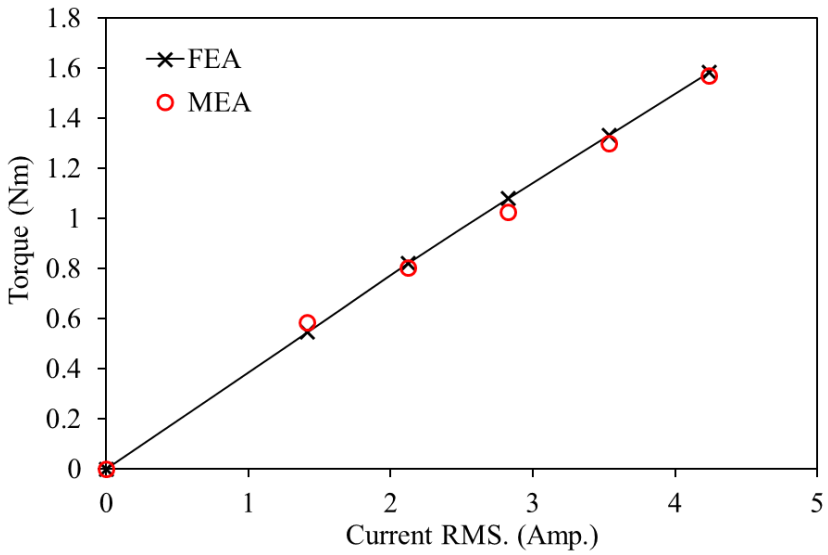

(b) Torque – current characteristics

Fig. 6.7. Comparison of the predicted and measured static torque of YASA machine.

6.2.2 Magnetically geared machine prototype and validation of test results

A prototype of the magnetically geared machine was assembled for experimental tests. It was done by replacing one 10-pole rotor of the YASA machine prototype with a 14-pole rotor. Both rotors were held to an aluminium holder with two ball bearings, and an axial thrust bearing was used in between the rotor shaft centres to allow free rotation of both rotors at different speeds. The stator with concentrated windings was kept the same as YASA machine. The complete prototype and the prototype dimensions are shown in Fig. 6.2 and Table 6.1. In addition, the connection way between two rotors is presented in detail in Appendix D.

6.2.2.1 Cogging torque

The individual cogging torques of HSR and LSR were firstly measured with the aid of the test rig shown in Fig. 6.3. The same method of cogging torque measurement of the YASA machine was used for the magnetically geared machine. However, one rotor was connected to the balanced beam while the other rotor was able to freely rotate. By changing the stator angular position, the cogging torque at different rotor positions could be measured for each rotor. Fig. 6.8 shows the measured and predicted LSR cogging torques for the proposed magnetically geared machine. Similarly, Fig. 6.9 shows the measured and predicted HSR cogging torque. It is obvious that the predicted cogging torques of LSR and HSR are relatively small. However, due to manufacturing tolerances, accurate measurements were difficult to achieve for HSR and LSR cogging torques. Moreover, the cogging torque for the FEA model was analysed and compared with the measured result to identify the type of rotor manufacturing tolerance. Therefore, it should be emphasized that the prototype should have a mix of manufacturing imperfections, in which slightly uneven gap between both rotors and the stator were detected. Nevertheless, according to the FEA result, the rotor/stator misalignment has the most significant effect on the cogging torque. As can be seen in Fig. 6.8 and Fig. 6.9, both LSR and HSR misaligned with the machine stator which were predicted of approximately 0.7 mm and 1 mm respectively.

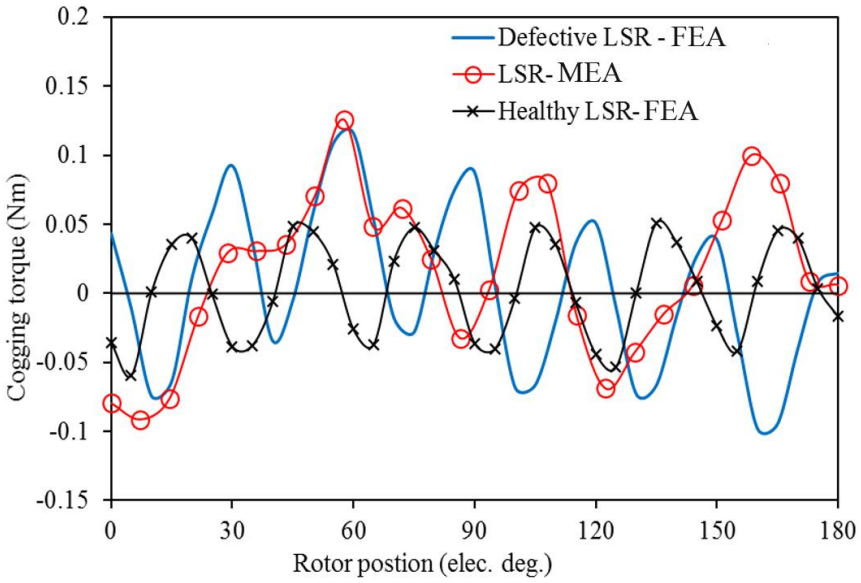

(a) Waveforms

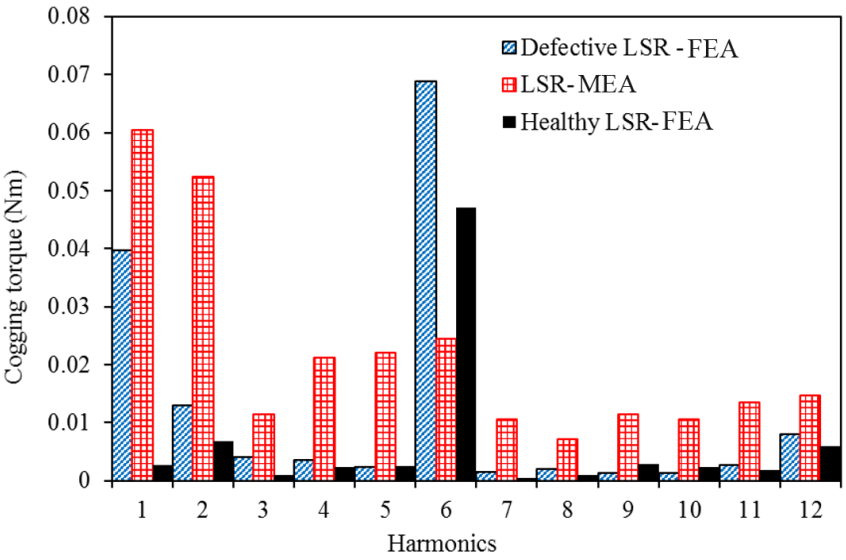

(b) Harmonic spectra

Fig. 6.8. Comparison of measured and predicted LSR cogging torques.

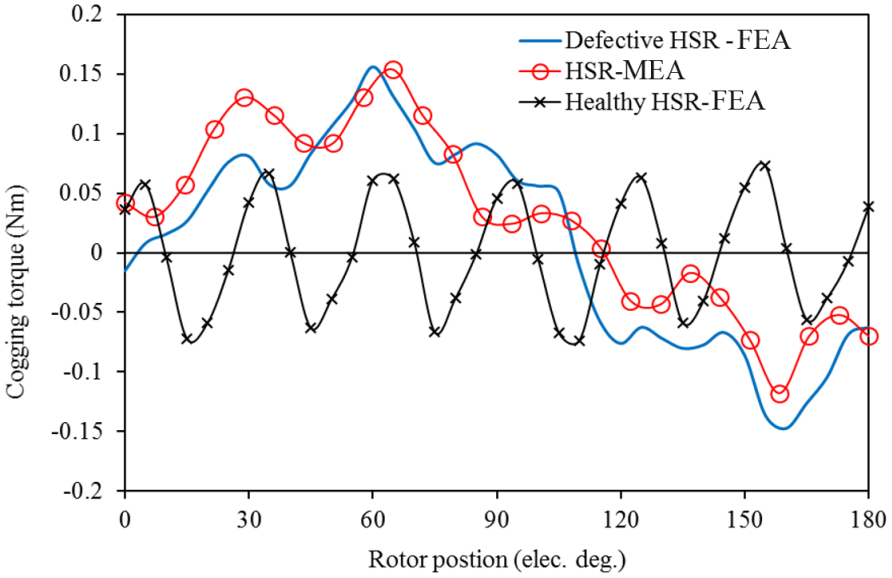

(a) Waveforms

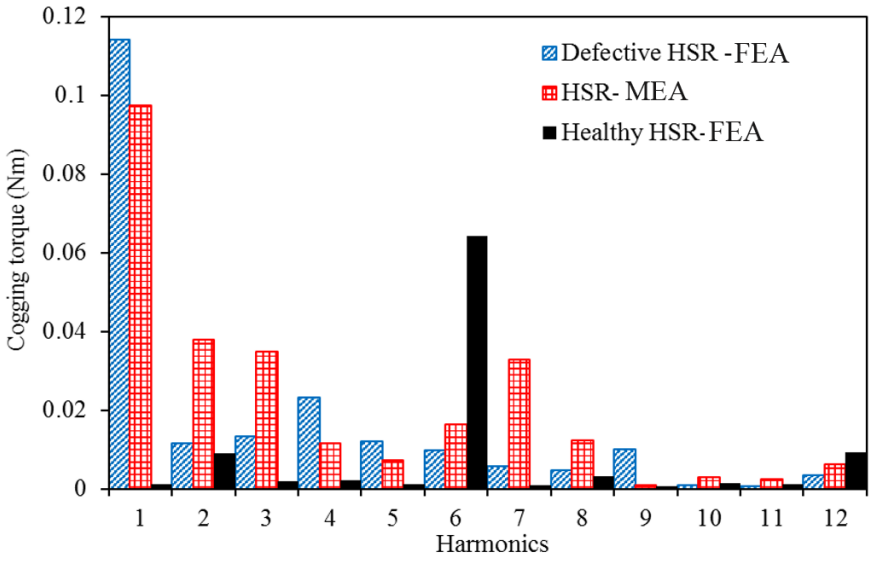

(b) Harmonic spectra

Fig. 6.9. Comparison of measured and predicted HSR cogging torques.

However, since the magnet shape has been changed for manufacturing consideration, the machine cogging torque is expected to be changed. It is clear that utilizing a rectangular magnet significantly increase the HSR cogging torque amplitude, whereas the cogging torque of the LSR is reduced by utilizing a rectangular magnet shape as shown in Fig. 6.10 and Fig. 6.11, respectively.

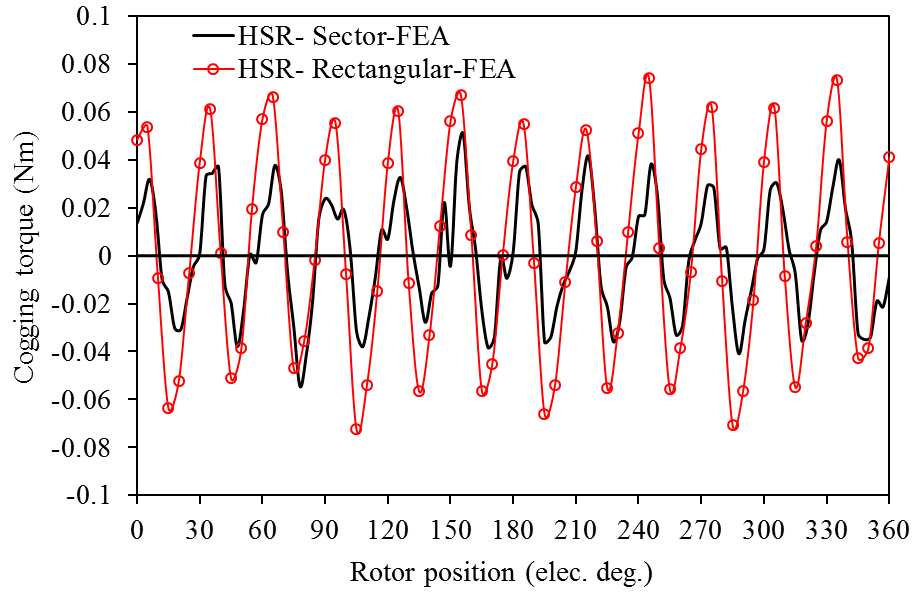

(a) Waveforms

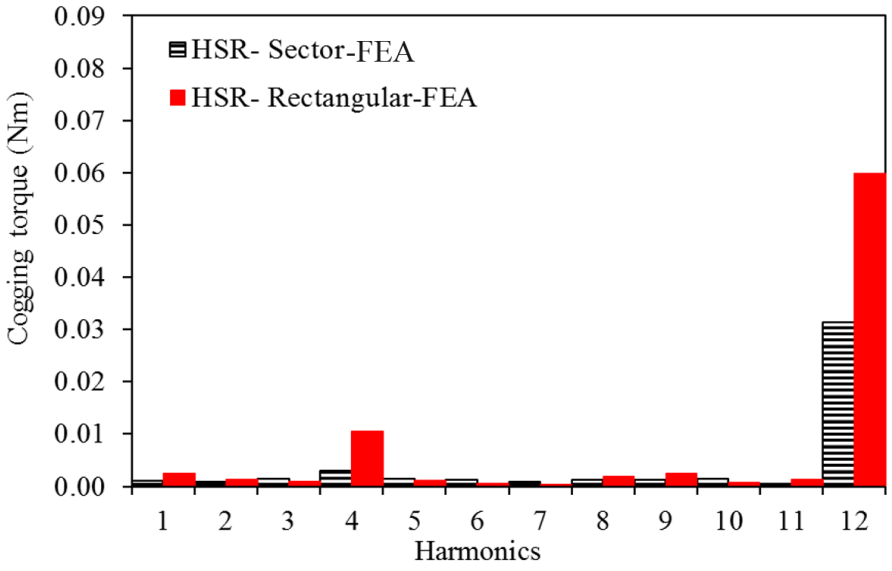

(b) Harmonic spectra

Fig. 6.10. Comparison of predicted HSR cogging torques for different magnet shapes.

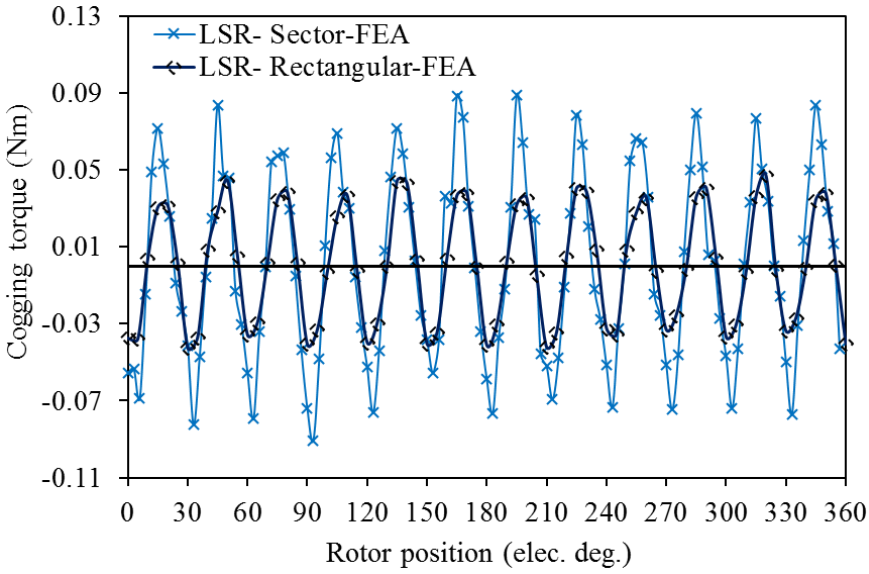

(a) Waveforms

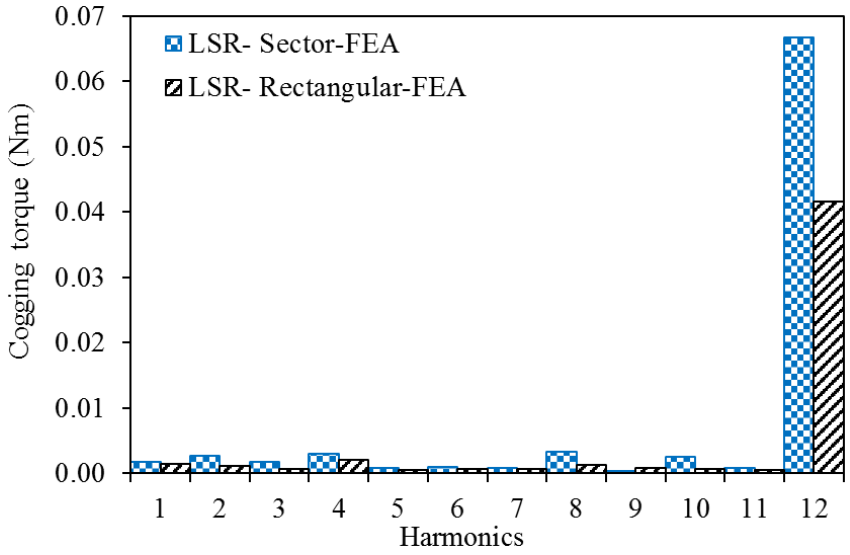

(b) Harmonic spectra

Fig. 6.11. Comparison of predicted LSR cogging torques for different magnet shapes.

6.2.2.2 Back –EMF

The phase back EMF of the magnetically geared prototype was measured when a rotation speed of 400 rpm was given to the HSR. Fig. 6.12 indicates the measured three phase back EMFs compared to the predicted FEA result: Fig. 6.13 shows a comparison of the phase (A) coils back EMFs. It is obvious that the measured and predicted back-EMF amplitudes are approximately 5.9V and 6.2V, respectively in which a good validation was obtained where the difference between the measured and the predicted EMF amplitudes is approximately 5 %. Moreover, the amplitude of the predicted back EMF for each coil is 1.57 V while the measured amplitude is

slightly different for each coil, whereby the average amplitude is approximately 1.56 V. Furthermore, the unbalanced amplitude of the coil back EMF has a minor effect on the phase back EMF amplitude as each reduction on coil EMF amplitude is compensated by the coil on the opposite stator side.

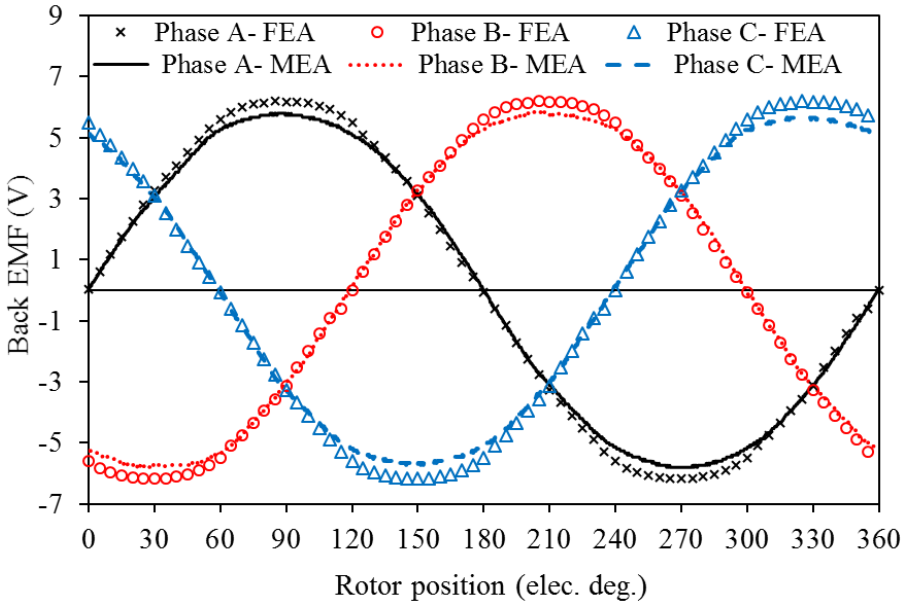

(a) Waveforms

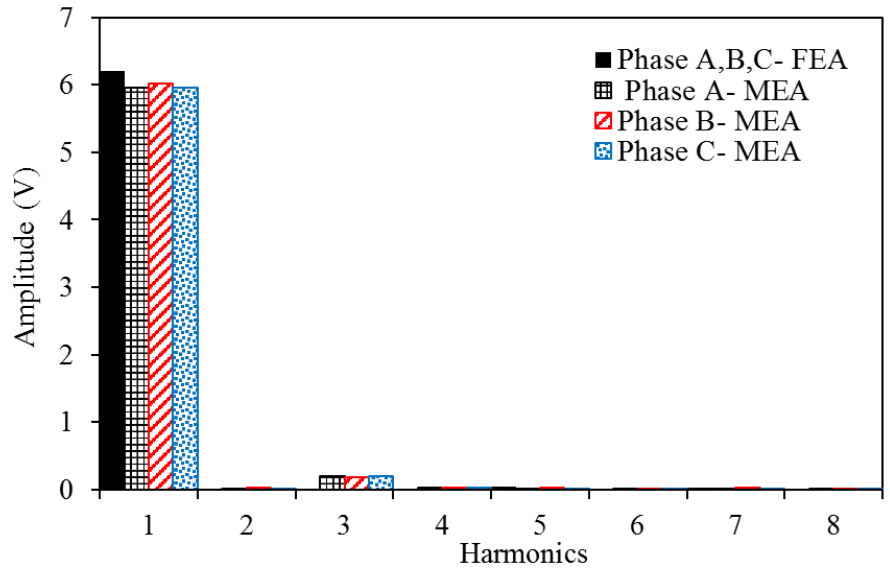

(b) Harmonic spectra

Fig. 6.12. Comparison of the predicted and measured phase back EMFs of the magnetically geared machine at rated speeds.

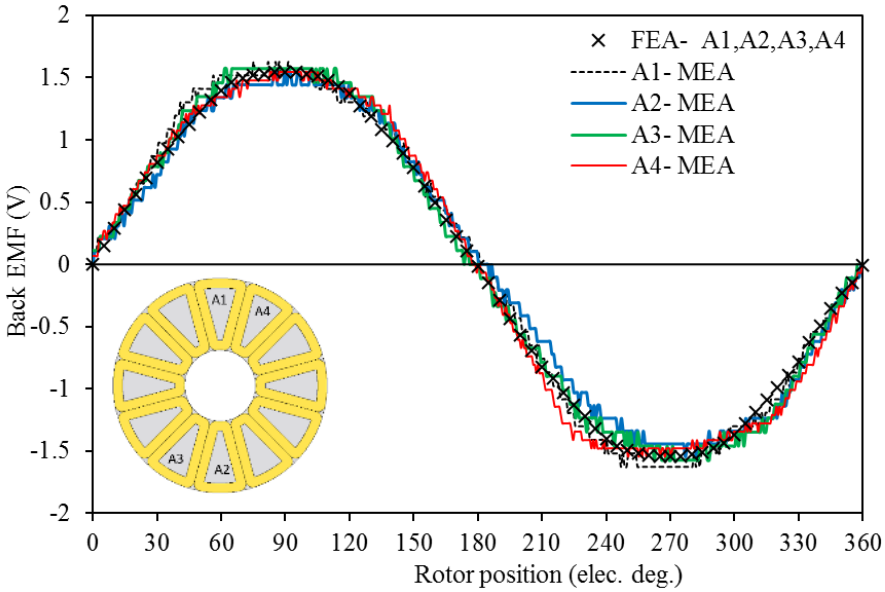

(a) Waveforms

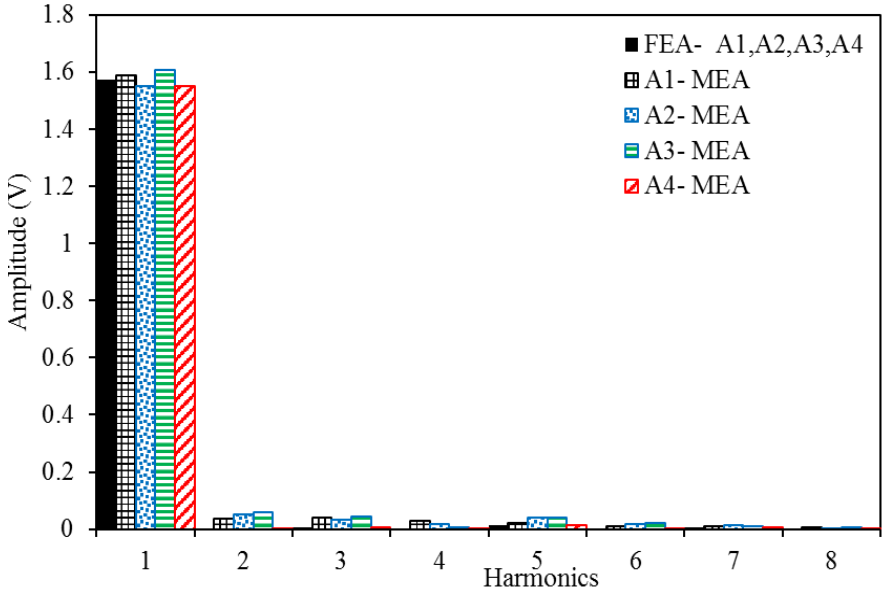

(b) Harmonic spectra

Fig. 6.13. Comparison of the predicted and measured phase back EMF waveforms of phase (A) coils of the magnetically geared machine at rated speeds.

6.2.2.3 Static torque

With the aim of validating the MG ratio of the proposed prototype, the no-load MG torque was initially measured. Both HSR and LSR were connected to an individual beam. The stator was kept stationary while different forces were applied to the HSR by applying different weights to the HSR beam. The HSR force and position were measured along with the corresponding LSR MG static torque with the aid of a digital scale, as indicated in Fig. 6.14. The torque was calculated with the same method used in the YASA machine calculation. The predicted and

measured HSR and LSR static torques at different rotor positions are indicated in Fig. 6.15. It is evident that the MG ratio between LSR and HSR is approximately 1.40, and a good match between predicted and measured results has thus been obtained.

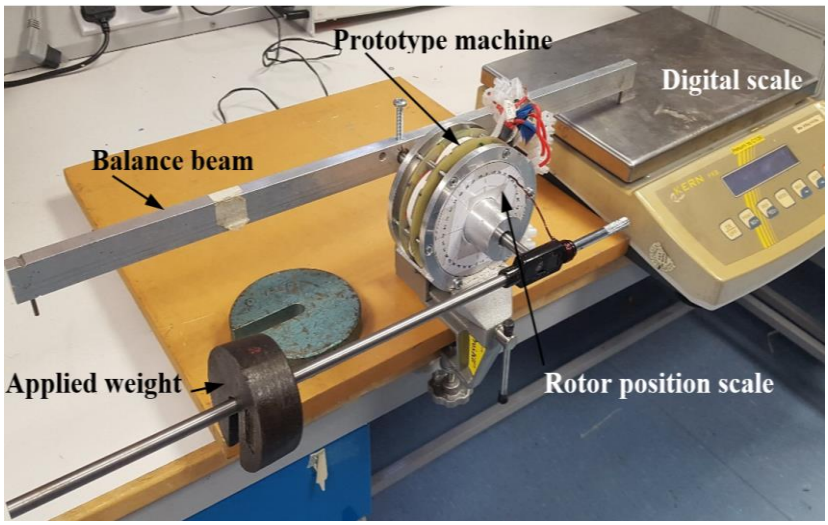

Fig. 6.14. Magnetically geared prototype no-load static torque test rig.

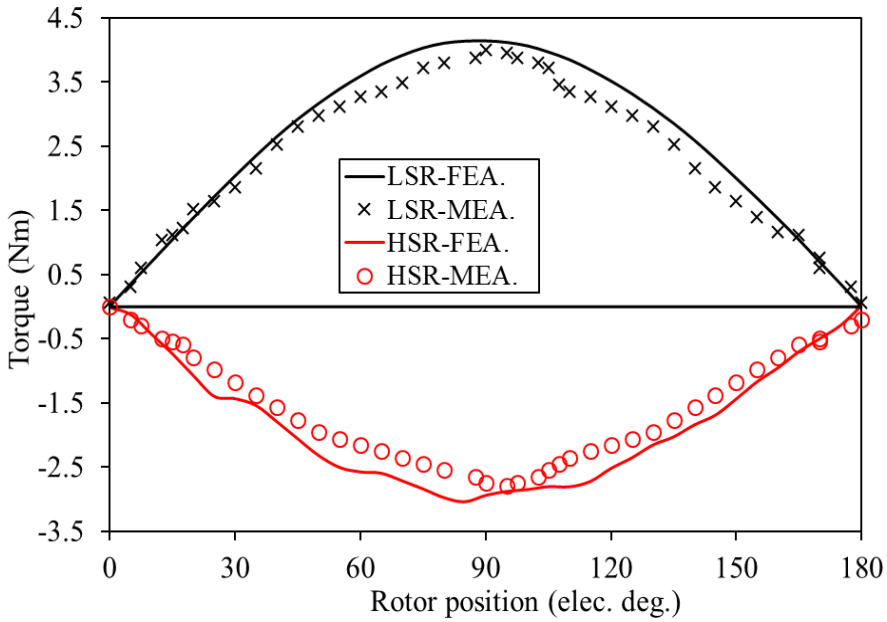

Fig. 6.15. Prototype predicted and measured HSR and LSR static torques at no-load.

The static torque at on-load was also examined with the aid of the test rig shown in Fig. 6.3 and the same static torque measuring method described for the YASA machine. It should be mentioned that due to HSR and LSR have different pole number, the static torque for the proposed magnetically geared prototype was measured for each rotor individually. To do this, one rotor was fixed in place to the stator with a clamp which was fixed into the jaws of the lathe machine,

as indicated in Fig. 6.16. The other rotor shaft was connected to the balance beam to measure the force produced by the prototype using a digital scale. In this case, the rotor was stationary, and the fixed stator and rotor were then rotated at the same relative position to vary the other rotor's position. The prototype on-load static torque was measured by supplying the stator windings with a DC current ($I_a=I$, $I_b=I_c=-½I$). Moreover, to maximise the on-load LSR/HSR torques, the d-axis of the fixed rotor pole and the phase (A) stator pole had to be aligned. Fig. 6.17 indicates different HSR relative positions for instance with respect to the stator position and the corresponding measured and predicted static LSR torque results. Clearly, the LSR static torque reached its maximum value when the d-axis of the fixed HSR and d-axis of phase (A) were aligned (Position 1) while the torque had a trivial decrease at Position 2. However, the peak torque is at minimum value at Position 3, in which the d-axis of the HSR pole differs by 90 deg. elec. from the axis of phase (A) (18 mech. deg.). Moreover, Fig. 6.18 illustrates the flux line of the armature current and the fixed rotor fluxes at different positions. It can be seen that at positions 1 and 2, the stator pole and the rotor pole are facing each other in which the flux passes to the stator pole is maximised. However, at position 3 the rotor pole flux is partly passing between the rotor pole and the stator, and high circulating leakage flux exists at this position. Therefore, Position 1 for the fixed rotor was always adjusted for the static torque measurement of the other rotor. This position can be practically obtained by applied DC current into the winding of phase A while both rotors are free. In this case both rotors are dragged to the position where the d-axes of both rotors and the d-axis of phase A are located at the same line which is the same as Position 1.

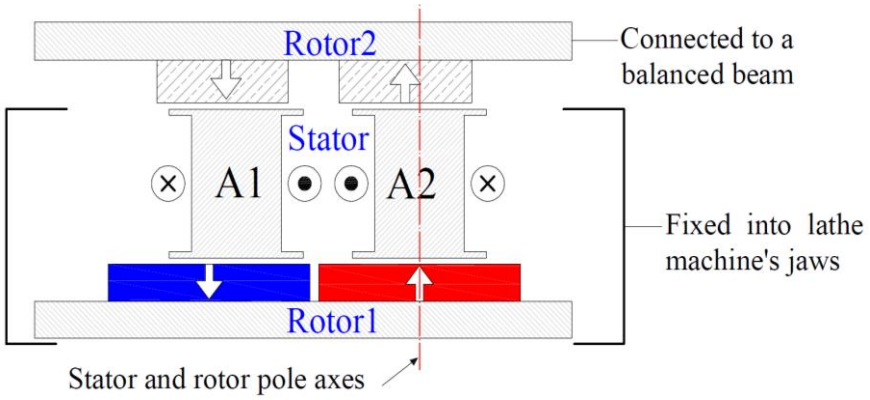

Fig. 6.16. Alignment of the fixed rotor pole and stator pole positions.

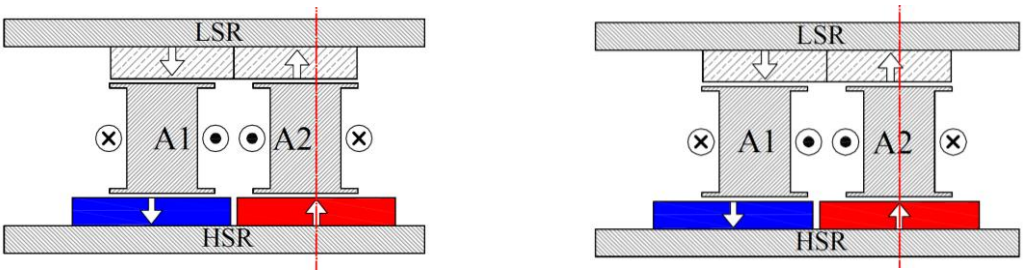

(a) HSR pole Position 1

(b) HSR pole Position 2

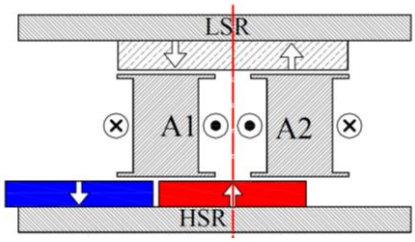

(c) HSR pole Position 3

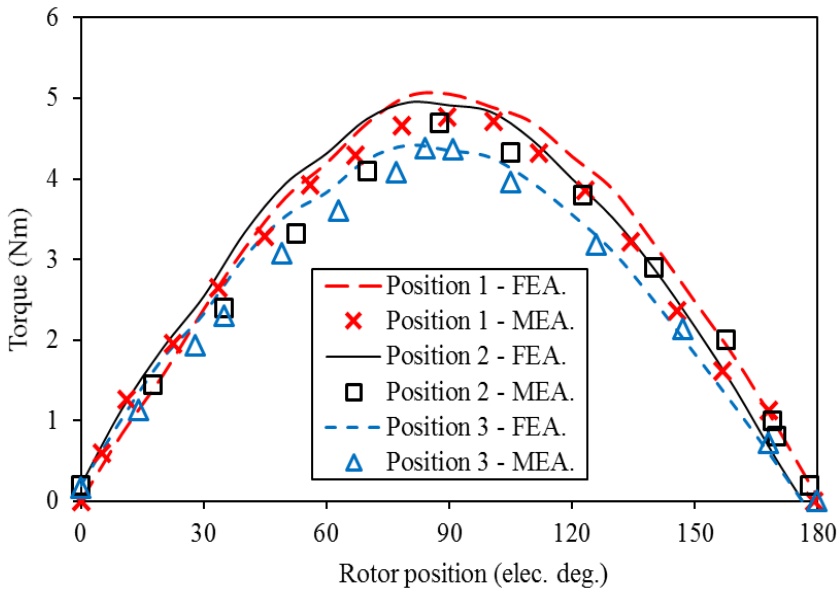

(d) Static torque

Fig. 6.17. The predicted and measured LSR static torques of the prototype at 6 Amp. for different HSR positions.

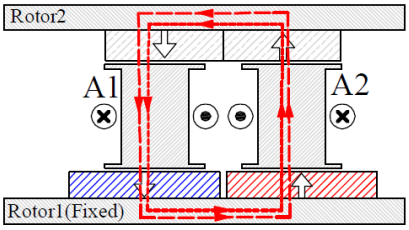

(a) HSR pole Position 1

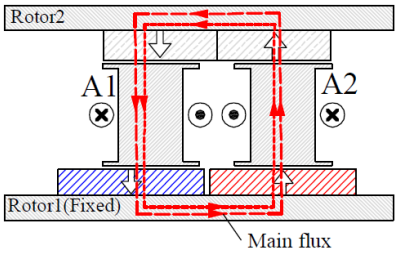

(b) HSR pole Position 2

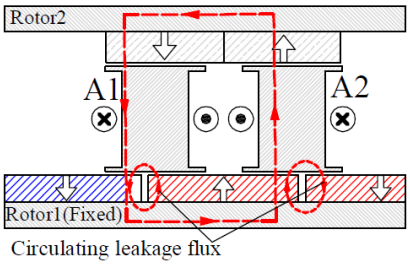

(c) HSR pole Position 3

Fig. 6.18. Main flux and leakage flux lines of fixed rotor.

The measured and predicted LSR static torques at different stator currents are firstly compared in Fig. 6.19(a). When the stator winding is fed a specific current, electromagnetic torque can be obtained, and the total torque increases further as the LSR position changes. Moreover, the maximum torque linearly increases with the current and the predicted and measured torque constants are approximately 0.19 Nm/A, and 0.18 Nm/A, respectively, as can be seen in Fig. 6.19(b). Similarly, a comparison between the measured and predicted HSR static torques at different stator currents is shown in Fig. 6.20(a). In this case, the rotor was stationary, and the fixed stator and rotor were then rotated at the same relative position to vary the other rotor's position. It is clear that the HSR has the same characteristics of the LSR torque and the torque is also prepositional to the stator current where the predicted and measured torque constants are approximately 0.15 Nm/A, as shown in Fig. 6.20 (b). Furthermore, a good validation between measured and predicted results for LSR and HSR torques has been achieved.

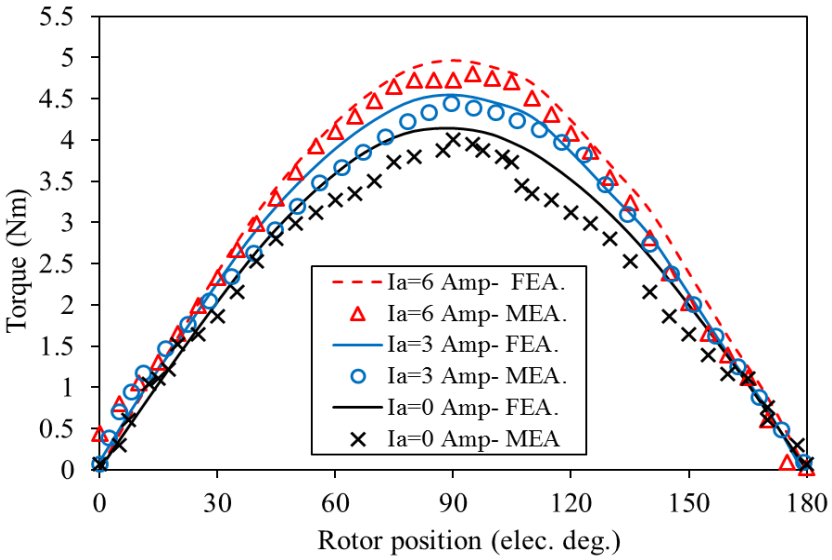

(a) LSR static torque curves at different maximum currents

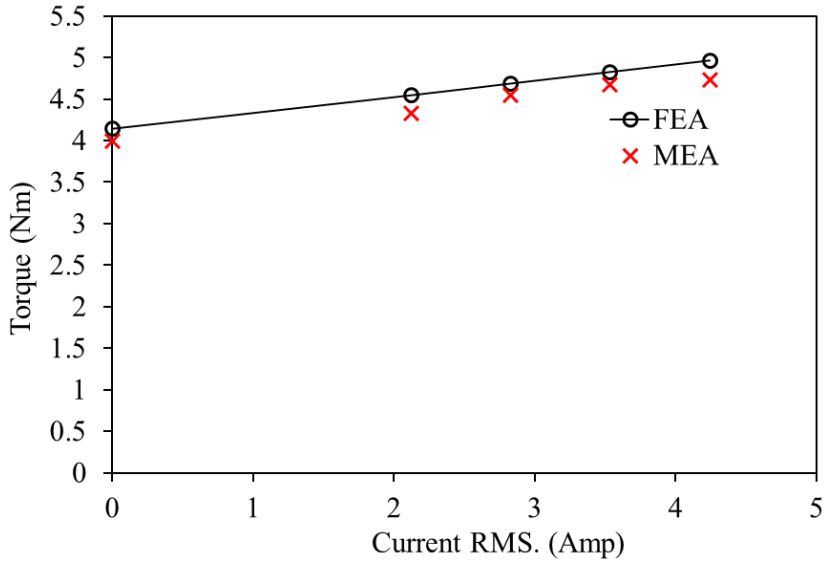

(b) Torque-current curves.

Fig. 6.19. Comparison of the predicted and measured LSR static torques.

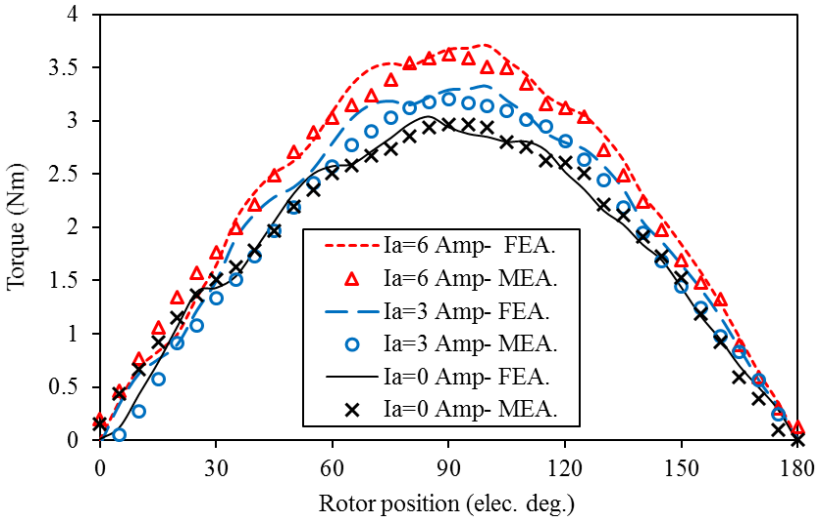

(b) HSR static torque curves at different maximum current.

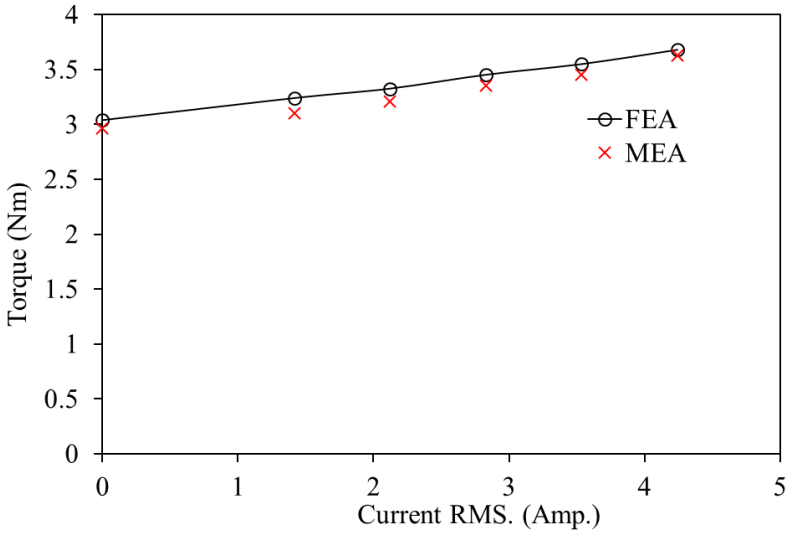

(c) Torque- current curves

Fig. 6.20. Comparison of the predicted and measured HSR static torques

However, according to the obtained results shown in Fig. 6.19 (b) and Fig. 6.20 (b), the magnetic geared prototype has a slightly lower peak torque at all current values. This may be due to manufacturing tolerances, such as stator/rotor misalignment, which thus results in considerable torque reduction.

6.3 Performance comparison of magnetically geared and YASA prototypes

Following the prototyping and testing of the proposed magnetically geared and YASA machine, a performance comparison between the machines' results and the FE results was carried out. The main objective of the comparison is to investigate the feasibility of improving the machine performance by combining the MG machine with a conventional PM machine.

6.3.1 Cogging torque

A comparison of the measured and predicted cogging torques of the proposed MG12/5-7 and YASA prototypes is performed. The cogging torques of the LSR of AFMGPM and YASA12/10 machines are compared in Fig. 6.21, whereas Fig. 6.22 shows a comparison between the HSR and YASA12/10 cogging torques. It is clear that the predicted LSR cogging torque of the proposed machine has the lowest cogging torque amplitude of 0.06 Nm while amplitudes of the measured HSR and YASA cogging torques are approximately identical of 0.1 Nm.

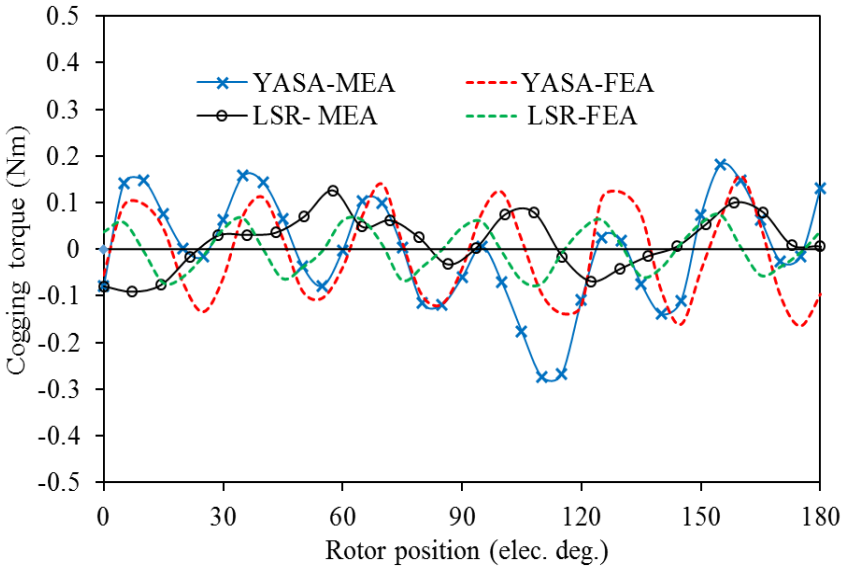

(a) Waveforms

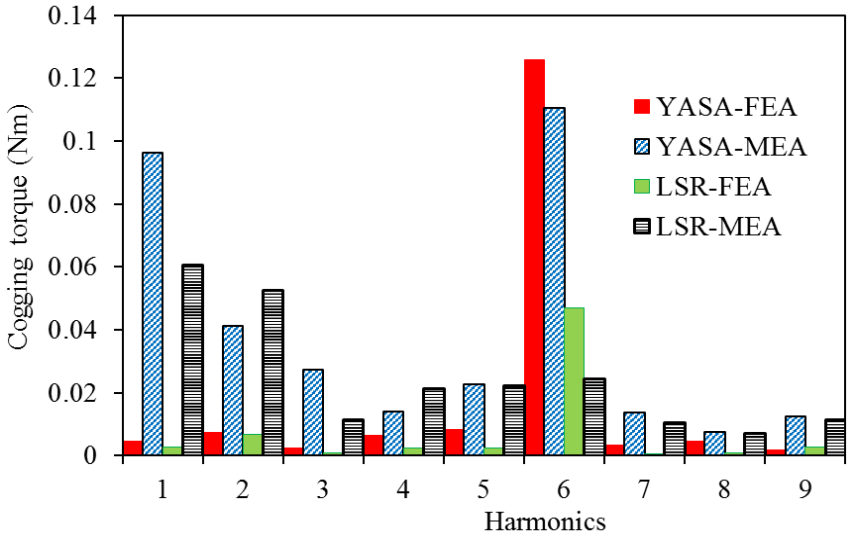

(b) Harmonic spectra

Fig. 6.21 Comparison of cogging torques for the proposed magnetically geared machine LSR and YASA machine.

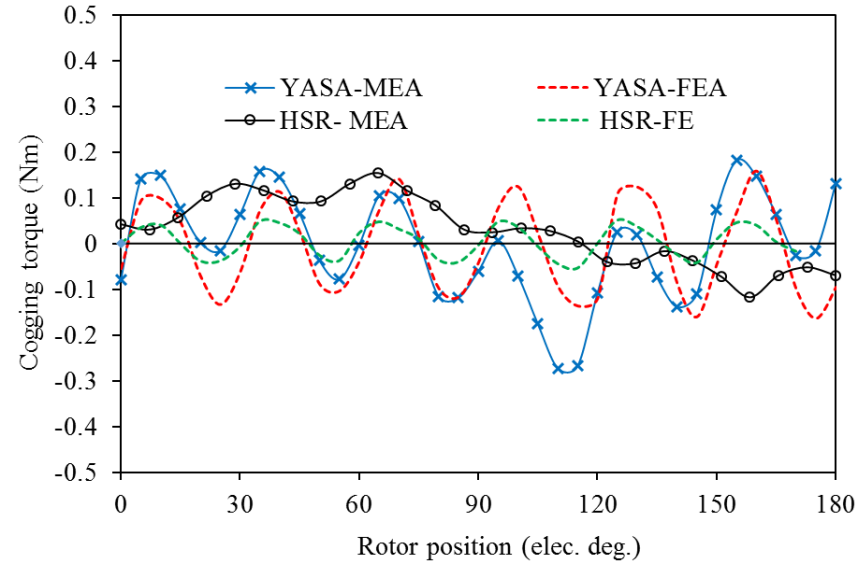

(a) Waveforms

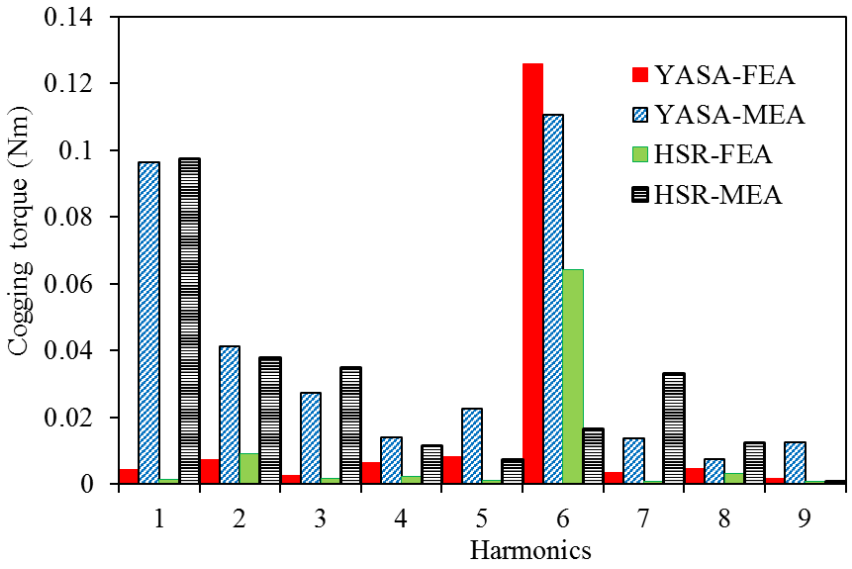

(b) Harmonic spectra

Fig. 6.22 Comparison of cogging torques for the proposed magnetically geared machine HSR and YASA machine.

6.3.2 No load back –EMF

The no-load phase back EMFs of the magnetically geared machine and YASA machine prototypes were performed and validated with the 3D-FE results. To do that, the YASA prototype and the HSR of the AFMGPM prototype are driven by a prime-mover at 400 rpm. Fig. 6.23 shows a comparison of predicted and measured back EMFs of YASA machine together with AFMGPM machine. It can be evidenced that, the phase back EMF amplitude of YASA machine is slightly

higher for the predicted and measured values, being approximately 7V and 6.7V, respectively. Whereas, the AFMGPM machine has the predicted and measured back EMF amplitudes of approximately 6.2V and 5.9V, respectively.

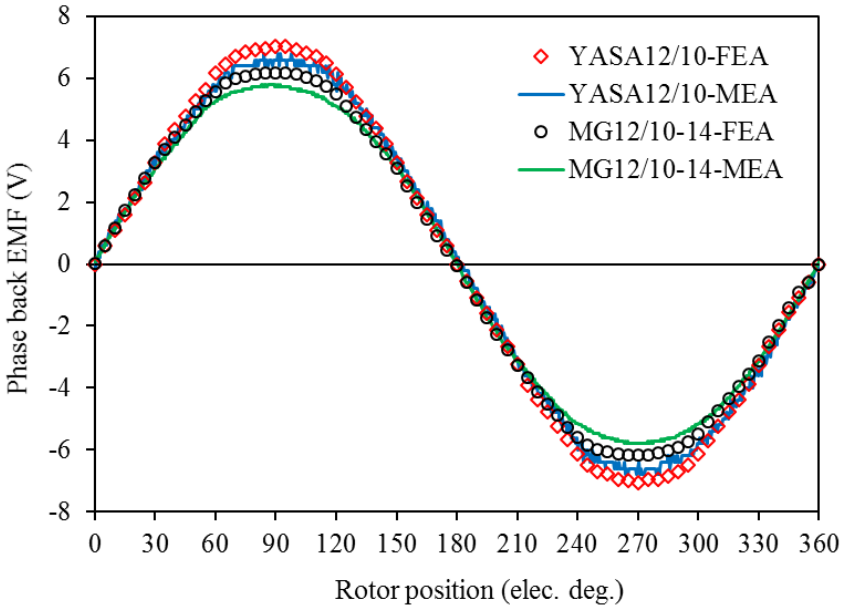

(a) Waveforms

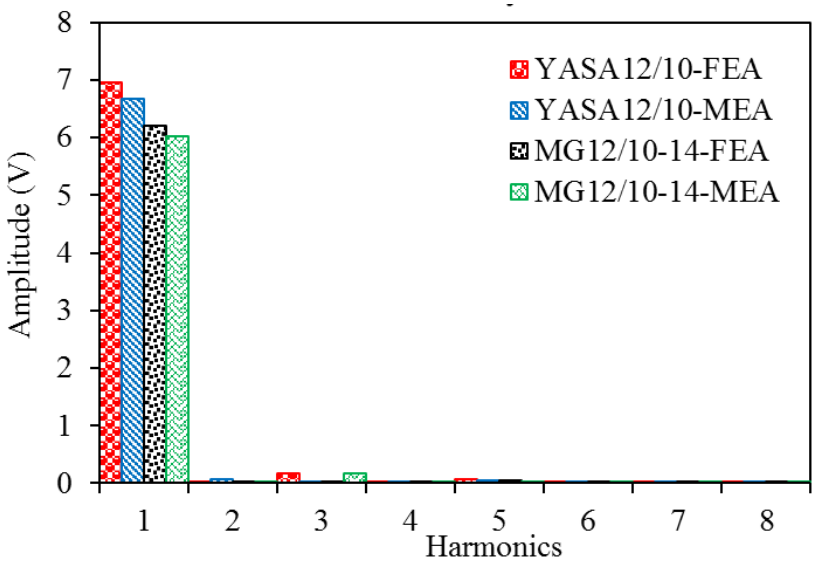

(b) Harmonic spectra

Fig. 6.23. Comparison of phase back EMFs for the proposed magnetically geared machine and YASA machine rated speeds.

6.3.3 Static torque

Fig. 6.24 shows a comparison of the static torque of YASA machine and LSR of the magnetically geared machine at half-load and full-load whereby the LSR of magnetically geared machine is assumed as output rotor. Similarly, Fig. 6.25 shows a comparison of the static torque of YASA

machine and HSR static torque of the proposed magnetically geared machine. It is evident that for both prototype machines, the measured and predicted results are in good agreement. However, maximum torques of LSR and HSR are significantly higher than those of the conventional YASA machine maximum torque at the same current. The MG effect noticeably increases the torque density since the resulting torque of the magnetically geared machine is the summation of the armature current and MG effect torques.

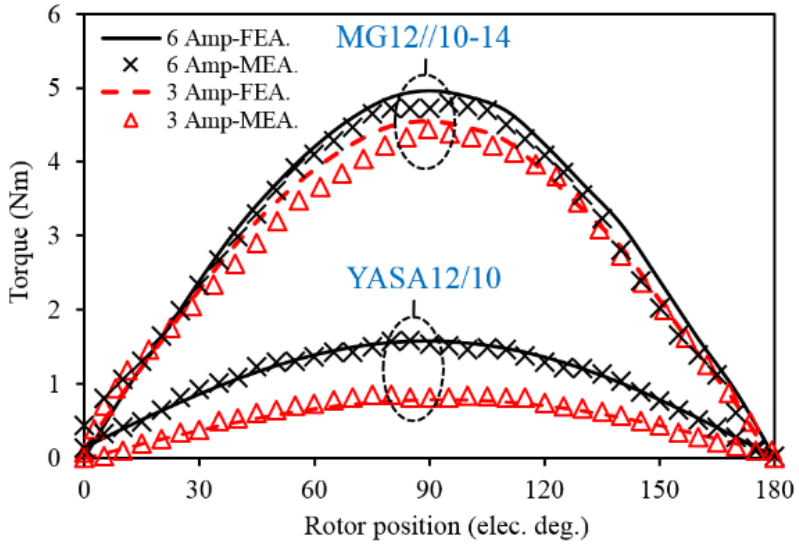

(a) Static torque at half load and full load

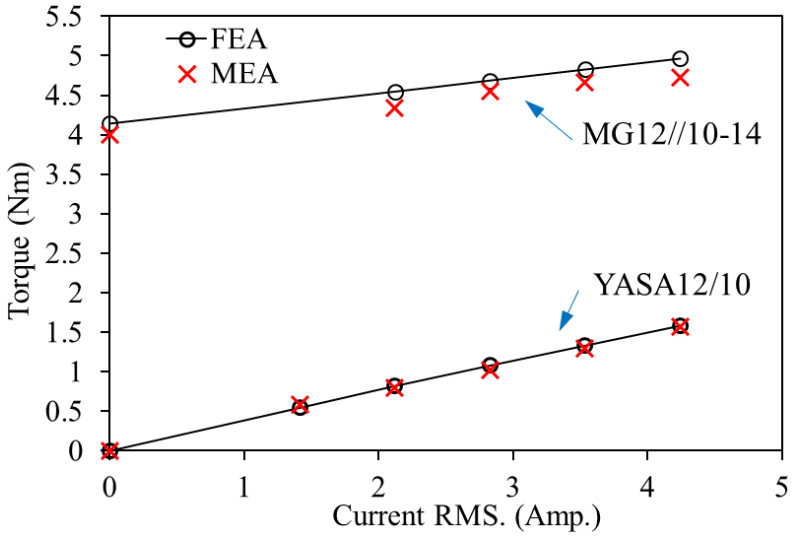

(b) Torque – current curves

Fig. 6.24. Comparison of measured and predicted torques of LSR and YASA12/10.

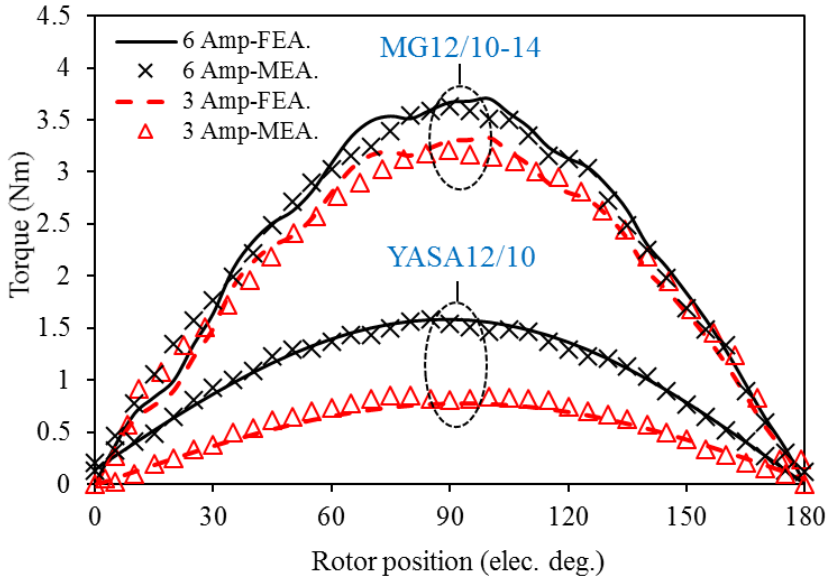

(a) Static torque at half load and full load

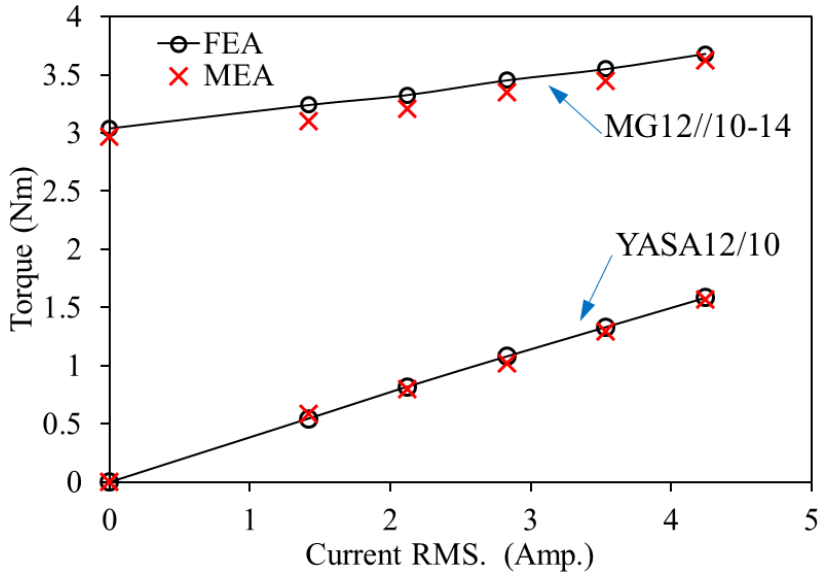

(b) Torque – current curves

Fig. 6.25. Comparison of measured and predicted torques of HSR and YASA12/10.

6.4 Summary

In this chapter, following the operation principles of a magnetically geared and YASA machine, prototype machines were fabricated for experimental tests. Both machine structures were investigated and the experimental methodology fully described. The results at no-load and on-load were measured and compared with the FEA results. Finally, the measured and predicted results for the proposed magnetically geared machine and YASA machine at no-load and on-load have been compared. The measured results indicate that the YASA machine has a slightly superior performance at generating mode, whereas the axial flux magnetically geared prototype has significantly higher torque at the motoring mode compared with the conventional YASA prototype. Therefore, the torque density of conventional AFPM machine can be improved by combining the MG machine with such AFPM machine. However, the dynamic control of the machines with double rotors is difficult in term of both control and test rig setup. A test rig with two torque transducers and controllers must be utilized to determine the position of both rotors. Therefore, due to the time and equipment limits, it cannot be done for the moment.

CHAPTER 7

CONCLUSIONS AND FUTURE WORK

7.1 Conclusions

Research has shown that among the AFPM topologies the YASA machine has the merits of unique structure and superior performance, and can be used for various applications. Different rotor pole combinations of the YASA machine with the same stator pole have been optimised and the performance comparisons have been carried out. The proposed axial flux magnetically geared machine is then designed based on YASA topology by utilising two rotors with different poles. In order to investigate the performance of the proposed axial flux magnetically geared machine for HEVs applications, the 3D-FE models were utilised to optimise the topology for maximum output torque. The optimisations have been presented, together with some design guidelines to achieve the design objectives. Two topologies have been studied for the new machine, the first of which employs an HSR of 5 pole pairs and an LSR of 7 pole pairs, rotating at speeds of 400 rpm and 285.7 rpm, respectively. Meanwhile, the second topology employs an HSR of 4 pole pairs and an LSR of 8 pole pairs that rotate at 400 rpm and 200 rpm, respectively. The influence of the machine parameters on the machine HSR and LSR torques was then studied comparatively. The proposed topology for power split applications in HEVs has also been investigated. Various operating modes of the proposed topologies were studied comparatively. Moreover, in order to examine the machine under the proposed application, some practical considerations have been taken into account. A method for matching the armature current torque with the output MG torque has been described. The machine can realise MG and generator functions (power split) in which the applied input mechanical torque can be scaled up or down, while an electrical power can be obtained by the stator windings to charge a battery. The output torque, which is delivered by magnetic gearing effect, can be increased by an adjustment of the armature current torque through current angle control.

It was found that at the same stator pole number, the torque performance of the YASA machine increases with the rise of rotor pole number since the slot opening has a significant effect on the improvement of the obtained torque. Moreover, at constant AFMGPM machine volume, the PM dimensions, slot opening, and inner diameter have significant impacts on the torque performance. In addition, the proposed topology has balanced and sinusoidal back EMF since asymmetric EMF is a common problem in many configurations of magnetically geared machines due to the

imbalance in the magnetic circuits of the windings. However, the topology with an HSR of 4 pole pairs and an LSR of 8 pole pairs showed high leakage flux that results in low power factor and hence lower electrical output power at generating mode. In addition, at motoring mode of the proposed machine, the current should be applied when the initial relative angle is approached to 90^0 for superior performance. When the current is applied at a small relative angle, the input rotor is affected by the armature current torque, which results in a portion of this torque being added to the input torque. Therefore, a method for controlling the machine under the proposed application was described. It has been shown that at motoring mode, the armature current is utilised to keep the machine operating point at the stable region during the changing of the load torque. In addition, the performance of each AFMGPM topology was compared to its YASA machine counterparts at different load conditions. The comparison shows that a higher torque density and a significantly lower cogging torque can be obtained by the proposed machine compared with the YASA machine counterparts since the proposed machine has a gearing effect torque in addition to the armature reaction torque.

Moreover, rotor/stator misalignment, which is one of the most significant aspects in terms of manufacturing tolerance for AFPM machines, has been studied for the proposed MG12/5-7 machine. The influence of static and dynamic LSR/stator misalignments on the performance of the proposed machine was analysed and compared with reference to the healthy case. Regarding the two misalignment types considered -axis LSR misalignment and angular LSR misalignment- it was found that, with reference to the previous researches on conventional AFPM topologies, the effects of rotor misalignment on the magnetically geared and conventional AFPM machines are approximately the same. The LSR/stator axis misalignment results in a fair reduction in the average torque due to the fringing flux and additional cogging torque harmonics caused by the additional air-gap flux density harmonics. A slight change occurs in the 3-phase back-EMF waveform, with the degree of such change depending on the misalignment distance. This study also examined the influence of LSR/stator angular misalignments on the performance of the proposed machine. The results clearly indicate that angular misalignment has an insignificant effect on the machine performance compared with LSR/stator axis misalignment since the study has been carried out at low misalignment factor due to the air-gap being small and the studied angular misalignment being limited by the gap distance. More effects of the influence of angular misalignment such as unbalanced back EMF and cogging torque may be expected at larger air-gap width.

Finally, prototype machines of the proposed AFMGPM machine and the YASA machine were designed and fabricated for experimental tests. Both machines shared the same stator comprising 12 poles and the same 10 pole rotor. The AFMGPM machine prototype could be assembled by replacing one rotor of the YASA machine with a rotor of 14 poles. The experimental methodology was then fully described. It has been shown that the static torque can be measured using the same methodology as for the conventional PM machine. This can be done by keeping both the stator and one rotor stationary while the rotor position is changed by the other rotor. Moreover, the results of both prototypes at no-load and on-load were measured and validated with the FEA results. The measured results indicate that both prototypes have sinusoidal and approximately symmetrical 3-phase back EMF waveforms and the YASA machine prototype has a slightly higher phase back EMF amplitude since the magnetically geared topology has two rotors with different pole pairs. The AFMGPM machine has significantly higher maximum torque compared with the YASA prototype, which demonstrates that the torque density of the conventional AFPM machine can be improved by combining the MG machine with this type of axial flux machine.

7.2 Future work

The aim of this thesis was achieved as the proposed machine demonstrated the expected electromagnetic performance. However, as a result of this work some research areas for future development have emerged and are presented as follows:

- During the optimisation process for the proposed machine, the slot opening of the stator slots was assumed as identical for both the HSR and the LSR sides. It has also been shown that the slot opening has an important effect on the machine performance. However, since the rotor pole arcs of both rotors were unequal, individual optimisation of the slot opening of each stator side should have an impact on the leakage flux as well as the material volume of the machine. Therefore, the machine performance such as torque, iron loss and power factor at generating and motoring modes can be expected to be improved when the slot opening is optimised individually. Moreover, investigations of the slot opening effect for different gear ratios which can be obtained by other stator / rotor pole combinations (for example, stator with segments of 18 poles), which have more potential rotor pole combinations according to the MG operation principle should be conducted. Undertaking a comparative study of machines with different stator segments, examining the effect of the slot opening width for different stator/rotor poles on the gearing effect performance, and predicting which stator/rotor combination can be combined with conventional machines to design a magnetically geared machine with high quality performance is also recommended. Optimisation of the machine parameters including

air-gap width is essential for this study and a comparative electromagnetic performance can be carried out under different slot opening of both sides of the stator at different air-gap widths. This investigation would be a good reference for axial flux magnetically geared machine design and therefore recommended for future work.

- Regarding machine design, surface mounted PMs with axial magnetisation were considered for the machine topology in which the NdFeB magnet was utilised. Therefore, it would be interesting to conduct further investigation and performance comparison for various PM arrangements, such as flux focusing PM, consequent pole and Halbach permanent magnet arrays, since these arrangements have been utilised for MG topologies and the investigations show that such topologies have high performance potential. Additionally, while it has been proved that the flux focusing type has the merit of high air-gap flux density, with the aim of reducing cost, it would also be interesting to investigate the machine performance with different rotor PM arrangements utilising different magnet types which have low remanence, such as Ferrite magnets. Many aspects can be investigated for these topologies. Regarding the magnet type, a performance comparison can be conducted between surface mounted PM machine, consequent pole, and Halbach PM array. By introducing a consequent pole, the PM material would be reduced. In addition, a high torque density could be obtained by Halbach array according to the previous topologies. On the other hand, the performance of these topologies can be compared with different low cost PM materials. Therefore, these topologies can be optimised utilising 2D-FEM, then, with the aid of 3D models, the performance of different machine topologies (i.e. back EMF, torque, torque ripple and efficiency) should be compared and investigated.
- For HEV application, further investigation is recommended of a real driving cycle by undertaking the control model of the machine under various patterns such as acceleration and deceleration and preferably in a typical driving cycle of the HEV. Control strategy of this kind of machine has been describe and the control design is highly recommended. The first part of the method should be to describe the machine's dynamic equations and the main control method. Additionally, practical issues, such as the dynamic start up function, the rotor position estimation, and the performance of the speed/torque control should be considered. Furthermore, a control model for the proposed machine utilising MATLAB simulation of the machine under electric vehicles environments would be recommended for future work.
- The design and analysis of the machines presented in this thesis have been restricted to electromagnetic performance: thermal and mechanical aspects were not covered due to time

constraints. For these types of machines in which a modulator with windings is located between two rotors, a cooling system may be difficult to set up when the machine is operating at high electrical load. Thus, a thermal analysis should be studied through the design process. Moreover, the machine suffers from high axial force applied on the machine stator due to different rotors. Therefore, these aspects are vital to the design. A study can be conducted using FEM analysis of the machine topology. A thermal lumped circuit method can be also conducted and then compared to the results obtained by FEM. Moreover, the investigation of the mechanical aspects such as the forces applied on the rotor back iron and the shaft bearing are important for the machine mechanical design. By calculating the stress applied on the machine rotors, the force acting on the rotor shaft and then the bearing system can be estimated. Since both thermal and mechanical studies are important for axial flux topologies, they are recommended as worthy topics for future work.

REFERENCES

[ABD12a] A. Abdel-Khalik, A. Massoud, A. Elserougi, and S. Ahmed, "A coaxial magnetic gearbox with magnetic levitation capabilities", *20th Int. Conf. Elec. Mach.*, 2012, pp. 542-548.

[ABD12b] A. Abdel-Khalik, A. Massoud, A. Elserougi, and S. Ahmed, "A coaxial magnetic gearbox with magnetic levitation capabilities", *XXth Int. Conf. on Elec. Mach. (ICEM), , 2012*, pp. 542-548.

[ACH13] V. M. Acharya, J. Z. Bird, and M. Calvin, "A Flux focusing axial magnetic gear", *IEEE Trans. on Magn.*, vol. 49, no. 7, pp. 4092-4095, July 2013.

[AFS15] S. A. Afsari, H. Heydari, and B. Dianati, "Cogging torque mitigation in axial flux magnetic gear system based on skew effects using an improved quasi 3-D analytical method", *IEEE Trans. on Magn.*, vol. 51,no. 9, pp. 1-11, Sep.2015.

[ATA01] K. Atallah and D. Howe, "A novel high-performance magnetic gear", *IEEE Trans. on Magn.*, vol. 37, no.4, pp. 2844-2846, July 2001.

[ATA04] K. Atallah, S. D. Calverley, and D. Howe, "Design, analysis and realisation of a high-performance magnetic gear", *IEE Proc. Elec. power Appl.*, vol. 151, no. 2 pp. 135-143, Mar. 2004.

[ATA08] K. Atallah, J. Rens, S. Mezani, and D. Howe "A novel "pseudo" direct-drive brushless permanent magnet machine", *IEEE Trans. on Magn.*, vol. 44, no.11, pp. 4349-4352, Nov. 2008.

[AYD02] M. Aydin, H. Surong, and T. A. Lipo, "A new axial flux surface mounted permanent magnet machine capable of field control", *IEEE Ind. Appl. Conf.*, 2002, pp. 1250-1257.

[AYD04] M. Aydin, H. Surong, T.A. Lipo "Axial flux permanent magnet disc machines: A review", *Research Report*, 2004.

[AYD06] M., Aydin, Surong Huang, T.A. Lipo, "Torque quality and comparison of internal and external rotor axial flux surface-magnet disc machines", *IEEE Trans. on Ind. Electronics*, vol.53, no.3, pp.822,830, June 2006.

[AYD07] Aydin, M., Zhu, Z.Q., Lipo, T.A., Howe, D., "Minimization of cogging torque in axial-flux permanent-magnet machines: design concepts", *IEEE Trans. on Magn.*, vol.43, no.9, pp.3614,3622, Sep. 2007.

[BIA06] N. Bianchi and M. D. Pre, “Use of the star of slots in designing fractional-slot single-layer synchronous motors”, *IEE Proc. Elect. Power Appl.*, vol. 153, no. 3, pp. 459-466, May 2006.

[BOB15] D. Bobba, Y. Li and B. Sarlioglu, “Harmonic analysis of low-stator-slot and rotor-pole combination FSPM machine topology for high speed”, *IEEE Trans. on Magn.*, vol. 51, no. 11, pp. 1-4, Nov. 2015.

[BOM14] W. Bomela, J. Z. Bird, and V. M. Acharya, “The performance of a transverse flux magnetic gear”, *IEEE Trans. on Magn.*, vol. 50, no. 1, pp. 1-4, Jan. 2014.

[BOR09] H. A. Borhan, A. Vahidi, A. M. Phillips, M. L. Kuang, and I. V. Kolmanovsky, “Predictive energy management of a power-split hybrid electric vehicle”, *American Control Conf.*, 2009, pp. 3970-3976.

[CAM12] R. Camilleri, T. Woolmer, A. Court and M. D. McCulloch, “Investigation into the temperature profile of a liquid cooled YASA© AFPM machine”, *6th IET Inter. Conf. on Power Elect., Mach. and Drives (PEMD)*, Bristol, 2012, pp. 1-8.

[CAP14] F. G. Capponi, G. De Donato, G. Borocci, and F. Caricchi, “Axial-Flux Hybrid-Excitation Synchronous Machine: Analysis, Design, and Experimental Evaluation”, *IEEE Trans. on Ind. Appl.*, vol. 50, no. 5, pp. 3173-3184, Sep.-Oct. 2014.

[CHA07] K. T. Chau, Z. Dong, J. Z. Jiang, L. Chunhua, and Z. Yuejin, “Design of a magnetic-geared outer-rotor permanent-magnet brushless motor for electric vehicles”, *IEEE Trans. on Magn.*, vol. 43, no.6, pp. 2504-2506, June 2007.

[CHE03] L. Cheng-Tsung, T. S. Chiang, J. F. D. Zamora, and S. C. Lin, “Field-oriented control evaluations of a single-sided permanent magnet axial-flux motor for an electric vehicle”, *IEEE Trans. on Magn.*, vol. 39, no. 5, pp. 3280-3282, Sep.2003.

[CHE14] Y. Chen, W. N. Fu, S. L. Ho, and H. Liu, “A quantitative comparison analysis of radial-flux, transverse-flux, and axial-flux magnetic gears”, *IEEE Trans. on Magn.*, vol. 50, no. 11, pp. 1-4, Nov. 2014.

[COL08] J. Colton, D. Patterson, and J. Hudgins, “Design of a low-cost and efficient integrated starter-alternator, *4th IET Conf. on Power Electr., Mach. and Drives*,(PEMD), 2008, pp. 357-361.

[CRO02] J. Cros and P. Viarouge, “Synthesis of high performance PM motors with concentrated windings”, *IEEE Trans. on Energy Conv.*, vol. 17, no.2, pp. 248-253, June, 2002.

[DU10] A. Du, X. Yu, and J. Song, “Structure design for power-split hybrid transmission”, *IEEE Int. Conf. on Mechatronics and Automation,* 2010, pp. 884-887.

[EGE12] A. Egea, G. Almandoz, J. Poza, G. Ugalde, and A. J. Escalada, “Axial-Flux-Machine Modeling With the Combination of FEM-2-D and Analytical Tools”, *IEEE Trans. on Ind. Appl.,* vol. 48,no. 4 pp. 1318-1326, July/Aug. 2012.

[EHS07] M. Ehsani, Y. Gao, and J. M. Miller, “Hybrid electric vehicles: architecture and motor drives”, *Proc. of the IEEE,* vol. 95, no. 4, pp. 719-728, April 2007.

[FRA09] N. W. Frank and H. A. Toliyat, “Gearing ratios of a magnetic gear for wind turbines”, *in Proc. IEEE Int. Conf*. on *Elec. Mach. Drives,* 2009, pp. 1224-1230.

[GAS09] L. Gasparin, A. Cernigoj, S. Markic, and R. Fiser, “Additional cogging torque components in permanent-magnet motors due to manufacturing imperfections”, *IEEE Trans. Magn.*, vol. 45, no. 3, pp. 1210–1213, Mar. 2009

[GER14] A. D. Gerlando, G. M. Foglia, M. F. Iacchetti, and R. Perini, “Analysis of stray paths for parasitic currents in some topologies of yokeless and segmented armature axial flux PM machines” *Int. Conf. on Elect. Mach. (ICEM)*, 2014, pp. 390-395.

[GIE08] J. F. Gieras, R. J. Wang, M. J. Kamper, “Axial flux permanent magnet brushless machines”, Second Edition, Springer. 2018.

[GIU12] Giulii Capponi, F., De Donato, G., Caricchi, F., “Recent advances in axial-flux permanent-magnet machine technology”, *IEEE Trans. on Ind. Appl.*, vol.48, no.6, pp.2190,2205, Nov.-Dec. 2012.

[GOU11] E. Gouda, S. Mezani, L. Baghli, and A. Rezzoug, “Comparative Study Between Mechanical and Magnetic Planetary Gears”, *IEEE Trans. on Magn.,* vol. 47, no. 2, pp. 439-450, Feb. 2011.

[GUO17] B. Guo; Y. Huang; F. Peng; Y. Guo; J. Zhu, “Analytical modeling of manufacturing imperfections in double rotor axial flux PM machines: effects on back EMF”, *IEEE Trans. on Magn.,* vol.53, no.6, pp.1-1, June 2017.

[HAN94] D.C. Hanselman. “Brushless Permanent-Magnet Motor Design”, No. 2. McGraw-Hill, Inc., 1994.

[HAO12] Li Hao, Mingyao Lin, Wan Li, Hao Luo, Xinghe Fu, Ping Jin, “Novel dual-rotor axial field flux-switching permanent magnet machine”, *IEEE Trans. on Magn.* , vol.48, no.11, pp.4232,4235, Nov. 2012.

[HEM14] A. Hemeida and P. Sergeant, “Analytical modeling of eddy current losses in Axial Flux PMSM using resistance network”, *Inte. Conf. on Elect. Mach., (ICEM), 2014*, 2014, pp. 2688-2694.

[HES80] D. E. Hesmondhalgh, D. Tipping, “A multielement magnetic gear”, *IEE Pro. Elec. Power Appl.*, vol. 127, no. 3, pp. 129-138, May1980.

[HUA01] S., Huang, M., Aydin, T.A., Lipo, “TORUS concept machines: pre-prototyping design assessment for two major topologies”, *Thirty-Sixth IAS Annual Meeting Ind. Appl. Conf.*, 2001, vol.3, pp.1619, 1625.

[HUA02] S. Huang, M. Aydin, and T.A. Lipo. “A direct approach to electrical machine performance evaluation: Torque density assessment and sizing optimisation”, I*nt. Conf. on Elec. Mach.(ICEM)*, V. Art. 235, 2002.

[HUA14a] Li, Hua-Yang, Shen, Jian-Xin, “Optimal design of an axial flux permanent magnet motor”, *17th Int. Conf. on Elec. Mach. and Sys. (ICEMS),*pp. 3350,3355, 22-25 Oct. 2014.

[HUA14b] Y. Huang, T. Zhou, J. Dong, H. Lin, H. Yang, and M. Cheng, “Magnetic equivalent circuit modeling of yokeless axial flux permanent magnet machine with segmented armature”, *IEEE Trans. on Magn.* , vol. 50, no. 11, pp. 1-4, Nov. 2014.

[ISH05] D. Ishak, Z. Q. Zhu, and D. Howe, “Permanent magnet brushless machines with unequal tooth widths and similar slot and pole numbers”, *IEEE Trans. Ind. Appl.*, vol. l41, no. 2, pp. 584-590, March-April 2005.

[JIA09] L. Jian, K. T. Chau, and J. Z. Jiang, “A Magnetic-geared outer-rotor permanent-magnet brushless machine for wind power generation”, *IEEE Trans. on Ind. Appl.*, vol. 45, no. 3, pp. 954-962, May-June 2009.

[JIA10] L. Jian and K. T. Chau, “Design and analysis of a magnetic-geared electronic-continuously variable system using finite element method”, *Progress in Electromagnetics Research (PIER),* vol. 107, pp. 47-61, July 2010.

[JIA11] L. Jian, G. Xu, “Electromagnetic design and analysis of a novel magnetic gear integrated wind power generator using time stepping finite element method,” *Prog. Electro. Res. (PIER),* vol. 113, pp. 351-367, Feb. 2011.

[JIN10] L. Jian and K. T. Chau, “Design and analysis of a magnetic-geared electronic-continuously variable transmission system using finite element method,” Progress in Electromagnetics Research-Pier, vol. 107, pp. 47-61, 210, 2010.

[JOH17] M. Johnson, M. C. Gardner, and H. A. Toliyat, “Design and analysis of an axial flux magnetically geared generator”. *IEEE Tran. on Ind. Appl.,* vol. 53, no. 1, pp. 97-105, Jan/Feb. 2017.

[KAH14] S. Kahourzade, A. Mahmoudi, P. Hew Wooi, and M. N. Uddin, “A Comprehensive review of axial-flux permanent-magnet machines”, *Canadian Journal of Elec. and Comp. Engin.,* vol. 37, no. 1, pp. 19-33, Winter 2014.

[KHA15] M. F. Khatab, A. L. Shuraiji, and Z. Q. Zhu, “Parametric design optimisation of axial field partitioned stator switched flux PM machine” , *Inte. Conf. on Sustainable Mobility Appl., Renewables and Technology (SMART),* 2015, pp. 1-6.

[KIK93] S. Kikuchi and K. Tsurumoto, “Design and characteristics of a new magnetic worm gear using permanent magnet”, *IEEE Trans. on Magn.,* vol. 29, no. 6, pp. 2923-2925, Nov. 1993.

[KIM17] C. W. Kim, G. H. Jang, J. M. Kim, J. H. Ahn, C. H. Baek, and J. Y. Choi, “Comparison of axial flux permanent magnet synchronous machines with electrical steel core and soft magnetic composite core”, *IEEE Trans. on Mag.s,* vol. 53, no. 11, pp. 1-4, Nov. 2017.

[KOU17] M. B. Kouhshahi, J. Z. Bird, V. Acharya, K. Li, M. Calvin, and W. Williams, “An axial flux-focusing magnetically geared motor”, *IEEE Energy Conv. Cong. and Exposition (ECCE),* 2017, pp. 307-313.

[LAI16] J. Lai, J. Li, R. Qu, R. Zhang, and D. Li, “A novel axial flux magnetic-field-modulated dual-mechanical-port dual-electrical-port machine for hybrid electric vehicle”, *IEEE Vehicle Power and Propulsion Conf. (VPPC),* 2016, pp. 1-6.

[LEZ11] Y. Lezhi, L. Desheng, M. Yuanjing, J. Jiao, “Design and performance of a water-cooled permanent magnet retarder for heavy vehicles,” *IEEE Trans. on Energy Conv.,* vol. 26, no. 3, pp. 953-958, 2011.

[LI16] Y. Li, Q. Lu, Z. Q. Zhu, D. Wu and G. Li, “Superposition method for cogging torque prediction in permanent magnet machines with rotor eccentricity”, *IEEE Trans. on Magn.,* vol. 52, no. 6, pp. 1-10, June 2016.

[LIU17] Y. Liu and Z. Q. Zhu, “Comparative study of magnetic gearing effect in integral slot, fractional slot winding and vernier PM machines”, *20th Inter. Conf. on Elec. Mach. and Sys. (ICEMS),* 2017, pp. 1-6.

[LUB13] T. Lubin, S. Mezani, and A. Rezzoug, “Development of a 2-D Analytical Model for the Electromagnetic Computation of Axial-Field Magnetic Gears”, *IEEE Trans. on Magn.,* vol. 49, no. 11,pp. 5507-5521,Nov. 2013.

[LUO17] X. Luo and S. Niu, “A novel contra-rotating power split transmission system for wind power generation and its dual MPPT control Strategy”, *IEEE Trans. on Power Electronics*, vol. 32, no. 9, pp. 6942-6935, Sep. 2017.

[MAL14] O. Maloberti, R. Figueredo, C. Marchand, Y. Choua, D. Condamin, L. Kobylanski, et al., “3-D-2-D dynamic magnetic modelling of an axial flux permanent magnet motor with soft magnetic composites for hybrid electric vehicles”, *IEEE Trans. on Magn.*, vol. 50, no. 6, pp. 1-11, June 2014.

[MAR08] F. Marignetti, V. D. Colli, and Y. Coia, “Design of Axial Flux PM Synchronous Machines Through 3-D Coupled Electromagnetic Thermal and Fluid-Dynamical Finite-Element Analysis”, *IEEE Trans. on Ind. Electr.,* vol. 55, no. 10, pp. 3591-3601, Oct. 2008.

[MEZ06] S. Mezani, K. Atallah, and D. Howe, “A high-performance axial-field magnetic gear,” *J. Appl. Phys.*, vol. 99, no. 8, pp. 08R303-1-08R303-3, Apr. 2006.

[MIL06] J. M. Miller, “Hybrid electric vehicle propulsion system architectures of the e-CVT type”, *IEEE Trans. on Power Elect.*, vol. 21, no. 3, pp. 756-767, May 2006.

[MIN11] Mingyao Lin, Li Hao, Xin Li, Xuming Zhao, Zhu, Z.Q., “A novel axial field flux-switching permanent magnet wind power generator” , *IEEE Trans. on Magn.*, vol.47, no.10, pp.4457,4460, Oct. 2011.

[MIR12] S. M. Mirimani, A. Vahedi, F. Marignetti, and E. De Santis, “Static eccentricity fault detection in single stator-single rotor axial flux permanent magnet machines”, *IEEE Trans. on Ind. Appl.*, vol. 48, no. 6, pp. 1838–1845, Nov./Dec. 2012.

[NEV14] C. G. C. Neves, D. L. Figueiredo, A. Ferreira Flores, and A. Santos Nunes, “Magnetic gear: A review”, *11th IEEE/IAS Int. Conf. on Ind. Appl. (INDUSCON),* 2014, pp. 1-6.

[NIG12a] N. Niguchi, K. Hirata, A. Zaini, and S. Nagai, “Proposal of an axial-type magnetic-geared motor,” *in Proc, 20th Int. Conf. Elect. Mach.*, 2012, pp. 738-743.

[NIG12b] N. Niguchi and K. Hirata, “Cogging Torque Analysis of Magnetic Gear”, *IEEE Trans. on Ind. Electro.*, vol. 59, no.5, pp. 2189-2197, May 2012.

[NIU13a] S. Niu, S. L. Ho, and W. N. Fu, "Design of a novel electrical continuously variable transmission system based on harmonic spectra analysis of magnetic field", *IEEE Trans. on Magn.*, vol. 49, no.5, pp. 2161-2164, May 2013.

[NIU13b] S. Niu, S. L. Ho, and W. N. Fu, "A novel double-stator double-rotor brushless electrical continuously variable transmission system," *IEEE Trans. on Magn.*, vol. 49, no.7, pp. 3909-3912, Jul. 2013.

[NIU14] S. Niu, Y. Liu, S. L. Ho, and W. N. Fu, "Development of a novel brushless power split transmission system for wind power generation application" , *IEEE Trans. on Magn.*, vol. 50, no. 11, pp. 1-4, Nov.2014

[PAR05] A. Parviainen, J. Pyrhonen, and P. Kontkanen, "Axial Flux Permanent Magnet Generator with Concentrated Winding for Small Wind Power Applications", *IEEE Int. Conf. on Elec. Mach. and Drives,* 2005, pp. 1187-1191.

[QIN16] Qinfen Lu, Huanwen Li, Xiaoyan Huang, Yunyue Ye, "Research on yokeless double-sided multi-tooth flux-switching linear motor", COMPEL, vol.35, no.2, pp.832- 843, 2016.

[RAS03] P. O. Rasmussen, T. O. Andersen, F. T. Jorgensen, and O. Nielsen, "Development of a high-performance magnetic gear", *IEEE Trans. on Ind. Appl.*, vol. 41, no. 3, pp. 764-770, May-June 2005.

[SAS98] S. Sasaki, "Toyota's newly developed hybrid powertrain", *Proceedings of the 10th Int. Symposium on Power Semiconductor Devices and ICs, ISPSD,* 1998, pp. 17-22.

[SHA15] Z. Shabahang, M. Shahnazari and A. Sedighi, "Analysis of dynamic eccentricity in a coreless axial flux permanent magnet machine", *30th Int. Power Sys. Conf. (PSC),* Tehran, 2015, pp. 358-362.

[SON10] A. Du, X. Yu, and J. Song, "Structure design for power-split hybrid transmission", I*nt. Conf. on Mechatronics and Automation (ICMA),* 2010, pp. 884-887.

[SOU16] A. Souissi, I. Abdennadher, A. Masmoudi, F. Marignetti, and R. D. Stefano, "On the design of fractional slot T-LPMSMs: effect of the slot-pole combination," *Eleventh Int. Conf. on Ecological Vehicles and Renewable Energies (EVER),* 2016, pp. 1-7.

[SPA14] C. M. Spargo, B. C. Mecrow, and J. D. Widmer, "A seminumerical finite element postprocessing torque ripple analysis technique for synchronous electric

machines utilizing the air-gap Maxwell stress tensor", *IEEE Trans. Magn.*, vol. 50, no. 5, May 2014.

[SPO92] E., Spooner, B.J., Chalmers, "'TORUS': a slotless, toroidal-stator, permanent-magnet generator", *IEE Proc. Electric Power Appl.*, vol.139, no.6, pp.497,506, Nov. 1992.

[STA15] N. J. Stannard, J. G. Washington, and G. J. Atkinson, "A comparison of axial field topologies employing SMC for traction applications," *19th Int. Conf. on Elec. Mach. and Sys. (ICEMS)*, 2016, pp. 1-6.

[SUN08] X. Sun, M. Cheng, L. Xu, and W. Hua, "A novel dual power flow wind power generation system," *in Proc. Int. Conf. Electr. Mach. Syst.*, Wuhan, China, 2008, pp. 2573–2578.

[SUN09] X. Sun, M. Cheng, W. Hua, and L. Xu, "Optimal design of double-layer permanent magnet dual mechanical port machine for wind power application", *IEEE Trans. on Magn.*, vol. 45, no.10, pp.4613-4616, Oct.2009.

[THI12] M. Thiele and G. Heins, "Identifying cogging torque harmonics affected by misalignment in axial flux fractional pitch PMSM", in *Proc. XXth Int. Conf. Elect. Mach.*, 2012, pp. 2969–2974.

[THI14] M. Thiele, G. Heins, and D. Patterson, "Identifying manufacturing induced rotor and stator misalignment in brushless permanent magnet motors," in *Proc. Int. Conf. Elect. Mach.*, 2014, pp. 2728–2733.

[THI16] M. Thiele and G. Heins, "Computationally efficient method for identifying manufacturing induced rotor and stator misalignment in permanent magnet brushless machines", *IEEE Trans. on Ind. App.*, vol. 52, no. 4, pp. 3033-3040, July-Aug. 2016.

[TLA14] P. M. Tlali, R. J. Wang, and S. Gerber, "Magnetic gear technologies: A review," *Int. Conf. on Elec. Mach. (ICEM)*, 2014, pp. 544-550.

[TON14] C. Tong, Z. Song, P. Zheng, J. Bai, and Q. Zhao, "Research on electromagnetic performance of an axial magnetic-field-modulated brushless double-rotor machine for hybrid electric vehicles", *in Proc. 17th Int. Conf. Elec. Mach. Sys.*, 2014, pp. 2896-2902.

[TSA15] M. C. Tsai and L. H. Ku, "3-D printing-based design of axial flux magnetic gear for high torque density", *IEEE Trans. on Magn.*, vol. 51, no. 11, pp. 1-4, Nov. 2015.

[TUT12] L. N. Tutelea, I. Boldea, and S. I. Deaconu, “Optimal design of dual rotor single stator PMSM drive for automobiles”, *IEEE Inter. Elec. Vehic. Conf.*, 2012, pp. 1-8.

[VAN03] P. V. Tichelen and E. Peeters, “Design of a new axial flux permanent magnet generator for hybrid electric vehicles”, *IEEE 58th Vehicular Tech. Conf. VTC*, 2003, vol.5, pp. 3192-3196.

[VAN10] H. Vansompel, P. Sergeant, and L. Dupre, “Optimised design considering the mass influence of an axial flux permanent-magnet synchronous generator with concentrated pole windings”, *IEEE Trans. on Magn.*, vol. 46, no. 12, pp. 4101-4107, Dec. 2010.

[VAN12] H. Vansompel, P. Sergeant, and L. Dupré, “Effect of segmentation on eddy-current loss in permanent-magnets of axial-flux PM machines using a multilayer-2D-2D coupled model”, *XXth Inter. Conf. on Elect. Mach.*, 2012, pp. 228-232.

[VUN11] S. T. Vun, M. D. McCulloch, and C. Y. Leong, “The development of an electromagnetic analytical design tool for megawatt-scale YASA generators”, *IET Conf. Rene. Power Generation (RPG 2011)*, 2011, pp. 1-6.

[WAN08] J.B. Wang, K. Atallah, Z. Q. Zhu, and D. Howe, “Modular three-phase permanent-magnet brushless machines for in-wheel applications”, *IEEE Trans. on Vehicular Tech.*, vol. 57, no. 5, pp. 2714-2720, Sep.2008.

[WAN09] L. L. Wang, J. X. Shen, P. C. K. Luk, W. Z. Fei, C. F. Wang, and H. Hao, “Development of a magnetic-geared permanent-magnet brushless motor,” *IEEE Trans. on Magn.*, vol. 45, no.10, pp. 4578-4581, 2009.

[WAN13] R. J. Wang, L. Bronn, S. Gerber, and P. M. Tlali, “Design and evaluation of a disc-type magnetically geared PM wind generator”, *4th Int. Conf. Power Eng., Energy and Elect. Drives*, May 2013, pp. 1259-1264.

[WOO06] T. J. Woolmer and M. D. McCulloch, “Axial flux permanent magnet machines: A new topology for high performance applications”, *IET Conf. on Hybrid Vehicle (Conf. Pub. CP526)*, pp. 27-42, 2006.

[WOO06] T. J. Woolmer and M. D. McCulloch, “Axial flux permanent magnet machines: A new topology for high performance applications”, *IET Hybrid Vehicle Conf.*, 2006, pp. 27-42.

[WOO07] T. J. Woolmer and M. D. McCulloch, “Analysis of the yokeless and segmented armature machine”, *in Proc. IEEE Int. Elec. Mach. Drives Conf.*, 2007., pp. 704-708.

[WU13] L. J. Wu, Z. Q. Zhu and M. L. Mohd Jamil, “Unbalanced magnetic force in permanent magnet machines having asymmetric windings and static/ rotating eccentricities”, *Int. Conf. on Elec. Mach. and Sys. (ICEMS)*, Busan, 2013, pp. 937-942.

[WU15] D. Wu and Z. Q. Zhu, “Influence of slot and pole number combinations on voltage distortion in surface-mounted permanent magnet machines with local magnetic saturation”, *IEEE Trans. Energy Conv.*, vol. 30, no. 4, pp. 1460-1471, Dec.2015.

[XIA15] B. Xia, J. X. Shen, P. C. K. Luk, and W. Fei, “Comparative study of air-cored axial-flux permanent-magnet machines with different stator winding configurations”, *IEEE Trans. on Ind. Electro.*, vol. 62, no. 2, pp. 846-856, Feb. 2015.

[YAN12] L. Yanhe and N. C. Kar, “Investigating the effects of power split PHEV transmission gear ratio to operation cost”, *IEEE Conf. on Transportation Electrification and Expo (ITEC)*, 2012, pp. 1-6.

[YIN15] X. Yin, P. D. Pfister, and Y. Fang, “A novel magnetic gear: toward a higher torque density”, *IEEE Trans. on Magn.*, vol. 51, no. 11, pp. 1-4, Nov. 2015.

[ZAY14] H. Zaytoon, A. S. Abdel-khalik, A. M. Massoud, and S. Ahmed, “An axial magnetic gearbox with an electric power output port”, *29th Annual IEEE App. Power Electronics Conf. Expo.*, 2014, pp. 2621-2627.

[ZHA16] B. Zhang, T. Seidler, R. Dierken and M. Doppelbauer, “Development of a Yokeless and Segmented Armature Axial Flux Machine” *IEEE Trans. on Ind. Elect.*, vol. 63, no. 4, pp. 2062-2071, April 2016.

[ZHE13] P. Zheng, Z. Song, J. Bai, C. Tong and B. Yu, “Research on an Axial Magnetic-Field-Modulated Brushless Double Rotor Machine”, *Energies*, vol. 6, no. 9, pp. 4799–4829, Dec. 2013.

[ZHU00] Z. Q. Zhu and D. Howe, “Influence of design parameters on cogging torque in permanent magnet machines”, *IEEE Trans. on Energy Convers.*, vol. 15, no. 4, pp. 407-412, Dec. 2000.

[ZHU09a] Z. Q. Zhu, Z. P. Xia, L. J. Wu, and G. W. Jewell, “Influence of slot and pole number combination on radial force and vibration modes in fractional slot PM

brushless machines having single- and double-layer windings", *IEEE Energy Convers. Conf. and Exposition*, 2009, pp. 3443-3450.

[ZHU09b] Z. Q. Zhu. "A simple method for measuring cogging torque in permanent magnet machines", *in Proc. IEEE. Power & Energy Society General Meeting (PES)*, Calgary, 26–30 July 2009; pp. 1–4.

[ZHU13a] Z. Q. Zhu, L. J. Wu, and M. L. M. Jamil, "Influence of pole and slot number combinations on cogging torque in permanent magnet machines with static and rotating eccentricities", in *Proc. IEEE Energy Convers. Congr. Expo.*, 2013, pp. 2834–2841.

[ZHU13b] Z. Q. Zhu, L. J. Wu and M. L. Mohd Jamil, "Distortion of back-EMF and torque of PM brushless machines due to eccentricity," I*EEE Trans. on Magn.*, vol. 49, no. 8, pp. 4927-4936, Aug. 2013.

[ZHU14] Z. Q. Zhu, L. J. Wu and M. L. Mohd Jamil, "Influence of pole and slot number combinations on cogging torque in permanent-magnet machines with static and rotating eccentricities", I*EEE Trans. on Ind. Appl.*, vol. 50, no. 5, pp. 3265-3277, Sept.-Oct. 2014.

[ZHU15] Z. Q. Zhu, Y. J. Zhou, and J. T. Chen, "Investigation of axial field partitioned stator switched flux machines", *10th Int. Conf. on Ecological Vehicles and Renewable Energies (EVER)*, 2015, pp. 1-7.

APPENDIXES

APPENDIX A.

THEORY OF ELECTROMAGNETIC AND DESIGN METHODOLOGY

A.1 Introduction

This section firstly presents the principle of electromagnetic design of PM machines followed by the optimisation procedures used in this study. The methodology used for studying the machine under investigation in this thesis is then presented, including design assumptions, the finite element method setting, and optimisation processes.

A.2 Basic magnetic principle of PM machines

A.2.1 PM magnetic flux density

In PM synchronous machines, the PM is the main flux source since the torque production is proportional to the flux. The machine's magnets can be located either in the rotor or stator. The magnetic flux density obtained by the PM can be classified as having two components. One is the normal component (residual) which is therefore due to the PM material characteristics during the magnetisation process. This value is constant and does not increase with the applied magnetic flux intensity. The second component of the flux density is caused by the external magnetic flux intensity. Therefore, the flux density obtained by PM material can be given by:

$$B_m = B_r + \mu_o \mu_r H_m \tag{A.1}$$

where B_r and μ_r are the magnet remanence and the relative permeability, respectively. The typical flux density characteristic of the magnet can be presented in the second quadrant of its B-H curve (demagnetisation curve) as indicated in Fig. A.1. The magnet demagnetisation curve has a straight line which can be presented by (A.1), and the flux density at zero excitation is the remanent flux density B_r. When external excitation is acting against the magnet flux, the flux density collapses to zero and the corresponding magnetic field strength in this case is known as coercivity H_c. The behaviour of PM can be obtained in terms of the relationship of the magnetic flux density B_m and the magnetic field strength H_m (Operation point). This point changes along the demagnetisation line according to the air-gap length and the stator demagnetisation flux.

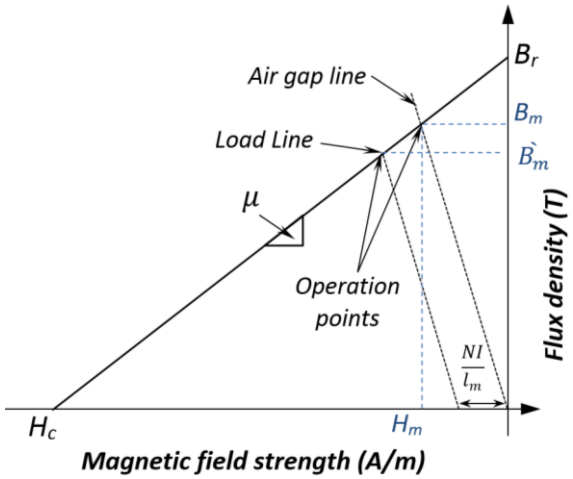

Fig. A.1 Demagnetization curve of PM material.

For surface mounted PM rotors, a simplified method can be used to calculate the operating point of the demagnetisation characteristics of the magnet. This method is described for application to the proposed axial flux surface mounted PM topology. Fig. A.2 shows the radial cross-section of the proposed topology where the flux paths are indicated. Utilising the flux path scheme, the air-gap flux density can be derived from the following equation [HAN94]:

$$\vec{\nabla} \times \vec{H} = \vec{J} \tag{A.2}$$

By assuming that the stator and rotor iron have infinite permeability and when the magnet leakage flux is neglected, the topology no-load axial flux per pole can be approximated and expressed by:

$$H_m L_m + H_g L_g = 0 \tag{A.3}$$

where: H_m and H_g are the magnetic flux intensities in magnet and air-gap, respectively. L_m and L_g are the length of the magnet and air-gap, respectively. The air-gap flux density B_g can be obtained in terms of its magnetic field intensity by $B_g = \mu_o H_g$, where μ_o is the vacuum permeability.

From (A.3) and (A.1), the PM flux density can be derived as:

$$B_m = B_r - \mu_r \frac{B_g L_g}{L_m} \tag{A.4}$$

When the leakage flux is neglected, the flux passing through the air-gap ϕ_g is equal to the PM flux ϕ_m, and the PM flux density in terms of air-gap flux density can be expressed as:

$$\begin{aligned} \phi_m &= \phi_g \\ B_m A_m &= B_g A_g \end{aligned} \tag{A.5}$$

Substituting (A.5) into (A.4), the operating PM flux density is:

$$B_m = \frac{B_r}{1+\mu_r \frac{L_g A_m}{L_m A_g}} \tag{A.6}$$

When the PM and the air-gap areas are assumed to be approximately the same ($\alpha_p = 1$) this leads to:

$$B_m = B_g = \frac{B_r}{1+\mu_r \frac{L_g}{L_m}} \tag{A.7}$$

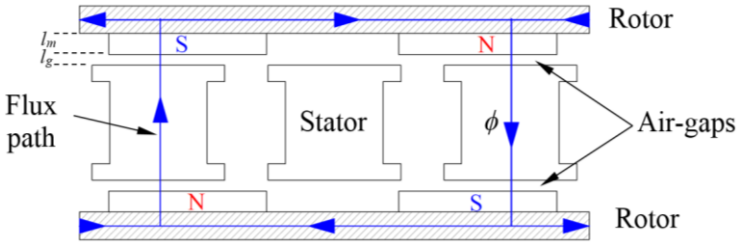

Fig. A.2 Axial cross section of double rotor AFPM topology.

However, when the stator phase winding is fed by current *I*, (A.3) can be rewritten as

$$H_m L_m + H_g L_g = NI \tag{A.8}$$

Therefore, the PM flux density $\grave{B_m}$ in the air-gap with the presence of stator excitation is expressed by

$$\grave{B_m} = -\mu_0 \frac{A_g}{A_m} \frac{L_m}{L_g} (H_m - \frac{NI}{L_m}) \tag{A.9}$$

This indicates that the air-gap line explained in Fig. A.1 moves parallel to the original load line by approximately ($\frac{-NI}{L_m}$), and the operating flux density is further reduced to a new value of $\grave{B_m}$, (Fig. A.1).

A.2.2 Electromagnetic torque production

With the presence of current-carrying stator coils, a linear current density in a conducting medium induces alternating field strength outside the surface. This linear current density (*A*) corresponds to the tangential magnetic field. The torque can be obtained by the tangential force acting on the rotor disc produced by the armature current flux, which can be calculated according to Ampere's equation [GIE08]

$$dF_T = A(r)(B_g \times dS) \tag{A.10}$$

where B_g is the average air-gap flux density produced by the rotor magnet and, *dS* is the surface element. *A*(*r*) is the RMS linear current density which is a function of the radius and can be expressed by

$$A(r) = \frac{mNI_s}{\pi r} \tag{A.11}$$

where: m and N are the number of phases and the number of turns per phase, respectively. I_s is the stator phase RMS current. By assuming that $dS = 2\pi r dr$, and considering the fundamental winding factor k_w, the average electromagnetic torque can be in general represented by

$$\begin{aligned} dT = rdF_T = A(r)(B_g \times 2\pi r^2 dr) &= \frac{mNk_w I_s}{\pi r}(B_g \times 2\pi r^2 dr) \\ T = 2mNI_s\, k_w B_g \int_{R_i}^{R_o} rdr &= mNI_s\, k_w B_g\,(R_o^2 - R_i^2) \end{aligned} \tag{A.12}$$

A.3 Design and analysis methodologies of axial flux machines

For radial machines, 2D-FEM has been utilised to optimise and analyse the machine topologies. The accurate electromagnetic study of axial flux machines requires a 3-D model FEM due to the inherent 3D geometry and flux distribution [PAR05], [MAR08]. However, for many researchers this is not preferred method since it is time consuming. Therefore, numerical analysis and 2-D FEA have been used as alternative solutions for machine analysis [VAN03]. In this thesis, both 2-D and 3-D analyses are utilised. For the machine optimisation, a 2-D FEA model is developed for the proposed axial flux machines by utilising ANSYS Maxwell software. In addition, the 3D model based on the optimal dimensions obtained by 2-D FEA is designed and analysed utilising JMAG 3-D software.

A.3.1 Design assumptions and constant parameters

Before beginning the design and analysis of the proposed axial flux machine, certain initial constraints must be considered. In fact, every design has its practical constraints, and these differ with the type of application. It is well known that a machine's inner and outer diameters are the two most important design parameters. Since, the outer diameter is always limited by the system of the application, and the ratio of inner to outer diameter (split ratio) needs to be considered as it has a crucial impact on the machine characteristics. Generally, the torque/power of the machine can be maximised for a given machine diameter at a given speed. By considering the simulation time of the machine model as well as the manufacturing costs, the outer diameter of the proposed machine was selected to be 90 mm with axial length of about 25 mm. Moreover, in the case of small machines, the number of stator poles is mostly limited due to the reduced available winding space. Therefore, 12 segments are selected for the stator poles since this number is preferred for small machines and the machine is proposed for low speed application. On the other hand, the machine stator current is calculated by considering constant copper loss of 30 W. This value is

selected for the proposed machine according to the previous prototypes which have been built in the university laboratory and allow for the maximisation of the efficiency.

A.3.2 Design and analysis methodology of 2-D models

The axial flux machines can be calculated analytically or by 2-D FEM approximation. 2D-FEA is based on taking a 2-D plane of the model at a specific radius value. The modelling can be executed by a radial cutting plane at the axial machine average radius, which is then analysed into a 2D radial or linear model [GIR08]. In the current study, where a 2-D linear topology is considered: if the corresponding radial topology had been utilised for the proposed machine which has two rotors, an accurate PM angle and its stator side slot opening for the inner rotor might not been obtained. Therefore, a 2-D plane was obtained using a linear machine, as described in Fig. A.3.

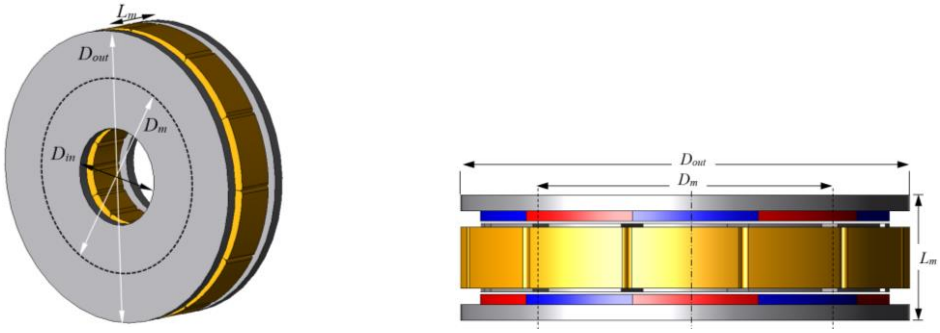

(a) Axial flux machine model

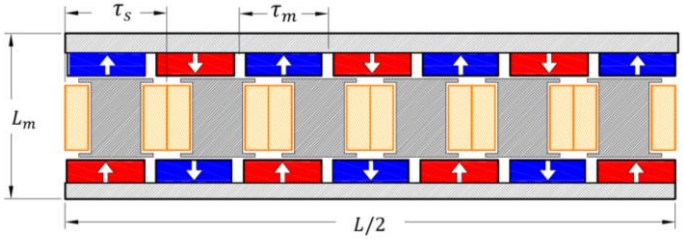

(b) Linear model of the proposed axial machine.

Fig. A.3 Process of the 2-D plane approximation.

For axial flux machines, normally a symmetrical section of the machine is modelled to reduce the simulation time. The results can therefore be multiplied by the symmetrical machine sections which can be used for YASA machines. However, the proposed AFMGPM machine is not symmetrical since it has two different rotors, which means that the machine has to be completely designed and modelled. As indicated in the figure, the axial length L_m of the axial machine is the same as the width of the linear topology. The total length L of the linear topology is the same as

the circumferential length of the axial topology at the mean diameter (D_m), and can be calculated by:

$$L = \pi D_m \tag{A.13}$$

where the mean diameter D_m is obtained by the inner (D_{in}) and outer (D_{out}) diameters of the axial topology.

$$D_m = \frac{D_{in} + D_{out}}{2} \tag{A.14}$$

Moreover, the machine's circumferential lengths can be converted to linear with the same method; for example, the rotor and stator pole pitches for the linear model $\tau_{s,m}$ can be calculated utilising the axial flux machine stator pole pitch angle and the rotor pole pitch angle $\theta_{s,m}$ as:

$$\tau_{s,m} = \frac{D_m}{2} \times \theta_{s,m} \tag{A.15}$$

where θ_s and θ_m are measured in radius, in which all the machine arcs need to be converted utilising (A.15). The 2-D software was used for global optimisation of the proposed machines in this thesis. During the optimisation process, the machine volume was kept constant (constant outer diameter and axial length). Fig. A.4 shows the no-load flux line results of the 2-D model design of the proposed machines utilising 2-D FEA.

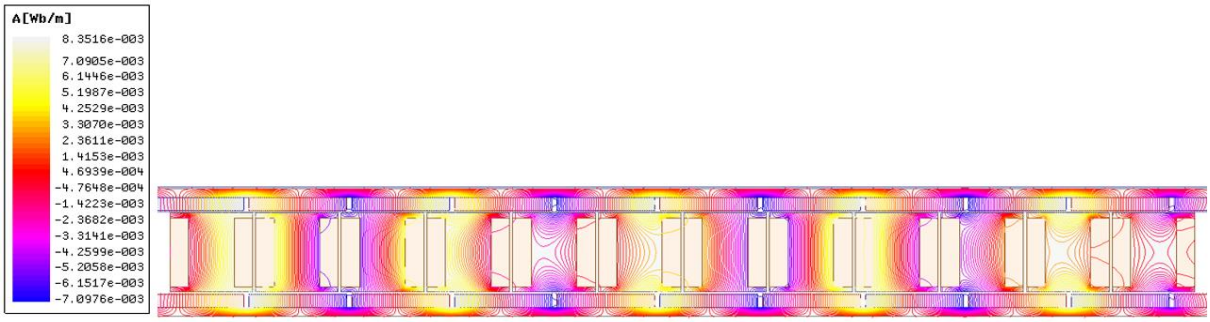

(a) YASA12/10 machine

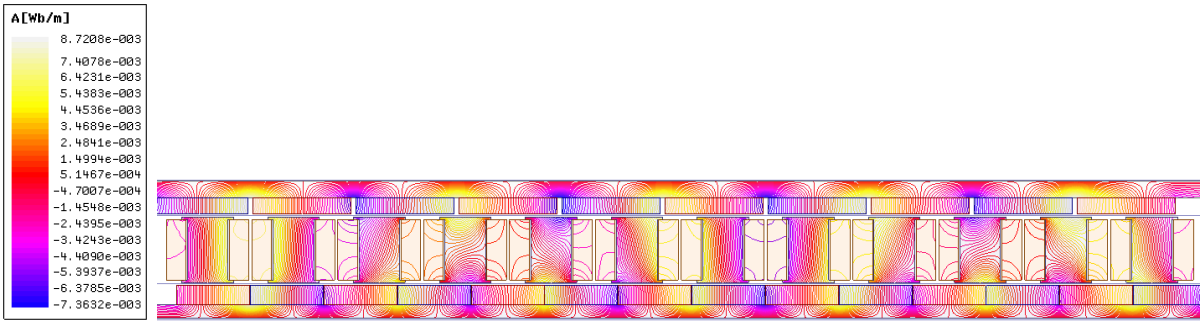

(b) MG12/5-7 machine

Fig. A.4 Flux lines of the 2-D model of the machines under study.

A.3.3 Design and analysis methodology of 3-D model

Since the radial edge effects is not considered when the 2D model of axial flux machine is developed, 3D-FEM was preferred for accurate analysis. Due to asymmetric shape of the proposed topology, a full 3-D model is designed with the aid of JMAG software. The optimal dimensions produced by the 2-D model are utilised for the design of the 3-D model for the proposed machines. The machine has constant outer diameter and axial length of 90 mm and 25 mm, respectively. Electromagnetic analysis of the proposed machines has been implemented using a non-linear FEM model with time step simulation. The software settings used to perform the performance of the machines is described as follows.

The software is prepared for the proposed topologies analysis. A transient response analysis is chosen since the MMF and the rotational motion of the rotors have time varying phenomena. In order to calculate the machine performance involving rotational motion, a mesh generation has to be obtained. The mesh generation in 3-D models involved division of the motor model to a set of elements to define the machine's geometry. Moreover, each part in the machine constriction may be defined by a different generated mesh size according to the behaviour of the flux passing through the machine element. For radial machines, a slide mesh function could be selected to generate a mesh in the air-gap. However, in JMAG software, automatic meshing of the surrounding air volume of the model is offered. The meshing of an axial model could be generated automatically according to the position of the moving part at each analysis step. The meshing for stator and rotor parts is created once, while the mesh of the air-gap between the stationary and movable parts for the 3-D model is regenerated for each moving part position. The mesh at each analysis step (patch mesh) is utilised to link stator and rotor meshes across the boundary. The mesh size of the 3-D model of the machine determines the accuracy and the time of the analysis results. Therefore, to examine the accuracy of results and the time of the proposed topologies, different mesh sizes of the proposed machine are utilised. It should be mentioned that the meshing size differs according to the change in the direction and amount of magnetic flux on each part.

Fig. A.5 depicts the influence of the air-gap mesh size on the machine performance. The mesh sizes of the rotor back iron, stator core and the PM are fixed, while the air-gap meshing size is changed in each case. The air-gap mesh is created by selecting the surface of the PM of both rotors and both stator surfaces facing the air-gaps. It can be seen that the LSR average torque is slightly affected by the mesh size in general, while the torque equality is significantly improved at finer mesh as indicated in Fig. A.5(a) and (b), respectively. In addition, the fundamental components of the machine back EMF and the machine PM eddy current loss are examined at

different mesh sizes, as indicated in Fig. A.5 (c) and (d), respectively. The mesh size in general has an insignificant effect on the back EMF amplitude, while it has a minor changing on the eddy current loss.

Generally, according to the obtained results, the mesh size of the machine parts should be finer than 1.5 mm. However, for high torque equality and accurate torque ripple and eddy current loss, a fine mesh of the air-gap (> 1 mm) is always preferred for this machine.

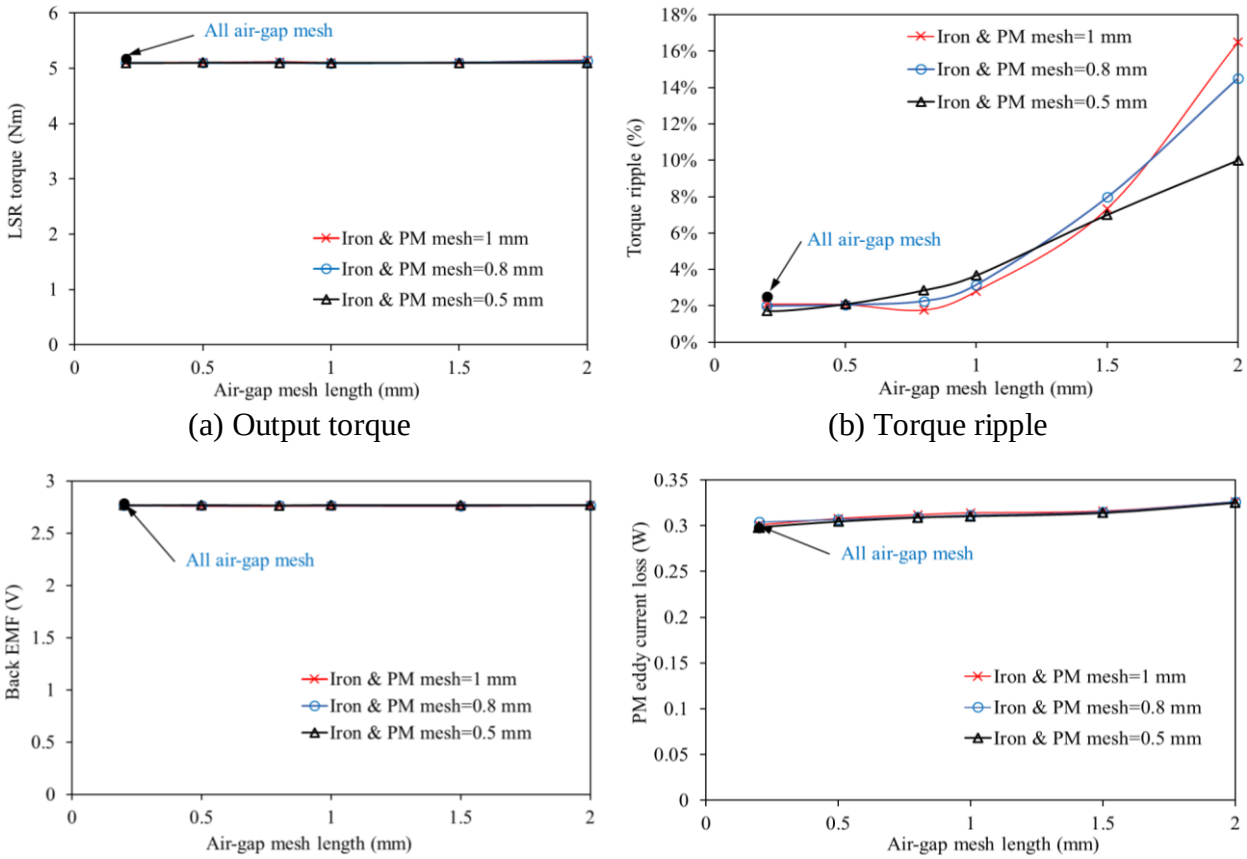

(a) Output torque

(b) Torque ripple

(c) Fundamental back EMF amplitude

(d) Eddy current loss

Fig. A.5 Influence of the mesh size on the AFMGPM machine performance.

Therefore, a machine mesh size of 1.2 mm for the PM, stator and rotor cores is selected for assessing the influence of machine parameters on the output torque. However, for losses and cogging torque performance studies, a finer mesh size of the air-gap is preferable to improve the flux performance and more results accuracy. Hence, for such calculations, at the magnet and the stator surfaces facing the air-gap a surface mesh of 0.2 mm can be assigned. Table A.1 indicates the size of mesh for each part utilised for different performance studies of the proposed machines. Fig. A.6 also shows the mesh generated in the proposed topology for different study cases.

Alternatively, the air gap meshing can be created by designing the air-gap as a part attached to both stator and rotor inner sides and assigned as a vacuum, (see Fig. A.7(a)). In this case, a very small distance between the assigned gaps attached to stator and rotor could be achieved here corresponds to the slide meshing in radial topologies as indicated in Fig. A.7(b). This method is used in the proposed machine to confirm the selected mesh method, in which the machine performance is studied at small air-gap mesh size of (0.2 mm) and with 1 mm for the stator core and the rotor PMs. The machine performance utilising this meshing method is included in Fig. A.5, as (All air-gap meshing) point. As can be seen in Fig. A.5, the machine performance is slightly changed compared to the proposed meshing method. Moreover, this method is time consuming to simulate the machine for one electrical cycle.

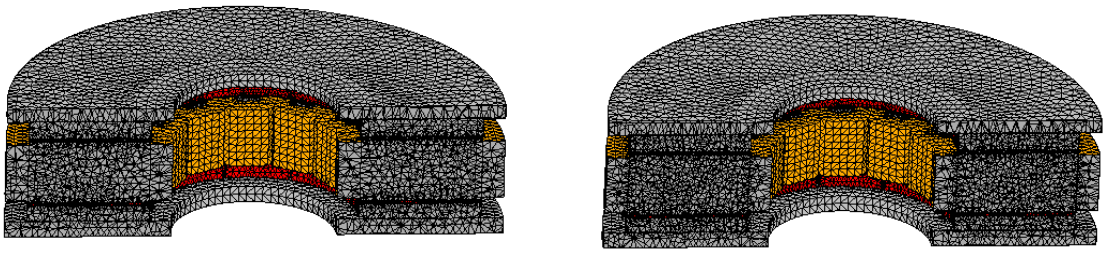

(a) Mesh view for the machine performance study

(b) Mesh view for loss and cogging torque calculations

Fig. A.6 Mesh generation for the proposed axial flux model.

Table A.1 Mesh size of each element

Study	Element	Mesh size (mm)
Influence of the machine parameters on the output torque	Stator, rotor cores and PMs	1.5
	Stator windings	2
	Stator and PM surfaces (Facing the air-gap)	0.4
	Air boundaries	2
Machine performances (torque, EMF and flux)	Stator, rotor cores and PMs	1.2
	Stator windings	1.5
	Stator and PM surfaces (Facing the air-gap)	0.4
	Air boundaries	1.5
Cogging torque and tosses	Stator, rotor cores and PMs	1
	Stator windings	1.5
	Stator and PM surfaces (Facing the air-gap)	0.2
	Air boundaries	1

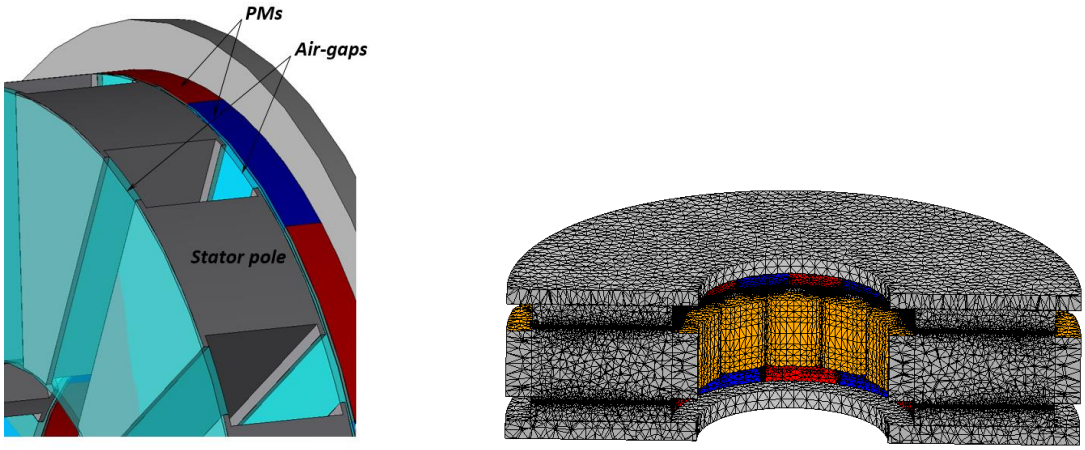

(a) Air-gap geometry.

(b) Mesh view for all gap meshing
(Air-gap =0.2 mm, stator and PMs=1mm)

Fig. A.7 Air-gap manual geometry and the corresponding mesh size.

On the other hand, for the proposed magnetically geared machine, transient analysis is carried out under the software settings described as follows:

1. The periodic time for one electrical cycle is calculated according to the considered rotor speed n_r , in which a speed of 400 rpm is always assumed for the YASA machine and the HSR of the AFMGPM machine. Therefore, the periodic *T* time can be calculated as:

$$T = \frac{1}{f} = \frac{60}{n_r\, p} \quad Sec. \tag{A.16}$$

   where f and p are the frequency and the rotor pole pairs, respectively.

2. The number of steps can be decided according to the required accuracy. For example, the number of steps per electrical angle needs to be high when the cogging torque / loss are calculated at normal and for manufacturing tolerance studies. Therefore, for normal calculations such as torque and back EMF, a minimum step of 2 is considered for each electrical angle.

In JMAG software, the iron loss is calculated according to the loss curves of the material provided by the manufacturer which were imported to the software (see Appendix C). Additionally, the magnet eddy current loss is calculated according to the magnet conductivity without considering the skin effect since the machine is analysed at low speed. Basically, the cause of eddy current is the variation of the flux density, which is transmitted through the magnet surface. Therefore, the eddy current can be obtained by the magnetic flux passes through the magnet surface. The PM skin depth σ caused by its eddy current could be calculated by [LEZ11].

$$\sigma = \sqrt{\frac{2\,\rho}{\omega\,\mu}} \tag{A.17}$$

where: ρ and μ are the resistivity and the permeability of the PM, and ω is the angular frequency ($2\pi f$). By calculating the variation of the flux density on the magnet surface, and by applying FFT for the obtained flux density, the frequency dominated the eddy current loss can be known. Therefore, to do this, the flux density is calculated at different locations in the middle of the rotor magnet. These locations are explained in Fig. A.8(a), in which Point (1) is located on the PM surface, Point (2) is located at approximately 0.75 mm from the magnet surface, and Point (3) is located in the middle of the magnet thickness of 1.5 mm from the PM surface. Moreover, at each point, the axial flux density waveforms and the corresponding harmonics at no-load and at rated current are calculated and plotted in Fig. A.8(c) and Fig. A.8(c), respectively. Meanwhile, Fig. A.9 shows the x-y flux density components which are also measured on the surface of the magnet at the middle air-gap radii. It can be seen that the working fundamental harmonic, which should dominate to the eddy current through the magnet is the same as the flux density fundamental harmonic for all components. Therefore, for the utilised magnet, the resistivity ρ and the relative permeability μ_r are 1.4e-06 Ω.m and 1.05, respectively. The calculated skin depth of the magnet at the fundamental frequency of 33.33 Hz is 100 mm. Moreover, the eddy-current component which can be induced in the PM because of the variation of the magnetic flux harmonics caused by the stator slotting is negligible.

As indicated in Fig. A.8(c) and Fig. A.9, the effect of the stator flux density is insignificant at the frequency of the fundamental harmonic. In addition, the eddy current loss is studied for different HSR speeds with the highest frequency of the highest speed being 833.3 Hz. The calculated skin depths of the magnet at the fundamental frequency of 833.3 Hz are approximately 21 mm. Therefore, the skin depth being neglected at all studied frequencies.

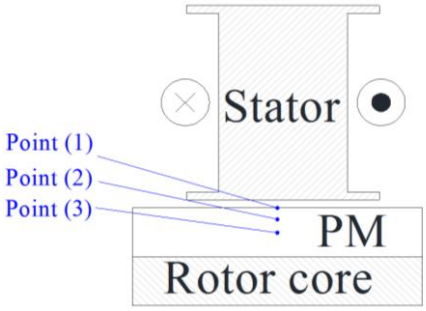

(a) Locations of the examined points.

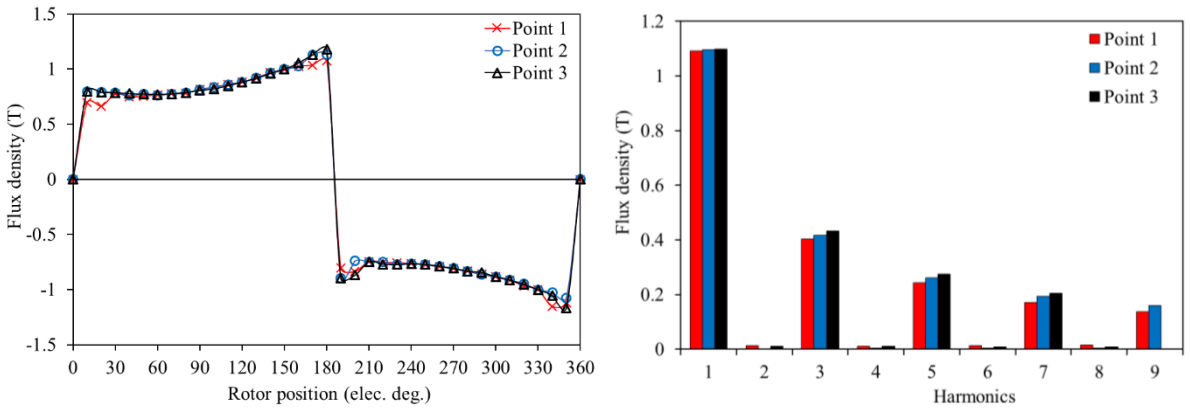

(b) Flux densities at open circuit

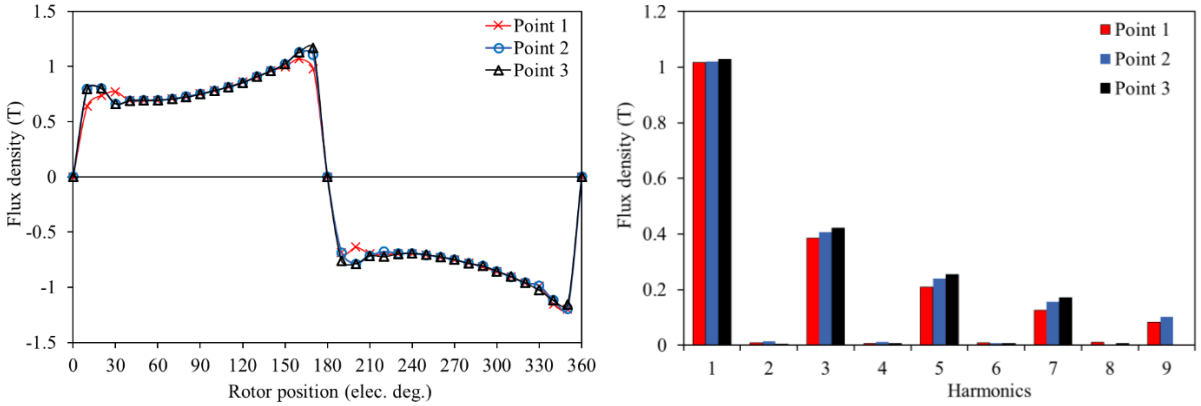

(c) Flux densities at rated current applied into the stator windings.

Fig. A.8 Flux densities inside the magnet at different magnet locations.

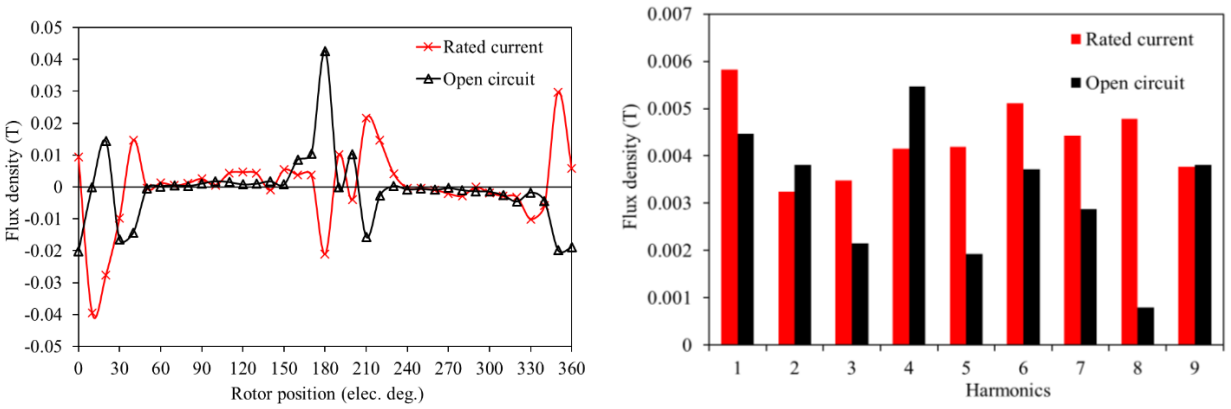

(b) Circumferential flux densities at no-load and at rated current.

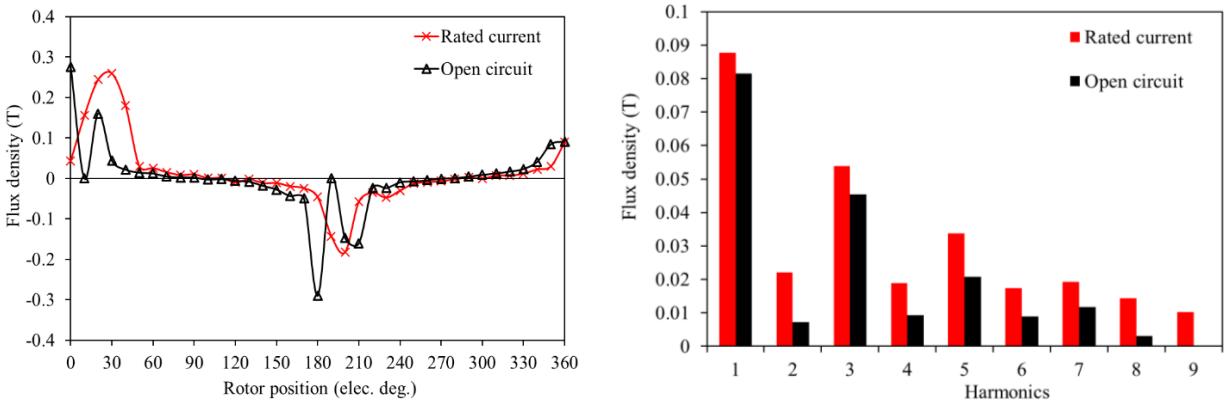

(c) Radial flux densities at no-load and at rated current.

Fig. A.9 Flux density at the magnet surface (Point 1).

APPENDIX B.

COMPARATIVE STUDY OF AXIAL FLUX MAGNETICALLY GEARED MACHINE AND YASA MACHINE.

B.1 Introduction

The proposed machine is based on a conventional YASA machine in that it has approximately the same structure. The main difference is that YASA machine includes two identical PM rotors while the proposed AFMGPM machine is created with different rotor pole pairs for the two rotors shown in Fig. B.1 . A performance comparison between AFMGPM and the corresponding conventional axial flux YASA machine is presented in this section. The AFMGPM and YASA machines have the same stator construction in which iron segments are equipped with concentrated windings to form the stator. However, since the AFMGPM machine has two rotors with different pole-pair numbers, the magnetic gear effect can be obtained to increase the machine torque density. The performance comparisons at no-load and on-load conditions are then studied using 3D-FEM.

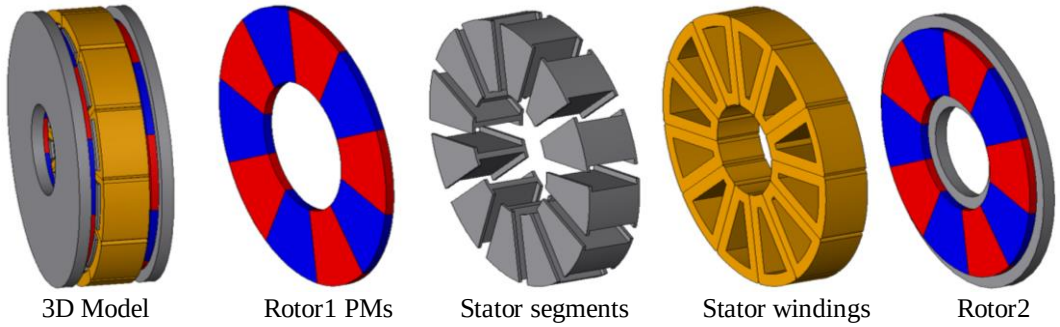

(a) YASA machine

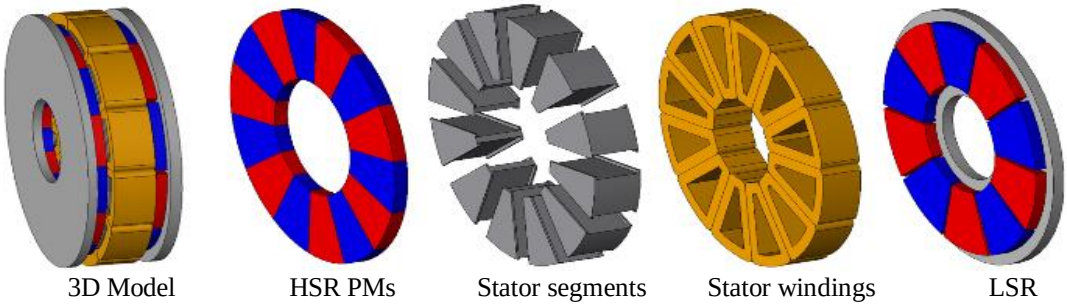

(b) AFMGPM machine

Fig. B.1 Machine topologies.

B.2 AFMGPM and YASA machine geometries

Since the first topology of the proposed magnetically geared machine, designated as MG12/5-7, has a 12 pole stator and two different rotors of a 10 pole HSR and a 14 pole LSR, two YASA machine topologies with 12 pole stators are considered for comparison. The first YASA machine topology, designated as YASA12/10, has a 10 pole rotor: the second topology, designated as YASA12/14, has a 14 pole rotor. Similarly, the proposed MG12/4-8 topology is compared with YASA12/8 with 8 rotor poles and YASA12/16 with 16 poles. With the same machine volume, axial length and copper loss, the AFMGPM machine and YASA machine topologies have been optimised for maximum torque. The specifications, optimal dimensions and materials of the machines are listed in Table B.1.

Table B.1. Machine optimal dimensions and rated parameters

Parameter	MG 12/5-7	YASA 12/10	YASA 12/14	MG 12/4-8	YASA 12/8	YASA 12/16
High speed (RPM)	400	400	-	400	400	-
Low speed (RPM)	285.5	-	285.5	200	-	200
High speed rotor pole No. (P_h)	10	10	-	8	8	-
Low speed rotor pole No. (P_l)	14	-	14	16	-	16
Stator Pole Number (St)	12	12	12	12	12	12
Machine Inner Diameter (mm)	30	30	30	30	30	30
Machine Outer Diameter (mm)	90	90	90	90	90	90
Axial Length (mm)	25	25	25	25	25	25
Air gap Length (mm)	0.5	0.5	0.5	0.5	0.5	0.5
Number of turns of armature coil/phase	80	80	80	80	80	80
Packing factor	0.5	0.5	0.5	0.5	0.5	0.5
High speed rotor pole arc (degree)	34	36	-	39	38.7	-
High speed rotor PM Thickness (mm)	3	2	-	2.5	1.81	-
Low speed rotor pole arc (degree)	25.4	-	22.8	22.5	-	18.9
Low speed rotor PM Thickness (mm)	3.5	-	2.2	2.5	-	2.42
Slot Area (mm^2)	44	48	52	52	49	52
Armature stator Axial Length (mm)	12	13.66	14	13	14.2	14.3
Rotor Axial Length (mm)	6	5.17	4.9	5	4.9	4.85
I_{rms} (A)	13.5	14.5	14.8	14.8	14.3	15
PM volume (mm^3)	26263.6	16587.6	16691.2	19348	13270	17509.1

B.3 Comparison of MG12/5-7 with conventional YASA12/10 and YASA12/14 machines

For the AFMGPM machine, two no-load conditions are taken into consideration in this study. The first condition is that in which the relative angle between HSR and LSR pole axes is zero elec. deg., and thus, the MG effect torque is cancelled. Moreover, with the aim of obtaining maximum MG effect torque, both rotors are located at a relative angle of 90 elec. deg. between the rotor pole axes. Furthermore, since the proposed machine has two rotors with two different poles and speeds, either HSR or LSR can be considered as an output rotor, which connects to the drive load. Therefore, the MG12/5-7 machine performance is compared with YASA12/10 when the 10 pole HSR is assumed to be an output rotor in which the LSR of 14 poles is connected to the prime-mover. Similarly, the machine is compared with YASA12/14 when the 14 pole LSR is assumed to be an output rotor.

B.3.1 Cogging torque

A comparison of the no-load results of the proposed MG12/5-7 and YASA topologies is firstly obtained. For the magnetically geared machine simulation, the initial positions for HSR and LSR are adjusted at zero. Moreover, for comparison purposes, the cogging torque for one rotor of the YASA machines is individually examined using FEA, which allows the calculation of the cogging torque of each rotor separately. Furthermore, the YASA and AFMGPM machines are driven by a prime-mover at rated speeds. The cogging torques of the HSR of AFMGPM and YASA12/10 machines are compared in Fig. B.2. It is clear that the HSR of the proposed machine has the lowest cogging torque amplitude of 0.03 Nm while amplitudes of the total and individual rotor cogging torques are approximately 0.16 Nm and 0.08 Nm, respectively. Moreover, Fig. B.3 indicates a comparison between the LSR and YASA12/14 cogging torques. As shown, the LSR also has a small cogging torque amplitude of 0.06 Nm compared to the YASA12/14 total and individual cogging torques of 0.24 Nm and 0.12 Nm, respectively.

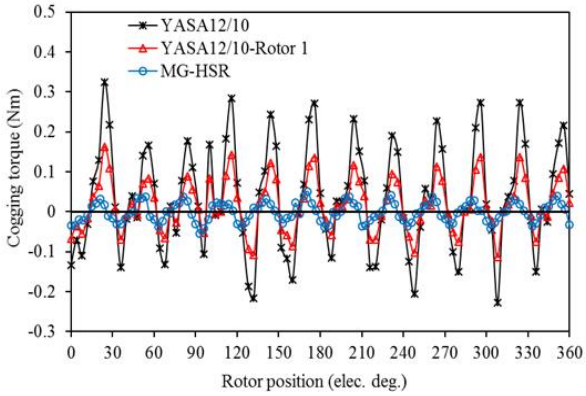

(a) Waveforms

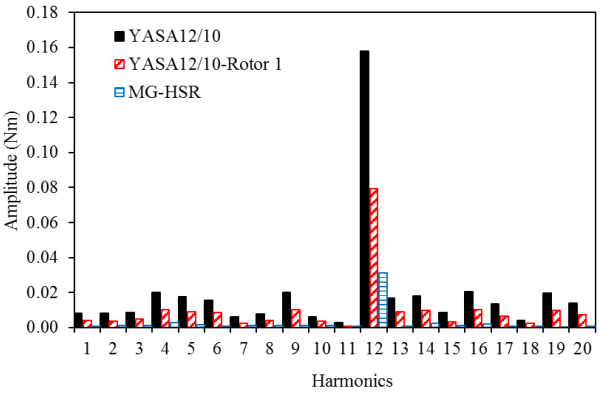

(b) Harmonic spectra

Fig. B.2 Comparison of HSR and YASA12/10 cogging torques and the corresponding harmonics.

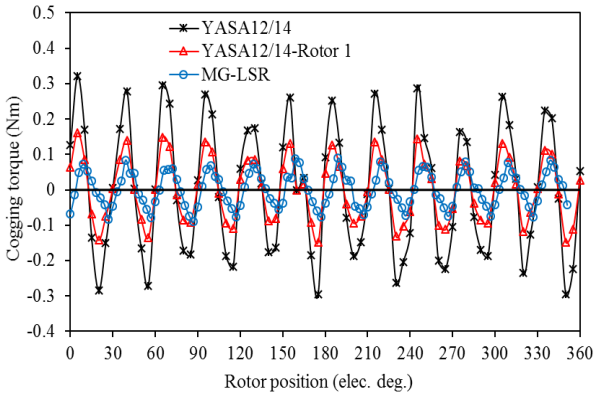

(a) Waveforms

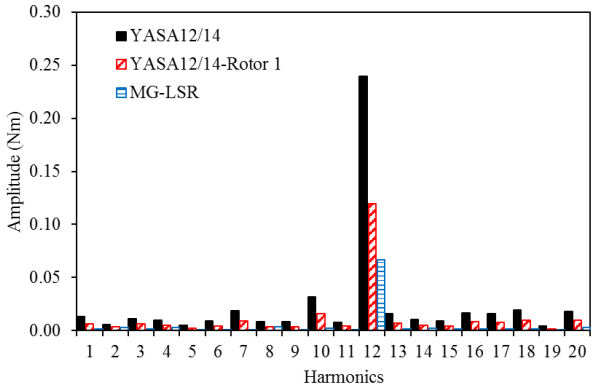

(b) Harmonic spectra

Fig. B.3 Comparison of LSR and YASA12/14 cogging torques and the corresponding harmonics.

B.3.2 No-load air-gap flux density

Fig. B.4 plots a comparison between the air-gap flux density of YASA12/10 and the air-gap flux density measured on the HSR air-gap, together with Fig. B.5 showing the air-gap flux density of YASA12/14 compared to the air-gap flux density of the LSR. The flux density is measured in the middle thickness at the mean circumferential radii of the air-gaps. It is obvious that the fundamental component amplitudes of the HSR and LSR flux density are slightly higher than those of YASA12/10 and YASA12/14, respectively. However, the harmonic profile is almost identical for the compared air-gap flux densities.

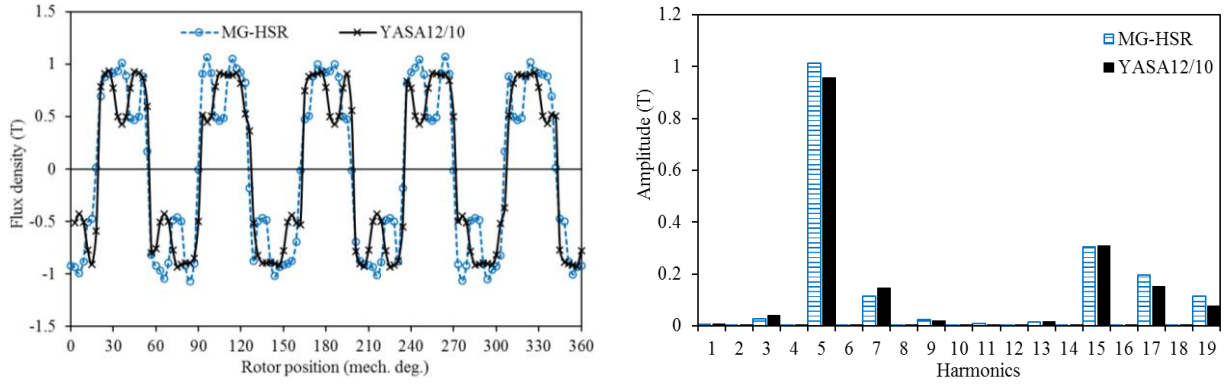

(a) Waveforms (b) Harmonic spectra

Fig. B.4 Comparison of the HSR air-gap flux densities of MG12/5-7 and YASA12/10.

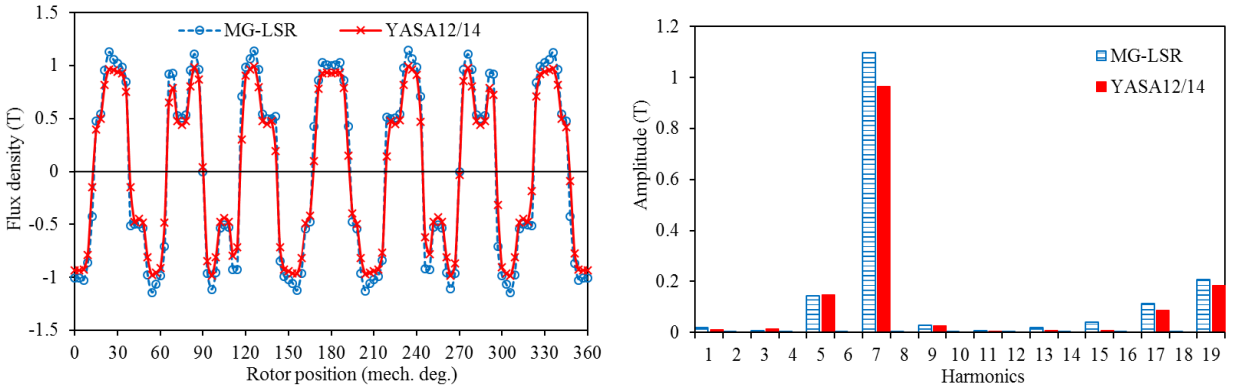

(a) Waveforms (b) Harmonic spectra

Fig. B.5 Comparison of the LSR air-gap flux densities of MG12/5-7 and YASA12/14.

B.3.3 Electromagnetic torque

In addition to the MG and on-load torques, the torque of the AFMGPM machine at no MG effect is obtained and also compared with YASA machine torque. The torque can be obtained when the relative angle is adjusted to zero elec. deg. and the rated current is applied to the stator winding. In this case, only the armature current torque which results from the interaction between the rotor PM field and the current in the stator windings is obtained for both rotors. Fig. B.6 compares the LSR torque with the total and individual rotor torques of YASA12/14 and Fig. B.7 illustrates a comparison between the HSR torque and the torques of YASA12/10. The results indicate that the electromagnetic torques of YASA12/10 and YASA12/14 are significantly higher than HSR and LSR torques, respectively, meaning that the torque of the YASA machines is dominated by both rotors. However, compared to the YASA machines' individual rotor torque, LSR torque is approximately the same as the individual rotor torque of the YASA12/14 machine while HSR is slightly higher than the torque of YASA12/10 produced by one rotor. Moreover, the torques produced by both AFMGPM machine rotors have low torque ripple compared to the YASA machine torque.

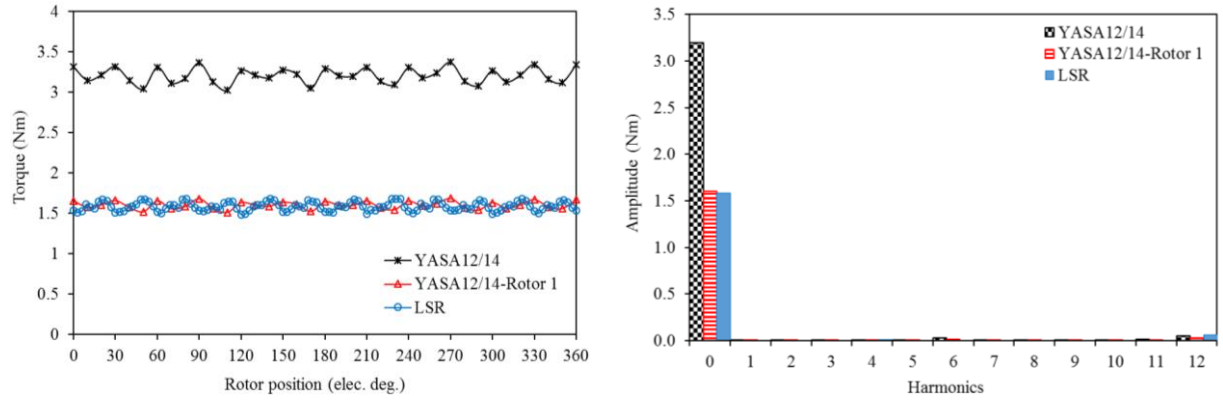

(a) Waveforms (b) Harmonic spectra

Fig. B.6 Comparison of the torque of HSR at no MG effect with the torque of YASA12/10.

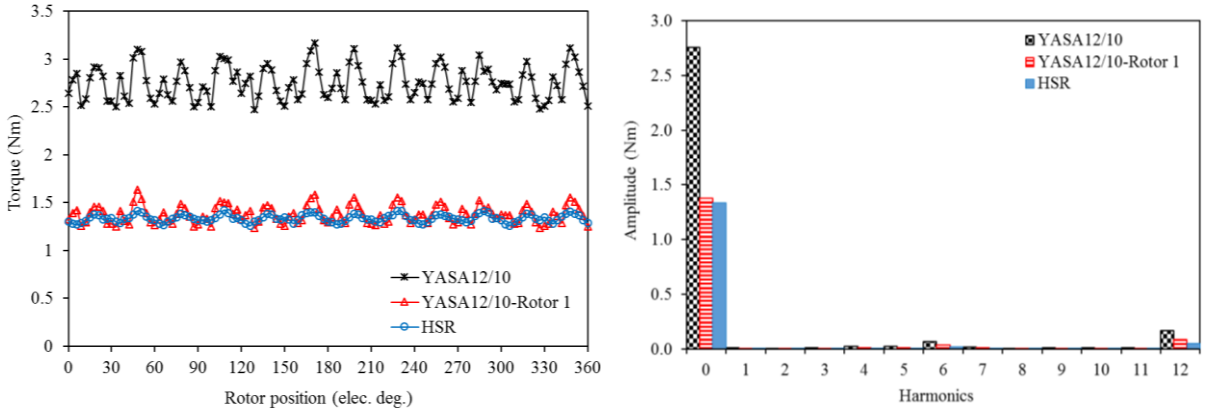

(a) Waveforms (b) Harmonic spectra

Fig. B.7 Comparison of the torque of LSR at no MG effect with the torque of YASA12/10.

B.4 Comparison of MG12/4-8 with conventional YASA12/8 and YASA12/16 machines

Correspondingly, since the MG12/4-8 machine has two rotors in which the HSR and the LSR have 8 and 16 poles, respectively, a performance comparison between this machine and YASA machines is also performed. The performance of YASA12/8 with 8 poles and YASA12/16 with 16 poles at different load conditions is compared with the AFMGPM machine.

B.4.1 Cogging torque

Fig. B.8 compares the HSR cogging torque with total and individual rotor cogging torques of YASA12/8. It can be seen that the cogging torques of both machines are generally high. Moreover, the cogging torque of YASA12/8 has the highest amplitude of approximately 0.8 Nm while the cogging torque amplitude of the HSR is slightly lower by approximately 0.1 Nm. The cogging torque of one rotor of YASA12/8 machine has low amplitude compared to the HSR cogging torque: approximately half of the total cogging torque of YASA12/8. Similarly, the

cogging torques of the LSR and YASA12/16 are compared in Fig. B.9. The LSR has a significantly lower cogging torque amplitude of approximately 0.03 Nm while the total and individual cogging torque amplitudes of YASA12/16 are approximately 0.36 Nm and 0.18 Nm, respectively.

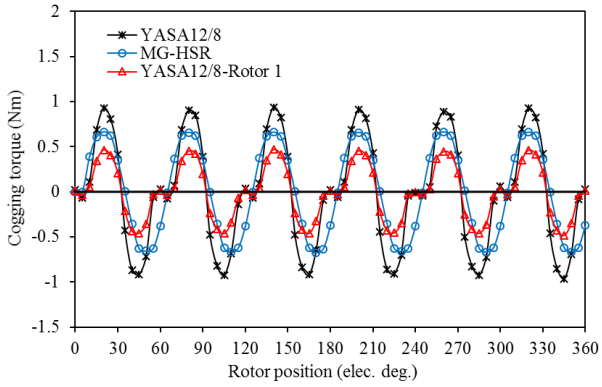

(a) Waveforms

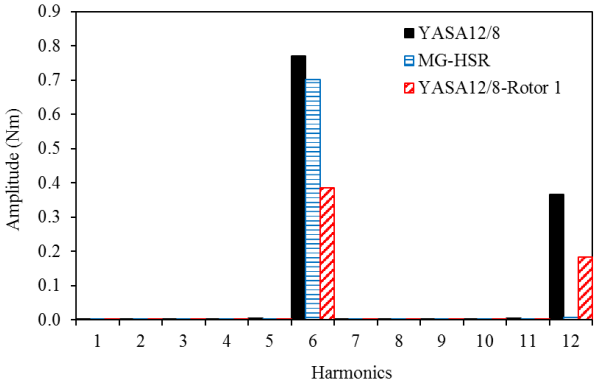

(b) Harmonic spectra

Fig. B.8 Comparison of the cogging torques of HSR and YASA12/8.

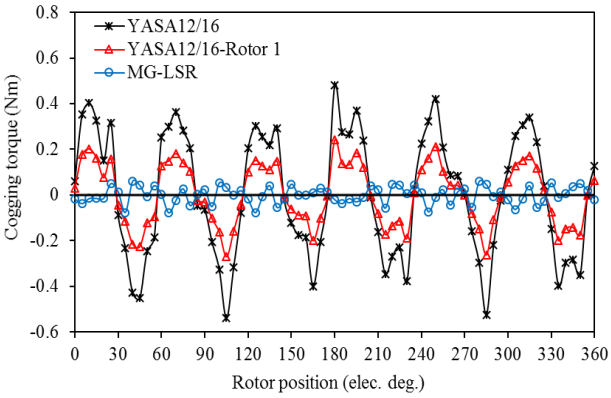

(a) Waveforms

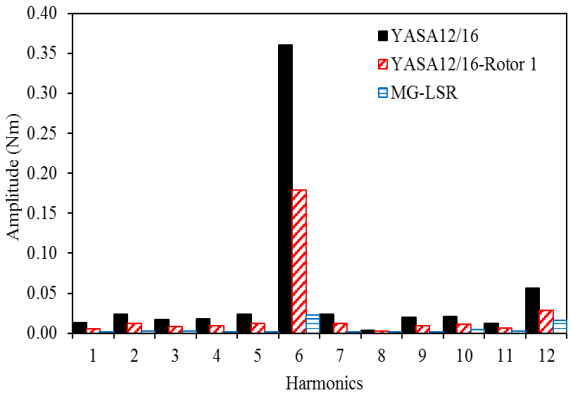

(b) Harmonic spectra

Fig. B.9 Comparison of the cogging torques of LSR and YASA12/16.

B.4.2 No-load air-gap flux density

Fig. B.10 shows a comparison between the air-gap flux densities of HSR and YASA12/8 and Fig. B.11 compares the air-gap flux density measured in the LSR air-gap with the air-gap flux density of YASA12/16. It is obvious that the fundamental harmonic amplitude of flux density of YASA12/8 of approximately 0.95 T is slightly higher than the flux density amplitude of the HSR of 0.85 T. However, the LSR has an amplitude of the fundamental component of just over 1 T while the flux density amplitude of YASA12/16 is approximately 0.95 T. The flux density in Fig. B.10(b) and Fig. B.11(b).

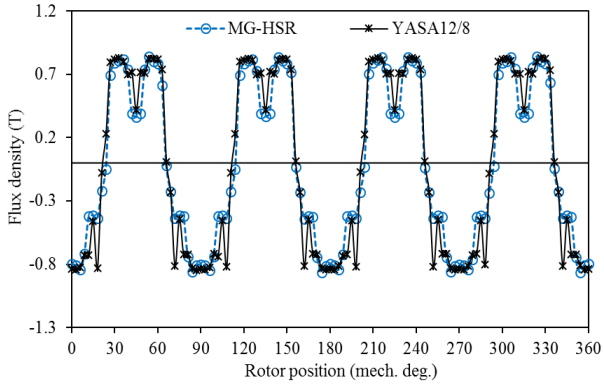

(a) Waveforms

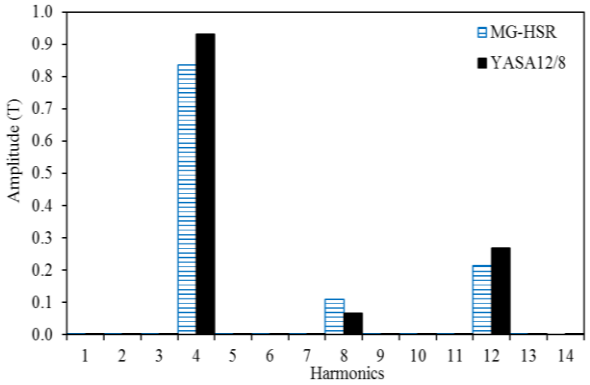

(b) Harmonic spectra

Fig. B.10 Comparison of air-gap flux densities of HSR and YASA12/8.

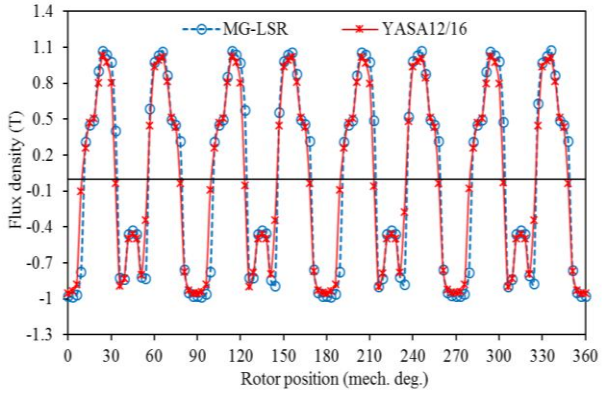

(a) Waveforms

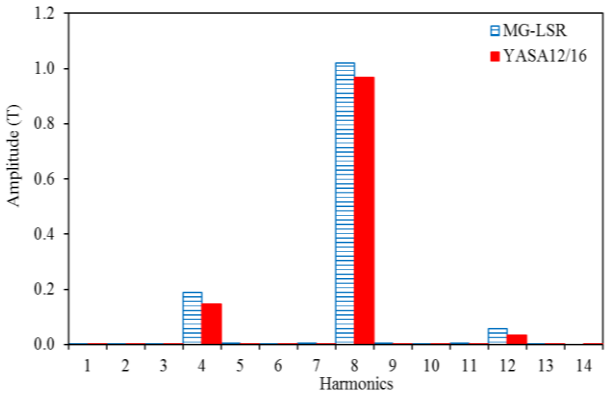

(b) Harmonic spectra

Fig. B.11 Comparison of air-gap flux densities of LSR and YASA12/16.

B.4.3 Electromagnetic torque

Similarly, the HSR and LSR torques are calculated at rated current and at a relative angle between both rotors of zero elec. deg. In this case, the MG effect is cancelled, and the torque obtained by both rotors is due to the armature current only. The LSR and YASA12/16 torques are studied and compared in Fig. B.12. YASA12/16 has a significantly higher total torque of 3.2 Nm, obtained by both rotors; however, the torque obtained by the LSR and torque of the individual rotor of YASA12/16 are approximately the same average torque of approximately 1.55 Nm. Moreover, the HSR and YASA12/8 torques are compared in Fig. B.13. It can be noticed that the torque of YASA12/8 is also high compared to the torque of the HSR of the proposed machine. However, the torque obtained by the HSR of approximately 1.28 Nm is slightly higher than the torque of 1.2 Nm obtained by the individual rotor of YASA12/8.

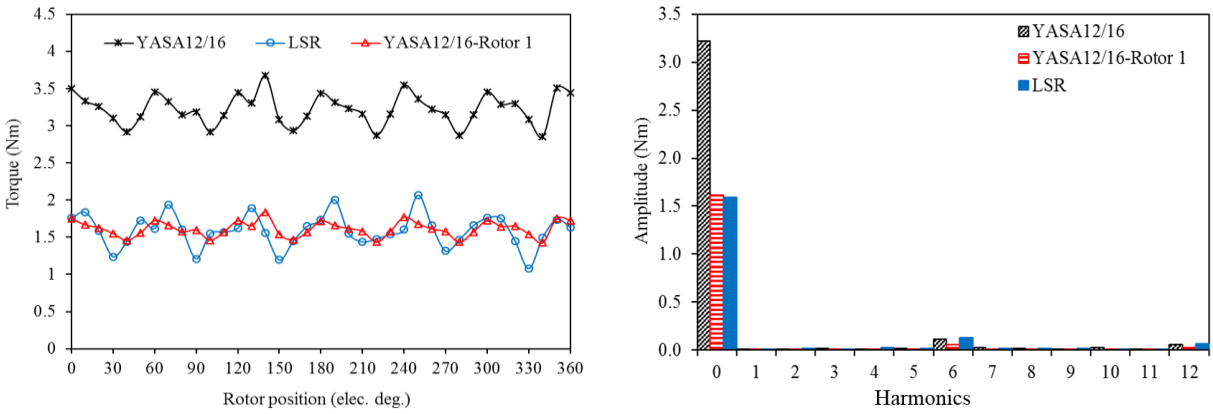

(a) Waveforms (b) Harmonic spectra

Fig. B.12 Comparison of YASA12/16 machine torque with on-load LSR torque at no MG effect.

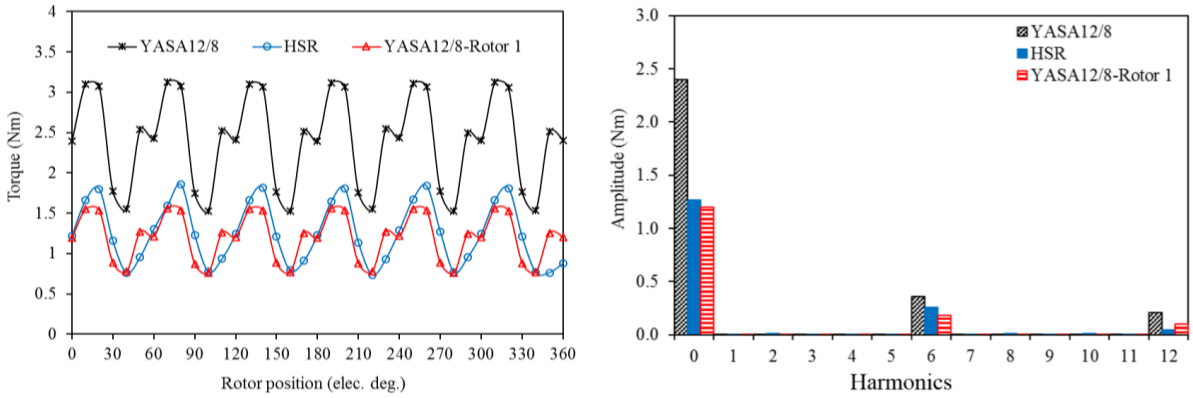

(a) Waveforms (b) Harmonic spectra

Fig. B.13 Comparison of YASA12/8 machine torque with on-load LSR torque at no MG effect.

In addition, the torque performance of the proposed MG12/4-8 machine at different current densities and copper loss is also compared with the YASA machines. Fig. B.14 compares the torque of MG12/4-8 with those of YASA12/16 and YASA12/8 at different current densities. It can be seen that the torque – current density characteristics of all machines are linear. However, when the LSR is assumed as output torque, the LSR has greater torque compared to the total torque of YASA12/16 when the current density is lower than 27 A/mm^2, as can be seen in Fig. B.14(a). Additionally, the HSR has a superior torque over current density up to 17 A/mm^2 compared with YASA12/8, as indicated in Fig. B.14(b). Moreover, in comparing the torque of the individual rotor of the YASA machines, the HSR and LSR always have superior torque performance over the current density range.

Fig. B.15 (a) shows a comparison of the LSR and YASA12/16 torques over the variation of copper loss. Fig. B.15(b) indicates a comparison between the HSR and YASA12/8 at different copper losses. Obviously, the LSR has a greater torque performance at low copper loss range. YASA12/16 has a higher torque performance above copper loss values of approximately 200 W. Moreover, the HSR has larger torque when the copper loss is lower than 100 W when compared with YASA12/8. Fig. B.16 shows a comparison of the output torque per used magnet volume against the current density performance between AFMGPM and YASA machines. It is obvious that both LSR and HSR have higher performance over the current density values compared to the individual rotors of YASA12/16 and YASA12/10, respectively. However, compared to the total torque per PM volume, LSR has a superior performance when the current density is below approximately 25 A/mm^2. The HSR has a higher performance of current density up to 12 A/mm^2.

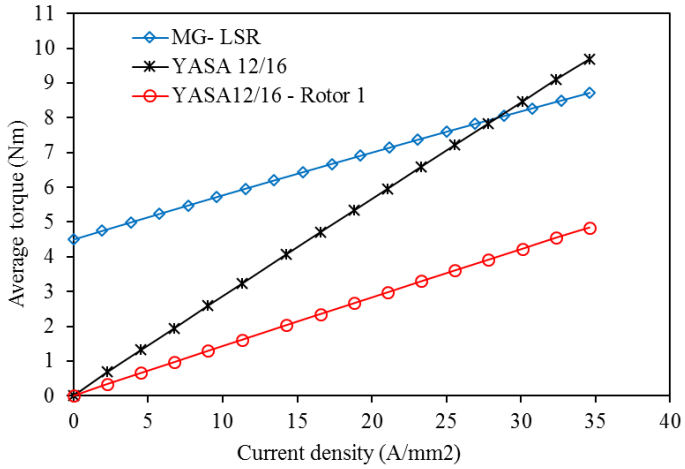

(a) Torque-current density curves of LSR and YASA12/16

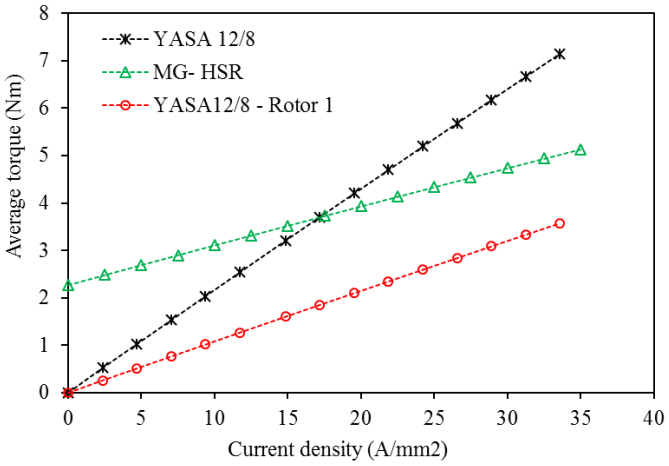

(b) Torque-current density curves of HSR and YASA12/8

Fig. B.14 Comparison of torque – current density curves of MG12/4-8 with YASA12/16 and YASA12/8.

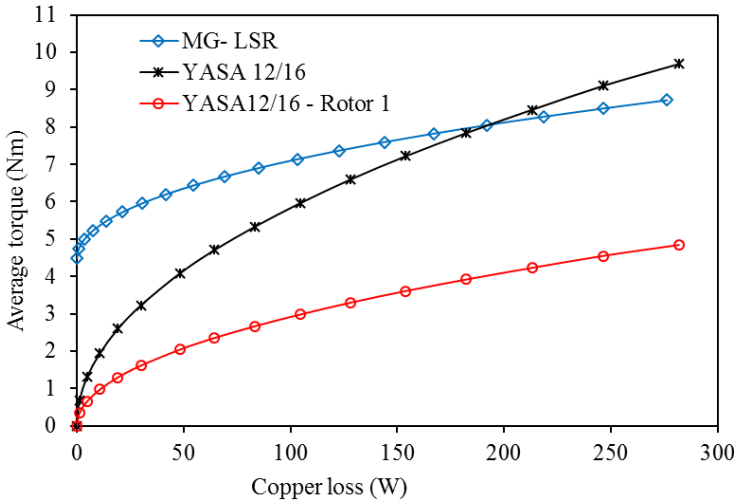

(a) Torque-copper loss curves of LSR and YASA12/16

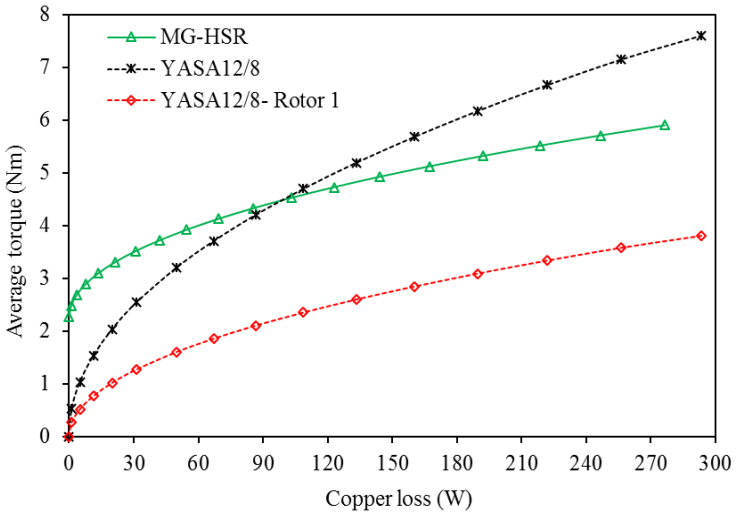

(b) Torque – copper loss curves of HSR and YASA12/8

Fig. B.15 Comparison of torque – copper loss curves of MG12/4-8 with YASA12/16 and YASA12/8.

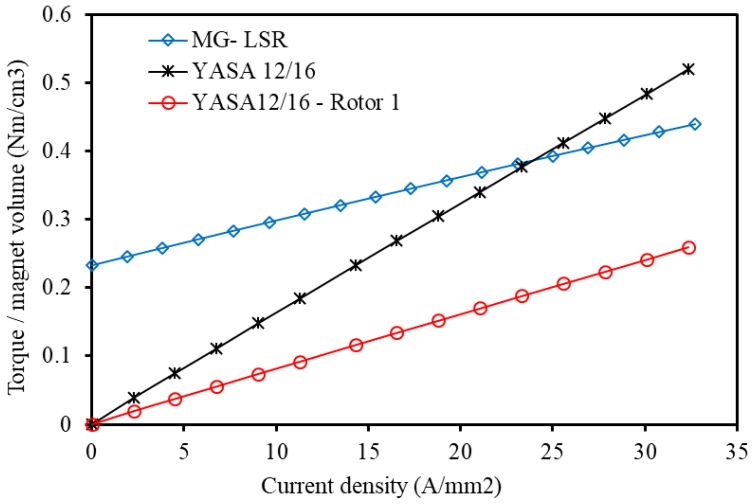

(a) Torque /PM volume – current density curves of LSR and YASA12/16

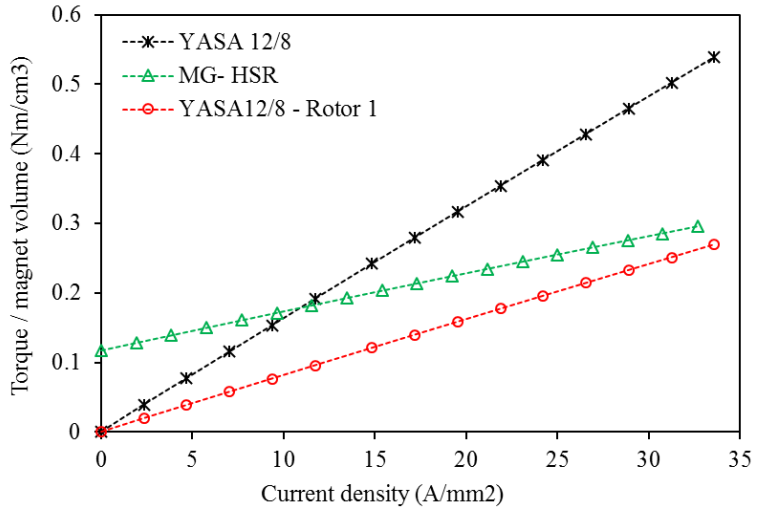

(b) Torque / PM volume – current density curves of HSR and YASA12/8

Fig. B.16 Comparison of torque/PM volume – current density curves of MG12/4-8 with YASA12/16 and YASA12/8.

In addition, when the magnetic gear effect is cancelled, and a rated current is applied to the AFMGPM machine windings, the performance of HSR and LSR torques are compared with the electromagnetic torque of YASA12/16 and YASA12/8, respectively. Fig. B.17 compares the torque at different current densities and Fig. B.18 shows the comparison of torque – copper loss between MG12/4-8 and YASA machine topologies. It can be seen that when the magnetic gearing effect is cancelled for MG12/4-8, the total torque performance over the current density and copper loss variations of the YASA machines is always higher. However, the HSR and LSR torque performances are approximately the same as the individual rotors of YASA12/8 and YASA12/16, respectively, over current density and copper loss variations.

The torque per magnet volume against the current density of both machines is also compared in Fig. B.19. It is clear that the total torque per PM volume performance over the current density of both YASA topologies is higher compared with the proposed MG12/4-8. Moreover, both LSR and HSR have considerably lower torques per PM volume performance at different current densities compared with YASA12/16 and YASA12/8, respectively. It should be noted that more magnet volume is used for MG12/4-8 (19348 mm^3) whereas YASA12/8 and YASA12/16 have a magnet volume of approximately 13270 mm^3 and 17509 mm^3, respectively.

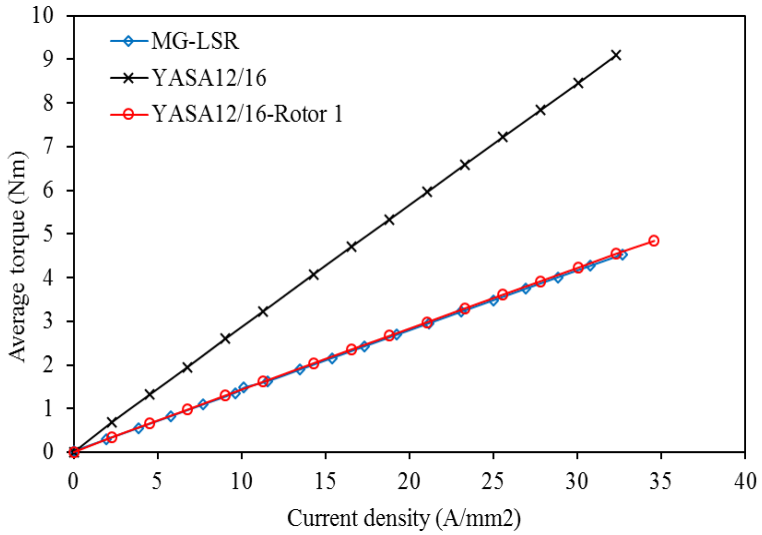

(a) Torque – current density curves of LSR and YASA12/16

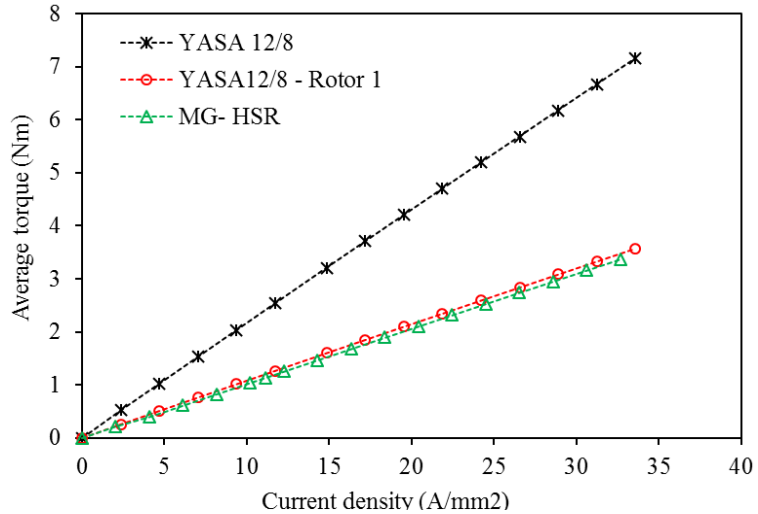

(b) Torque – current density curves of HSR and YASA12/8

Fig. B.17 Comparison of torque – current density curves of MG12/4-8 at no magnetic gear effect with YASA12/16 and YASA12/8.

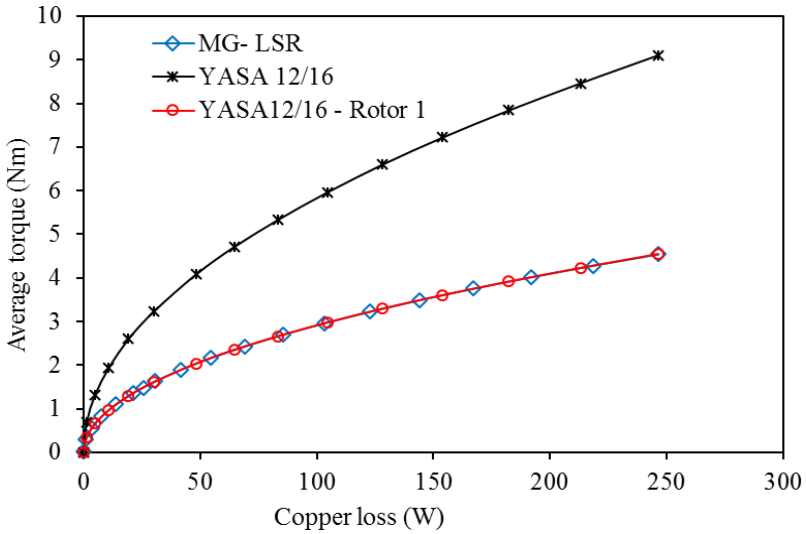

(a) Torque – copper loss curves of LSR and YASA12/16

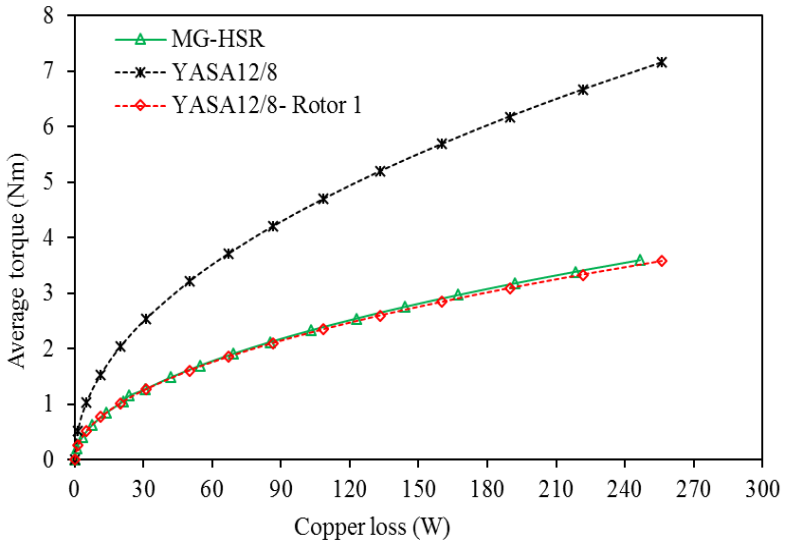

(b) Torque– copper loss curves of HSR and YASA12/8

Fig. B.18 Comparison of torque – copper loss curves of MG12/4-8 at no magnetic gear effect with YASA12/16 and YASA12/8.

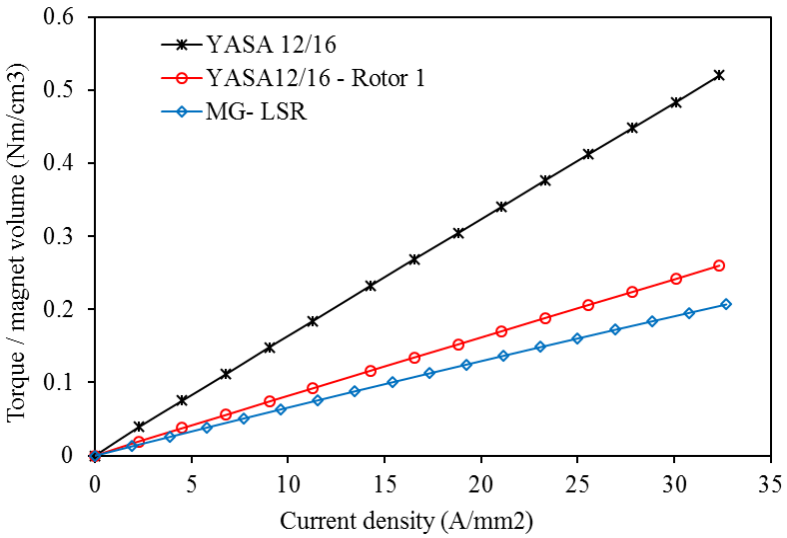

(a) Torque/magnet volume – current density curves of LSR and YASA12/16.

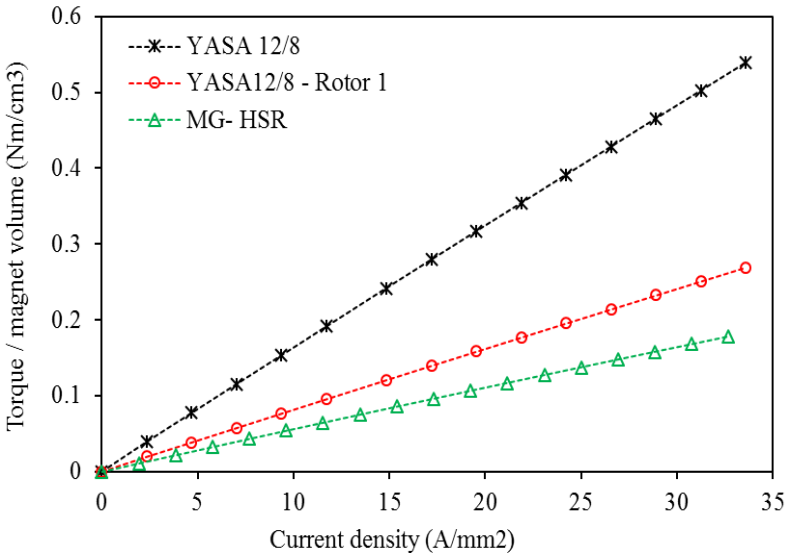

(b) Torque per magnet volume – current density curves of HSR and YASA12/8

Fig. B.19 Comparison of torque per PM volume – current density curves of MG12/4-8 at no MG effect with YASA12/16 and YASA12/8.

B.5 Losses and efficiency

With the aid of 3D-FEA, iron loss and eddy current PM loss have been calculated for the machine topologies. Moreover, since MG12/4-8 has two rotors with different speeds, the iron losses of YASA12/8 and YASA12/10 are calculated at the same speed of HSR (400 rpm). Moreover, the loss of YASA12/16 is calculated at the same speed of LSR of MG12/4-8 (200 rpm) and YASA12/14 at rated speed of 285.7 rpm which is the same speed as LSR of MG12/5-7. The iron and eddy current PM losses in AFMGPM and YASA machine topologies at rated speeds under

no-load condition are compared in Fig. B.20. The compression indicates that MG12/5-7 has higher iron loss and hence higher total losses. However, YASA12/10 has the highest PM loss among the other topologies whereas low PM losses are noted for YASA12/16 and YASA12/14 in which the losses are calculated at low speeds. Moreover, Fig. B.21 compares the on-load iron and eddy current PM losses as well as the corresponding efficiency of the topologies. Overall, the iron and PM eddy current losses slightly increase compared to the no-load condition. Moreover, the efficiency at rated conditions is calculated and compared. The copper loss is assumed to be constant of 30 W for all topologies. It is clear that in spite of a relatively high iron loss of MG12/5-7, a superior efficiency of approximately 86 % is obtained due to higher output torque compared to the other topologies. However, YASA12/16 has a significant low efficiency as it is calculated at low speed.

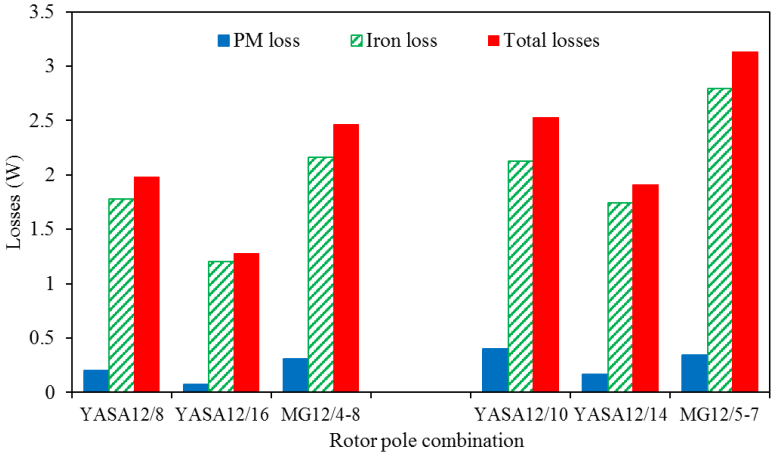

Fig. B.20 Comparison of no-load losses of the proposed magnetically geared machine topologies with YASA machine topologies.

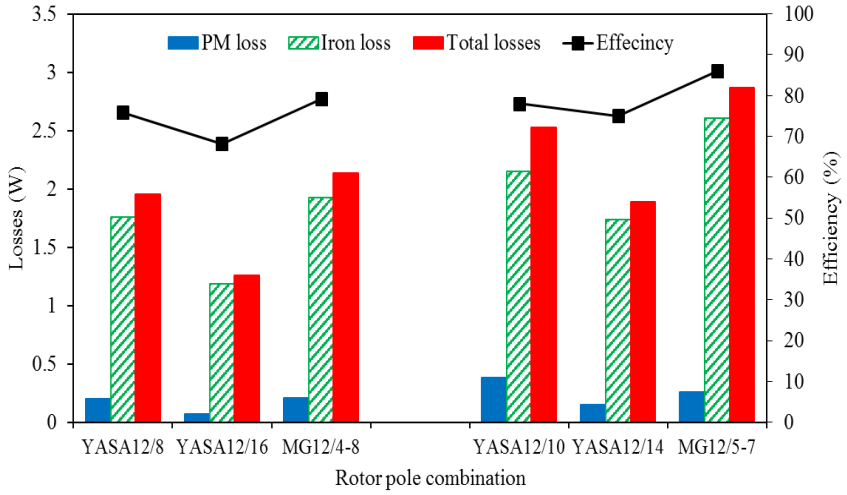

Fig. B.21 Comparison of on-load losses and efficiency of the proposed magnetically geared machine topologies with YASA machine topologies.

B.6 Summary

A comparative study of AFMGPM topologies with the corresponding YASA machine topologies has been performed and investigated with the aid of 3D-FEA. Two AFMGPM topologies are compared with four YASA machine topologies: the performance of MG12/5-7 is compared to YASA12/10 and YASA12/14; MG12/4-8 is compared to YASA12/8 and YASA12/16. The no-load performances, such as cogging torque, flux density, flux linkage and back EMF, have been analysed and compared. Moreover, the torque performance of the AFMGPM machine at different load conditions is compared to the torque of YASA topologies. The simulation results show that a significantly lower cogging torque can be obtained by the proposed machine compared with the YASA machine. Moreover, the back EMF amplitude of MG12/5-7 is higher than YASA12/14 and slightly lower than YASA12/10 when calculated at rated speeds. Moreover, the proposed machine compared with the YASA machine can obtain a significantly higher torque density at no-load and on-load conditions. Furthermore, the torque performance is higher when the LSR is considered as an output rotor. In addition, the HSR and LSR of the proposed machine have higher torque performance compared to the YASA machines' individual rotor torques.

As indicated by the data presented in this Chapter, it can be concluded that the proposed magnetically geared machine has high performance in any operating condition. In other words, the proposed machine has high torque and efficiency at MG and magnetically geared machine modes. Moreover, when the MG effect is cancelled and with the benefit of two different pole rotors, the proposed machine can work as two synchronous PM machines with different speeds and torques, which cannot be achieved with a conventional YASA machine.

APPENDIX C.

MATERIAL CHARACTERISTICS

C.1 **Soft magnetic composite material characteristics**

SMC material has been used for the FEA of the machines in this thesis. This material is widely used for AFPM machines due to its manufacturing simplicity as well as low iron loss. Typical B-H curve characteristic is shown in Fig.C.1. Moreover, the material iron loss variation with the frequency of the flux density is plotted in Fig. C.2.

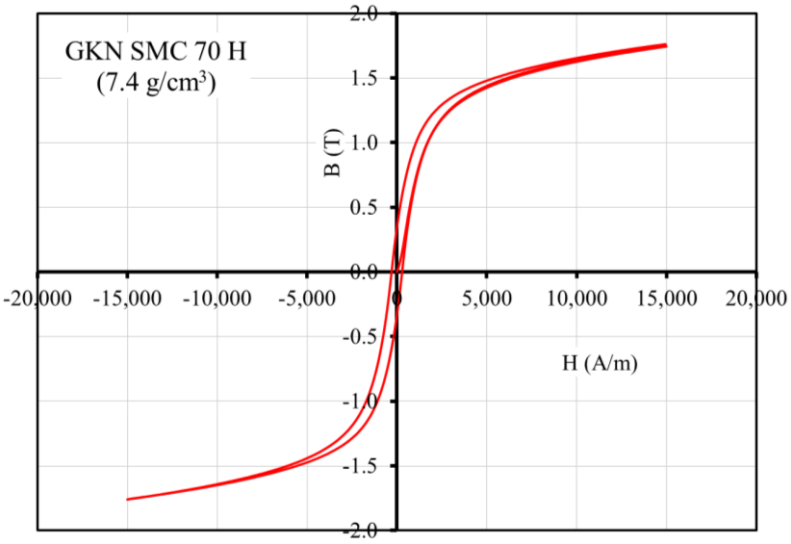

Fig.C.1. B-H curve characteristic of SMC material.

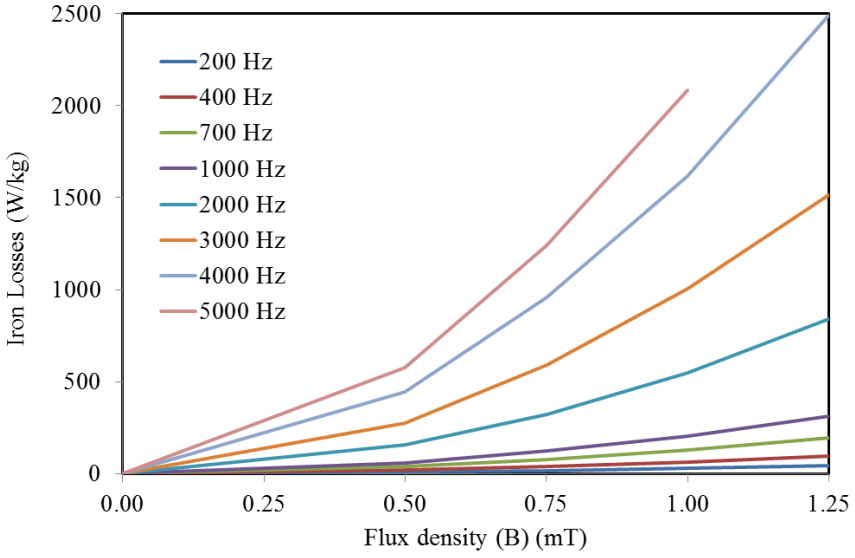

Fig. C.2. Iron loss characteristics for different flux density amplitudes and frequencies.

C.2 **Mild steel lamination B-H curve**

Laminated steel has been utilised for the stator segments of the prototype machine. The B-H curve of the material is obtained in Fig. C.3.

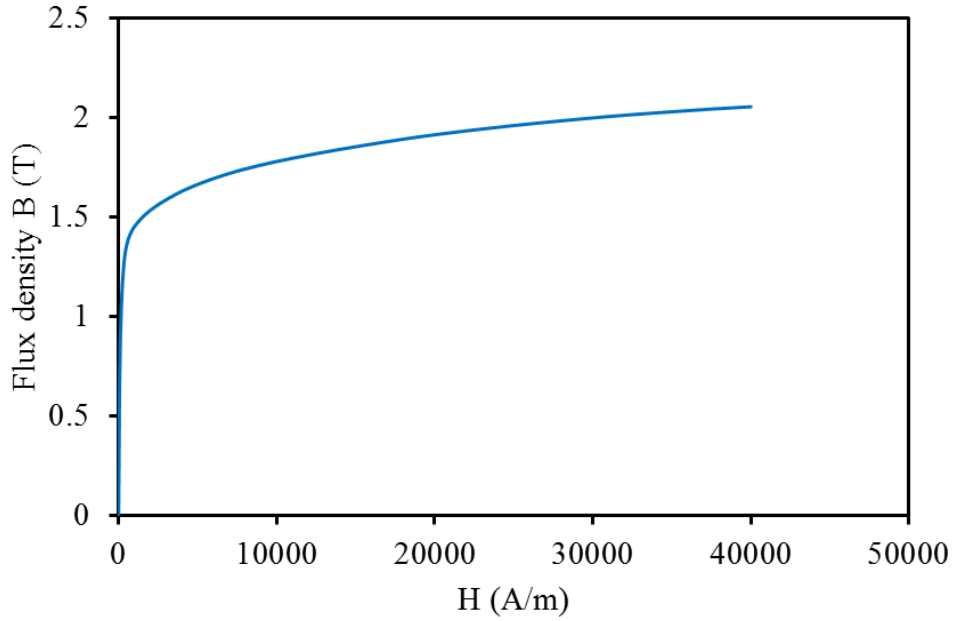

Fig. C.3. B-H curve characteristic of mild steel lamination.

APPENDIX D.

PROTOTYPE DESIGN DRAWINGS

For experimental test purposes, the proposed AFMGPM machine and the YASA machine are designed. The construction and the prototype used materials are explained in Fig. D.1 With 12 stator segments and two identical 10 rotor pole rotors in which both rotor shafts are physically connected to each other. The YASA prototype construction and dimensions are shown in Fig. D.2 (a). For the same prototype of YASA machine, the proposed AFMGPM prototype is assembled by replacing one 10 pole rotor by 14 pole rotor as indicated in Fig. D.2 (b). In this case, both rotors are connected utilising axial thrust bearing to allow free rotating of both rotors. The rotor connection diagram of both machines is indicated in Fig. D.3. In addition, Fig. D.4, shows the details of the prototype parts and their dimensions.

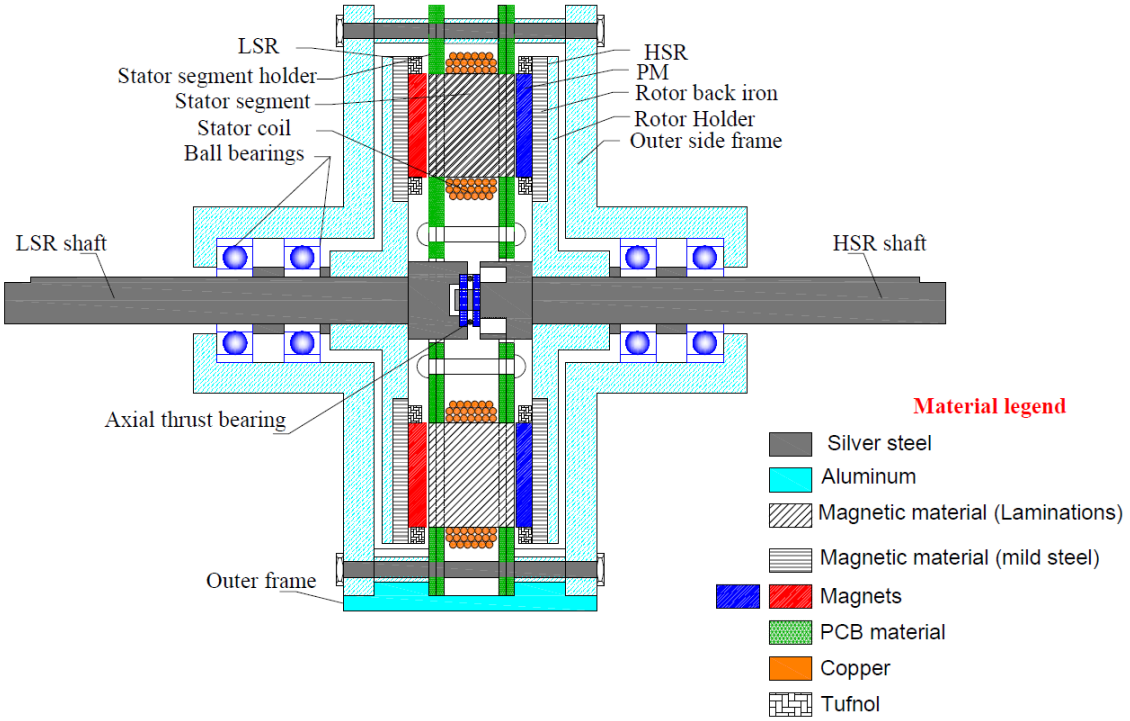

Fig. D.1. Prototype machine and material legends.

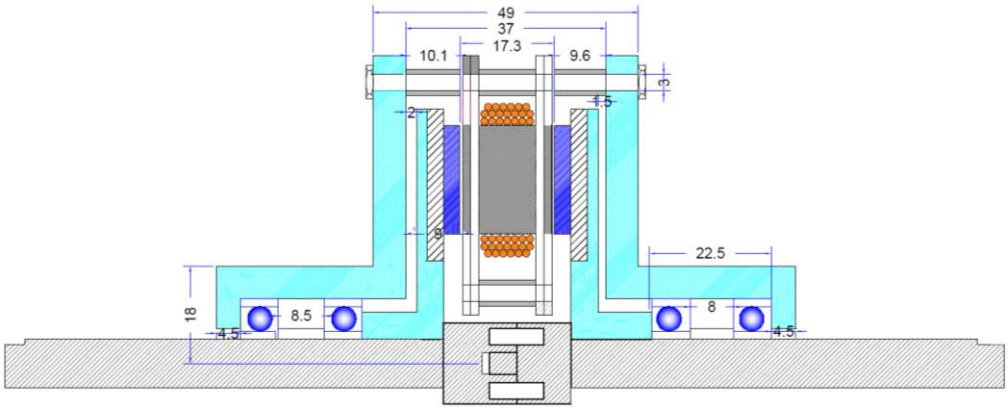

(a) YASA machine

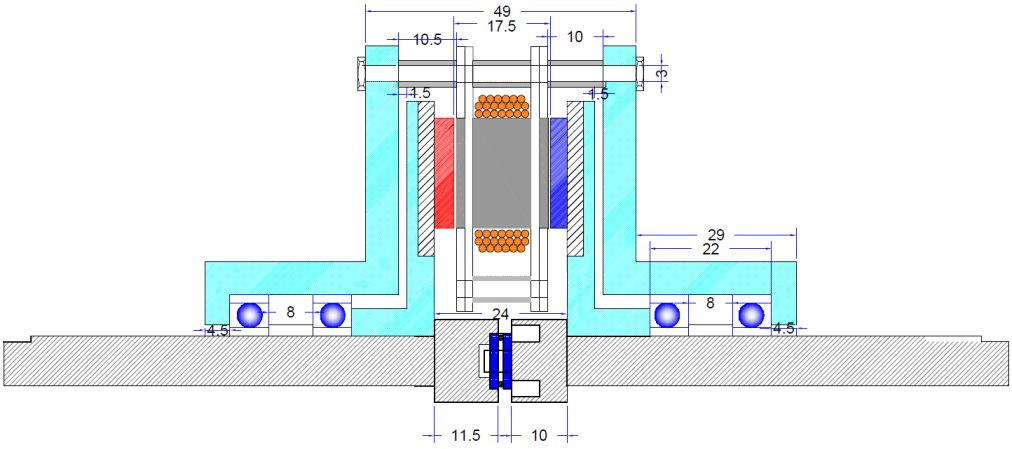

(b) AFMGPM machine

Fig. D.2. Prototype dimensions.

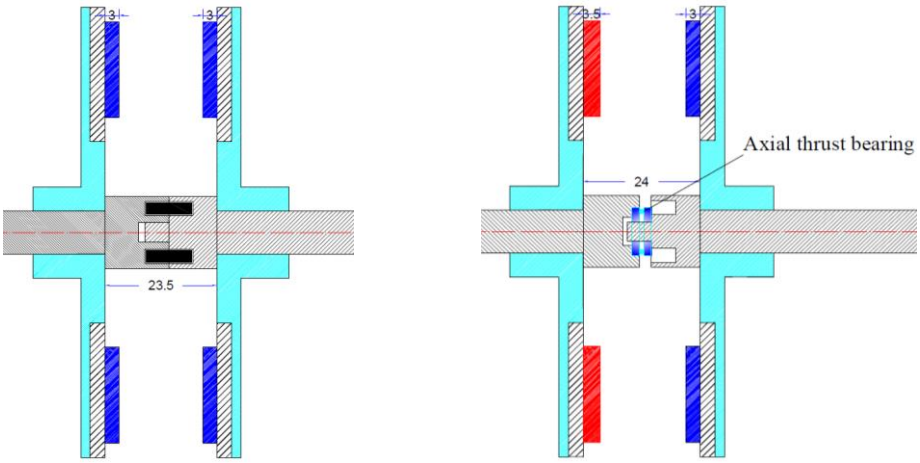

(a) YASA machine rotors (b) AFMGPM machine rotors

Fig. D.3. Assembled machine rotors.

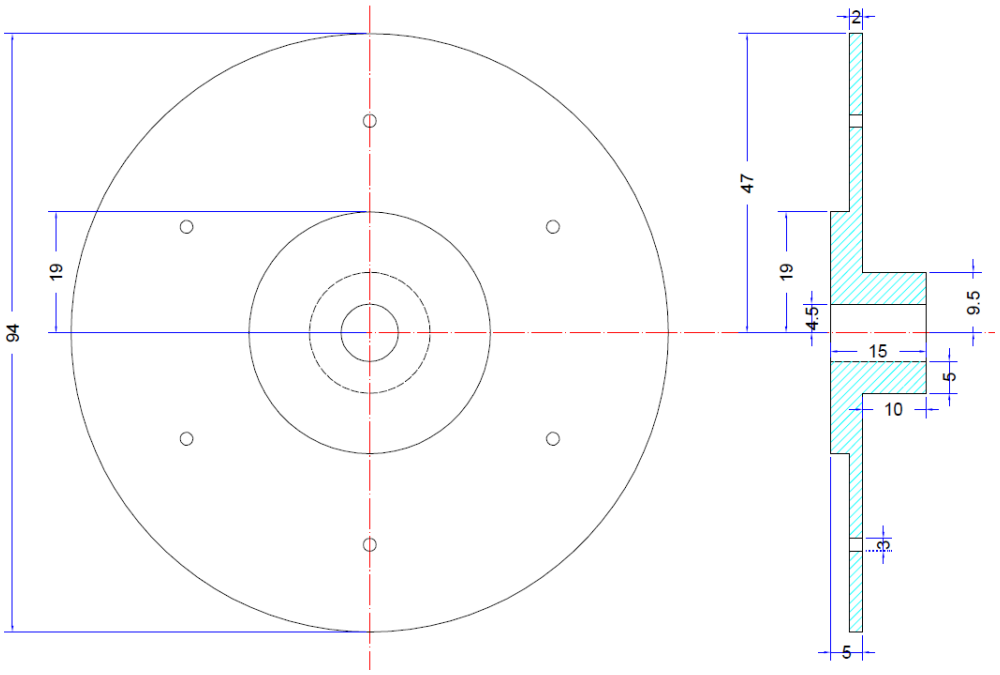

(a) Rotor holder

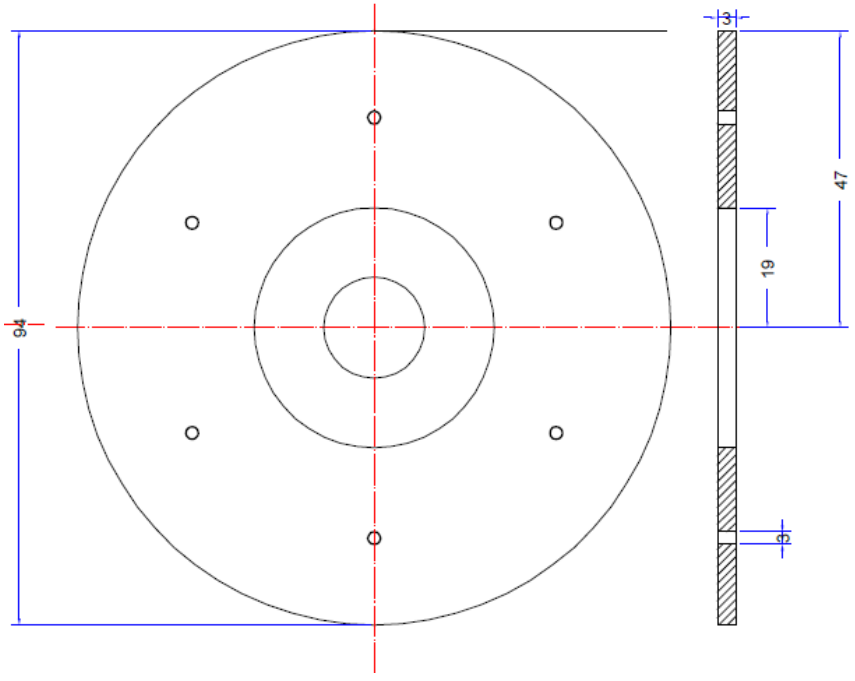

(b) Rotor back iron

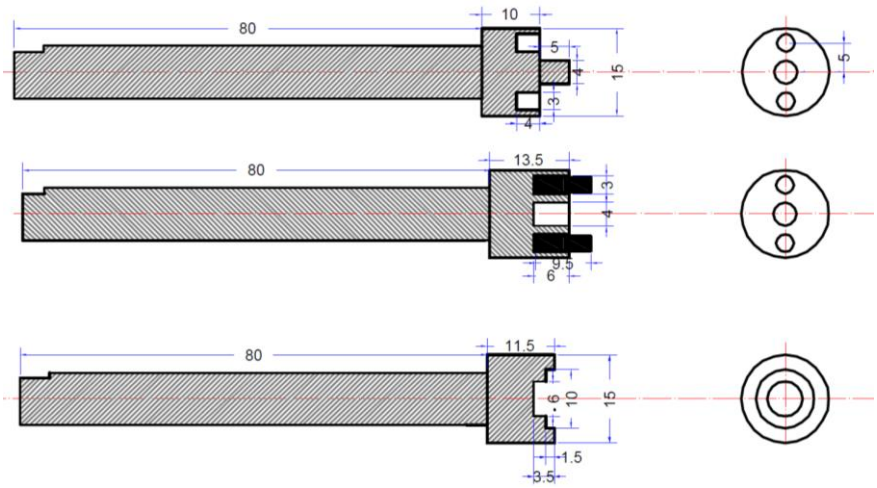

(c) Rotor shaft details

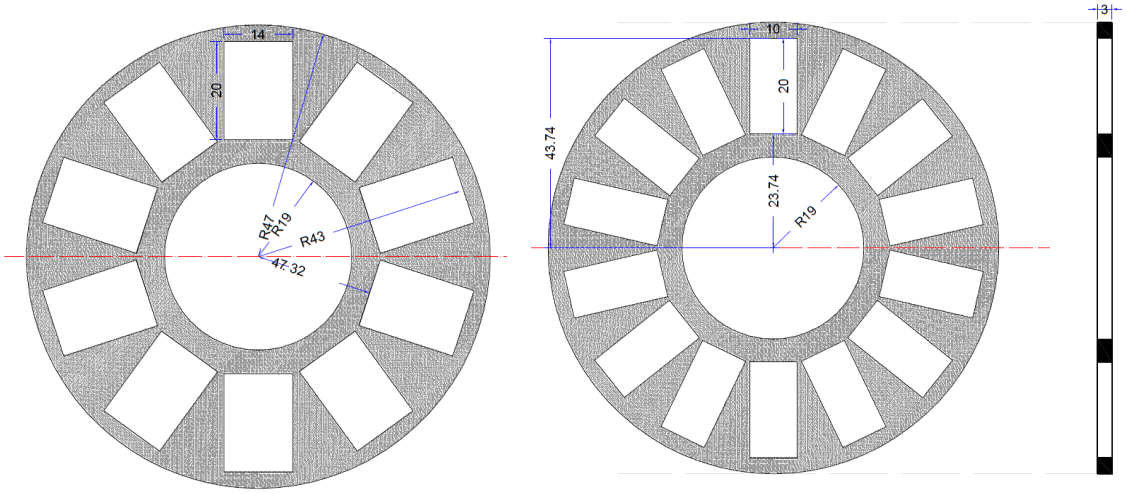

(d) Rotor magnet holders

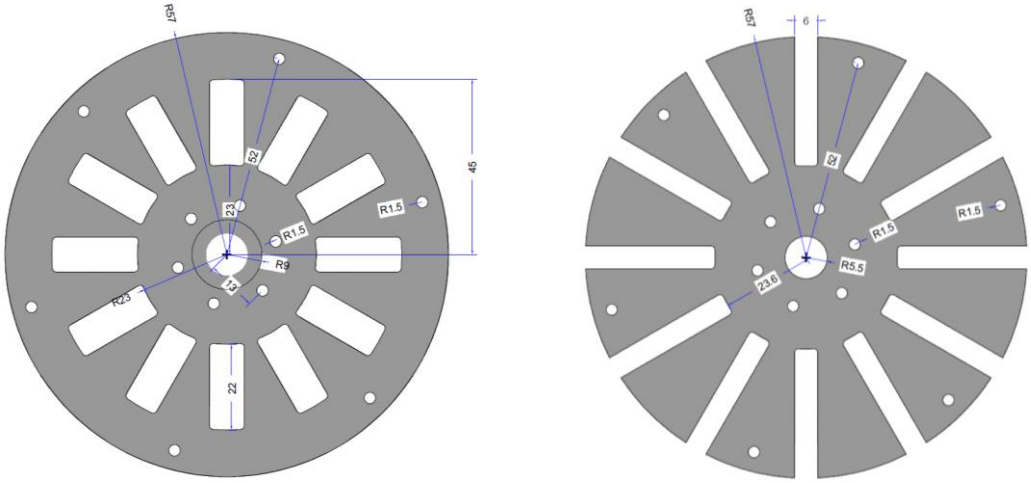

(e) Stator segment holders

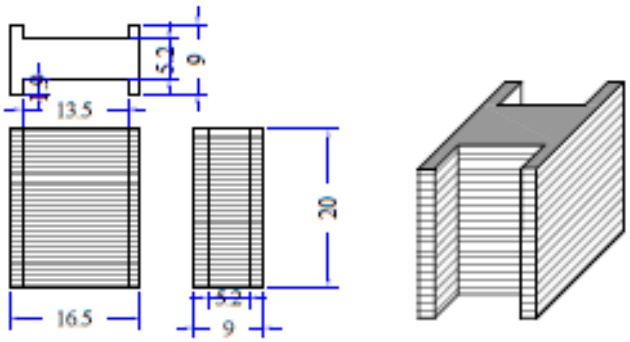

(f) Stator segment

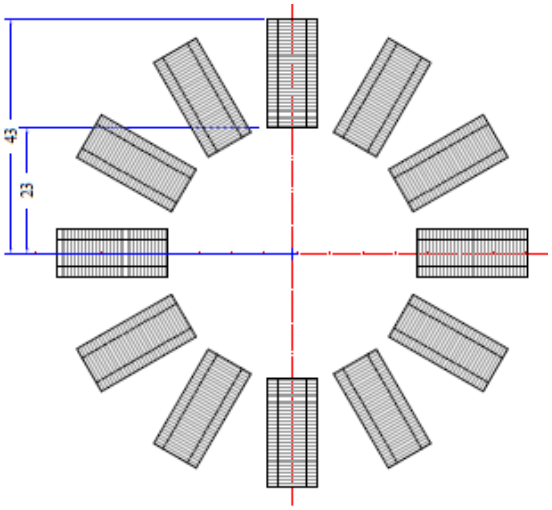

(g) Stator segment arrangement

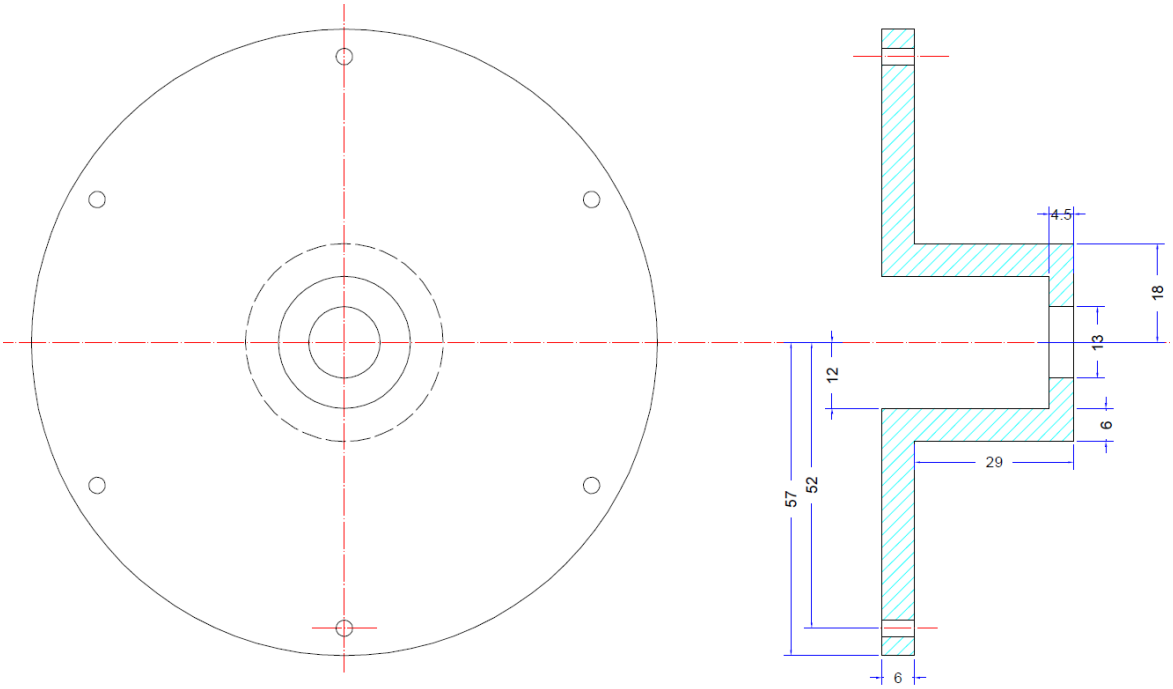

(h) Prototype side frame

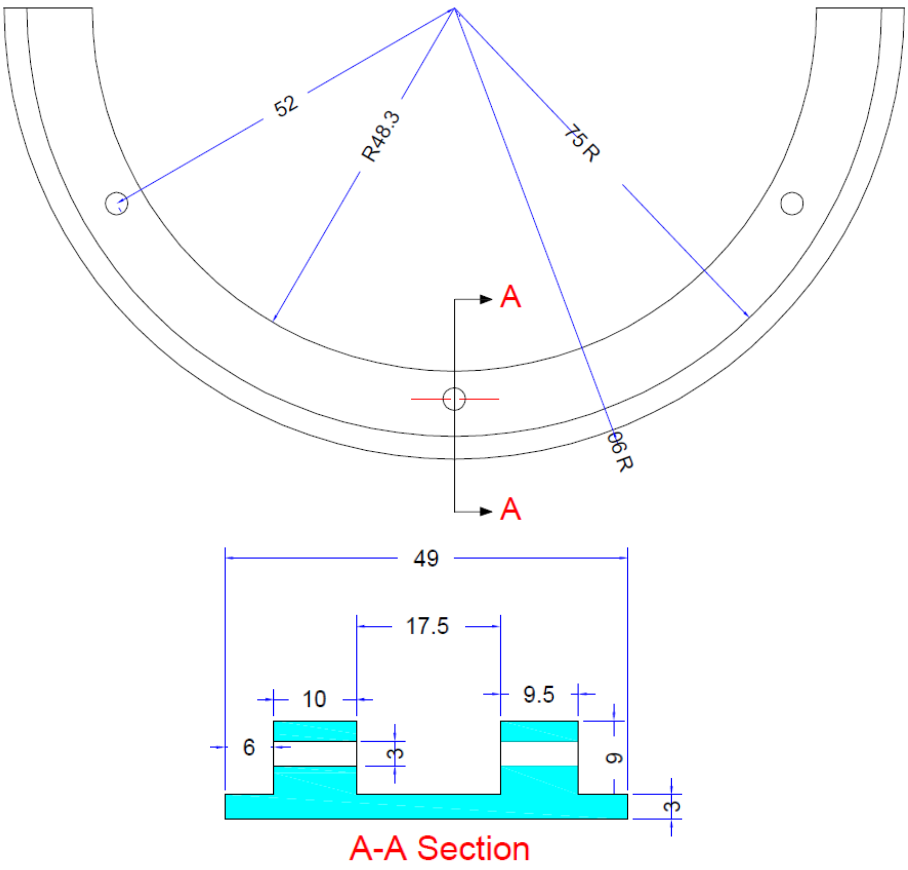

(i) Prototype outer frame

Fig. D.4. Construction and dimensions of prototype parts.